

Final Report

Title: Investigation of Innovative Lightcraft Designs for Hypersonic Air Breathing and Rocket Flight by Beamed Energy Propulsion

AFOSR/AOARD Reference Number: AOARD-FA2386-09-1-4088

AFOSR/AOARD Program Manager: Ponnappan Rengasamy

Period of Performance: June 1 2009 – May 31 2012

Submission Date: June 2012

PI: Dr Con Doolan, University of Adelaide
Dr Vince Wheatley, University of Queensland
David Froning, University of Adelaide

Report Documentation Page				Form Approved OMB No. 0704-0188	
Public reporting burden for the collection of information is estimated to average 1 hour per response, including the time for reviewing instructions, searching existing data sources, gathering and maintaining the data needed, and completing and reviewing the collection of information. Send comments regarding this burden estimate or any other aspect of this collection of information, including suggestions for reducing this burden, to Washington Headquarters Services, Directorate for Information Operations and Reports, 1215 Jefferson Davis Highway, Suite 1204, Arlington VA 22202-4302. Respondents should be aware that notwithstanding any other provision of law, no person shall be subject to a penalty for failing to comply with a collection of information if it does not display a currently valid OMB control number.					
1. REPORT DATE 03 JUN 2012		2. REPORT TYPE Final		3. DATES COVERED 01-06-2009 to 31-05-2012	
4. TITLE AND SUBTITLE Investigation of Innovative Lightcraft Designs for Hypersonic Air Breathing and Rocket Flight by Beamed Energy Propulsion				5a. CONTRACT NUMBER FA23860914088	
				5b. GRANT NUMBER	
				5c. PROGRAM ELEMENT NUMBER	
6. AUTHOR(S) Con Doolan				5d. PROJECT NUMBER	
				5e. TASK NUMBER	
				5f. WORK UNIT NUMBER	
7. PERFORMING ORGANIZATION NAME(S) AND ADDRESS(ES) University of Adelaide,North TCE,Adelaide, Australia,SA 5005,AU,5005				8. PERFORMING ORGANIZATION REPORT NUMBER N/A	
9. SPONSORING/MONITORING AGENCY NAME(S) AND ADDRESS(ES) AOARD, UNIT 45002, APO, AP, 96338-5002				10. SPONSOR/MONITOR'S ACRONYM(S) AOARD	
				11. SPONSOR/MONITOR'S REPORT NUMBER(S) AOARD-094088	
12. DISTRIBUTION/AVAILABILITY STATEMENT Approved for public release; distribution unlimited					
13. SUPPLEMENTARY NOTES					
14. ABSTRACT The report has three parts: 1) Lightcraft inlet design: The work outlines the innovative streamtraced design methodology and a number of suitable lightcraft inlet designs. It also contains an analysis of laser detonation, a system level analysis of lightcraft flight and analysis of a ground test model. 2) Experimental ground testing. The lightcraft design documented in Part 1 was tested at the University of Southern Queensland's hypersonic test facility. This report documents these tests that include both flow visualization and surface pressure measurements for a range of angles of attack. 3) Future flight test program. A feasibility study was performed to investigate how a future lightcraft test program may be conducted. A multi-part test program is described including trajectory and cost estimates.					
15. SUBJECT TERMS Propulsion, Beamed Energy Propulsion, lightcraft					
16. SECURITY CLASSIFICATION OF:			17. LIMITATION OF ABSTRACT Same as Report (SAR)	18. NUMBER OF PAGES 250	19a. NAME OF RESPONSIBLE PERSON
a. REPORT unclassified	b. ABSTRACT unclassified	c. THIS PAGE unclassified			

Summary

This document contains the final report for AOARD-FA2386-09-1-4088 "Investigation of Innovative Lightcraft Designs for Hypersonic Air Breathing and Rocket Flight by Beamed Energy Propulsion".

The report has three parts, listed below.

Part 1: Lightcraft inlet design. The work conducted on the design of suitable inlets for a lightcraft is contained in a Masters thesis by Alan Harrland. The thesis outlines the innovative streamtraced design methodology and a number of suitable lightcraft inlet designs. It also contains an analysis of laser detonation, a system level analysis of lightcraft flight and analysis of a ground test model.

Part 2: Experimental ground testing. The lightcraft design documented in Part 1 was tested at the University of Southern Queensland's hypersonic test facility. This report documents these tests that includes both flow visualisation and surface pressure measurements for a range of angles of attack.

Part 3: Future flight test program. A feasibility study was performed to investigate how a future lightcraft test program may be conducted. A multi-part test program is described including trajectory and cost estimates.

Part 1

Lightcraft inlet design

HYPERSONIC INLET FOR A LASER POWERED PROPULSION SYSTEM

Alan Harrland

Master of Philosophy (Engineering)

March 2012

School of Engineering, Computer and Mathematical Sciences



THE UNIVERSITY OF ADELAIDE

Statement of originality

This work contains no material which has been accepted for the award of any other degree or diploma in any university or other tertiary institution to Alan Harrland and, to the best of my knowledge and belief, contains no material previously published or written by another person, except where due reference has been made in the text. I give consent to this copy of my thesis, when deposited in the University Library, being made available for loan and photocopying, subject to the provisions of the Copyright Act 1968. I also give permission for the digital version of my thesis to be made available on the web, via the University's digital research repository, the Library catalogue, the Australasian Digital Theses Program (ADTP) and also through web search engines, unless permission has been granted by the University to restrict access for a period of time.

I also permit use and modification of the codes contained in the appendices of this body of work, on the provision that any modifications are made available in the public domain.

Alan Harrland

March 2012

Abstract

The idea of laser powered lightcraft was first conceptualised in the early 1970's as a means of launching small scale satellite payloads into orbit at a much lower cost in comparison to conventional techniques. Propulsion in the lightcraft is produced via laser induced detonation of the incoming air stream, which results in the energy source for propulsion being decoupled from the vehicle. In air breathing mode the lightcraft carries no onboard fuel or oxidiser, allowing theoretically infinite specific impulses to be achieved. Recently interest has been renewed in this innovative technology through cross-continent and industry research programs aimed at making laser propulsion a reality.

In a ground launched satellite, the vehicle must travel through the atmosphere at speeds greatly in excess of the speed of sound in order to achieve the required orbital velocities. Supersonic, and in particular hypersonic, flight regimes exhibit complicated physics that render traditional subsonic inlet design techniques inadequate. The laser induced detonation propulsion system requires a suitable engine configuration that offers good performance over all flight speeds and angles of attack to ensure the required thrust is maintained throughout the mission. Currently a hypersonic inlet has not been developed for the laser powered lightcraft vehicle.

Stream traced hypersonic inlets have demonstrated the required performance in conventional hydrocarbon fuelled scramjet engines. This design technique is applied to the laser powered lightcraft vehicle, with its performance evaluated against the traditional lightcraft inlet design. Four different hypersonic lightcraft inlets have been produced employing both the stream traced inlet design methodology, and traditional axi-symmetric inlet techniques. This thesis outlines the inlet design methodologies employed, with a detailed analysis of the performance of the lightcraft inlet at angles of attack and off-design conditions. Fully three-dimensional turbulent computational fluid dynamics simulations have been performed on a variety of inlet configurations. The performance of the lightcraft inlets have been evaluated at differing angles of attack. An idealised laser detonation simulation has also been performed to verify that the lightcraft inlet does not unstart during the laser powered propulsion cycle.

Acknowledgements

Firstly and foremost I would like to sincerely thank my supervisors Con, Vince and Dave. All have helped the development of my research and thesis farther than what I had ever thought capable of. I would particularly like to thank Con for his continued guidance, patience and encouragement above and beyond what would be reasonably expected from a supervisor. I would also like to extend my gratitude to the University of Adelaide staff within the School of Mechanical engineering for making all the other necessary house-keeping tasks as smooth as possible.

I would secondly like to thank the Asian Office for Aerospace Research and Development for their generous support of this research. Without their support it would not have been possible to simulate and build the lightcraft inlet design.

Finally I would like to thank my friends and family for their support and guidance throughout my research. Without their help I would not have been able to get to where I am today.

Contents

1	Introduction	1
1.1	Background information	1
1.1.1	What is a lightcraft	1
1.1.2	Current flight achievements	3
1.1.3	Current limitations/design challenges	3
1.2	Aim of thesis	4
1.3	Remainder of thesis	5
1.4	Outline of new work contained in thesis	6
2	Literature review	7
2.1	Introduction	7
2.2	Laser propulsion system	7
2.2.1	Introduction	7
2.2.2	Modelling of the laser induced detonation process	9
2.2.3	Research developments	15
2.3	The lightcraft vehicle inlet	17
2.4	Hypersonic inlet design	21
2.4.1	Introduction	21
2.4.2	Stream traced inlet design	24
2.4.3	Hypersonic inlet design issues	36
2.5	Summary and conclusions	40
2.5.1	Gap statement	41
3	System level analysis	43
3.1	Introduction	43
3.2	Flight path model	43
3.3	Aerodynamic model	45
3.4	Propulsion model	48
3.4.1	Numerical simulation verification	51
3.5	Flight path results	52
3.6	Summary and Conclusions	59

4	Inlet design	61
4.1	Introduction	61
4.2	Conical forebody	62
4.3	Axi-symmetric inlet	63
4.4	Stream traced axi-symmetric inlet	66
4.4.1	Inlet design methodology	66
4.4.2	Stream traced inlet design code - streamTracer	70
4.4.3	Inlet truncation	74
4.5	Stream traced modular axi-symmetric inlet	78
4.6	Stream traced modular scalloped inlet	80
4.7	Inlet performance parameters	82
4.8	Summary and conclusions	83
5	Numerical Analysis	85
5.1	Introduction	85
5.2	Mesh refinement study	87
5.3	Axi-symmetric inlet design	90
5.3.1	Numerical results at Mach 8 conditions	90
5.3.2	Numerical results at Mach 5 conditions	99
5.4	Axi-symmetric stream traced inlet design	102
5.4.1	Numerical results at Mach 8 conditions	102
5.4.2	Numerical results at Mach 5 conditions	108
5.5	Stream traced axi-symmetric modular inlet design	113
5.5.1	Numerical results at Mach 8 conditions	113
5.5.2	Numerical results at Mach 5 conditions	119
5.6	Stream traced modular ‘scallop’ inlet design	122
5.6.1	Numerical results at Mach 8 conditions	122
5.6.2	Numerical results at Mach 5 conditions	128
5.7	Summary and conclusions	133
6	Inlet performance evaluation	135
6.1	Summary and conclusions	146
7	Additional inlet numerical investigations	149
7.1	Laser induced detonation wave simulation	149

7.2	Gun tunnel model	154
7.2.1	Test specimen geometry	155
7.2.2	Inlet gun tunnel start verification	156
7.2.3	Inlet angle of attack simulations	159
8	Conclusions and future work	163
8.1	Conclusions	163
8.2	Future Work	165
8.2.1	Numerical simulations	165
8.2.2	Experimental work	165
9	References	167
A	Trajectory analysis code	173
B	streamTracer code	174

List of Figures

1.1	Current lightcraft configuration	3
2.1	Schematics of flow regimes: a) LSD wave; b) LSC wave (Reilly <i>et al.</i> , 1979).	10
2.2	$x - t$ diagrams of constant flux LSD (Reilly <i>et al.</i> , 1979).	11
2.3	Radial pressure and velocity profiles at time t (Reilly <i>et al.</i> , 1979).	12
2.4	Laser induced flowfield in supersonic cross-flow (Woodroffe <i>et al.</i> , 1979).	13
2.5	Pressure contours of a laser supported detonation wave (Katsurayama <i>et al.</i> , 2003).	15
2.6	Time history of the generation and extinction of two laser supported DEAS in medium enthalpy flow (Minucci, 2008).	16
2.7	Schematic of two-dimensional laser propulsion experimental setup (Minucci, 2008).	17
2.8	Current lightcraft inlet configuration; internal laser induced detonation (Ushio <i>et al.</i> , 2004).	18
2.9	Current lightcraft inlet configuration; external laser induced detonation.	18
2.10	Lightcraft nozzle configuration utilised in flight experiments performed in Germany (Bohn & Schall, 2003).	19
2.11	Laser propulsion testing inlet configurations (Myrabo <i>et al.</i> , 1998).	20
2.12	Coefficient of drag for lightcraft forebody configurations (Langener <i>et al.</i> , 2009).	21
2.13	Lightcraft configuration.	22
2.14	The Busemann inlet (Molder & Szpiro, 1966).	26
2.15	Generating flow field for modular stream traced inlet design (Billig & Kothari, 2000).	27
2.16	Generating flow field for modular stream traced inlet design (Smart, 1999).	27
2.17	Generating flow field for modular stream traced inlet design (Matthews & Jones, 2006).	28
2.18	Stream traced inlet capture area profile (Smart, 1999).	29
2.19	Sector capture shapes for the modular waverider inlet (Matthews & Jones, 2006).	29
2.20	Stream traced inlet capture profile (You & Liang, 2009).	29
2.21	Stream traced inlet capture profile (Gollan & Smart, 2010).	30
2.22	Stream traced modular inlet geometry (Billig, 1995).	30

2.23	Stream traced modular inlet geometry (Smart, 1999).	30
2.24	Stream traced modular inlet geometry (Matthews & Jones, 2006).	31
2.25	Stream traced modular inlet geometry (You & Liang, 2009).	31
2.26	Symmetry plane pressure contours for the Mach 6.0 REST inlet at $M =$ a) 3.6, b) 4.8, and c) 6.0 Smart (1999).	33
2.27	Mach number contours and Schlieren imaging for a stream traced inlet (Sun <i>et al.</i> , 2010).	34
2.28	Comparison of inlet designs Matthews & Jones (2006).	34
2.29	Final modular intake shape (Billig & Kothari, 2000).	35
2.30	Final modular intake shape (Smart & Trexler, 2003).	35
2.31	Final modular intake shape (Matthews & Jones, 2006).	35
2.32	Final modular intake shape (Sun <i>et al.</i> , 2010)	36
2.33	Flow patterns of supersonic and hypersonic inlets at unstarted conditions (Tan & Guo, 2007).	36
2.34	Schlieren imagery of inlet unstart in a hypersonic inlet (Tan <i>et al.</i> , 2009).	38
2.35	Two and three-dimensional shockwave/boundary layer interactions (Van Wie (2000), reproduced from Stollery (1990) and Delery (1985)).	39
3.1	Forces acting on the lightcraft during flight.	44
3.2	Coefficient of drag for a 30° half angle cone (Hoerner, 1965).	46
3.3	Newtonian theory (Anderson, 2000).	47
3.4	Newtonian theory applied to simplified lightcraft geometry.	48
3.5	Typical blast wave simulation results. a) Impulsive force; b) Wave front pressure; c) Wave front velocity; d) Position	51
3.6	Analytical and Computational result comparison.	52
3.7	Flight path geometries for varying thrust and lift inputs.	54
3.8	Mach number vs time for varying flight trajectories.	55
3.9	Flight conditions for varying flight path geometries.	56
3.10	Flight conditions for varying flight path geometries.	57
3.11	Range vs altitude plot for varying flight path geometries.	58
3.12	Required density compared to stagnation density over flight envelope.	59
4.1	Inlet geometries investigated.	61
4.2	Coefficient of drag for lightcraft forebody configurations (Davis & Mead Jr, 2007).	63
4.3	Axi-symmetric inlet design.	64

4.4	CAD representation of axi-symmetric inlet geometry employed in this study.	65
4.5	Technical CAD drawing of axi-symmetric inlet geometry.	66
4.6	Stream traced methodology.	67
4.7	Generating flow field for lightcraft inlets.	69
4.8	Stream tracing technique.	70
4.9	Stream traced inlet geometry from generating stream lines.	70
4.10	streamTracer code flowchart.	71
4.11	Position of an arbitrary particle within the generating flowfield.	72
4.12	Flat plate verification.	73
4.13	Boundary layer displacement thickness correction.	74
4.14	Generating flow fields of turning angles 7.58° and 15° , respectively.	75
4.15	Original and truncated inlet simulations illustrating amount of total compression lost.	77
4.16	CAD representation of Stream traced axi-symmetric inlet geometry employed in this study.	78
4.17	Dimensioned CAD drawing of the Stream traced axi-symmetric inlet geometry.	78
4.18	CAD representation of Stream traced axi-symmetric inlet geometry employed in this study.	79
4.19	Technical CAD drawing of Stream traced modular axi-symmetric inlet geometry.	80
4.20	Three dimensional streamline tracing of scalloped inlet module	81
4.21	Modified generating flow field geometry used in stream traced modular scalloped inlet geometry.	81
4.22	CAD representation of Stream traced modular scalloped inlet geometry employed in this study.	82
4.23	Dimensioned CAD drawing of Stream traced modular scalloped inlet geometry.	82
5.1	Computational domain for numerical simulations.	86
5.2	Density profile at mesh outlet for different mesh densities.	88
5.3	Contours of Mach number for angles of attack of 0° , 3° and 6° for three dimensional mesh at Mach 8.	92
5.4	Close up of inlet contours of static pressure for an angle of attack of 0° at Mach 8 - 2D high resolution grid (top) and 3D grid (bottom).	93

5.5	Static pressure profiles at isolator exit for 0° angle of attack and Mach 8.	94
5.6	Contours of density for an angle of attack of 0° , 3D mesh (top) and 2D mesh (bottom).	95
5.7	Contours of density for an angle of attack of 3° , 3D mesh.	96
5.8	Contours of density for an angle of attack of 6° , 3D mesh.	96
5.9	Contours of density at isolator outlet for angles of attack of 0° , 3° and 6° at Mach 8.	97
5.10	Contours of surface pressure along lightcraft walls for angles of attack of 0° , 3° and 6° at Mach 8.	98
5.11	Contours of Mach number for 3D mesh at angles of attack of 0° , 3° and 6° and Mach 5.	99
5.12	Contours of density for 3D mesh at angles of attack of 0° , 3° and 6° and Mach 5.	101
5.13	Contours of Mach number for the 3D mesh at angles of attack of 0° , 3° and 6° and Mach 8.	103
5.14	Contours of density for an angle of attack of 0° at Mach 8 - 3D mesh (top) and 2D mesh (bottom).	104
5.15	Contours of density for an angle of attack of 3° at Mach 8 - 3D mesh.	105
5.16	Contours of density for an angle of attack of 6° at Mach 8 - 3D mesh.	105
5.17	Contours of density at isolator outlet for angles of attack of 0° , 3° and 6° .	106
5.18	Close up of isolator flow field, Mach 8 at 0° angle of attack for the 2D mesh.	107
5.19	Illustration of flow processes about separation bubble. (Segal, 2009)	108
5.20	Contours of Mach number for angles of attack of 0° , 3° and 6°	109
5.21	Contours of density for angles of attack of 0° , 3° and 6°	110
5.22	Contours of density at isolator outlet for angles of attack of 0° , 3° and 6°	112
5.23	Contours of Mach number for angles of attack of 0° , 3° and 6° at Mach 8.	114
5.24	Contours of density at isolator outlet for angles of attack of 0° , 3° and 6°	116
5.25	Surface contours of density for angles of attack of 0° , 3° and 6° at Mach 8 (logarithmic scale).	118
5.26	Contours of Mach number for angles of attack of 0° , 3° and 6° at Mach 5.	119
5.27	Contours of density at isolator outlet for angles of attack of 0° , 3° and 6° at Mach 5.	121
5.28	Contours of Mach number, illustrating three-dimensional shock structure for angles of attack of 0° , 3° and 6° at Mach 8.	123

5.29	Contours of Mach number for angles of attack of 0° , 3° and 6° at Mach 8.	125
5.30	Contours of density at isolator outlet for angles of attack of 0° , 3° and 6° .	127
5.31	Contours of Mach number, illustrating three-dimensional shock structure for angles of attack of 0° , 3° and 6° at Mach 5.	129
5.32	Contours of Mach number for angles of attack of 0° , 3° and 6° at Mach 5.	130
5.33	Contours of density for angles of attack of 0° , 3° and 6° at Mach 5.	132
5.34	Contours of density at isolator outlet for angles of attack of 0° , 3° and 6° at Mach 5.	133
6.1	Inlet performance comparison, Mach 8 flight conditions.	140
6.2	Inlet performance comparison, Mach 8 flight conditions.	141
6.3	Inlet performance comparison, Mach 8 flight conditions.	142
6.4	Inlet performance comparison, Mach 5 flight conditions.	144
6.5	Inlet performance comparison, Mach 5 flight conditions.	145
6.6	Inlet performance comparison, Mach 5 flight conditions.	146
7.1	LTD inlet geometry at $M=9.43$ with laser induced breakdown (Salvador, 2010)	150
7.2	Laser induced detonation wave simulation initial setup.	151
7.3	Contours of pressure for detonation wave evolution.	153
7.4	Inlet isolator normal wave.	154
7.5	CAD representation of lightcraft configuration	155
7.6	CAD representation of inlet geometry with outer surface of cowl removed	155
7.7	Lightcraft geometry section through inlet	156
7.8	Transient gun tunnel simulation, contours of density	158
7.9	Static pressure values along pressure transducer locations of 0° and 180° for a lightcraft angle of attack of 0°	160
7.10	Static pressure values along pressure transducer locations of 0° and 180° for a lightcraft angle of attack of 3°	160
7.11	Static pressure values along pressure transducer locations of 0° and 180° for a lightcraft angle of attack of 6°	161

List of Tables

3.1	Flow conditions for blast-wave analytical solution.	50
3.2	Trajectory code input parameters, flight path 1.	53
3.3	Trajectory code input parameters, flight path 2.	53
3.4	Trajectory code input parameters, flight path 3.	53
3.5	Trajectory code input parameters, flight path 4.	54
3.6	Trajectory code input parameters, flight path 5.	54
3.7	Inlet design parameters.	59
5.1	Inlet off design simulation values.	86
5.2	Mesh sizes employed in mesh refinement study.	88
5.3	Grids employed in mesh refinement study.	90
7.1	Laser induced detonation wave initial conditions	151
7.2	Pressure far field boundary conditions	157
7.3	Transient gun tunnel simulation initial conditions	157
7.4	Comparison on inlet design conditions in flight and gun tunnel	159

1 Introduction

1.1 Background information

1.1.1 What is a lightcraft

Conventional rocket technology involves the launching of satellite payloads into orbit via the means of chemical propellants. Current rocket technology is inherently expensive - a figure of \$10,000/kg of payload is typically considered ‘best practice’ (Salvador, 2010), with typical payload fractions of 3-4% (Langener *et al.* , 2009). This is due to the large amounts of chemical propellant required to be carried during launch. Both fuel and oxidizer are required during launch of traditional chemical rocket, resulting in significant mass penalties. One method of improvement is through using air breathing engines, such as ramjets and scramjets or combined cycle engines. These vehicles do not carry an on-board oxidizer, atmospheric oxygen is used instead either completely replacing or supplementing the requirement for on-board oxidizer. These types of vehicles are able to substantially increase the mass fraction carried by removing the weight penalty of carrying an oxidizer. Scramjets typically employ hydrogen or a hydrocarbon as the main fuel source. There are significant difficulties with traditional hydrogen fuelled scramjet engines. Hydrogen has a very low molecular mass, resulting in large volumes required for realistic flight missions (Segal, 2009). Hydrocarbon fuels such as kerosene or jet fuels have been proposed, however the residence times within scramjet combustors result in long flowpaths which add significantly to the vehicle drag.

The laser lightcraft vehicle is a novel concept which goes one step further than the high speed air breathing concepts by removing the need to carry both the oxidizer and fuel on board (Kantrowitz, 1972). In the laser propelled lightcraft, the energy source for flight is provided by a ground based laser. The laser energy is used in the craft to provide forward momentum, leaving the heavy propulsion energy system in the form of a re-usable ground based infrastructure. Lightcraft will operate in either air breathing or ablative propulsion modes (Myrabo *et al.* , 1998), depending on the phase of the launch. Air is utilised as the propulsion medium during flight within the sensible atmosphere. The incoming air is initially compressed by the lightcraft forebody, then energy is added to the air stream via focused laser energy. A detonation wave is formed by focusing this laser beam adjacent to a thrust surface, thereby breaking down the air and forming a hot a plasma. The expanding wave is then used to provide the craft with the required thrust.

When the Lightcraft exits this region of usable atmosphere, the laser is then used to heat an ablative fuel source providing anaerobic propulsion.

By decoupling the main power source from the vehicle, lightcraft designs are very simple with little to no moving parts in their current form. This leads to a relatively reliable, lightweight and economically advantageous prospect for frequently and repetitively launching small earth-to-orbit satellites. Current designs are envisaged to be single-stage to orbit, and completely reusable. High specific impulse values are possible from the lightcraft engine; in air breathing mode the working medium is air, with the energy being provided by a ground-based laser - no on board fuel is required to be carried. During air-breathing flight, the specific impulse of the Lightcraft can be theoretically infinite. In the case where non-air breathing flight is required (i.e. in an earth-to-orbit satellite launch) the specific impulse is very high as the only fuel carried is the ablative propellant required for the non-air breathing stage. With this decoupling of the fuel source from the launch vehicle, and the re-usability of the ground based laser, the costs of launch can be significantly reduced. A study performed by Myrabo *et al.* (1998) suggests that for payload sizes of approximately 1 to 10kg, costs of as little as \$100/kg can be realisable in the foreseeable future. High payload mass fractions are achievable, in the order of 50-95% (Davis & Mead Jr, 2007). The economic benefits of Lightcraft vehicles are substantial when compared to conventional rocket systems. A life-cycle cost analysis conducted Davis & Mead Jr (2007) has placed the launch to lower earth orbit cost per kilogram of payload of a Lightcraft at \$532/kg. This is 41 times lower than the standard industry cost of \$22,000/kg for a conventional chemical propulsion rocket. The majority of the costs lie in the initial purchase of the laser, which effects would be substantially reduced when frequent launches occur.

Further benefits lie in the increased safety of the laser powered propulsion system (Mead Jr. *et al.* , 2005). With the removal of chemical propulsion there would be no toxic fuels, no explosive hazards and no large, environmentally unfriendly propellant farms. The launch infrastructure would also be significantly reduced - there would be no requirement for motorised tractors to shift vehicles, no skyscraper gantries and the number of mechanics and technicians on standby would be significantly reduced. The lightcraft would be simply wheeled onto the launch pad by a small cart when required.

Current conceptual and experimental designs of Lightcraft consist of three main sections; the forebody, the engine cowl and the afterbody - shown in Figure 1.1. The conical forebody acts as both an aerodynamic shape for providing lift to the craft, and a super-

sonic ramp to compress the incoming air before it enters the engine cowl for combustion. The engine cowl acts as both an inlet and an impulsive thrust surface for the combustion. The parabolic afterbody acts as both a primary receptive optic for the incident laser beam, and an expansion nozzle for the heated exhaust flow.

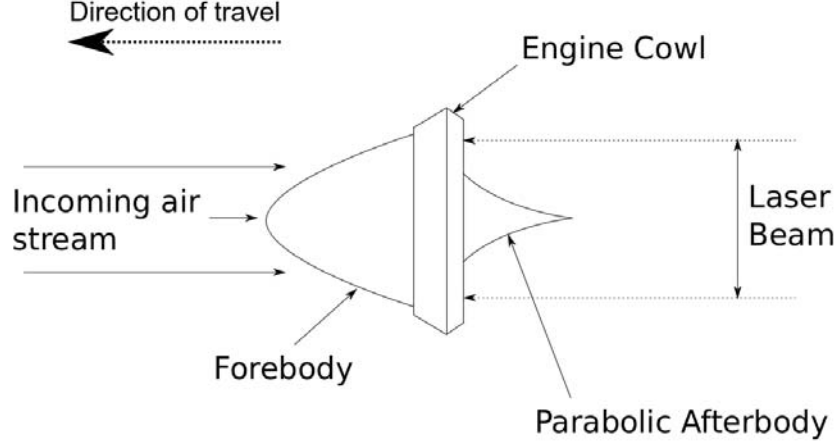


Figure 1.1: Current lightcraft configuration

1.1.2 Current flight achievements

An experiment involving the launch of a flight demonstration vehicle to a significant altitude (0.6km and 1km) using the existing laser at the High Energy Laser Systems Test Facility (HELSTF) and White Sands Missile Range (WSMR) was performed (Myrabo *et al.*, 1998). 14cm diameter vehicles of 50-60gm were flown on a 10kW pulsed carbon dioxide laser, which operates with 10kJ pulses at 10 Hz, with a 30 μ s pulse duration. Spin stabilized, free vertical flights up to an altitude of 4.27m were achieved. Horizontal, wire guided flights of 121.3m were also performed.

In Germany, parabolic lightcraft have been flown in experimental conditions to an altitude of 1.7m (Scharring *et al.*, 2008). The lightcraft were of parabolic nozzle shape, with height 62.5mm and 100mm base radius. A pulsed carbon dioxide laser, operating at 200J pulse energies with a 10 μ s pulse duration repeated at a frequency of up to 40 Hz.

1.1.3 Current limitations/design challenges

Current laser technologies do not provide sufficient power to launch a lightcraft to LEO. The necessary laser power required to launch useful payloads is in the order of 10MW for orbit-to-orbit maneuvering, and 1GW for Earth-to-orbit launching (Birkan, 2007). Current laser technologies can only provide power levels of a few MW for continuously

working lasers, and average powers of a few hundred KW average power for pulsed lasers. There does however appear to be no theoretical limit to the scaling of laser systems, and it is believed that the power requirements of laser powered lightcraft vehicles can be met by future development of current laser technology. The major obstacles for laser energy transmission outlined by Birkan are;

1. Atmospheric absorption and scattering by particulates. It has been found, however, that this effect can be reduced by choice of laser wavelength
2. Thermal blooming due to the heating of the air in the laser beam's path
3. Refraction and scattering of the beam by atmospheric turbulence
4. Optical losses such as mirror absorption, scattering, etc

The amount of thermal blooming that occurs depends on both the wavelength and the peak intensity of the laser beam. Generally, the longer the wavelength of the laser, the less thermal blooming that occurs. However longer wavelength beams require larger reflective mirrors, which adds difficulty in the fabrication and operation of such systems. The 11.2 micron wavelength has been suggested as the optimum compromise (Davis & Mead Jr, 2007). Significant effort is currently being applied to laser systems in the lightcraft community, with technology fast approaching the required levels for vehicle launch.

An area where lightcraft development is lacking is in inlet designs for supersonic and hypersonic speeds. Currently there has been no detailed investigation into hypersonic inlets for the lightcraft, with the minimal effort that has been expended concentrating on subsonic inlet designs. As a well designed inlet is essential for all types of hypersonic vehicles, it is important that it is addressed such that it does not become a limiting factor in vehicle development. The interaction between the air-breathing inlet and the laser induced detonation engine is also not well understood, with research only beginning recently (Salvador, 2010).

1.2 Aim of thesis

This thesis addresses the current gap in knowledge of lightcraft systems by documenting the design and evaluation of an air-breathing hypersonic inlet for the lightcraft vehicle. Hypersonic inlet design techniques have been produced for a notional lightcraft, with the performance compared through numerical simulation. This work documents the inlet design process in sufficient detail such that future investigations into hypersonic lightcraft

(and conventionally fuelled scramjet) inlets may use this text as a base to further extend the knowledge in this area. In addition to the aerodynamic performance of the lightcraft inlet designs, this work aims to augment the understanding of the inlet process by investigating the effect of the laser induced detonation wave on the inlets behaviour.

1.3 Remainder of thesis

The content of this thesis is divided into eight chapters, with appendices attached at the end. Chapter 2 begins the main body of the work with a critical literature review of the relevant past and present research into laser propelled lightcraft vehicles and hypersonic inlet design. The current state of knowledge, and the specific gaps in the research are documented to provide a basis for the motivation of this work. In Chapter 3 a system level analysis of the lightcraft mission is produced. This investigation is important as it sets the baseline requirements and constraints of the lightcraft flight. From the system level analysis, the atmospheric conditions used in the inlet design can be defined.

Once the design conditions for the inlet have been obtained from the system level analysis, the lightcraft inlets can be produced. Chapter 4 provides a detailed outline of the inlet design process. The four hypersonic inlet design techniques are presented in a fashion that would allow the reader to reproduce quickly and easily. After the establishment of the four inlet designs, numerical simulations are performed in the computational fluid dynamics code, Fluent. Chapter 5 presents the results from the numerical simulations. The behaviour of the inlets at both on and off design conditions is discussed. Chapter 6 uses the results from the inlet simulations to quantitatively compare the performance of the inlets across a range of performance parameters.

Chapters 3 through 6 are the bulk of the work of the thesis, with Chapters 7 and 8 containing ancillary simulations and conclusions, respectively. In Chapter 7, the method of operation of the laser induced detonation engine and its interaction with the lightcraft propulsion system is investigated through a transient detonation wave simulation. An inlet self-start simulation is also performed to verify the starting of the model within the experimental gun tunnel conditions. Chapter 8 then concludes and summarises the work contained within the thesis, and also provides an outline of the future work that may follow this thesis.

Appendices follow, containing the codes produced (trajectory analysis and stream tracing code) and a list of references.

1.4 Outline of new work contained in thesis

The body of new work performed in this thesis is;

- A trajectory study performed for the specific lightcraft application. Although studies similar to this have been performed before, an improved hypersonic aerodynamic lift and drag model has been incorporated, as well as a propulsion system model.
- Four hypersonic inlet designs for the lightcraft have been produced. These inlet designs have addressed the requirement for a hypersonic inlet for the lightcraft vehicle. The inlets apply traditional scramjet inlet design methodologies, suitably adjusted for the lightcraft propulsion system. The axi-symmetric stream traced inlet design technique, although adapted from the stream traced design technique, has not previously been performed for any vehicle.
- The performance of the hypersonic inlet designs have been quantitatively compared for the lightcraft case study. A direct comparison has been performed, giving comparable data for a range of inlet designs. This data is of use for all airbreathing hypersonic vehicles, not just lightcraft.
- The performance of the hypersonic inlet designs and their sensitivity to vehicle angles of attack has also been investigated. No numerical simulations for stream traced inlet designs at angle of attack have been previously produced.
- A point source detonation numerical simulation for the stream traced inlet design model using laser induced detonation theory has been produced at hypersonic flight conditions. This simulation has been used to verify the operation of the inlet at hypersonic speeds.
- Gun tunnel starting numerical simulations have been performed to ensure successful operation of the inlet during gun tunnel experimental testing.

2 Literature review

2.1 Introduction

The idea of Laser Propelled Lightcraft Vehicles was first conceptualised in the early 1970's (Kantrowitz, 1972) as a means of achieving low cost earth to orbit payload launches. The concept of using beamed laser energy as a propulsion system stemmed from research into laser induced breakdown of gases performed in the previous decade (Pirri & Weiss, 1972). A similar system was proposed in the same year involving a space-based laser rocket (Minovitch, 1972). Research interest was continued in the 1980's by the Strategic Defense Initiative Organisation (SDIO), with both air breathing and ablative rocket powered configurations considered (Cook, 2008). Laser propulsion fell out of favour with the SDIO, as it was unable to produce systems capable of demonstrating a real applicability. As the SDIO program was winding up, interest in the laser powered propulsion system was renewed by NASA (Rather, 2003).

A number of extensive reviews of lightcraft history developments have been previously published (Salvador (2010), Phipps *et al.* (2010), Komurasaki *et al.* (2006), Pakhomov (2007) and Phipps *et al.* (2009)), and as such will not be detailed in this thesis. Instead, the focus of this literature review has been on the laser propulsion system, current lightcraft inlets and the inlet design methodology.

2.2 Laser propulsion system

2.2.1 Introduction

Thrust is generated in the lightcraft vehicle by focusing a high powered laser beam adjacent to a solid surface. When the laser beam is intensified, the working gas is broken down and a detonation wave is formed. This wave then imparts an impulse on the adjacent surface, generating the desired momentum (Feikema, 2000). Due to the disruptive nature of the ionization and plasma generation process, the laser induced breakdown has been likened to a nuclear explosion, or fireball. Either a steady state or continuously working laser pulse can be employed in thrust generation, however it has been found that the plasma created by a steady state laser propulsion system is inherently unstable (Simons & Pirri, 1977). By pulsing the laser at a duration that is sufficiently short, the thrust generation can be highly efficient and much more stable.

The pulsed laser induced detonation process is complex, involving many different phys-

ical phenomena occurring during the intermittent laser pulses. Quantum electrodynamics, optics, fluid mechanics, gas dynamics and high temperature plasma dynamics all play a role in the laser induced detonation wave formation (Salvador, 2010). The laser induced detonation process can be divided into three stages, all of which occur in the minute time scales between consecutive pulses, which can be less than the order of ten microseconds:

1. The initial air breakdown, where ionization occurs in the cold gas and the initial plasma appears
2. Interaction between the between the remainder of the laser pulse energy and the initial plasma gas
3. Formation of the detonation process, where the blast wave relaxes in an unpowered manner across the thrust surface.

The three stages are then followed by the extinction of the detonation wave.

When the focused energy of the pulsed laser beam is higher than the threshold value of the gas, the initial optical breakdown stage occurs. The breakdown stage is arbitrarily defined, typically being the electron concentration required to cause significant absorption and scattering of the incident laser radiation. The combination between the initial breakdown and formative growth stages is very small, the duration being a few nanoseconds or less. The molecular working gas is broken down into the ionized plasma via two processes; cascade ionization (the inverse Bremsstrahlung effect) and multiphoton ionization.

In cascade ionization, free electrons absorb electromagnetic radiation and undergo random oscillating motion, causing collisions with surrounding atoms. If the electron has sufficient kinetic energy, neutral particles can be ionized by collision (Salvador, 2010);



Kinetic energy is converted to other forms, and the resulting free electrons have a lower kinetic energy due to the collision. The laser radiation then again re-accelerates the electrons, increasing the kinetic energy to a point where they are both able to ionize another atom, causing ‘cascade’ effect of the number of free electrons available. If the gas pressure, pulse duration and laser intensity are sufficiently large, gas breakdown can be caused by the ionization and resulting exponential increase in the number of free electrons (Morgan, 1975). If the intensity of the beam is not strong enough, loss processes slow and prevent the cascade effect.

The second process, multiphoton ionization, increases the number of free electrons through the ionization of particles by the absorption of photons. When particles absorb photon energy above the particle ionization energy, electrons are caused to detach from the atom.



The multiphoton ionization process requires significantly higher laser intensities, and as such plays a much smaller role in the generation of the plasma cloud.

The ionization process occurs faster than the pulse duration of the laser, and therefore finishes while the laser pulse is still focused on the plasma. This results in additional energy being added to the highly ionized, conducting and hot expanding plasma. Free electrons in the working gas are continually accelerated until the end of the laser pulse. The plasma begins to move up the laser beam, until the pulse ends. During this period multiple plasmas may interact and combine.

A blast wave front exists due to the high amount of energy absorbed by the plasma. The front then expands across the surface, imparting thrust to the lightcraft. If the time of the pulse is short such that the plasma remains close to the momentum surface, momentum is imparted and thrust can be generated.

2.2.2 Modelling of the laser induced detonation process

There have been a number of attempts to analyze and model the physics behind the generation of thrust by the plasma, both experimentally and analytically. Reilly *et al.* (1979) have developed a simplified parametric model of the flow field produced by a high energy laser beam incident onto a non-ablative surface, based on the work of Raizer (1965). The flowfield present due to the laser supported detonation process can be generally classified into two different regimes, dependent on laser intensity. The laser supported combustion (LSC) wave has been observed at flux levels in excess of $3 \times 10^4 W/cm^2$, while the laser supported detonation (LSD) wave is apparent in flux levels around $10^7 W/cm^2$ and above. Figure 2.1 illustrates the flow regimes present for both types of laser supported waves. A transition flowfield often occurs between these intensities.

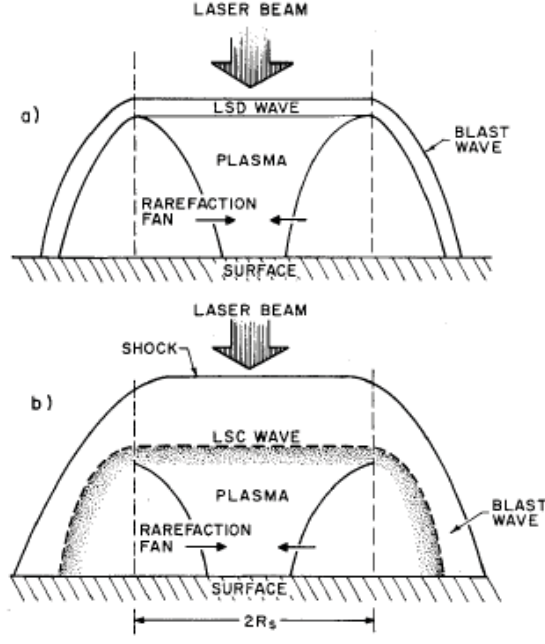


Figure 2.1: Schematics of flow regimes: a) LSD wave; b) LSC wave (Reilly *et al.* , 1979).

The surface pressure time histories for the laser supported detonation wave can be described in terms of two characteristic time scales, as shown in the $x-t$ diagrams (Figure 2.2). In these diagrams, τ_p represents the pulse length, τ_z the axial relaxation time and τ_{2D} is the radial relaxation time. The more important time scale in describing the process is the radial relaxation time, which represents the time taken for the rarefaction wave from the detonation wave outside edge to reach the spot centre. This is given by

$$\tau_{2D} = R_{LSD}/C_{LSD} \quad (2.3)$$

where R_s is the laser spot radius, and C_{LSD} is the sound speed in the hot plasma. For a laser supported detonation wave, the sound speed is typically taken as half of the detonation wave velocity (Reilly *et al.* , 1979).

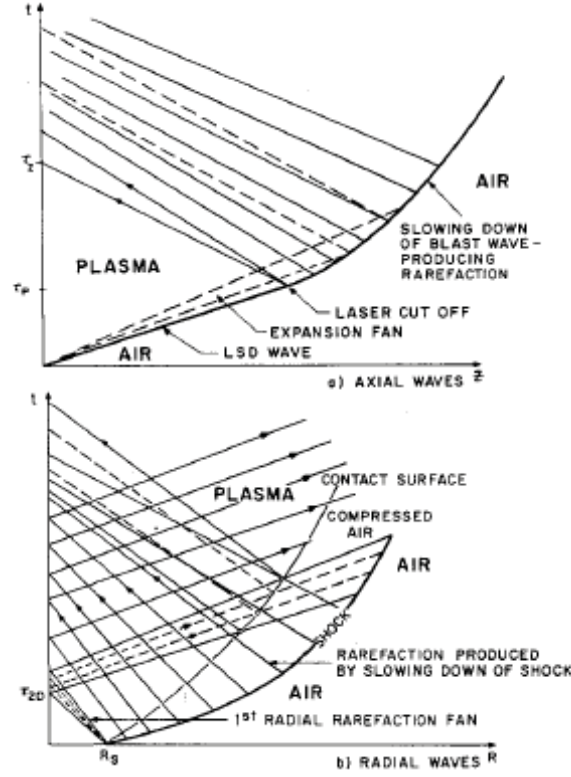


Figure 2.2: $x - t$ diagrams of constant flux LSD (Reilly *et al.* , 1979).

The initial surface pressure conditions, based on complete absorption of the laser flux into the detonation front is given by (Raizer, 1965);

$$P_{LSD} = \left[\frac{\gamma + 1}{2\gamma} \right]^{\frac{2\gamma}{\gamma-1}} \frac{\rho_0 V_{LSD}^2}{(\gamma + 1)} \quad (2.4)$$

where

$$V_{LSD} = \left[2(\gamma^2 - 1) \frac{I}{\rho_0} \right]^{1/3} \quad (2.5)$$

Here V_{LSD} is the initial laser supported detonation (LSD) wave velocity in ms^{-1} , and I is the laser intensity in Wm^{-2} , ρ_0 is the density of the working gas in kgm^{-3} and γ is the ratio of specific heats of the working gas. These equations are used to establish the flow and thermodynamic properties of a blast wave that has evolved to cylindrical geometry adjacent a flat plate. The solution to the pressure and velocity profiles are then found employing the method of characteristics, with typical pressure and velocity profiles shown in Figure 2.3.

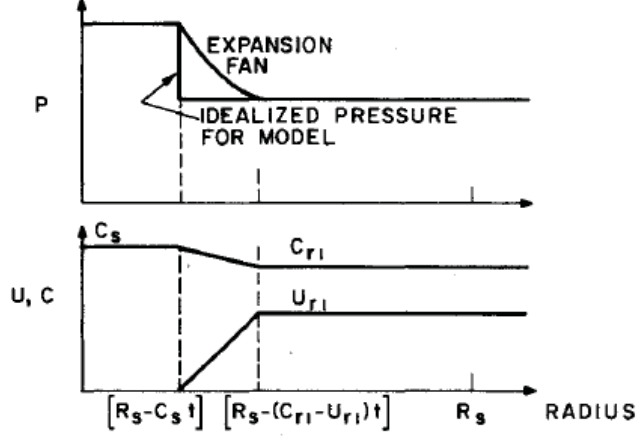


Figure 2.3: Radial pressure and velocity profiles at time t (Reilly *et al.* , 1979).

Feikema (2000) presents a similar approach to obtaining an analytical solution to the LSD wave, again based on the work of Raizer (1965). In this case Sedov's unpowered scaling laws are used to quantify the time dependent conditions of the detonation wave front for axi-symmetric and isentropic conditions (Sedov, 1959).

$$P/P_{REF} = (t/t_{REF})^{-1}; r/r_{REF} = (t/t_{REF})^{1/2} \quad (2.6)$$

where P_{REF} can be expressed as the maximum pressure on the exerted on a flat plate thrust surface by the detonation wave

$$P_{REF} = P_{LSD} \quad (2.7)$$

The value t_{REF} corresponds to the time taken for the blast wave to become completely cylindrical. The reference time is therefore given as

$$t_{REF} = \tau_{2D} = \frac{r_{LSD}}{C_{LSD}} = \frac{2r_{LSD}}{V_{LSD}} \quad (2.8)$$

A simple thermodynamic relation for the expansion of the plasma is then assumed, and using an equation of state and compressibility factor, Z , the temperature of behind the front can be calculated.

$$T = \frac{C_{LSD}^2}{\gamma Z \frac{R_u}{M}}$$

where M is the molecular weight and R_u is the universal gas constant. These first-order estimates neglect real gas effects such as excitation, dissociation and recombination, how-

ever they are suitable for generating initial estimates of the behavior of the laser induced detonation wave. Richard & Myrabo (2005) use this method to perform a performance analysis of the laser propelled lightcraft vehicle. The performance of the lightcraft design was evaluated at a range of flight speeds and altitudes.

Woodroffe *et al.* (1979) extend these preliminary studies to examine the interaction of the laser induced detonation wave and a surface with a supersonic cross flow. In these experiments, a 200-J-pulse CO_2 laser with $10\mu s$ pulse length was used in a mobile supersonic free jet wind tunnel operating at Mach 2.8. Impulse data was obtained through quartz pressure gauges with visualization via a shadow-graph system and a movie camera operating at 40,000fps. The behavior of the laser induced blast wave when it interacts with supersonic flow is illustrated in Figure 2.4. At low laser intensity levels (in the laser supported combustion regime) there is little interaction between the plasma and the supersonic flow. At higher flux levels leakage of the plasma into the upstream boundary layer creates an oblique shock wave. The resulting oblique shock wave then interacts with the blast wave, producing further secondary shock structures.

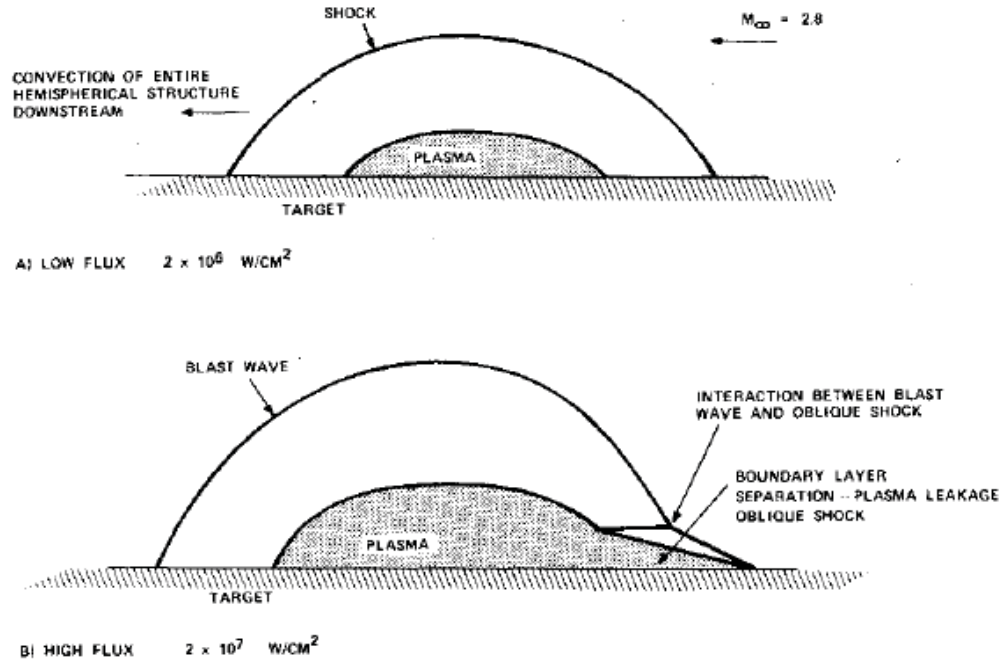


Figure 2.4: Laser induced flowfield in supersonic cross-flow (Woodroffe *et al.* , 1979).

Numerical models of the laser detonation process have been developed to solve the complex two-dimensional, axi-symmetric, unsteady, fully compressible Navier-Stokes equations coupled with laser radiation under certain conditions (Birkan, 2007). Due to as-

sumptions however, these state of the art models cannot accurately simulate systems operating at high power levels. The issues involved with high power laser systems summarised by Birkam are;

1. Diffraction of the laser beam due to the finite aperture of the lens and refraction due to the inhomogeneous refractive indexed within the plasma are not included
2. Generalised six-dimensional wide-band plasma re-radiation is not considered
3. Plasma chemistry is not included
4. Transient, three-dimensional models are not available
5. Turbulence is not considered.

Research has focused on developing an understanding of the mechanisms of optical breakdown, laser supported detonation waves, blast wave/flow field interaction and an understanding of the loss mechanisms present. Numerical codes developed to model the laser powered propulsion system range from simple detonation wave models (Brode, 1955) to complicated models accounting for plasma dynamics (Ghosh & Mahesh, 2008) and can be divided into two main categories - explosion point source and plasma dynamic models.

Ghosh & Mahesh (2008) have investigated the physical complexity required in the detonation wave modelling to adequately resolve the flow features observed in experiments. The flow field resulting from the deposition of laser energy into air is modelled by the Navier-Stokes equations, with radiation losses after the formation of the plasma spot assumed to be negligible. Three levels of physical complexity are considered, and the effect on the resolved flow field examined. The first model neglects real gas effects, and hence air is modelled as an ideal gas. The second model considers the effects of dissociation, ionization and recombination of different species in a 11 species model of air. The third and most complicated model also considers the effects of pressure variation on the gas properties. Quite significant difference in the results were observed between the three different models, verifying the requirement for complex physical numerical models when simulating plasma generation flow fields.

Explosion point source models have been applied as an effective tool for investigating the dynamics of the laser propulsion system in lightcraft engines. Katsurayama *et al.* (2003), in their preliminary feasibility study of a pulse laser ramjet vehicle, have conducted an explosion source model to analysis the effect of the laser induced detonation wave

during lightcraft flight. In the numerical simulations, the explosion source was modelled as a pressurised volume centred at the laser focus which was then used to validate an analytical engine cycle analysis. Figure 2.5 shows the evolution of the detonation wave in a supersonic ramjet lightcraft at Mach 5 and an altitude of 20km.

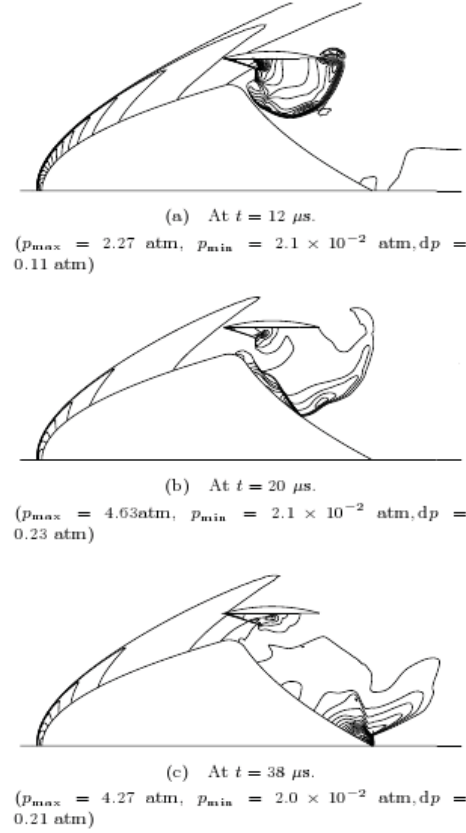


Figure 2.5: Pressure contours of a laser supported detonation wave (Katsurayama *et al.*, 2003).

2.2.3 Research developments

Minucci (2008) gives a detailed report on the developments in beamed aerospace propulsion occurring in the Prof T Nagamatsu Laboratory of Aerothermodynamics and Hypersonics in Brazil. Activity began in 2000, when it was first suggested that a laser beam be implemented to provide a heat source for directed energy air spike (DEAS) experiments. The initial experiments were conducted in a 0.3m Hypersonic Shock Tunnel that was employed to generate high, medium and low enthalpy hypersonic flow conditions. A single Transversely Excited Atmospheric pressure Carbon Dioxide Laser of pulse energy 4.5 Joule was used to initiate the DEAS, with a second similar laser added at a later stage. The two laser set-up allowed both single and double laser pulse experiments to be

carried out. Results were captured via both a high speed CCD camera and time-lapse photographs.

In 2005 a Schlieren visualization system integrated with a high speed camera was developed in conjunction with an improved laser delivery system. Figure 2.6 is a time lapse sequence of the visualization technique, showing the resulting flow structure from laser energy deposition in a supersonic flow stream. Laser energy is deposited upstream of a blunt body, and can be clearly seen to disrupt the upstream flow structure. Measurements of surface pressure and surface heat flux could also be measured.

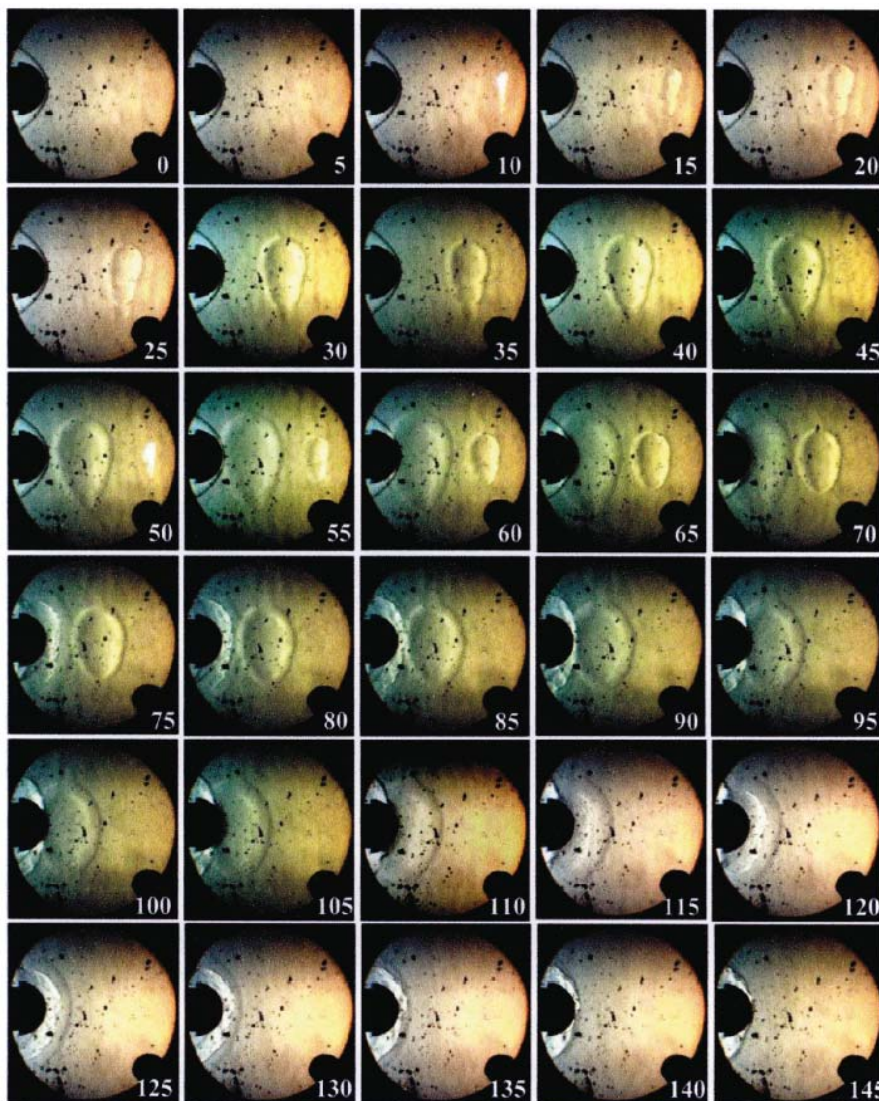


Figure 2.6: Time history of the generation and extinction of two laser supported DEAS in medium enthalpy flow (Minucci, 2008).

Following the DEAS investigations, the facility was upgraded to perform beamed energy propulsion experiments in both the air-breathing and rocket propulsion stages of

flight (Salvador, 2010). Flow Mach numbers of 6-25 are being investigated, with the setup allowing different laser pulse intervals to be investigated during the hypersonic useful test time. Pressure transducers and heat flux gauges employed to allow measurements at a number of points on the test model, being the model inlet, the laser energy addition zone, cowl and nozzle exit. The geometry of the experimental set-up is shown in Figure 2.7. The research aims to investigate the time-dependant pressure profiles over the lightcraft engine surfaces, and provide visualisation of the expanding blast wave and its interaction with the incoming hypersonic flow. This will allow the prediction of generated thrust within the supersonic and hypersonic flow regimes.

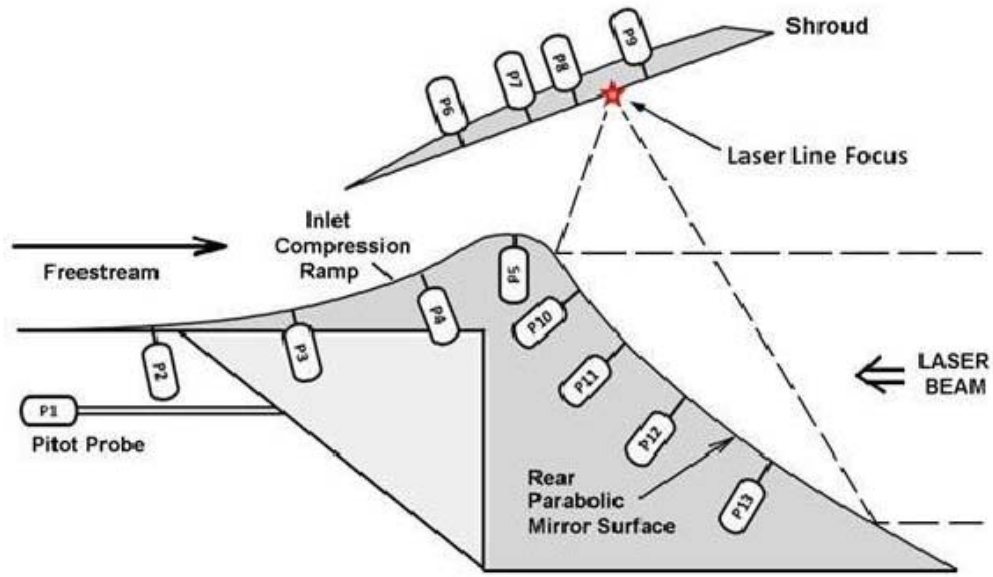


Figure 2.7: Schematic of two-dimensional laser propulsion experimental setup (Minucci, 2008).

2.3 The lightcraft vehicle inlet

The lightcraft vehicle operates in air-breathing mode during its ascent of the sensible atmosphere. Sufficient air must therefore be delivered throughout the lightcraft flight. This implies that an suitably designed inlet is required to deliver the atmospheric air to the laser induced detonation engine. A limited number of different air breathing inlets for the lightcraft project have been produced, with supersonic and hypersonic aerodynamic performance consideration remaining either unpublished or non-existent.

Two main configurations of lightcraft inlet are currently being investigated - external laser induced detonation and internal laser induced detonation. The two configurations can be seen in Figures 2.8 and 2.9. The difference between the two designs is in the

way the laser beam is focused. The internal laser induced detonation configuration uses a traditional bell nozzle rear optic to focus the laser energy along the axis of symmetry of the craft, and air is delivered by an axis-symmetric, internal compression inlet. The external laser induced detonation configuration focuses the laser energy in an external annular ring around the lightcraft centre-body, with air delivered by an external compression axis-symmetric (typically conical) forebody. Slight variations exist on both designs, however the underlying principles remain the same.

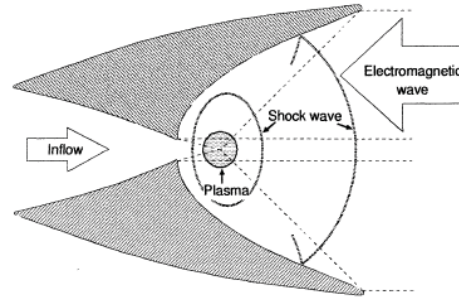


Figure 2.8: Current lightcraft inlet configuration; internal laser induced detonation (Ushio *et al.* , 2004).

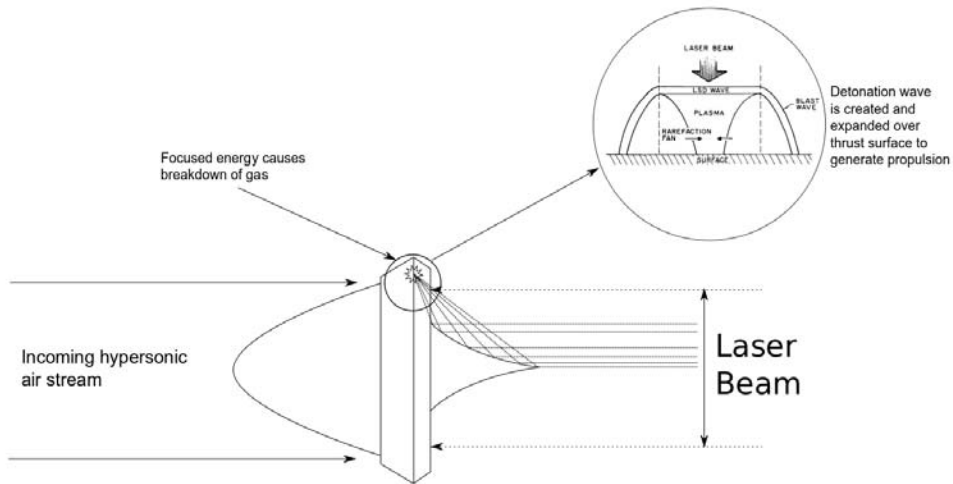


Figure 2.9: Current lightcraft inlet configuration; external laser induced detonation.

Research for the internal laser induced detonation configuration is centred in both Germany (Scharring *et al.* , 2008) and Japan (Ushio *et al.* , 2004), comprising of both theoretical and experimental investigations. Scharring *et al.* (2008) have conducted subsonic flight tests of parabolic lightcraft engines, in both air breathing and ablative rocket propulsion modes. The configuration employed in the experiments is shown in Figure

2.10, which has a bell diameter of 100mm, and a height of 62.5mm. Laser energy is transmitted into the rear of the bell nozzle, with the focal point of the parabolic shape being incident on a ‘firing pin’. The firing pin can be removed in experiments, or coated with an ablative fuel source. A laser induced detonation wave is initiated at the focal point, and expanded out the rear of the nozzle. Free flights up to a range of 1.7m were performed with this configuration. Ushio *et al.* (2004) have performed a feasibility study of the laser powered lightcraft configuration shown in Figure 2.8. The performance of the craft during supersonic air-breathing ‘ramjet’ mode is defined by calculating the coupling coefficient for a number of flight conditions using a numerical explosion source model. Strangely, the geometry employed in the numerical simulation is that of the external laser induced detonation configuration - possibly due to the availability of data for this configuration. It appears that in both investigations, the information on the inlet design and its applicability to higher flight velocities again remains unpublished, or does not exist.

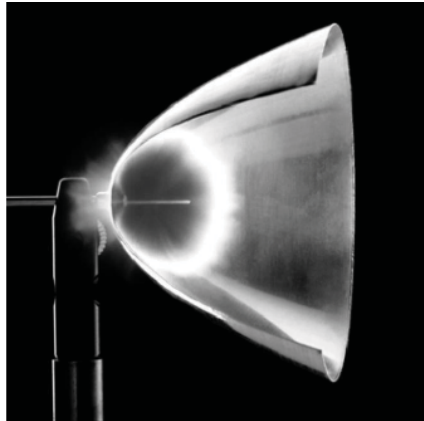


Figure 2.10: Lightcraft nozzle configuration utilised in flight experiments performed in Germany (Bohn & Schall, 2003).

The external laser induced detonation configuration appears to be the more popular configuration, mainly due to its ease of integration with ancillary equipment such as payload and flight electronics. Using an annular inlet external to the craft, a higher degree of flexibility exists with regards to payload location. The majority of the research on this configuration stems from the United States of America, with the Lightcraft Technology demonstrator project (Davis & Mead Jr, 2007).

In the late 1980’s, Prof. Leik Myrabo of the Rensselaer Polytechnic Institute (RPI) introduced the laser propelled trans-atmospheric vehicle concept (Myrabo *et al.* , 1998). The concept envisaged a combined cycle, laser powered engine would launch a 120kg dry mass, 1.4m diameter lightcraft with a mass fraction of 0.5 into orbit. The study

aimed to demonstrate that a laser powered propulsion system could successfully launch sensor satellites into orbit for less than \$1000/kg production cost, and a launch cost of less than \$100/kg. Although these ambitions have been scaled back, similar costs are still believed to be achievable for vehicles of size 1kg to 10kg. Several different Lightcraft design configurations were examined during the experiments, as shown in Figure 2.11. Due to the inlet configuration being chosen for subsonic flight tests, a closed cowl configuration (Vehicle A, Figure 2.11) was employed. Inlet performance during the hypersonic regime was either not considered, or deemed unimportant for the preliminary flight tests.





Vehicle Label	Description	Vehicle Shape
A	Final flight configuration. Closed inlet and reverse-curved nozzle. Parabolic optic and rounded nose.	
E	Original baseline, open inlet. Same optic and nose as configuration A.	
E-C	Same as configuration E but closed inlet.	
P	Closed inlet with cowl tangent to forebody contour.	

Figure 2.11: Laser propulsion testing inlet configurations (Myrabo *et al.* , 1998).

Langener *et al.* (2009) have performed a study on the Lightcraft Technology Demonstrator inlet aerodynamics. Numerical simulations were performed up to flight speeds of Mach 5 for three differing axi-symmetric forebody geometries based on either parabolic or power law shapes. The coefficient of drag was established for each geometry. Results of their simulations are shown in Figure 2.12, where coefficient of drag is plotted against Mach number for three different conical forebody geometries. Although this study has performed supersonic numerical simulations on the lightcraft configuration, only the design of the conical forebody and its impact on vehicle drag has been examined. No consideration to the inlet performance in relation to the laser induced detonation process

has been considered. Further, the inlet performance and sensitivity to changes in flight conditions has not been evaluated.

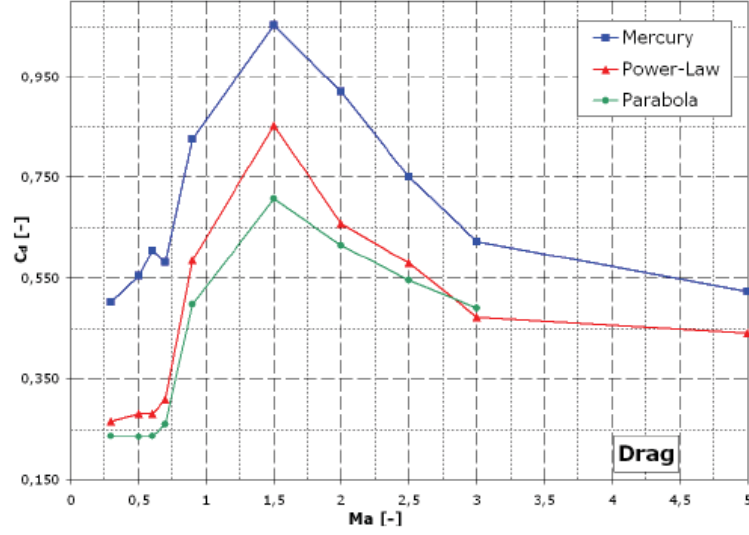


Figure 2.12: Coefficient of drag for lightcraft forebody configurations (Langener *et al.* , 2009).

2.4 Hypersonic inlet design

2.4.1 Introduction

Conventionally fueled hypersonic vehicle combustion systems traditionally consist of five main sections; compression ramp, inlet, isolator, combustor and expansion nozzle. Due to the inherent coupled nature of hypersonic vehicles, the designer is required to approach the design in a holistic manner. The compression ramp typically provides the majority of the freestream compression, and is integrated into the vehicle forebody. The hypersonic inlet then compresses and delivers the incoming air flow to the engine. An inlet isolator serves to contain the shock train, and provide some isolation of the flow before it enters the combustor. In the combustor, heat is added to the flow. The hot gases are then expanded in the nozzle to produce thrust.

Although the fundamental principles of compressing an incoming flow, adding heat and then expanding the hot gases to reclaim the kinetic energy apply to the lightcraft vehicle, the method of energy addition to flow renders the final design significantly different to a conventional hypersonic vehicle. The pulsed laser detonation engine does not require flow features such as combustors or flame holders, and hence the combustion system is much reduced. The laser induced detonation engine requires a system that delivers the

air with minimal flow losses, providing an efficient platform for the expansion of the gases. To achieve this, the lightcraft design consists of an initial compression ramp the (axi-symmetric forebody) , inlet cowl (to direct and further compress the incoming flow), an inlet isolator (to contain the expanding detonation wave and prevent inlet unstart) and an expansion nozzle (which also acts as the focusing optic). The lightcraft can then essentially be classed into three sections; the axi-symmetric forebody, the inlet including the isolator) and the expansion nozzle, a typical configuration is shown in Figure 2.13. Traditional hypersonic design techniques can then be applied to the inlet to achieve a robust design for the lightcraft project (the aims of this research).

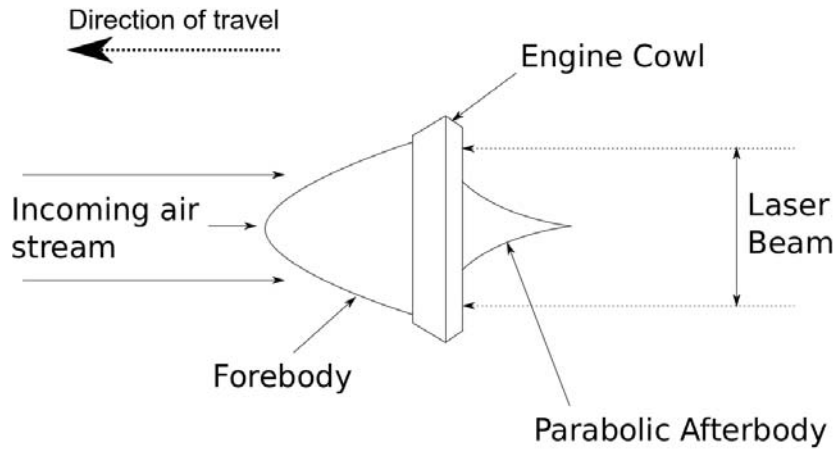


Figure 2.13: Lightcraft configuration.

Van Wie (2000) states the primary purpose of an inlet for any air breathing propulsion system is to “capture and compress air for processing by the remaining portion of the engine”. To achieve the best hypersonic air breathing engine performance, the inlet design must provide a high level of efficient compression, with minimal losses. Matthews *et al.* (2005) summarise the required properties of a hypersonic inlet:

- The intake should compress the flow as efficiently as possible, minimising viscous losses and shock-wave losses
- Intake contribution to vehicle drag should be minimised
- The intake should be self starting at the scramjet take-over Mach numbers and be able to operate over the required range of Mach numbers, with no significant deterioration in performance
- Intake performance should not be significantly reduced by operation at incidence

- The intake must be able to tolerate the back-pressures caused by heat addition
- The intake has to be able to withstand the internal pressures and heat loads
- Uniform velocity profiles are generally desirable at the intake exit

A complete and robust hypersonic inlet would take into account all of the above points, with each item given due attention. In practice, the design of hypersonic inlets is a very complicated affair with the design process being highly non-linear and based on a series of compromises. No current hypersonic inlet design can optimally address all of the required variables, and the designer is often left allocating an order of importance to each inlet characteristic. The optimal inlet design involves a compromise between these performance factors and requirements on structural and aerodynamic components.

It is highly desirable for the inlet to provide adequate conditions for propulsion system and a uniform velocity profile parallel to the freestream at the inlet exit. It is also desirable to maintain as much of this performance at off design conditions as possible. Sensitivities to changes in flight Mach number and angle of attack are to be minimised, and boundary layers in the inlet are to remain thin and attached. There are a number of challenges present to the hypersonic engine designer (Smart, 2007):

- Mixing and ignition of fuel and air in the short residence times of a supersonic combustor
- The high heat loads and friction losses that occur at hypersonic speeds
- The control of thermal choking
- Non-equilibrium nozzle flows and the loss of energy from the cycle due to incomplete combustion
- No thrust production below a flight Mach number ranging from 3.5-5, depending on the particular engine design. A booster or low-speed propulsion system is therefore required to raise the vehicle to the scramjet take-over Mach number.
- Operating over a large Mach number range with a “realistic” engine structure requires some finesse and many compromises for adequate performance at the upper and lower limits of the desired speed range.

Although Smart has developed this list for conventionally fueled scramjet propulsion systems, only the first point is not relevant to laser propulsion systems. An efficient, flexible

and powerful engine design is essential for the success of the lightcraft project. The inlet efficiency is critical to performance of a scramjet engine, with the compression efficiency, mass capture and combustion stability are all dependent on the inlet wave system. An addition of thermal energy can decelerate the flow to subsonic levels, causing unstart conditions in the engine. The free-stream Mach number, angle of attack, free stream gas properties, extent of heat addition and pressure variations due to the propulsion systems can all effect the flow through the inlet, thereby causing unstart conditions.

Supersonic inlet designs typically fall into one of three categories; two-dimensional planar, two-dimensional axisymmetric or three-dimensional (Van Wie, 2000). As previously discussed in Section 2.3, current lightcraft configurations typically employ a blunt-nosed axis-symmetric inlet configuration. This form of inlet has the desirable characteristic whereby the vehicle bow shock performs the initial compression, with the cowl providing secondary compression. The inlets also employ fixed geometry and no boundary layer bleed, greatly reducing structural complexity. Manufacturing is also simplified through the axis-symmetric configuration.

2.4.2 Stream traced inlet design

Stream traced inlet design has generated a lot of interest in the hypersonic research fraternity of late, due to the promise of higher levels of performance above traditional compression designs (Billig & Kothari, 2000). Three dimensional inlets traced from generating flowfields (using the stream traced inlet design methodology) have the benefit over traditional designs of alleviating the starting problem for internal compression flow fields, and also include swept leading edges which are favorable for heat transfer considerations (Matthews & Jones, 2006). Billig & Kothari (2000) have shown that their inlets, designed for a Mach number of 7.8, are self-starting at Mach numbers below 4. These inlets also have low cowl drag, however skin friction can be higher due to large wetted surface areas. Another benefit of the stream traced method is the inlets are formed in a modular arrangement allowing efficient side-by-side mounting. The inlets also exhibit good starting characteristics at ramjet takeover speeds (Mach 3-4) and efficient operation up to vehicle cruise condition (Smart, 1999). Flow velocities other than design Mach number create a shock profile that is not conical, and contains uncanceled expansion and compression waves. The efficiency of the compression process is still much higher than in conventional planar inlets (Billig & Jacobsen, 2003). This method has provided a means

for designing inlets with minimal shock losses that produce a uniform, diffused stream after compression and no theoretical upper limit on inviscid total pressure recovery.

The stream traced inlet design method is used to generate three dimensional hyper-sonic inlets from an inviscid compressive generating flowfield. Stream traced inlets work on the same principle as the wave-rider design (Anderson *et al.* , 1991) whereby a desired portion of a generating flow field is captured by replacing the flow streamlines with a solid, boundary layer corrected surface that defines the inlet geometry. As the solid boundary of the inlet is itself an inherent part of the flow field, the flow captured by the inlet is identical to the flow created by the fictitious generating body, with the leading-edge shockwave remaining attached to the inlet edges at design conditions. This allows the designer to effectively choose and dictate the flow properties that will be present in the stream traced inlet, while limiting flow spillage from the inlet capture area. The stream traced methodology can be applied, in its simplest form, from two dimensional planar inlets (Nonweiler, 1963) to more complicated three dimensional geometries (Smart, 1999).

Buseman (1942) first proposed the use of an axi-symmetric internal flow inlet consisting of isentropic conical compression, followed by a free-standing throat shock at the inlet isolator. The conically symmetric compression caused by the leading edge shock wave is initiated at the free-stream Mach angle, the shock reflection and Mach waves cancelling to create uniform flow parallel to the free-stream. Figure 2.14 is an illustration of a simple Busemann inlet design. For the numerical solution of the flow, both isolator Mach number M_2 and reflected shock θ_s are specified, allowing the designer to tailor the combustor flow properties to their specific application. After the compression shock, the flow is set to be parallel to the free stream flow, which allows the inclination of the flow upstream to be calculated through a solution to the Taylor-Maccoll equations.

The Busemann inlet results in long inlet geometries which are not optimized for realistic application due to excessive drag, and is likely to perform poorly in flight. They also suffer from poor self starting performance. To alleviate the self-starting issues of the Busemann inlet, sector capture shapes were employed and arranged annularly in the SCRAM weapon system in the 1960's (Billig, 1995). The SCRAM project introduced the technique of generating three dimensional inlets by carving shapes from generating flow field stream tubes, giving birth to stream traced inlet design. A fully three dimensional stream traced inlet was designed, built and tested under the SCRAM project.

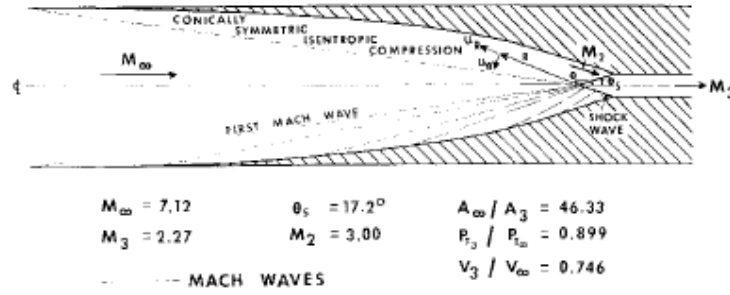


Figure 2.14: The Busemann inlet (Molder & Szpiro, 1966).

Research into stream traced inlet designs was somewhat limited after the initial investigations, due to it being a laborious and time consuming task. Interest has been recently renewed due to the advent of high powered computing automating a number of the design tasks (Billig & Kothari, 2000). The process has since been significantly refined and developed.

Smart (1999) investigates the stream traced inlet design process, using the technique to create three dimensional inlets with a rectangular to elliptical shape transition for coupling with traditional elliptical combustor designs. A complete design methodology for three dimensional hypersonic inlets is presented. The process can be broken up into two parts; the inviscid geometry generation, and the boundary layer correction. The first step in the inviscid geometry generation is the selection of the generating flow field. The key to an efficient inlet is the choice of the compressive flow field, as the features contained within this flow field will be present in the final inviscid inlet (Smart, 1999). The generating flow field should possess maximum total pressure recovery, maximum strength shock train to minimise length, but not strong enough to cause boundary layer separation and maximum flow exit uniformity (Smart, 1999). Typically axi-symmetric Busemann inlets are chosen because of the inherent isentropic compression (Billig & Kothari, 2000), however other shapes have been investigated such as constant slope flowfields (Matthews & Jones, 2006) or more arbitrary shaped flow fields (Billig & Kothari (2000), You & Liang (2009)). A number of the flow fields currently used are shown in Figures 2.15, 2.16 and 2.17. It is also often the case that the designer will include a constant radius centre body within the compression flow field. This feature is included to remove the shock focusing that occurs at the axis, which leads to efficiency losses (Gollan & Smart, 2010). Matthews & Jones (2006) compare the constant pressure (isentropic) and constant slope flow field geometries (see Figure 2.17). It was found that the constant slope generating flow field geometries produced significantly higher compression ratios above the constant pressure

design. At lower generating flow field angles the efficiency of the two geometries is similar, however as the flow field angle increases, the constant pressure boundary becomes more efficient. The constant pressure generating flow field is also significantly longer than the constant slope, creating elongated inlet geometries. One method of decreasing the length of isentropic generating flow fields is through the addition of a finite length lip angle (Song & Zhao, 2009), however the flow field quality is deteriorated through this approach.

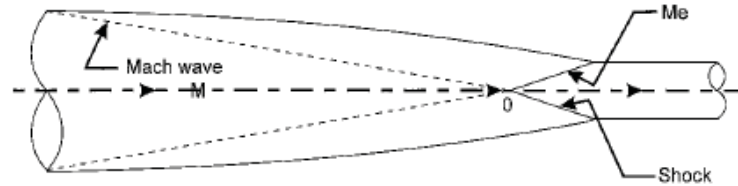


Figure 2.15: Generating flow field for modular stream traced inlet design (Billig & Kothari, 2000).

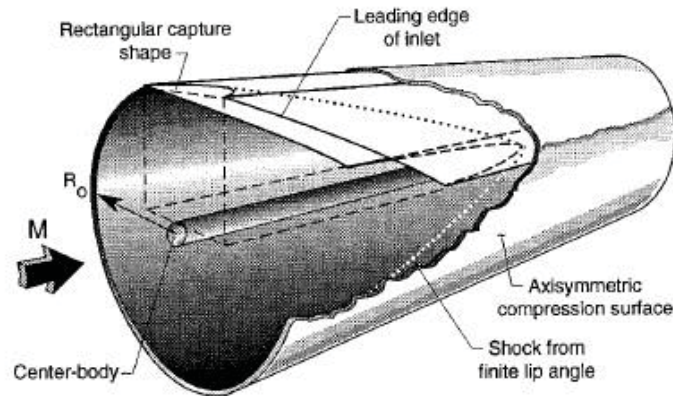


Figure 2.16: Generating flow field for modular stream traced inlet design (Smart, 1999).

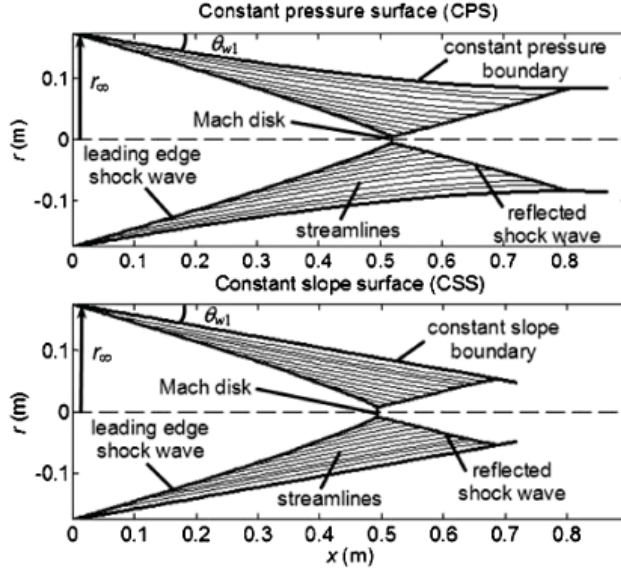


Figure 2.17: Generating flow field for modular stream traced inlet design (Matthews & Jones, 2006).

The next step in the stream traced inlet design methodology is the definition of the sector capture area from which the inlets will be traced. The streamline tracing technique enables the generation of inlet shapes that have characteristics almost identical to the predetermined flow field, but with independently specified capture shapes. The capture area shape is highly dependant on the application, a whole range of considerations will dictate the final chosen geometry. The two most important considerations are that of vehicle integration, and mass flow capture. Typically the modular inlets are arranged side by side on a planar vehicle or annularly around a conical vehicle. Smart (1999) employs a semi-rectangular shape with a horizontal top surface and parallel sides, shown in Figure 2.18. The bottom may form a more general shape, as it is not required to integrate to any other vehicle surfaces. Matthews & Jones (2006) have designed their modular inlets for a conical missile geometry, and a hence a capture area that allows annular spacing around the vehicle centre body is used. This configuration is shown in Figure 2.19. You & Liang (2009) investigate a number of different capture area geometries, shown in Figure 2.20. These shapes, along with those employed by Billig & Kothari (2000), are similar to that of Matthews & Jones (2006) due to the requirement that they are integrated into an axi-symmetric missile like geometry. Gollan & Smart (2010) are designing modular inlets for integration into a winged conical vehicle, and hence have employed a capture geometry that can be again annularly spaced around a vehicle centre-body, shown in Figure 2.21. It was found in their study that due to code sensitivity, certain stream tube capture shapes

would produce non-ideal inlet configurations with the combustor throat being located below the inlet entrance. This would increase the size of the vehicle, and also increase drag.

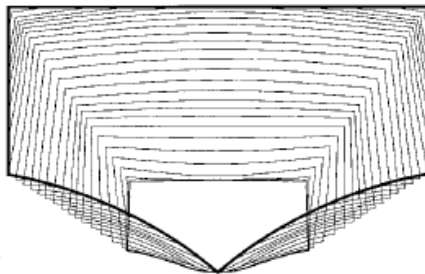


Figure 2.18: Stream traced inlet capture area profile (Smart, 1999).

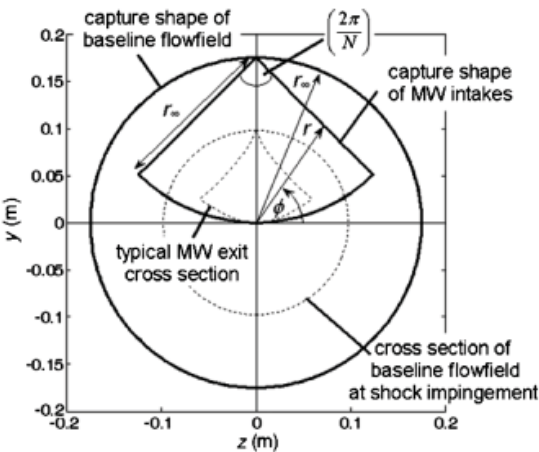


Figure 2.19: Sector capture shapes for the modular waverider inlet (Matthews & Jones, 2006).

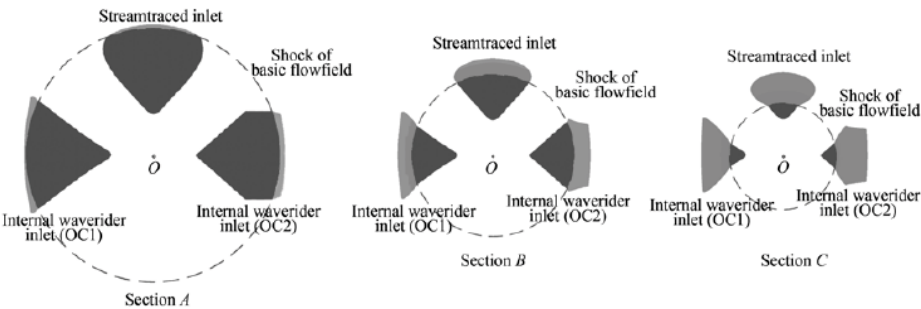


Figure 2.20: Stream traced inlet capture profile (You & Liang, 2009).

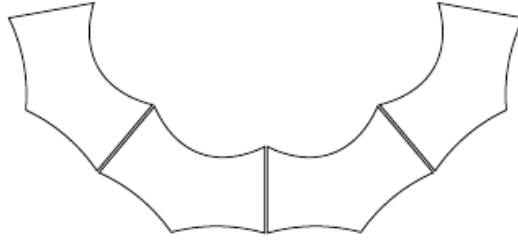


Figure 2.21: Stream traced inlet capture profile (Gollan & Smart, 2010).

The streamlines that pass through the defined capture area perimeter are then traced backwards through the flow field, creating the final inviscid shape. This process can be done in a number of ways, typically either using a post processing plotting tool (Smart, 1999) or by a space marching numerical scheme (Billig & Kothari, 2000). The geometries of a number of three dimensional modular stream traced inlet designs are shown in Figures 2.22 through 2.25.

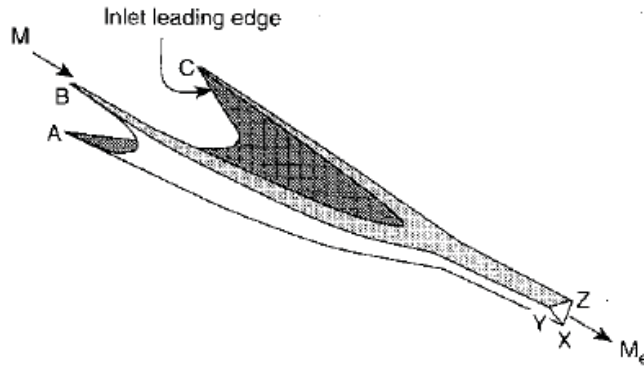


Figure 2.22: Stream traced modular inlet geometry (Billig, 1995).

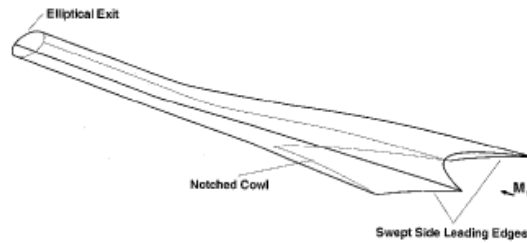


Figure 2.23: Stream traced modular inlet geometry (Smart, 1999).

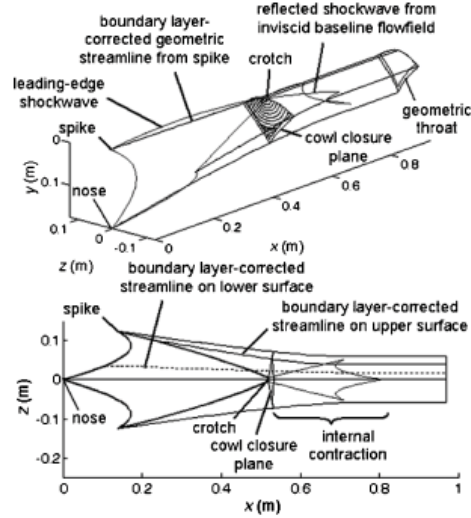


Fig. 3 CPS intake module with $N=4$ and $\theta_{w1} = 10$ deg.

Figure 2.24: Stream traced modular inlet geometry (Matthews & Jones, 2006).

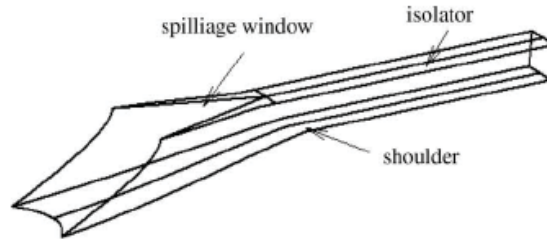


Figure 2.25: Stream traced modular inlet geometry (You & Liang, 2009).

To allow for the growing boundary layer within the inviscid inlet geometry, a boundary layer correction is required. A growing boundary layer will reduce the cross sectional area available to the flow, resulting in a greater pressure rise than predicted in the inviscid calculations (Smart, 1999). To allow for this growth within the inlet, Smart (1999) employs the small cross-flow equations to solve the boundary layer displacement thickness a boundary layer streamline co-ordinate system. Matthews & Jones (2006) have employed a local flat plate correction to the surface, estimating the boundary layer displacement thickness based on empirical correlations for a flat plate within supersonic flow at the inlet design conditions. It is believed that this method may underestimate the correct displacement thickness for the inlet flow fields due to the adverse pressure gradients and regions of strong lateral inward-turning curvature. This technique is supported however due to its simplicity and reasonable agreement with experiment and numerical simulations. To reduce the viscous drag of stream traced inlet designs, the length of the final inlet is required to be reduced through increasing the strength of the shock structure

within the generating flow field. This creates the issue of shock induced boundary layer separation, where the boundary layer is caused to separate from the inlet wall by strong adverse pressure gradients (Van Wie, 2000). Shock-induced boundary layer separation can produce significant losses within the inlet, possibly leading to inlet unstart. Large boundary layer separations also invalidate the use of the simplified boundary layer equations during the viscous correction of the inlet geometry. It is therefore important to include some form of treatment of turbulent shock-wave/boundary layer interactions within the inviscid portion of inlet design. Smart (1999) employs established incipient separation criteria (outlined in further detail in Van Wie (2000)) in his current design methodology to determine the maximum shock strength allowable within the inlet to avoid boundary-layer separation. This translates in practice into a minimum limit on the length of the inlet to avoid separation.

The performance of stream traced inlet designs has been evaluated extensively by the designers in their investigations. Both numerical and wind tunnel experiments have been performed, creating an extensive understanding of the behaviour of the inlets at both on and off design conditions. The REST inlet design has been tested with both numerical simulation (Smart, 1999) and wind tunnel testing (Smart & Trexler, 2003). The flow field inside the inlet was simulated using a cell-centered, finite volume upwind computational fluid dynamics code, with flow spillage upstream of the notched cowl modeled by using an extrapolation boundary condition for the boundary cell faces ahead of the leading edge. Inviscid flow field calculations at the design value of $M_1 = 6.0$, as well as off design conditions of $M_1 = 3.6$ and 4.8 can be seen in Figure 2.26. Significant flow spillage occurs below the notched cowl in the $M_1 = 3.6$ case. The reflected cowl shock also strikes well upstream of the throat, causing minimal cancellation of the shock train downstream of the throat. At Mach 4.8 , it can be seen that there is much less flow spillage, and the reflected shock moves closer to the throat, resulting in a more uniform flow through the closed portion of the inlet. As the flight Mach number approaches the design condition, it can be seen that the shock train is almost canceled at the throat, with minimal spillage before cowl closure. The flow field in the inlet, while not identical to the compression flow field, is only slightly degraded in terms of exit non uniformity and total pressure recovery. Wind tunnel tests were performed at a Mach number of 4.0 , which is well below the design Mach number of 5.7 for the REST inlet studied. Experimental results indicated that the inlet was not able to self-start at Mach 4 conditions, however self-starting was achieved by incorporating a small number of bleed holes on the inlet wall. These bleed holes created a

spillage penalty of an estimated 4%. Similar off-design Mach number investigations have been performed by Sun *et al.* (2010). Numerical and experimental wind tunnel testing was performed for an inlet with a Mach 5.3 design point at flight speeds of Mach 5.3 and 3.5. At both testing conditions, the flow spillage was minimal with the inlets remaining in a started state, however poor outlet flow profile was found from the current design. This was attributed to flow separation within the inlet. Figure 2.27 shows numerical simulation and experimental wind tunnel results from the investigations. Matthews & Jones (2006) compare the full mass capture engine performance of modular stream traced inlets against axisymmetric re-expansion (REX) inlets and external compression (EXC) inlets as a function of total contraction ratio in Figure 2.28. For a given contraction ratio, the full mass capture engine performances of the MW and isentropic-spike inlets do not differ significantly. Intakes with conical compression surfaces have lower performances and optimum contraction ratios due to increasing wave loss across the conical shock wave. It was suggested that because of the similarity of full mass capture engine performance of different intake concepts at a given contraction ratio, the criteria for selecting an intake design is most likely to depend on other factors such as intake self-starting ability, the back pressure that can be tolerated, isolator and combustor friction, performance over the flight trajectory, and operation at incidence.

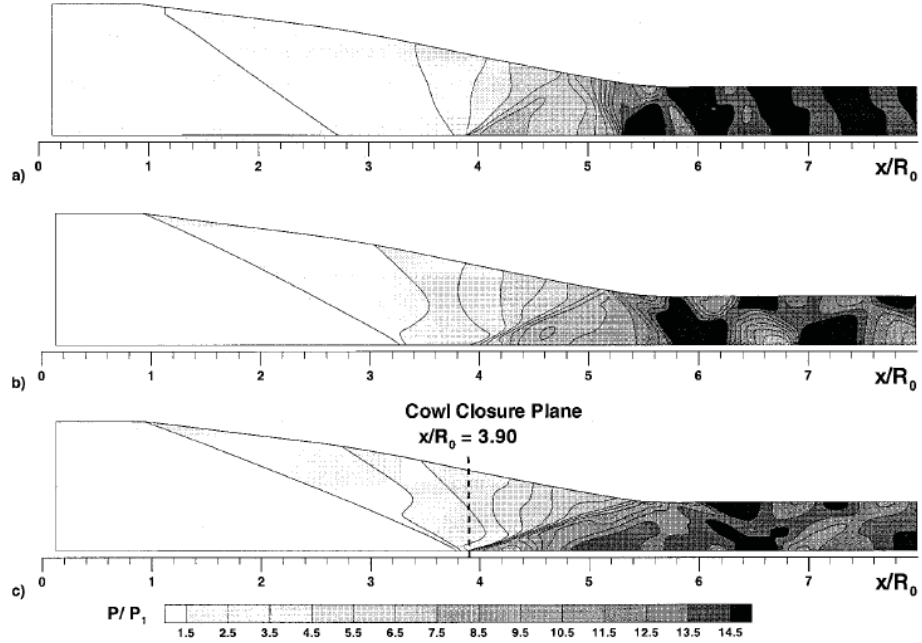


Figure 2.26: Symmetry plane pressure contours for the Mach 6.0 REST inlet at $M =$ a) 3.6, b) 4.8, and c) 6.0 Smart (1999).

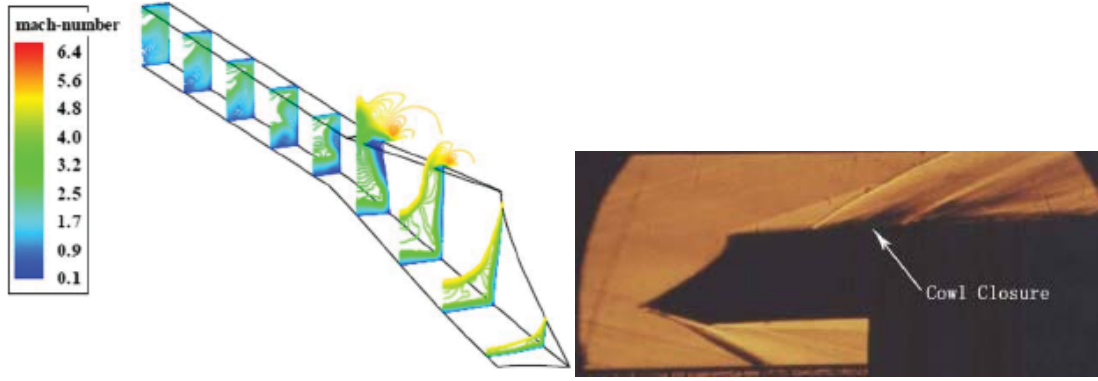


Figure 2.27: Mach number contours and Schlieren imaging for a stream traced inlet (Sun *et al.* , 2010).

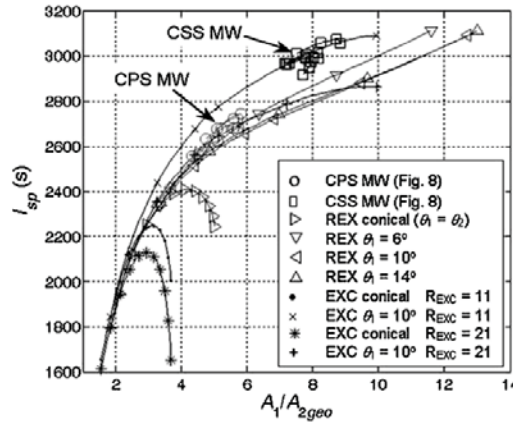


Figure 2.28: Comparison of inlet designs Matthews & Jones (2006).

From experimental and numerical investigations into the stream traced inlet design methodology, significant progress has been made towards the development of a robust, fixed geometry hypersonic inlet. The inlets possess good starting characteristics, particularly at Mach numbers significantly lower than the design point. The stream traced inlet design methodology has been shown to produce highly efficient, robust inlets and is hence a suitable candidate for the lightcraft project. One area of research lacking in the stream traced inlet design methodology is their performance at angles of attack. To this authors knowledge, the inlets behaviour at angles of attack remains un-investigated. This is an important aspect of the inlet design methodology, as craft maneuverability will be significantly limited if the inlet is to become unstated at low angles of attack. A thorough investigation into the behaviour at angles of attack is therefore required.

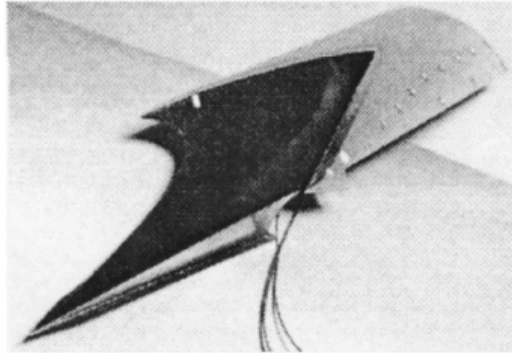
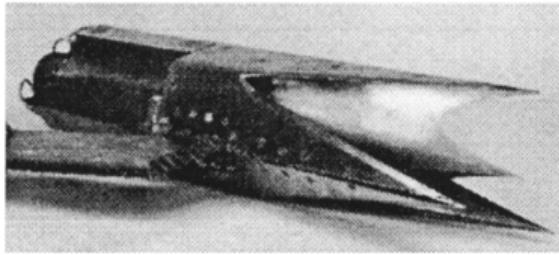


Figure 2.29: Final modular intake shape (Billig & Kothari, 2000).

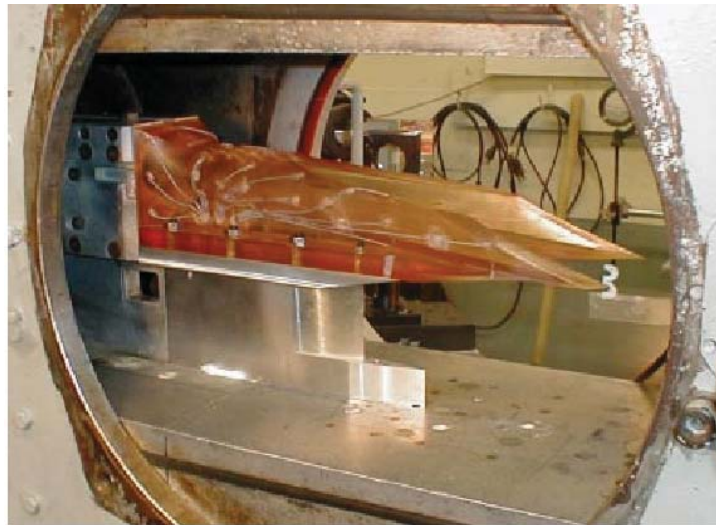


Figure 2.30: Final modular intake shape (Smart & Trexler, 2003).



Figure 2.31: Final modular intake shape (Matthews & Jones, 2006).

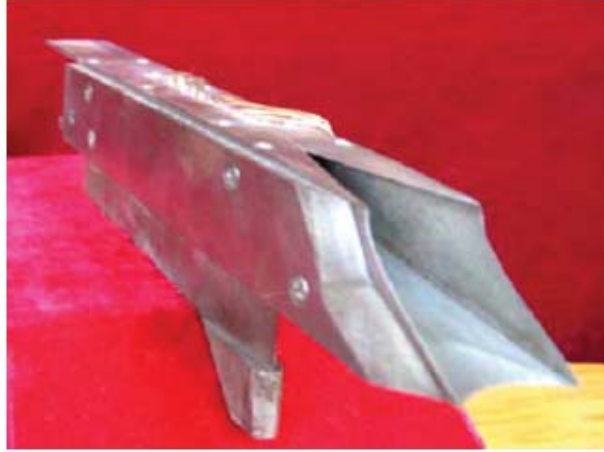


Figure 2.32: Final modular intake shape (Sun *et al.* , 2010)

2.4.3 Hypersonic inlet design issues

Inlet unstart is an important consideration in hypersonic inlet design as it can greatly affect inlet performance. Inlet unstart is defined as an abnormal operating state (Tan *et al.* , 2011), and is characterized by an abrupt decrease in captured flowfield and total pressure efficiency. Severe increases in aerodynamic and thermodynamic loads due to violent shock system oscillations and prominent pressure fluctuations may be present in the inlet during operation. These processes have highly detrimental effects on the thrust generated by the engine, and may cause catastrophic damage to the craft (Yu *et al.* , 2007). It is therefore essential that a hypersonic inlet remains in a started phase for proper operation throughout the flight envelope.

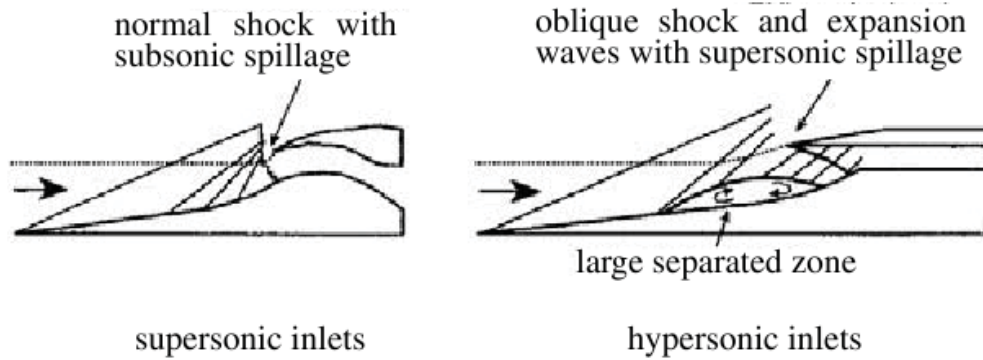


Figure 2.33: Flow patterns of supersonic and hypersonic inlets at unstarted conditions (Tan & Guo, 2007).

Hypersonic inlets are designed to operate always in the started phase, however a num-

ber of factors may lead to unstarted conditions in the application of the design in flight testing. Inlet unstart can be caused by disturbances to the inlet flowfield, either due to changes in flight conditions (i.e. angle of attack, flight speed or free-stream conditions) or disturbances due to the propulsion system. Unavoidable physical processes within the hypersonic inlet flowfields, such as strong-shock/boundary layer interactions, over compression from low operating Mach numbers, changes in angles of attack or even small perturbations in atmospheric conditions, lead to a situation where inlet unstart is often difficult to avoid. The immaturity of design methods, inaccuracy of CFD tools, inconsistency between the ground simulations and flight conditions, and the uncertainty of the engine thrust regulations (Tan & Guo, 2007) are some of the leading contributors to the sensitivity of hypersonic inlet designs. Determination of inlet start/unstart conditions is therefore important in establishing the performance of the inlet, and classifying its suitable operating range. More specifically relating to the lightcraft project, it is important to verify that the inlet will be able to restart (and consequently refresh the flow field) after each individual laser pulse. Failure to do so will severely compromise the performance of the pulsed laser engine.

Detection of inlet unstart in experimental and test flight situations is often difficult due to the transient nature of the pressure oscillations, however with CFD visualisation the process is much simpler. Figure 2.33 is an illustration of the different flow patterns between supersonic and hypersonic inlets in an unstarted state. In a supersonic inlet, flow is decelerated and spilled sub-sonically, whereas in a hypersonic inlet a large separation zone, or ‘bubble’, is formed at the inlet throat. The flow is spilled supersonically (Tan & Guo, 2007).

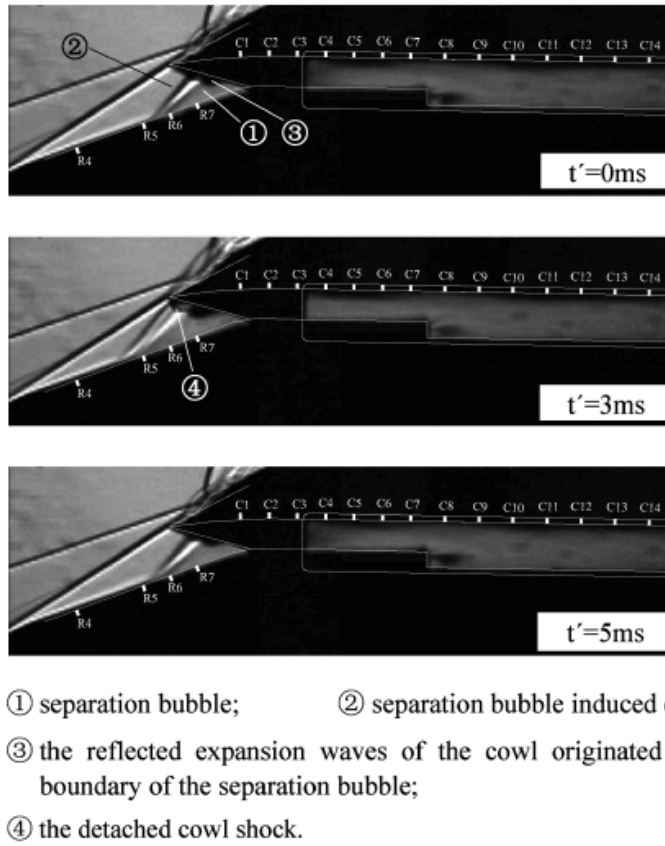


Figure 2.34: Schlieren imagery of inlet unstart in a hypersonic inlet (Tan *et al.* , 2009).

Figure 2.34 shows the typical structure of a hypersonic inlet unstart cycle. There exists a large separation bubble at the end of the initial compression ramp, with a resulting strong oblique shock due to the bubble. The separation bubble creates a restriction to the flow, and the upstream shock train Mach number is reduced to subsonic levels by the separation bubble oblique shock. In addition, there is flow spillage out of the inlet due to the abrupt rise in local pressure. The time sequence shows the oscillatory nature of the inlet unstart, with the bubble growing and shrinking in a regular cycle (Tan *et al.* , 2009).

Boundary layer separation is also highly undesirable during hypersonic inlet operation as it may lead to unstart even at design conditions. Figure 2.35 shows possible methods of shock wave and boundary layer interaction that can lead to boundary layer separation. In both situations, it is possible to define a maximum pressure rise that causes significant incipient separation of the boundary layer.

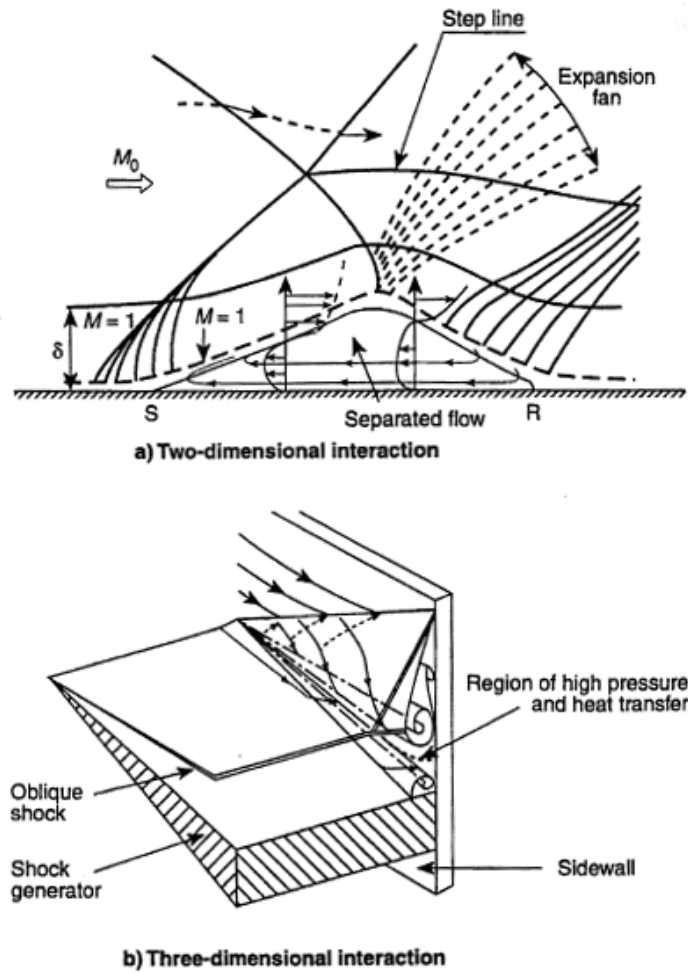


Figure 2.35: Two and three-dimensional shockwave/boundary layer interactions (Van Wie (2000), reproduced from Stollery (1990) and Delery (1985)).

One method of reducing the likelihood of inlet unstart or boundary layer separation is through bow shock location (Lewis, 1993). The angle of the forebody bow shockwave is dependent on the angle of the generating body of the craft, the ratio of specific heats of the working fluid, the angle of attack of the craft and the Mach number. A change in any of these variables will result in the change in the angle of the bow shock wave off the forebody. Careful consideration of bow shock location is required for efficient vehicle design. If the shock angle is such that the bow shock is located far from the vehicle, excessive drag will occur. It is therefore beneficial to keep the bow shock close to the inlet cowl. If the bow shock is allowed to fall such that it impinges on the lip of the inlet, excessive heating will occur that would be detrimental to the structure. The third scenario, where the bow shock is allowed to enter the engine cowl, would create detrimental shock reflections that will propagate through the engine, impeding the thrust generation process.

2.5 Summary and conclusions

The wide range of literature available on the lightcraft provides a significant insight into the concepts and ideas currently under investigation. The lightcraft concept, although somewhat established, is still in its infancy and extensive further research is required to bring it into reality. Research into the pulsed laser detonation continues to be the main area of research interest, with a large collection of international institutions and organisations involved in both theoretical and experimental research in this field. The sophistication of research facilities is increasing rapidly as interest is garnered in this promising new technology. Hypersonic research facilities for lightcraft are few, with the Prof Henry T. Nagamtsu facility being the most significant facility for laser induced breakdown in hypersonic flow investigations relevant to this research. Facilities in both Europe and Asia are fast being developed, with the Deutsches Zentrum für Luft- und Raumfahrt (DLR) facility in Germany and other facilities in China, Japan and Korea being continually developed as beamed energy propulsion projects expand.

With research concentrating on understanding the laser induced detonation physics, the hypersonic aerodynamics of the craft continues to be neglected and progress is falling behind other research areas. Little effort has been attributed to the aerodynamics of the inlet at hypersonic speeds, with no consideration given to reliable operation at off design conditions. As this is a very significant portion of the flight trajectory, the lightcraft project requires more research in this area if it is to be successful. A number of hypersonic inlet design techniques are available, all with their own benefits and drawbacks. To design a suitable lightcraft inlet it is essential to consider the specific requirements of the laser induced detonation process and select the most appropriate inlet design methodology. At present, a detailed hypersonic inlet design study has not been conducted for the lightcraft mission requirements.

Further to the lack of a hypersonic inlet design for the lightcraft, a detailed investigation into the inlets behaviour and response to realistic flight scenarios has not been conducted. The inlets' behaviour when subjected to reduced Mach numbers, vehicle angles of attack and laser energy deposition is currently unknown. It is essential that an understanding of these phenomena is developed.

2.5.1 Gap statement

This project aims to address the gaps within lightcraft research relating to hypersonic inlet design. No investigations have previously looked at the hypersonic flight requirements for the lightcraft, particularly relating to the air breathing propulsion system. To ensure sufficient air is delivered to the laser induced detonation engine at hypersonic speeds, a detailed investigation into inlet design is required. The inlet plays a vital role in the operation of the laser powered propulsion system during hypersonic flight, and a suitable design is required. A hypersonic inlet for the lightcraft vehicle is to be produced in this work through the application of traditionally fuelled hypersonic inlet design techniques. Consideration to the requirements of the lightcraft launch conditions, as well as the limitations of the laser induced detonation systems, have been given due attention. A range of inlet designs for the lightcraft vehicle sympathetic to the engines requirements at higher flight speeds are established, providing insight into both the design requirements and the expected performance achievable.

Further to this, the behaviour of the hypersonic inlet at angles of attack is not well understood. The sensitivity of hypersonic inlet designs to flight perturbations has currently been underestimated within the lightcraft community. No research to date has been conducted in these areas, with the assumption that the lightcraft can continue to produce thrust at high angles of attack, at all flight speeds. Extensive conventionally fuelled scramjet research has illustrated the sensitivity of inlets to unstart at hypersonic speeds, yet no investigation into how the proposed lightcraft trajectory relates to inlet dynamics has been performed. An investigation of the inlets behaviour at realistic flight angles of attack is essential to ensuring operation throughout the flight envelope. Not only does this research aim to establish the flight conditions that the hypersonic inlet will experience during its ascent to lower earth orbit through a detailed trajectory analysis, numerical simulations are performed at realistic vehicle angles of attack to ensure the inlet remains operable throughout the hypersonic flight envelope.

3 System level analysis

3.1 Introduction

In order to launch a satellite into orbit, it is necessary to optimise the flight path. This involves selecting a suitable flight path that minimises cost, while maximising the chance of success. The launch to lower earth orbit is a complicated task with many inter-related variables that must be balanced to achieve the optimal result. If, for example, the time to reach lower earth orbit is reduced by accelerating the vehicle at a higher rate, a significant increase in the heating of the craft will occur. This may result in vehicle failure - an undesired event. A wide range of considerations are required to choose the optimal flight path.

A system level analysis has been undertaken, determining the trajectory the lightcraft will follow during its ascent through the atmosphere. Once the trajectory has been established, the flight behaviour at each point in the launch is known. By combining this with knowledge of the atmospheric properties at specific altitudes, the basis of the lightcraft flight conditions can be established. A flight path simulation is especially important in the context of the air breathing inlet design, as it will establish the atmospheric conditions entering the propulsion system throughout the flight. By performing the system level design, real flight conditions obtained can then be used to form the basis of the inlet design.

Lightcraft launch trajectories are simulated using a numerical code programmed in Matlab. The code is able to produce, at each time step iteration, outputs such as altitude, horizontal range and flight speed. There are three main parts that form the system level analysis - a point mass equations of motion model, an aerodynamic model and a propulsion system model. With reduced order models for the components of the flight system, an accurate approximation of the physics for the air breathing portion of lightcraft flight has been produced.

3.2 Flight path model

The flight of the lightcraft is defined by Newton's laws of motion. Figure 3.1 illustrates the forces acting on the point mass approximation of a lightcraft during an arbitrary stage of the launch. The thrust imparted by the laser beam, T , acts co-linearly with the direction of velocity, V , and the drag, D , acts in the opposite direction to velocity. Lift, L , acts

perpendicular to the direction of the velocity vector of the lightcraft. The gravitational force, mg , acts towards the centre of the earth. It is the product of the mass of the lightcraft, m , and the acceleration due to gravity, g , at the current altitude. The flight path angle, γ , is defined as the angle between the velocity vector and the local horizontal. Additionally, the altitude (the distance between the lightcraft and the earth's surface) is defined as h , the horizontal range R and the radius of the earth R_E .

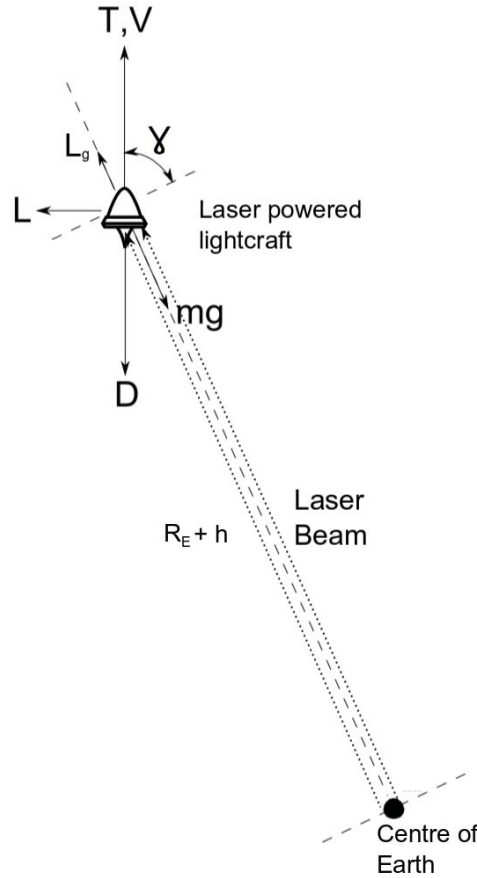


Figure 3.1: Forces acting on the lightcraft during flight.

Using the point mass equations of motion (Miele, 1962), four differential equations describing the dynamics of the flight can be established, where \dot{V} , $\dot{\gamma}$, \dot{x} and \dot{h} are the time derivatives of the respective variable.

$$\dot{V} = \frac{1}{m}(T - D - mg \sin \gamma) \quad (3.1)$$

$$\dot{\gamma} = \frac{1}{mV}(L_g \cos \gamma + L - mg \cos \gamma) \quad (3.2)$$

$$\dot{x} = V \frac{R_E}{R_E + h} \cos \gamma \quad (3.3)$$

$$\dot{h} = V \sin \gamma \quad (3.4)$$

Since the extent of flight duration is only considered within the sensible atmosphere, $R_E \gg h$ and Eqn. 3.3 can be approximated as

$$\dot{x} = V \cos \gamma \quad (3.5)$$

Differentiating Eqn. 3.4 and Eqn. 3.5 with respect to time, and then substituting into Eqn's. 3.1 and 3.2 yields the point mass equations of motion used in the system level design (Doolan, 2007)

$$m\ddot{x} = T \cos \gamma - D \cos \gamma - L \sin \gamma - L_g \cos \gamma \sin \gamma \quad (3.6)$$

$$m\ddot{h} = L_g \cos^2 \gamma + L \cos \gamma - mg + T \sin \gamma - D \sin \gamma \quad (3.7)$$

The lift due to the centripetal force associated with the gravitational acceleration, L_g , has been assumed to be small and is neglected in this study. The values of density, pressure, temperature and speed of sound are updated with altitude using the US standard atmosphere model (Stengel, 2004).

3.3 Aerodynamic model

The lift and drag of the lightcraft can be represented by the equations

$$L = \frac{1}{2} \rho V^2 C_L A \quad (3.8)$$

$$D = \frac{1}{2} \rho V^2 C_D A \quad (3.9)$$

where ρ is the density of the free stream atmosphere at the current lightcraft altitude, V is the velocity of the lightcraft, C_L is the coefficient of lift, C_D coefficient of drag and A is the plan-form area. The lightcraft geometry has been approximated as a three dimensional cone, with three flow regimes in the trajectory simulation; subsonic, transonic

and supersonic. The aerodynamic lift and drag change considerably during these regimes, and separate approximations are required to model the system with sufficient accuracy.

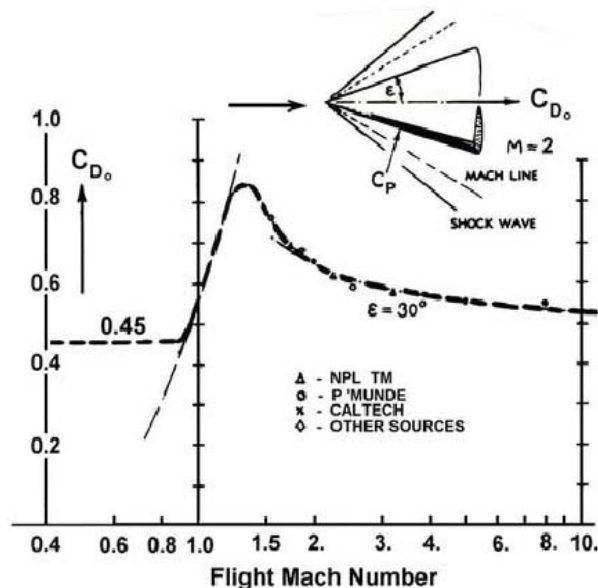


Figure 3.2: Coefficient of drag for a 30° half angle cone (Hoerner, 1965).

Flight velocities less than Mach 0.9 are considered subsonic, and the coefficient of drag is taken as a constant value of 0.45 (Richard *et al.*, 2006). Between flight velocities of Mach 0.9 and Mach 1.5, the transonic coefficient of drag is approximated by Eqn 3.10. This is a linear interpolation of the transonic drag in this transonic region (Hoerner, 1965).

$$C_D = 0.5833 * M - 0.07495 \quad (3.10)$$

For both the subsonic and transonic region, the data used is for a 30° half angle cone, as shown in Figure 2.12. The final lightcraft design uses a 15° half angle, so this estimate is considered conservative. For both the subsonic and transonic regimes, the lift is assumed to be zero. This is based on a vertical launch, with flight maneuverability occurring once supersonic flight has been established.

For flight velocities greater than Mach 1.5, the lift and drag coefficients are approximated using a local surface inclination model (Newton's method), with the angle of attack determining the amount of lift and drag the lightcraft produces at a specified velocity. Newton's flow theory is based on the principle that when a flow of particles encounters an inclined surface, each particle will lose all of its' momentum normal to the surface, but the momentum in the direction tangential to the surface will be maintained (Anderson, 2000). Figure 3.3 illustrates the mechanics of Newtonian theory for a single particle strik-

ing a two dimensional surface. The particle travels parallel to the free stream velocity, until it encounters the inclined surface. The particle is then forced to travel parallel to the inclined surface. The momentum required to change the trajectory of the particle is supported by an increased surface pressure on the inclined object.

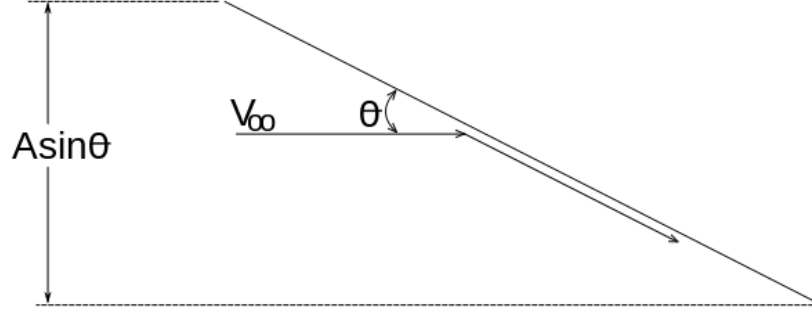


Figure 3.3: Newtonian theory (Anderson, 2000).

From Newton's second law, the rate of change of momentum of the particle is equal to the force exerted on the plate. This can be expressed as

$$\frac{F}{A} = \rho_\infty V_\infty^2 \sin^2 \theta \quad (3.11)$$

Due to Newton's assumption that the motion of particles is rectilinear, this pressure needs to be interpreted as the pressure above free stream conditions,

$$\frac{F}{A} = p - p_\infty \quad (3.12)$$

where p is the surface pressure and p_∞ is the free stream static pressure. Rearranging Eqn's 3.11 and 3.12 gives a result for the coefficient of pressure acting on the plate.

$$C_p = \frac{p - p_\infty}{\frac{1}{2} \rho_\infty V_\infty^2} = 2 \sin^2 \theta \quad (3.13)$$

The geometry of the lightcraft is assumed to be a three dimensional circular cone of base radius R and half-angle τ , as shown in Figure 3.4. The pressure acts normal to the conical surface, generating both vehicle lift and drag forces. By integrating the pressures over the upper and lower surfaces, the lift and drag of the lightcraft at each specific velocity and angle of attack can be calculated. The base of the lightcraft is essentially 'shielded' from the flow, and can therefore be assumed to have the freestream pressure acting on it (Anderson, 2000). Using the Cartesian co-ordinates of the body reference

frame, the velocity vector V is incident on the cone at an angle of α to the x axis, defining the angle of attack of the vehicle. Due to the assumption of no side slip of the craft, α is always defined in the $x - z$ plane.

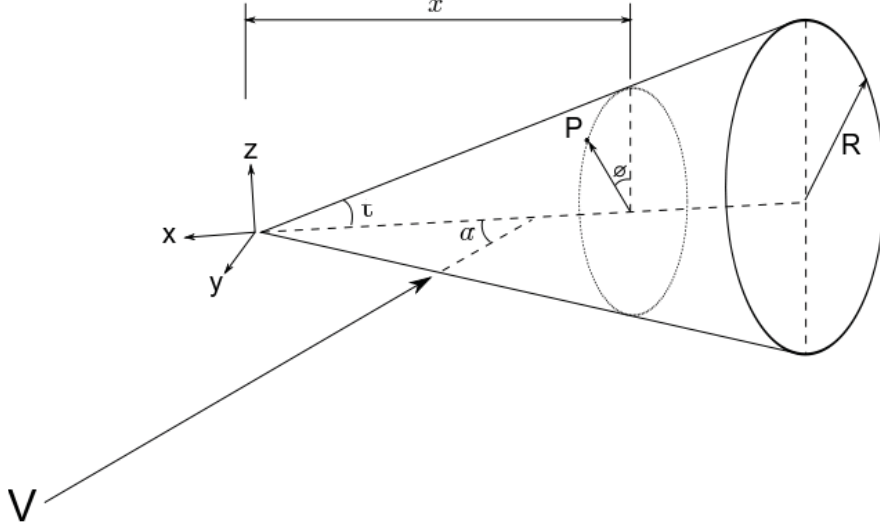


Figure 3.4: Newtonian theory applied to simplified lightcraft geometry.

Applying Newtonian flow theory to the conical geometry (Prime, 2011), the coefficient of pressure is defined as

$$C_{p,cone} = 2(\mathbf{n}_v \cdot \mathbf{n}_{cone})^2 = 2(\cos \alpha \sin \tau + \sin \alpha \cos \tau \sin \phi)^2$$

These expressions are in the body-reference frame of the lightcraft, and therefore need to be rotated back to the velocity reference frame. The resulting expressions for lift and drag in the aerodynamics model are then

$$L = \frac{1}{2} \pi \rho V^2 R^2 (\sin 2\alpha \cos^2 \tau \cos \alpha - (\sin^2 \alpha + 2 \sin^2 \tau - 3 \sin^2 \alpha \sin^2 \tau) \sin \alpha) \quad (3.14)$$

$$D = \frac{1}{2} \pi \rho V^2 R^2 (\sin 2\alpha \cos^2 \tau \sin \alpha + (\sin^2 \alpha + 2 \sin^2 \tau - 3 \sin^2 \alpha \sin^2 \tau) \cos \alpha) \quad (3.15)$$

3.4 Propulsion model

During aerobic operation the laser lightcraft vehicle utilises air from the atmosphere as the medium for converting the laser energy into usable thrust. The incoming air stream

is compressed by the inlet, and the intense laser energy deposited within the engine cowl. The resulting detonation wave is then expanded over the lightcraft afterbody to generate an impulsive force. An analytical model of the laser induced detonation wave has been used to determine the effect of the air conditions on the detonation cycle. From this model, an approximation to the amount of thrust produced given certain inlet conditions can be calculated. The model therefore establishes the required performance of the inlet, and also provides a verification of the final inlet design.

Numerous analytical studies of the laser induced detonation wave thrust generation process have been produced previously (Feikema (2000); Ushio *et al.* (2004); Richard & Myrabo (2005) and Salvador (2010)), with this model following a similar approach. The laser induced detonation wave is modeled as a cylindrical blast wave emanating from an initial plasma radius. Real gas effects, such as dissociation, recombination and ionisation are not considered. It is assumed that the time taken for the plasma to form is significantly less than the detonation formation process, and plays a sufficiently small part in the thrust generation process (Ghosh & Mahesh, 2008). The initial velocity of the expanding detonation wave front is

$$V_{LSD} = [2(\gamma^2 - 1) \frac{I}{\rho_0}]^{1/3} \quad (3.16)$$

where I is the laser intensity (W/m^2), γ is the ratio of specific heats of the gas and ρ_0 is the initial gas density (kg/m^3). The laser intensity is dependent on the design of the ground based laser, and published values vary from anywhere between $1 \times 10^{10} W/m^2$ (Reilly *et al.* , 1979) and $5 \times 10^{11} W/m^2$ (Feikema, 2000). A laser intensity of $5 \times 10^{10} W/m^2$ has been assumed in this study, as this ensures the laser supported detonation (LSD) wave is present (Reilly *et al.* , 1979). The maximum pressure exerted on the thrust surface by the detonation wave is

$$P_{LSD} = \left[\frac{\gamma + 1}{2\gamma} \right]^{\frac{2\gamma}{\gamma-1}} \frac{\rho_0 V_{LSD}^2}{(\gamma + 1)} \quad (3.17)$$

The time for the blast wave to become completely cylindrical is

$$t_{2D} = \frac{2r_{LSD}}{V_{LSD}} \quad (3.18)$$

where r_{LSD} is the radius of the blast wave. This value has been taken as $5mm$ (Feikema, 2000). The properties of the gas behind the detonation wave front are then

modeled using Sedov's scaling laws (Sedov, 1959)

$$P/P_{LSD} = (t/t_{2D})^{-1} \quad (3.19)$$

$$r/r_{LSD} = (t/t_{2D})^{1/2} \quad (3.20)$$

where r is the position and P the pressure of the wave front at time t . The conditions of the wave front are considered to be constant until the wave is cylindrical, then the scaling laws apply (Feikema, 2000). The thrust generated by each individual pulse is obtained by integrating the pressure of the blast wave front over the lightcraft afterbody as it expands. The conditions behind the wave front are assumed to be the same as the expanding front. This assumption will slightly overestimate the thrust produced by the lightcraft, however it is considered acceptable for this preliminary study.

A Matlab code has been produced that solves the analytical solution of the laser induced detonation wave for a specific pulse cycle configuration. The laser intensity, incoming air stream density, evolved plasma radius and lightcraft thrust surface geometry are specified, and the resulting detonation wave structure computed. Figure 3.5 shows a laser supported detonation wave profile for the conditions listed in Table 3.1. The time history of the generated thrust, pressure, velocity and position of the wave front are shown. We can see that the conditions remain constant while the plasma becomes completely cylindrical, then the expansion of the wave as time increases. The thrust is initially very small, until the wave expands and encompasses a greater area of the thrust surface. There is a peak period of thrust generation, which then tapers away as the wave expands and the pressure behind the front is reduced.

Radius of plasma	5 mm
Specific heat ratio of plasma	1.2
Laser intensity	$5 \times 10^{10} \text{ W/m}^2$
Air density	0.32 kg/m^3

Table 3.1: Flow conditions for blast-wave analytical solution.

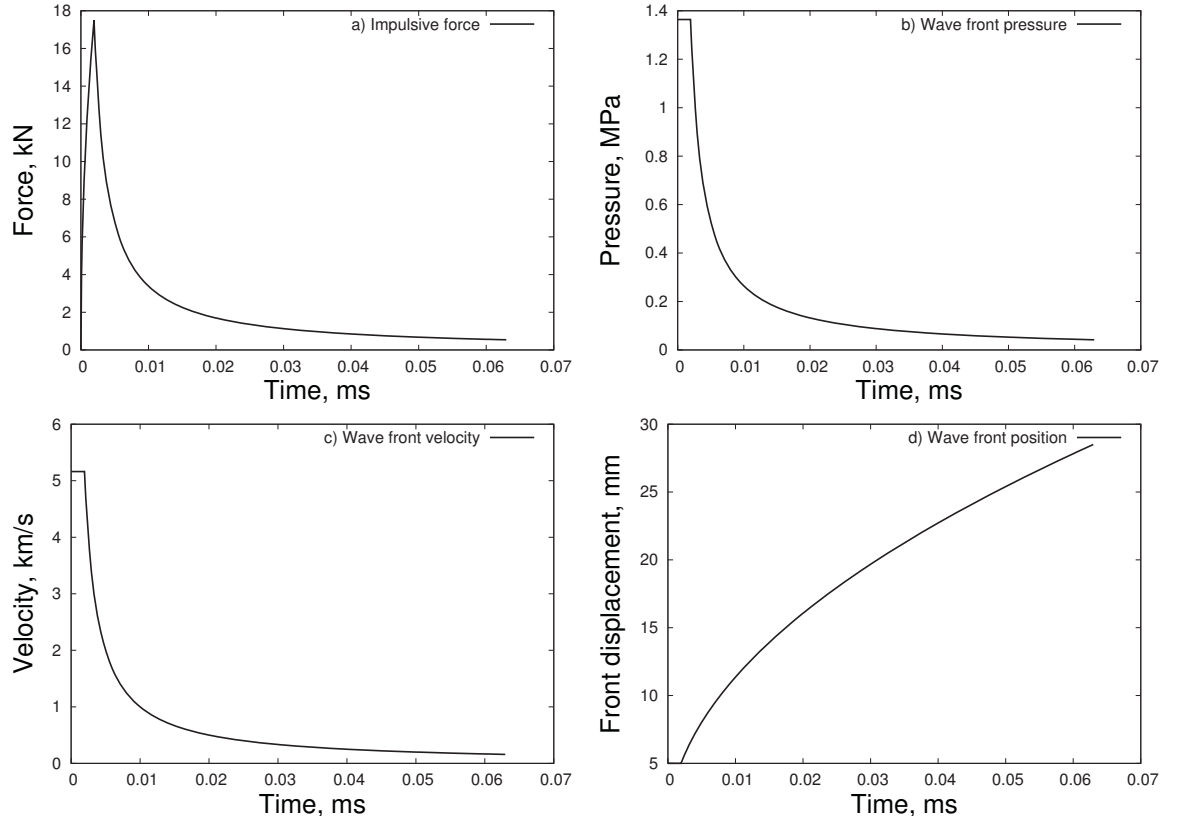


Figure 3.5: Typical blast wave simulation results. a) Impulsive force; b) Wave front pressure; c) Wave front velocity; d) Position

3.4.1 Numerical simulation verification

The results obtained from the one dimensional analytical model were then compared against a numerical simulation performed in Fluent as a means of cross-code verification. The analytical solution of the wave propagation was made using initial conditions calculated from Equation 3.17. The region of high pressure was then allowed to relax in a transient, compressible simulation. A two-dimensional structured grid of size 41,954 cells was found to be sufficient to ensure grid independence. By the final simulation time of $3 \times 10^{-5} s$, both pressure waves had relaxed to ambient conditions. Figure 3.6 shows the time-dependant pressure history of the gas wave front for both the analytical solution and the CFD numerical solution. The plot indicates that the solution of the wave profile obtained from the numerical simulation drops to atmospheric conditions more rapidly than the analytical solution. It has been previously noted that the Sedov solution to the expanding detonation wave does not accurately match the expansion at longer time scales (Salvador, 2010).

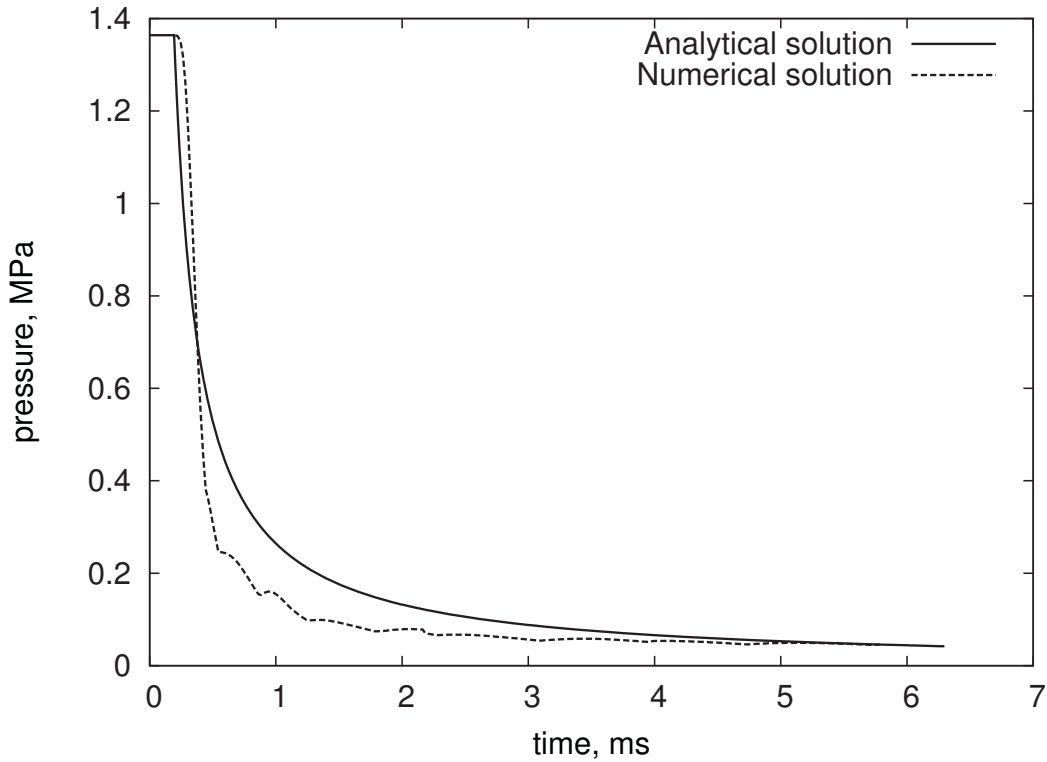


Figure 3.6: Analytical and Computational result comparison.

3.5 Flight path results

The lightcraft trajectory simulation schedules thrust and angle of attack over the flight path. Various scenarios are investigated to obtain realistic trajectories for lower earth orbit insertion. During the flight of a lightcraft, thrust will be controlled by modulation of the ground based laser beam, and in this model it is assumed that this can be done with a high degree of accuracy. The designer can dictate how much thrust can be applied at each stage of the flight, within the practical limits of the laser system. Although at this stage it is not yet known how the craft will manoeuvre, it is assumed that the angle of attack of the craft will be controllable throughout the entire flight. This can be achieved by adding a flight control system, however this is outside the scope of this project. A Matlab code to solve the general equations of motion has been modified to suit this application. The resulting system of differential equations, Eqn 3.6 and 3.7, are solved by the inbuilt Matlab ‘stiff’ ODE solver, ode15s (Stengel, 2004). The solution is marched through time, with values for velocity, flight path angle, altitude and horizontal range solved at each solution step. These updated values are then used to solve the subsequent iteration.

The values for thrust and angle of attack were scheduled over a number of altitude

envelopes, either by manual input from the user or by a coded function. Allowing input from a coded function gives the code significant flexibility, and the complexity of control input can be significantly reduced. If, for instance, the designer wishes to implement a complex control system based flight conditions at certain stages of the launch, they can implement a user developed code to interface with the flight path code.

It was chosen to specify the thrust and angle of attack values over distinct altitude ranges in order to be able to specifically limit the drag in the lower regions of the atmosphere. Five flight paths are presented, with the thrust and angle of attack schedules shown in Tables 3.2 through 3.6. The values for thrust and angle of attack were produced through a combination of previous studies, and trial and error. Previous studies acted as a guide on the upper limits on the thrust able to be practically achieved (Richard & Myrabo (2005), Ushio *et al.* (2004), Richard *et al.* (2006)). A change over altitude from aerobic to anaerobic propulsion of 35km was assumed, and a lightcraft velocity of Mach 8 was desired at this point (Davis & Mead Jr, 2007).

Altitude range (km)	Thrust (N)	Angle of attack (Degrees)
0 - 0.050	300	0
0.05 - 10	400	0
10 - 15	623	0
15 - 32	700	0
32 - 40	623	0
40 - 70	400	0

Table 3.2: Trajectory code input parameters, flight path 1.

Altitude range (km)	Thrust (N)	Angle of attack (Degrees)
0 - 0.050	300	0
0.05 - 10	300	2
10 - 45	700	0
45 - 70	700	0

Table 3.3: Trajectory code input parameters, flight path 2.

Altitude range (km)	Thrust (N)	Angle of attack (Degrees)
0 - 0.050	300	0
0.05 - 10	400	0
10 - 45	400	6
45 - 70	1000	6

Table 3.4: Trajectory code input parameters, flight path 3.

Altitude range (km)	Thrust (N)	Angle of attack (Degrees)
0 - 10	400	0
10 - 35	1100	4
35-53	500	4
53 - 70	400	6

Table 3.5: Trajectory code input parameters, flight path 4.

Altitude range (km)	Thrust (N)	Angle of attack (Degrees)
0 - 0.050	500	0
0.05 - 10	900	12
10 - 45	900	8
45 - 70	800	8

Table 3.6: Trajectory code input parameters, flight path 5.

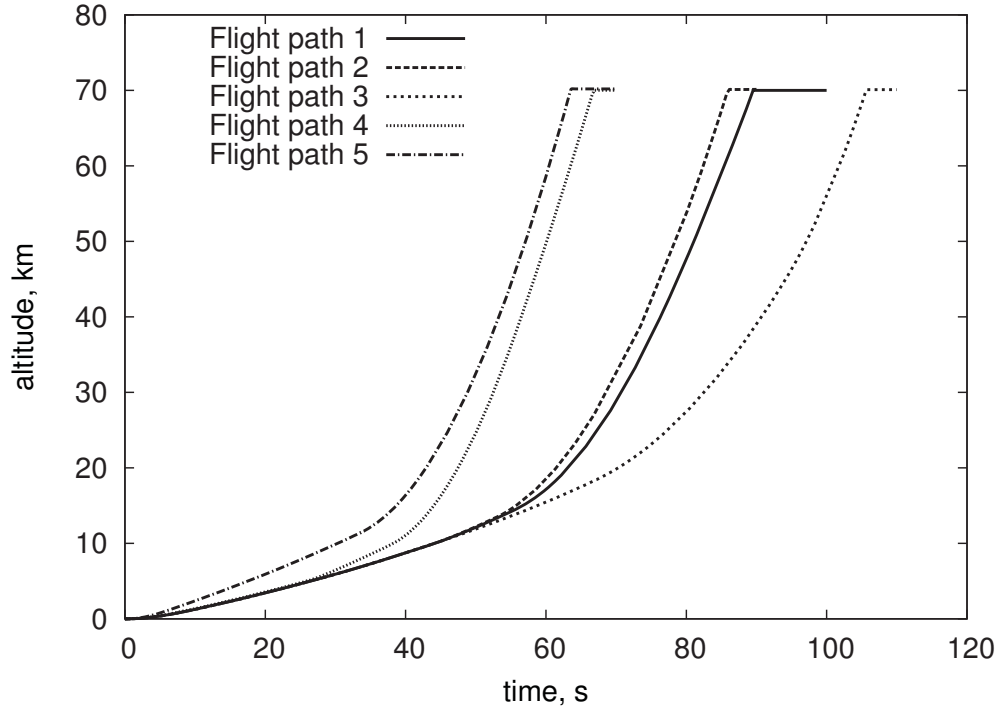


Figure 3.7: Flight path geometries for varying thrust and lift inputs.

Figure 3.7 shows the simulated flight paths for the thrust and angle of attack input conditions outlined in Tables 1 through 5. This figure illustrates the sensitivity of the physics of the lightcraft; the behavior of the lightcraft responds significantly to changes in thrust and angle of attack.

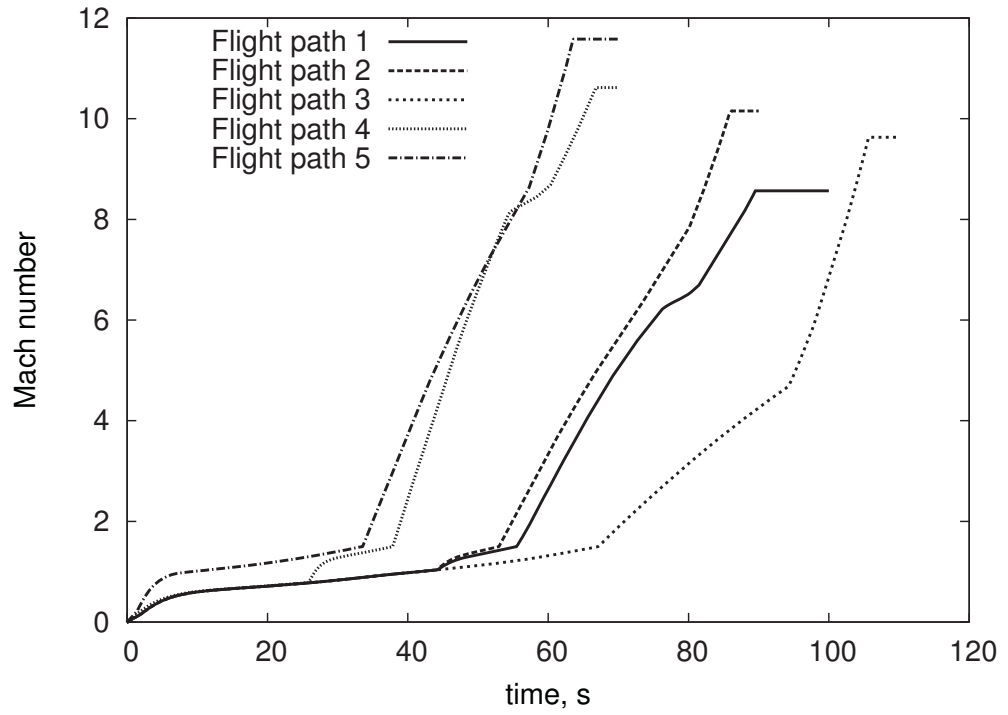


Figure 3.8: Mach number vs time for varying flight trajectories.

Figure 3.8 shows the Mach number of the lightcraft as a function of time. It can be seen from this plot, a number of different final exit velocities can be achieved.

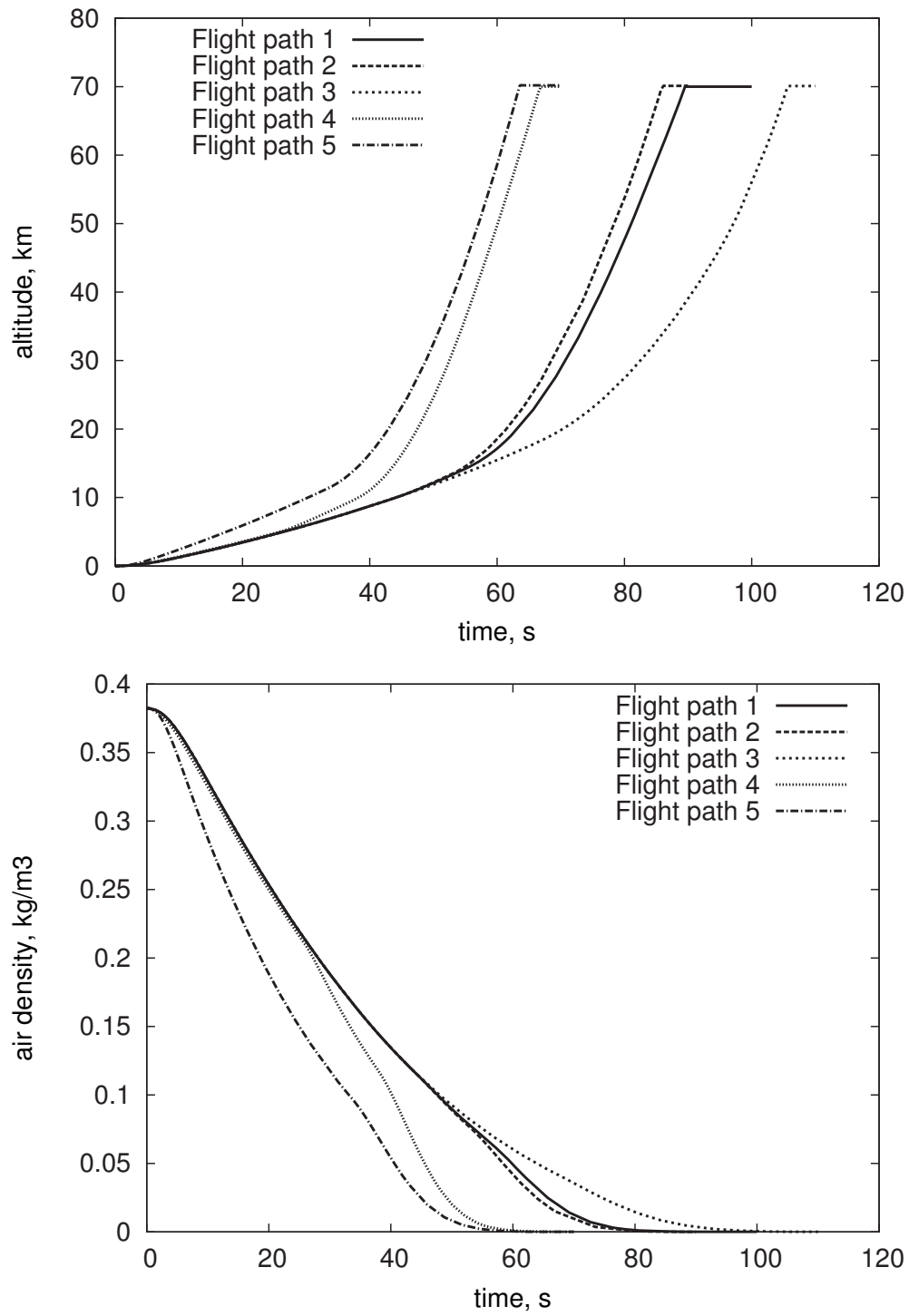


Figure 3.9: Flight conditions for varying flight path geometries.

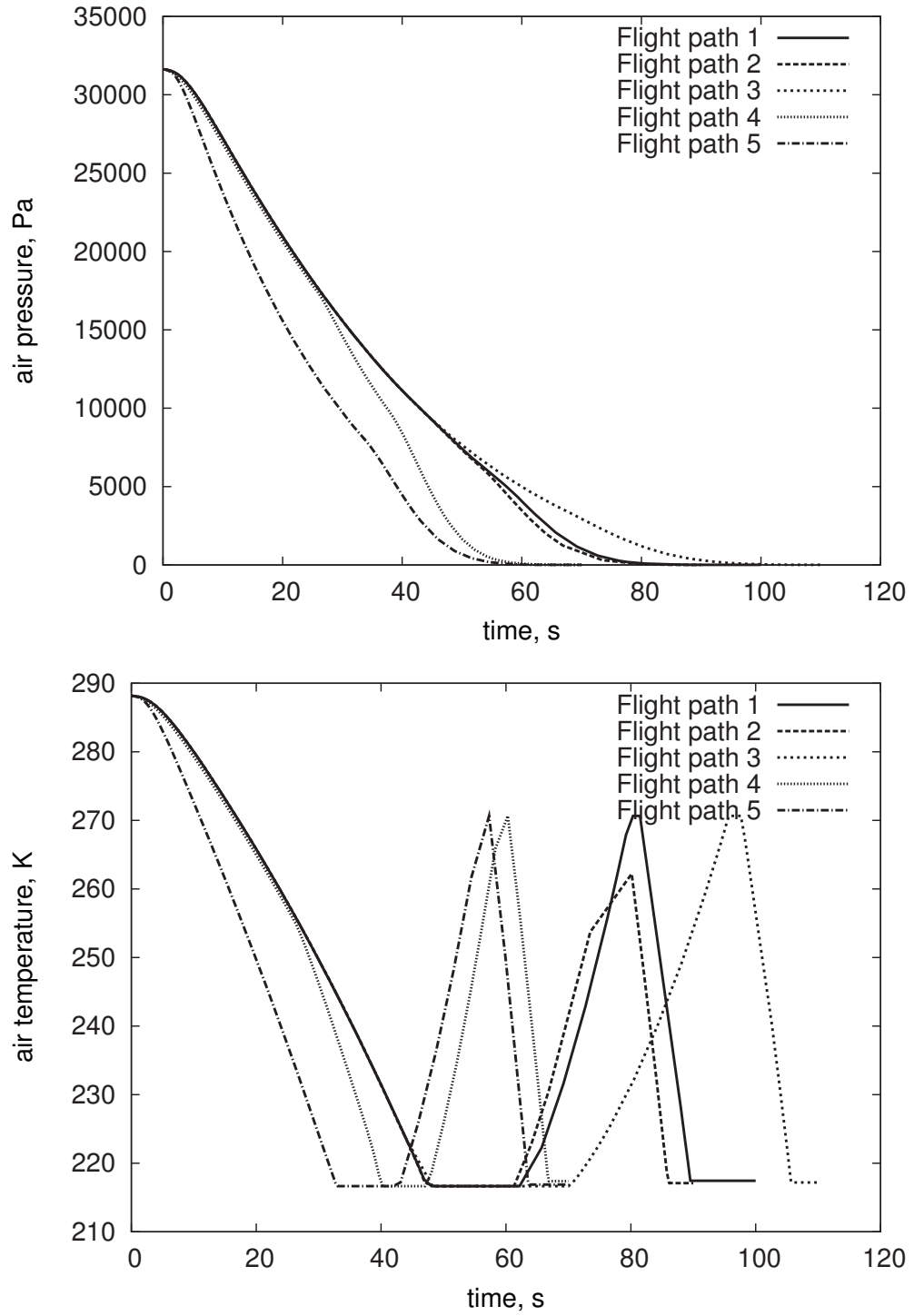


Figure 3.10: Flight conditions for varying flight path geometries.

Figures 3.9 and 3.10 show plots of altitude, air density, air pressure and temperature at each point in the flight, with Figure 3.11 showing the actual flight path taken by the vehicle. These plots were used to select the final flight path launch parameters, flight path number 4 (Table 3.2). This was selected as it provided a suitable exit velocity for change over to ablation propulsion, without placing onerous requirements on the inlet

compression and creating a sensible exit path from the atmosphere.

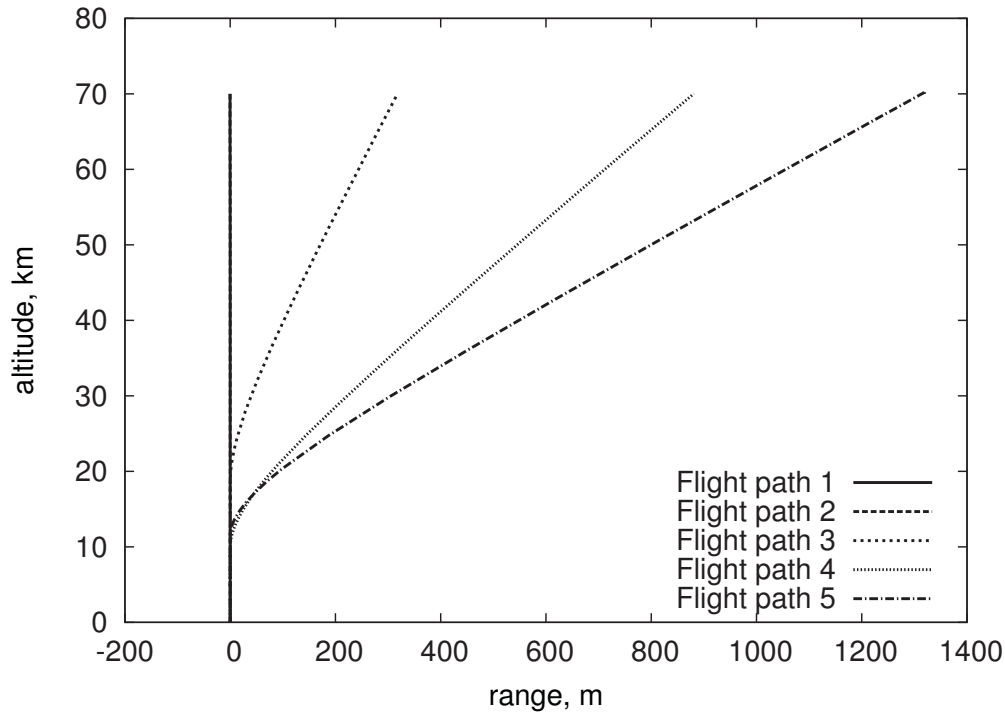


Figure 3.11: Range vs altitude plot for varying flight path geometries.

Figure 3.12 shows a plot of the density required at the laser detonation process (obtained using the propulsion system model, discussed in Section 3.4) against the stagnation density of the free stream air. This plot gives an indication as to whether the required compression of the flight path is physically achievable. If compression above the stagnation density is required, the flight path is deemed unacceptable. It should be noted that this is not an absolute indication as to whether the required compression is achievable by the inlet design, which is discussed further in Section 4. In this case, it may be necessary to increase the laser power to achieve the required thrust at lower densities than designed for, in the instance where an inlet cannot provide sufficient compression.

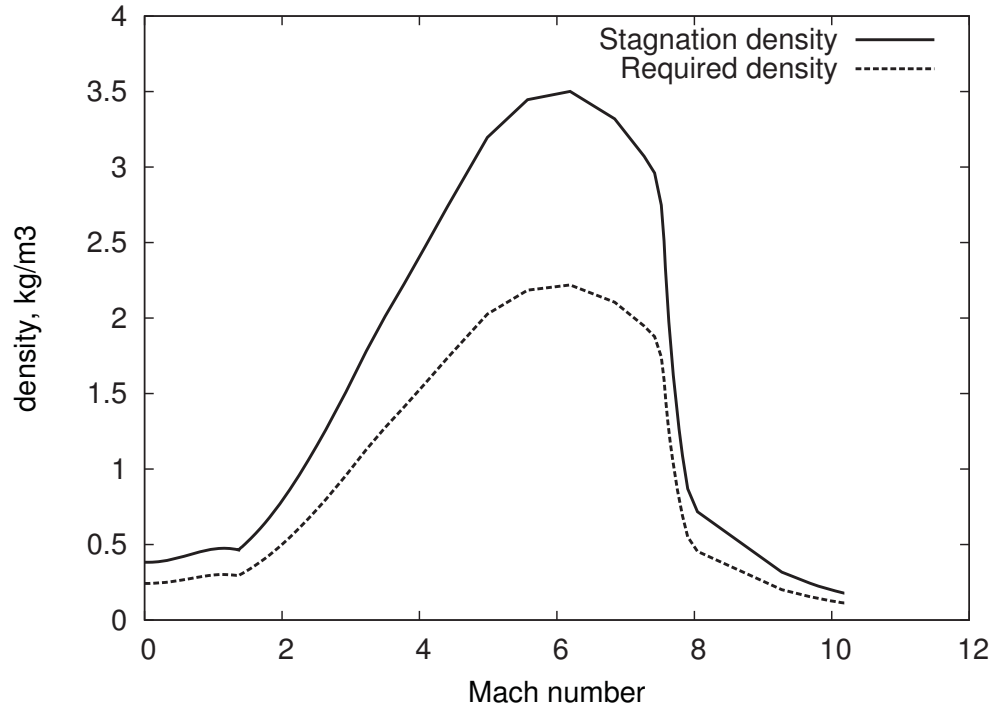


Figure 3.12: Required density compared to stagnation density over flight envelope.

It is now a matter of choosing a design point for the inlet, based on the trajectory study. The inlet design has been based on a flight speed of Mach 8, at an altitude of 35km. This design point was chosen as it is the highest Mach number the inlet will experience during air breathing propulsion. The highest Mach number will result in the lowest forebody shock angle. This allows the inlet to be designed such that the forebody shock is not ingested. As the speed is reduced, the shock moves away from the inlet. The relevant flight conditions are listed in Table 3.7.

Parameter	Design value
Mach number	8
Altitude	35,000 <i>m</i>
Freestream pressure	575 <i>Pa</i>
Freestream temperature	237 <i>K</i>
Freestream air density	0.00846 <i>kg/m³</i>
Target density for laser detonation thrust generation	0.651 <i>kg/m³</i>

Table 3.7: Inlet design parameters.

3.6 Summary and Conclusions

A system level design for the air breathing portion of flight has been successfully produced. Simplified, but accurate, approximations to the lightcraft flight physics were employed in

a numerical solution to the equations of motion. The design conditions for the lightcraft inlet have been established, allowing realistic values to be utilised in the inlet design.

The sensitivity of the flight craft flight dynamics were made apparent in the system level design. Small changes in the input parameters result in large changes to the flight path of the vehicle. Often non-real solutions to the equations were obtained if careful consideration of the trade-off between vehicle drag and acceleration was not applied. This highlights the significant control issues presented to the lightcraft designer. It was found that the thrust required by the lightcraft in the system level design correlated well to other studies (Richard & Myrabo (2005), Ushio *et al.* (2004), Richard *et al.* (2006)), giving confidence in the solution. It is also a promising result that the required compression of the hypersonic inlet is not significantly onerous throughout the hypersonic flight regime.

4 Inlet design

4.1 Introduction

The aim of this research is to produce a hypersonic inlet for a lightcraft vehicle. Four hypersonic inlet designs have been produced and evaluated. The best performing inlet is then to be used and tested in the final lightcraft inlet design. This chapter presents the lightcraft inlet design methodologies used in this research and the final inlet geometries that are numerically simulated (see Chapter 5). Three novel lightcraft inlet designs have been created, using stream traced hypersonic inlet design techniques. They are the stream traced axi-symmetric inlet geometry, the stream traced axi-symmetric modular geometry and the stream traced ‘scalloped’ modular inlet geometry. Further to these new inlet designs, the traditional axi-symmetric lightcraft inlet configuration based on the Lightcraft Technology Demonstrator (LTD) inlet geometry has been applied to the design conditions employed in this study to provide a performance baseline against which the other inlets can be compared.

Each inlet design serves the purpose of compressing and delivering air to the laser detonation process as efficiently and effectively as possible. In line with the traditional lightcraft vehicle, each design consists of three distinct sections; a conical forebody which provides the initial compression, and inlet cowl/isolator that further compresses the flow and provides a thrust surface for the expanded laser induced detonation wave, and the parabolic after body that expands the heated flow. A representation of each inlet design is shown in Figure 4.1.

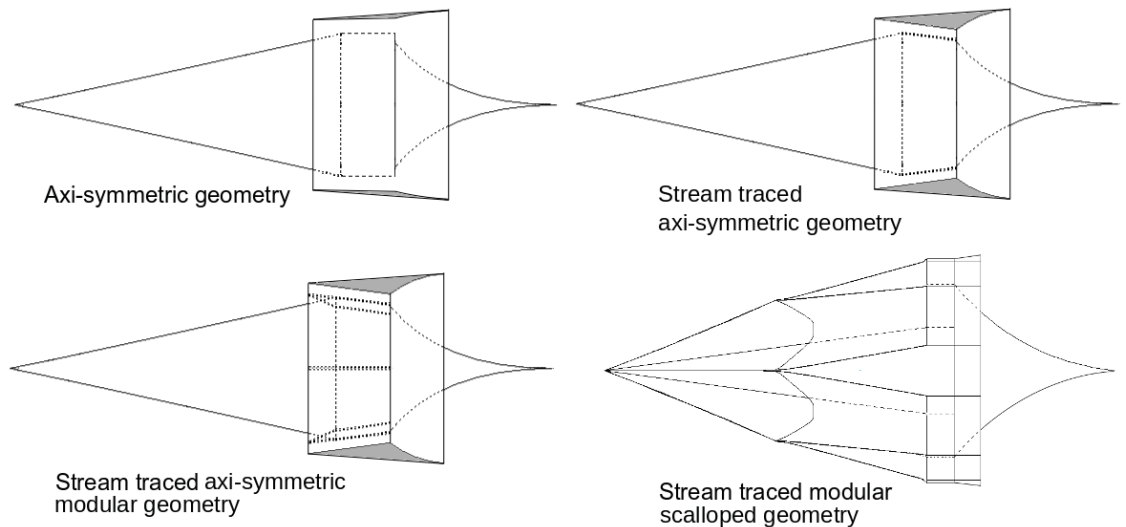


Figure 4.1: Inlet geometries investigated.

The design of the features downstream of the inlet flow (i.e. the nozzle/reflective optic) are outside the scope of this research, and hence have not been optimised for each individual application. Instead they have been based on parabolic curves currently employed to focus the incoming laser beam to a point at the isolator exit (Feikema, 2000). A parabolic nozzle has been included in the simulations to aid in the visualisation of the final numerical results. The ancillary lightcraft components (the conical forebody and the parabolic afterbody) have been kept identical for the different inlet geometries to allow a fair comparison between designs. This section of the thesis outlines the inlet design methodologies used in the study, and presents the final inlet designs produced.

4.2 Conical forebody

Although not specifically a part of the design aspect of this research, the conical forebody is an important aspect of the inlets' operation that must be considered. The conical forebody provides the initial compression of the incoming hypersonic freestream atmosphere, setting up the flow conditions at the inlet entrance. The lightcraft conical forebody is examined in greater detail in Langener *et al.* (2009) and Davis & Mead Jr (2007). As previously mentioned in Section 3.3, the drag of the lightcraft is proportional to the coefficient of drag, and the velocity squared;

$$D \propto C_D V^2$$

This implies at the extremely high velocities present in hypersonic flight, drag is tremendously high. Any reduction in the coefficient of drag will benefit the lightcraft project substantially, reducing the laser power required to launch the craft into orbit. Davis & Mead Jr (2007) have investigated reducing the drag of the lightcraft by altering the geometry of the conical forebody. Figure 4.2 illustrates that drag can be reduced significantly at transonic speeds by reducing the half angle of the conical forebody (hereafter referred to as θ_c). Although the benefits are far more apparent at transonic speeds, reductions in drag at these flight speeds also result in lower drag at higher Mach numbers.

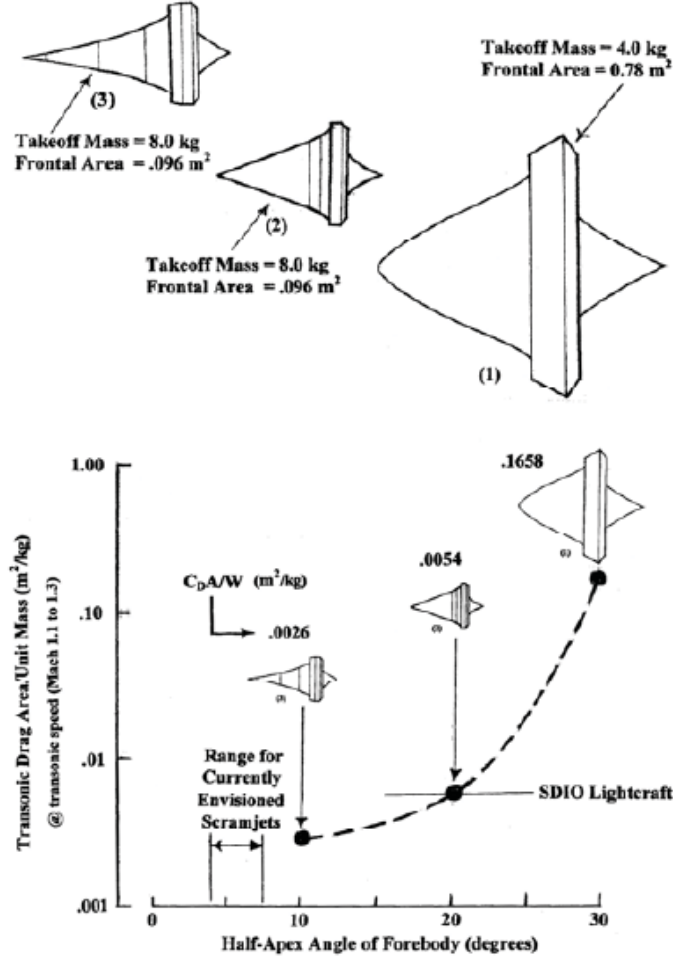


Figure 4.2: Coefficient of drag for lightcraft forebody configurations (Davis & Mead Jr, 2007).

A number of other techniques of varying complexity for reducing the drag of a conical compression ramp are available to the designer, such as multi-stage or isentropic compression ramps (Heiser *et al.*, 1994), however these have not been considered in this research. The inlet geometry has been designed using a conical forebody length of 60cm and base diameter 30cm in line with Davis & Mead Jr (2007). This geometry gives a conical forebody half angle θ_c of 14.04°. Although a sharper conical forebody has been employed in this research compared to the work of Langener *et al.* (2009), it is important to note that the following inlet design methodologies (with the exception of the stream traced modular scalloped inlet) can be applied to any forebody shape.

4.3 Axi-symmetric inlet

The first inlet design is based on the typical hypersonic inlet geometry that would be seen in an axi-symmetric spike configuration. As outlined in Section 2.3, investigations into

the performance of this inlet geometry at hypersonic flight speeds is limited at best. This implies that although the design of this inlet for the lightcraft project is not new work, its analysis will provide a broader depth of understanding for this inlet configuration at both on and off design conditions. It will also provide a baseline for the analysis of the stream traced inlet concepts.

The axi-symmetric inlet design is based on a traditional supersonic axi-symmetric spike inlet design, where an external cylindrical engine cowl is employed to turn the flow inwards after the initial leading edge compression; shown in Figure 4.3. The vehicle forebody is employed to provide the initial compression, with the secondary compression coming from the cowl shock. The final geometry is similar to inlets typically seen on supersonic air breathing missile configurations (Van Wie, 2000). The position of the cowl is designed so that the secondary shock created by the cowl lip comes to rest on the expansion of the forebody cone into the isolator, resulting in uniform flow parallel to the isolator walls. This inlet design methodology is the most straight-forward method with which an axi-symmetric inlet can be produced.

This design process revolves around a two-dimensional axi-symmetric solution to the shock structure of the resulting flow field. In Figure 4.3, the angle θ_c is the angle of the conical forebody, and is fixed for the specific lightcraft design (see Section 4.2). By employing a solution to the Taylor-Maccoll equations (Huwaldt, 2008), the resulting oblique shockwave angle β_1 can be determined. The next step then involves calculating the secondary shock angle of the cowl, β_2 ; again through conical shock theory. To obtain uniform flow through the isolator, it is required that position of the cowl lip and resulting the angle β_2 are such that the secondary shock wave comes to rest on the expansion of the conical forebody into the isolator.

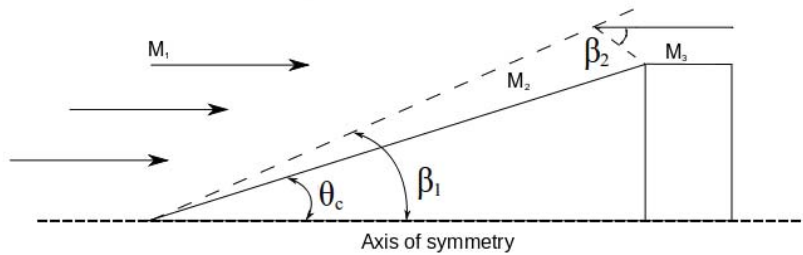


Figure 4.3: Axi-symmetric inlet design.

Once the inviscid shape has been calculated a viscous correction is applied to the conical forebody and inlet isolator geometry to allow for the growing boundary layer, further discussed in 4.4.2. After applying the viscous correction, the resulting flow field inherits some flow non-uniformities. Through careful adjustment of the inlet geometry these effects can be controlled satisfactorily. A re-expansion, similar to that described in Matthews *et al.* (2005), is added to the inlet throat to aid in the starting of the inlet, and also to allow a smoother transition for the conical forebody boundary layer as it enters the isolator. The re-expansion is incorporated into the lightcraft geometry by rounding the sharp angle where the conical forebody and inlet isolator meet into a smooth radius. It was found by providing this re-expansion, the strength of the expansion wave at the isolator could be reduced and the flow uniformity in the isolator increased. This is attributed to reduced shock/boundary layer interaction at the isolator throat. The optimal geometry of the re-expansion was found through a trial and error approach using numerical simulations to measure the flow uniformity through the inlet isolator. The radius of the re-expansion was increased until the radius that resulted in the most uniform isolator flow was achieved.

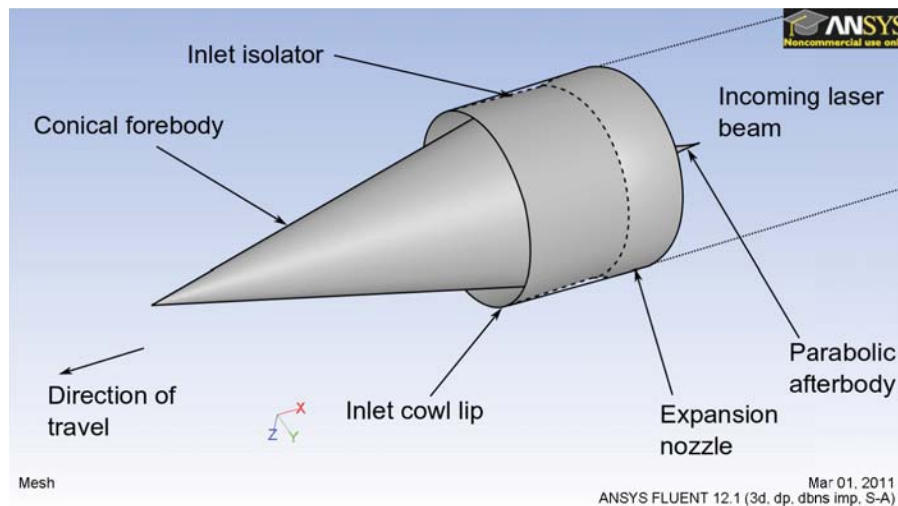


Figure 4.4: CAD representation of axi-symmetric inlet geometry employed in this study.

A CAD drawing has also been produced showing the dimensions of the craft used in the simulations, shown in Figure 4.5.

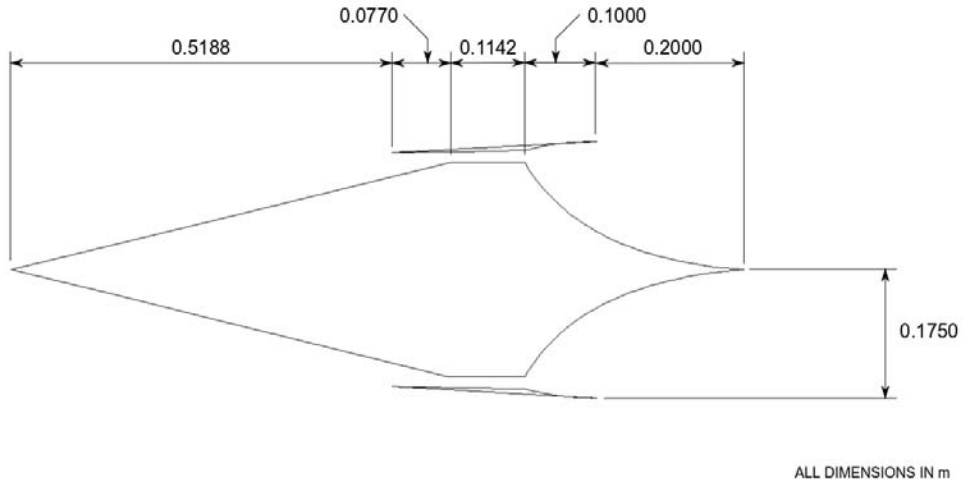


Figure 4.5: Technical CAD drawing of axis-symmetric inlet geometry.

4.4 Stream traced axis-symmetric inlet

The following three inlet design techniques are based on the stream traced inlet design methodology. The inlet and isolator geometry is formed by tracing streamlines through an axis-symmetric generating flow field. This process is essentially the same for the three inlet geometries, however there are some minor differences that will be highlighted. The general technique is discussed in this section, then the different inlet designs are discussed in the sections following. For simplicity the first inlet geometry, the stream traced axis-symmetric inlet, is designed in two dimensions, then rotated about the centre line to form an axis-symmetric, three dimensional geometry.

4.4.1 Inlet design methodology

The stream traced inlet design methodology is a technique used to design hypersonic inlets for integration into high speed craft. This technique has been applied to conventionally fuelled scramjet engines (Smart (1999), Billig & Kothari (2000) and Matthews & Jones (2006)), but has been modified in this work to suit the requirements of the lightcraft inlet. The method presented here will apply the main principles of the design technique to the axis-symmetric inlet design, with these principles then extended into three dimensions. This process allows a progressive introduction of complexity to the design procedure.

The stream traced inlet design methodology process is outlined in Figure 4.6. Specific desired inlet design conditions in the isolator can be chosen, and an inlet geometry generated to suit. This is done by employing an generating flow field that compresses

the incoming flow to the desired properties. Typically when using the stream traced inlet design methodology for a scramjet engine, the designer will choose a desired pressure ratio within the combustor at a certain inlet entrance Mach number (Smart, 1999). With the lightcraft design, performance is inherently linked to the density of the air delivered to the laser detonation process. It is therefore required to deliver the air to the laser induced detonation process at the required densities in order to achieve the required thrust (see Section 3.4), while maintaining flight operability. This implies that the incoming free stream air is compressed sufficiently to achieve the desired density, without the negative consequences of over compression. Such effects can include inlet unstart or excessive drag.

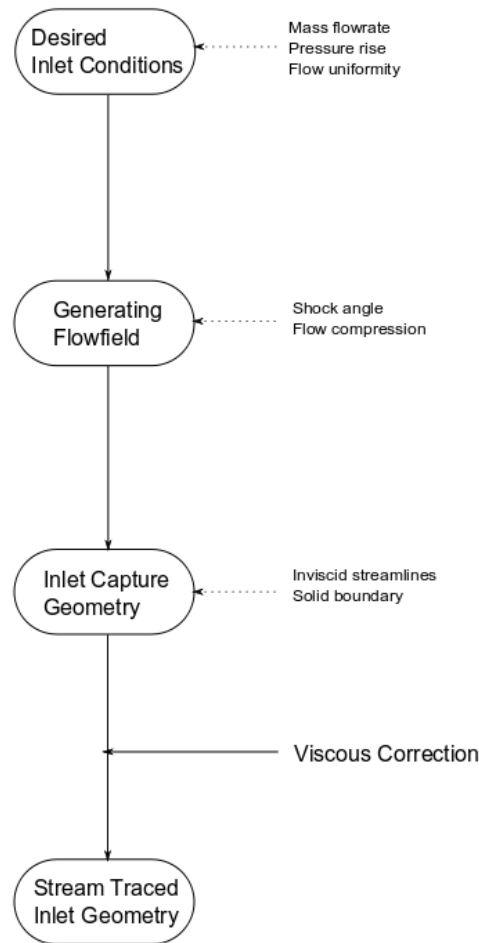


Figure 4.6: Stream traced methodology.

Once the required compression has been established, a generating flow field is created that performs the necessary compression of the inlet flow. From Section 3.4, the required density at the design conditions is found to be 0.651 kg/m^3 . At an altitude of 35km, the

freestream air density is 0.00846 kg/m^3 , requiring a compression ratio of 77. The conical forebody provides a compression ratio of 5.9, implying the generating flowfield is a required to compress the incoming flow a further 13 times. It was found that this compression ratio was too onerous for the generating flow field, resulting in Mach disks along the axis of symmetry. The compression requirements had to be somewhat downgraded from a flow field angle of 15° to 7.6° to reduce the size of the Mach disk. A reduction in the compression abilities of the inlet will reduce the peak thrust generated, however it necessary to avoid the inlet going into an unstated state. The streamlines of the generating flow field geometry, and resulting shock structure, dictate the final inlet geometry and hence careful consideration of the flow field is required. All properties of the chosen flow field, such as compression ratio, flow uniformity and uncanceled shock systems, will be present in the final inviscid inlet design. It was decided that by over compressing the incoming flow to sonic conditions, the inlets performance may suffer at angles of attack and reduced flight speeds.

The generating flow field shape can be classified into three types based on the radial deviation parameter (RDP); inward turning, planar and outward turning (Billig & Kothari, 2000). The *RDP* spans from values of $RDP = 1$ (inward turning) through to $RDP = -1$ (outward turning). At an $RDP = 0$, the flow field is planar. This is used for two dimensional inlet designs, with the generating body used shaped as an infinite wedge. For the lightcraft design an inward turning ($RDP > 0$) has been used. This is due to the nature of the flowfield surrounding the lightcraft geometry. The role of the generating flow field is the same as that of the two dimensional planar case - to manipulate the free stream supersonic flow via a fictitious generating surface into the desired combustor flow field. The flow is initially compressed by the lightcraft forebody in an outward turning, conical compression field. It is then desired to turn this flow back in towards the lightcraft centre line, directing it towards the laser propulsion system. For three dimensional inlet designs an axi-symmetric generating flow field is employed, having either an isentropic boundary to improve compression efficiency (Molder & Szpiro, 1966) or a constant slope boundary to decrease flow field length (Matthews & Jones, 2006). In this study the constant slope boundary has been chosen to limit the final length of the lightcraft vehicle.

The generating flow field used in the light craft inlet geometry creating is shown in Figure 2.16. This is generated for the design conditions listed in Section 3.4. In this image, the flow is moving from left to right, with the centre line being the axis of revolution. The conditions used at the entrance of the flow field are that of the flow off the conical forebody

- i.e. the initial compression has been taken into consideration in the inlet design. This is why the inlet conditions are at Mach 5.39, rather than Mach 8. The conical shock that provides the main compression can be seen meeting at a point in the centre of the flow field, with the resulting parallel flow after.

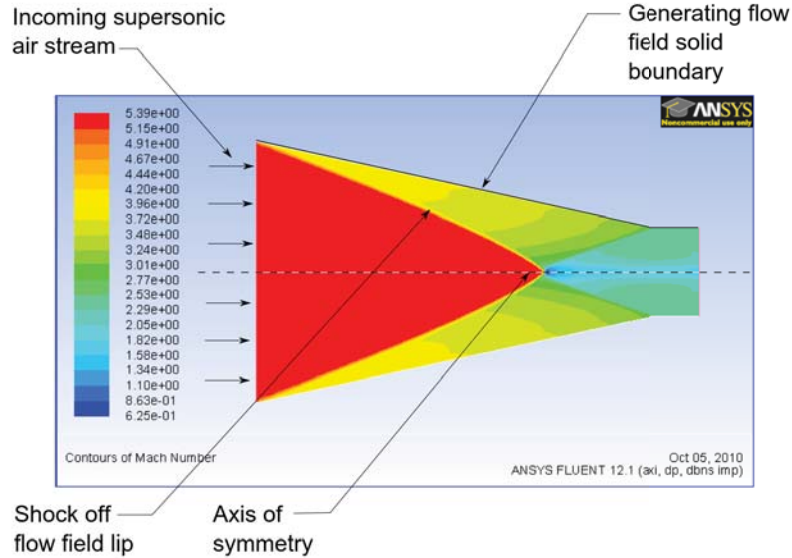


Figure 4.7: Generating flow field for lightcraft inlets.

The inlet geometry is then created by choosing a stream surface to form the solid inlet wall. The desired shaped can then be defined either upstream of the compression shock or at the end of the compression field. The streamlines that pass through the defined shaped are then followed or ‘traced’ downstream to the end of the compression field (or back towards the leading edge shock), defining the inlet shape. Figure 4.8 visualises the stream tracing technique for visual clarification. Each particle passing through this isolator profile is then traced back through the flow field along its streamline. This is further illustrated in Figure 2.18, where the final lightcraft geometry is mated to the stream traced inlet developed from the stream traced inlet design methodology. It is apparent in this image that the lightcraft is rotated slightly from the horizontal. This is due to the deflected flow off the conical forebody. This is required to be accounted for in the inlet design, and hence the final inlet geometry has been rotated an angle of 3° - the average value through which the chosen freestream streamlines are turned by the conical forebody.

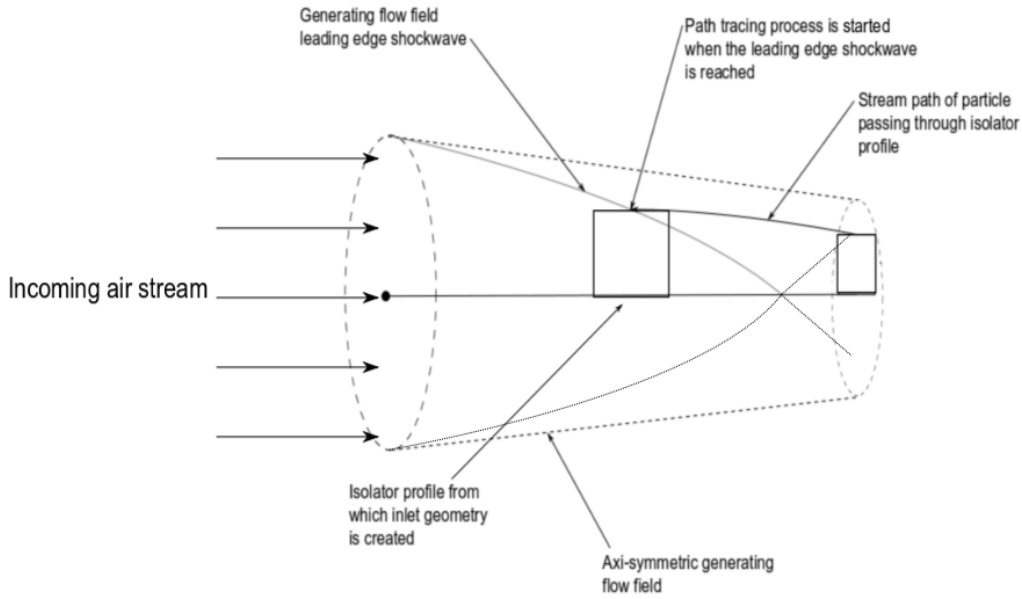


Figure 4.8: Stream tracing technique.

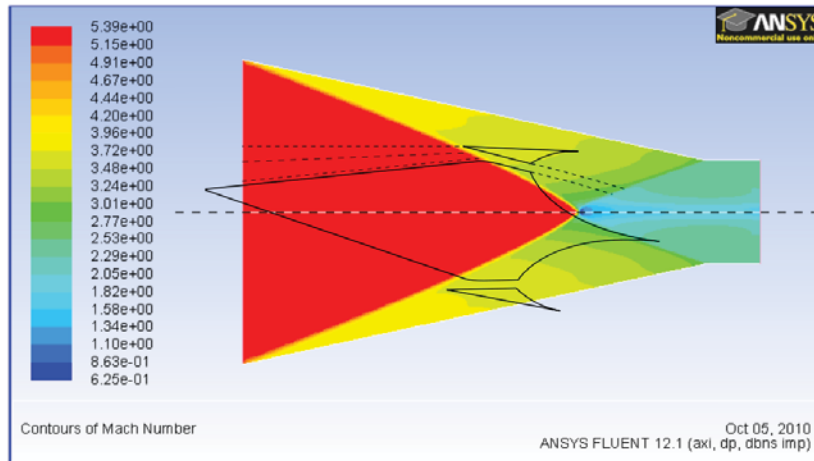


Figure 4.9: Stream traced inlet geometry from generating stream lines.

4.4.2 Stream traced inlet design code - streamTracer

The method of stream traced inlet design has traditionally been a laborious task, due to the complex analytical solutions required of the generating flow field and resulting stream traced inlet geometries. With the advent of modern computers, a number of research codes or techniques that allow the rapid generation of stream traced inlets have been developed (Smart (1999), Gollan & Smart (2010) and Croker (2007)). These are generally not available to the public. A code that allows the rapid generation of stream traced inlet designs has been created, called streamTracer (see Appendix B). The aim of the streamTracer code is to provide a simple, yet powerful, Matlab code to design three-dimensional

stream traced inlets from three-dimensional generating flow fields. StreamTracer allows the rapid prototyping and testing of different stream traced inlet geometries by acting as an ‘interface’ between flowfield design and inlet geometry. Figure 4.10 is a flow chart detailing the process involved in generating a viscous-corrected stream traced inlet design using the streamTracer code.

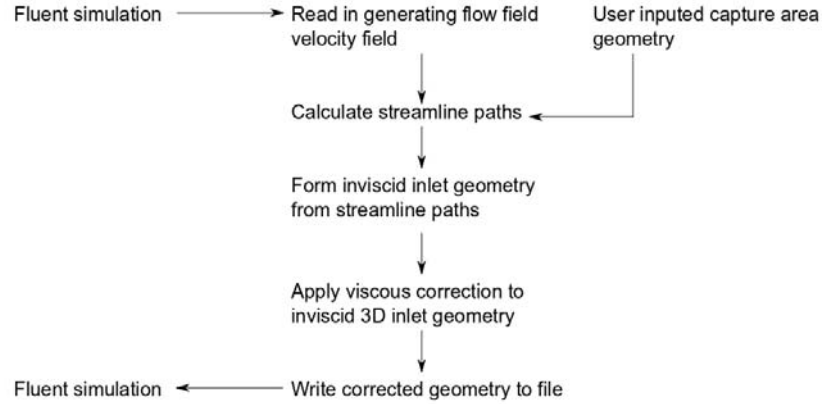


Figure 4.10: streamTracer code flowchart.

In the streamTracer code, flow field geometry selection is left up to the user - the current code is designed for quasi two-dimensional axi-symmetric flow fields, however it is possible to extend this to generic three dimensional flow fields. Quasi-two-dimensional axi-symmetric flow fields form the majority of flow field geometries used in inward turning inlet design, and hence are a suitable choice for the streamTracer code. StreamTracer takes input in the form of a velocity vector field from the CFD code Fluent; however any CFD code may be used.

Once the flow field has been imported into the streamTracer code, the user then defines the perimeter shape of the inlet capture area in Cartesian co-ordinates. The number of points defining the perimeter of the inlet shape is left up to the user - a lower number will reduce the accuracy of the final shape, but will also reduce computing time. The code then takes each individual point of the perimeter geometry, and uses the velocity flowfield data to generate Cartesian co-ordinate descriptions of their streamlines. The calculation of the inlet geometry in the three-dimensional space is handled by converting the Cartesian co-ordinates into a cylindrical co-ordinate system. Any point P in the flow field can be described by its position along the flowfield, x , its radial distance from the centre line, r , and its rotation about the z axis, ϕ as per Figure 4.11.

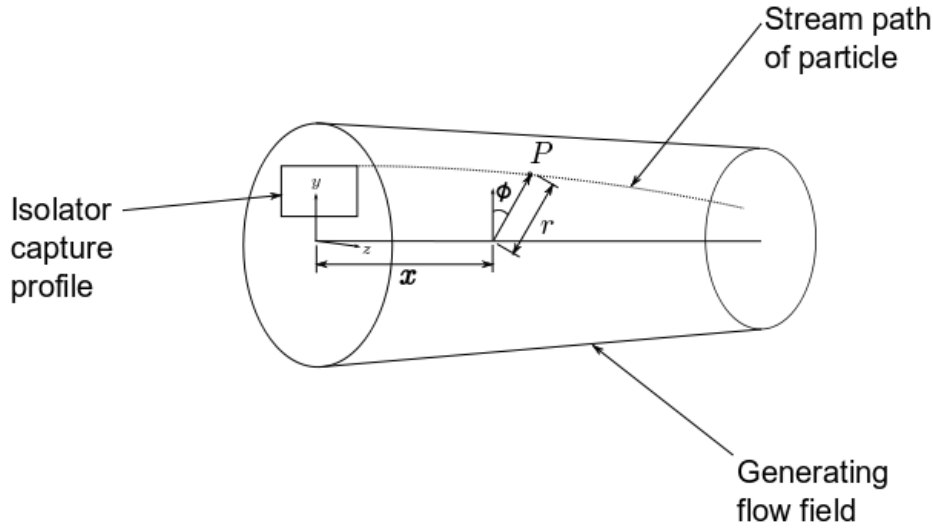


Figure 4.11: Position of an arbitrary particle within the generating flowfield.

Due to the axi-symmetric nature of the generating flow field, each streamline lies in planes of constant ϕ , depending on its initial point. The streamTracer code takes the initial Cartesian co-ordinate of the point and transforms it to cylindrical co-ordinates by transformation. The radial position of the point, r , is first calculated by

$$r = \sqrt{z^2 + y^2}$$

The rotation of the streamline plane, ϕ , is then calculated

$$\phi = \tan^{-1} \left(\frac{z}{y} \right)$$

Hence the transformation of the Cartesian profile point, P , into the cylindrical co-ordinates is

$$[x \ r \ \phi] = [x \ \sqrt{z^2 + y^2} \ \tan^{-1} \left(\frac{z}{y} \right)]$$

The x and r co-ordinates of the particles constant ϕ stream path are then calculated by the Matlab function 'streamline'. Each stream path co-ordinate is then converted back to the Cartesian co-ordinate system, using the transformation

$$[x \ y \ z] \rightarrow [x \ r \cos \phi \ r \sin \phi]$$

This works efficiently with the axi-symmetric flowfield, as the two-dimensional field can be used to create a three-dimensional space. This significantly reduces the computer

power required for the code, however some generality is lost in being limited to axisymmetric flow field geometries. For generic three-dimensional flow field geometries, a true three-dimensional method would be required to be implemented in the streamTracer code. The inlet geometry is then stored in the system memory as a series of Cartesian co-ordinates defining the three dimensional inviscid surface.

In order to account for the growth of the boundary layer within the inlet, we require an expression for its height above the surface at a specified distance. If we can obtain an expression for this value, the inlet geometry can be enlarged to allow for the boundary layer. In the streamTracer code the boundary is approximated using a flat plate estimation (Boyce *et al.* , 2000). The boundary layer thickness at a position x along the plate is

$$\delta^* = x \frac{0.2145M^{0.375}}{Re_x^{0.166}} (0.08801M + 0.06385) \quad (4.1)$$

where M is the local Mach number, and Re_x is the local Reynolds number. To ensure the validity of this method, the analytical solution has been compared to a flat plate simulation in Fluent at conditions similar to those experienced in the isolator of stream traced inlets. The flat plate shown in Figure 4.12 has been modelled at a free stream pressure of $P = 22000$ Pa, Mach number $M = 2.6$, density $\rho = 0.096 \text{ kg/m}^3$, and viscosity $\mu = 1.53 \times 10^{-5} \text{ kg/ms}$.

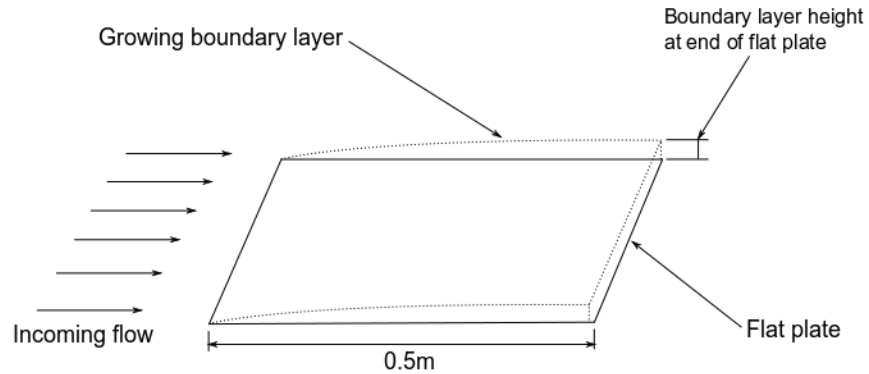


Figure 4.12: Flat plate verification.

The flat plate was then simulated in the CFD code Fluent with identical conditions to verify that the same boundary layer height was achieved. Both the Matlab code and Fluent simulation give a boundary layer height at the edge of the flat plate of 6.2mm, and this method can therefore be considered acceptable.

As the inlet walls do not lie in the x plane, a two-dimensional correction needs to be

applied to the above one-dimensional formula to allow for angled isolator walls. Consider a segment of the isolator wall, shown in Figure 4.13. Here x and y are the Cartesian co-ordinates of the endpoints of the segment, n is the normal direction vector, θ is the angle of the line segment and δ is the boundary layer thickness correction corresponding the boundary layer displacement height above the surface.

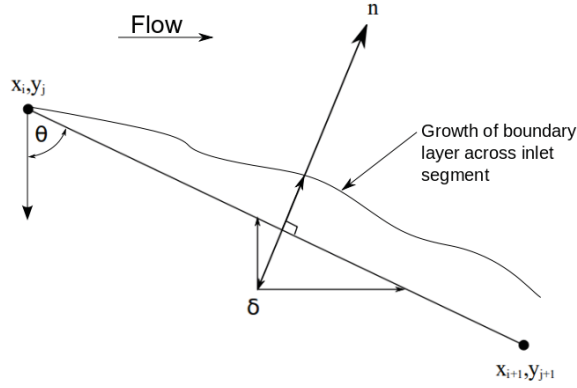


Figure 4.13: Boundary layer displacement thickness correction.

The angle of the line segment can be defined as

$$\tan \theta = \frac{x_{i+1} - x_i}{y_{j+1} - y_j}$$

By reducing the boundary layer displacement thickness correction into its components, the correction applied in the y direction is given by

$$\delta_y = \frac{\delta^*}{\sin \theta} \quad (4.2)$$

No correction is applied in the x direction (i.e. the length of the inlet remains unchanged). A constant Mach number within the isolator has been assumed, taken as the average value. The final step the streamTracer code undertakes is to write a text file defining the inlet geometry to allow its importation into CAD or meshing software. Currently the code is designed to allow the importation of its data into the meshing program Gridgen, and data is exported in the segment (*.dat) file format. In Gridgen, high quality meshes can be generated rapidly, allowing fast exportation to Fluent for simulation.

4.4.3 Inlet truncation

The stream traced method of inlet geometry typically results in substantially elongated inlets compared to traditional lightcraft designs, due to the shallow angles obtained from

the generating flow fields. It is not possible to simply increase the angle through which the flow is turned, as undesirable mach disks form in the region where the flow field shocks meet. This is illustrated in Figure 4.14, where the 7.58° flowfield used in the final inlet design is compared the original inlet flow field of compression angle 15° .

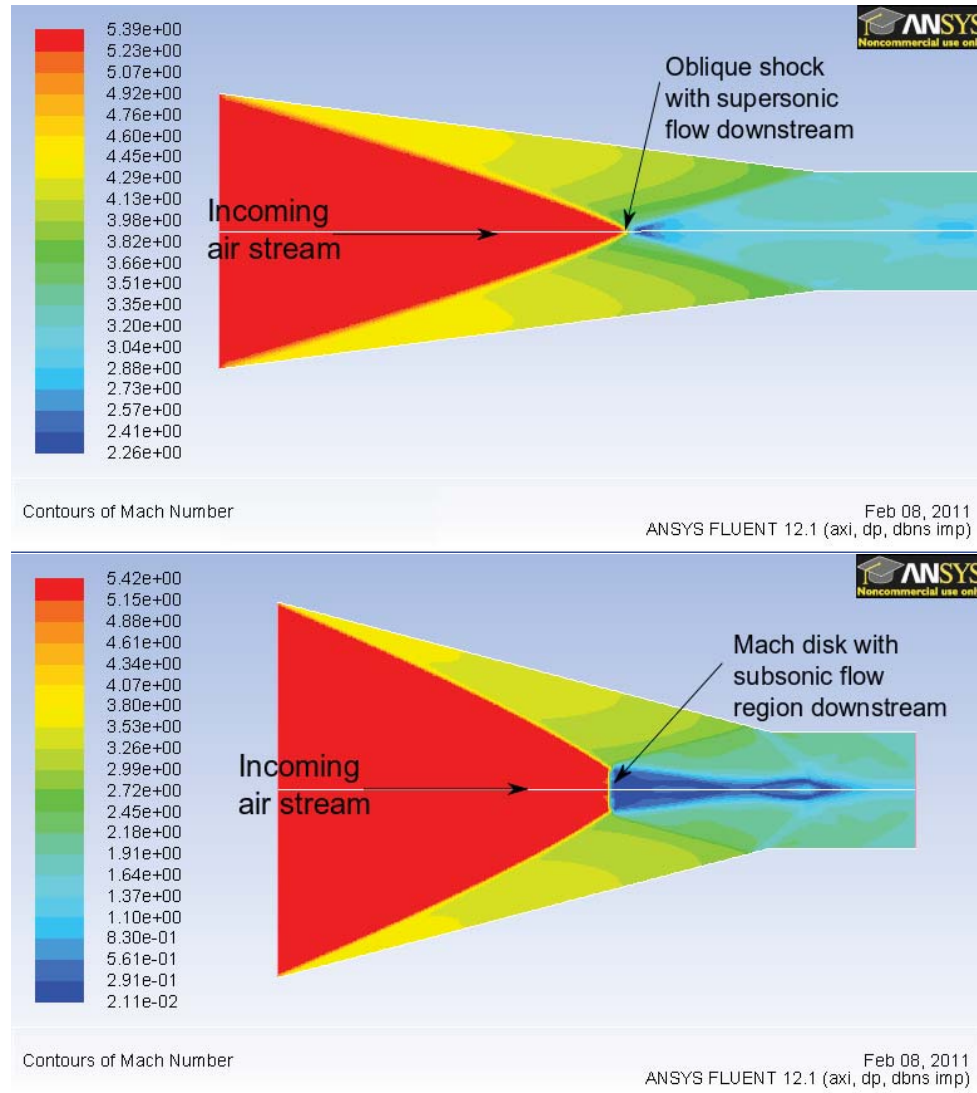


Figure 4.14: Generating flow fields of turning angles 7.58° and 15° , respectively.

The growing Mach disk, where flow is decelerated sub-sonically, can be seen along the centre line of the generating flow field. With a large Mach disk in the generating flow field, there is a much greater possibility that flow disturbances can cause undesirable inlet behaviour, such as inlet unstart. This is due in part to a higher portion of the flow being decelerated to near sonic and sub sonic speeds. There is, therefore, a trade off between total inlet drag and inlet flow stability. As a compressive flow field is made shorter, compression is increased while viscous drag on the internal surfaces is reduced, but the

form drag and likelihood of inlet unstart is also increased. One method of reducing the total inlet drag while maintaining flow field stability is to truncate the inlet before the secondary reflected shock off of the generating flow field centre line. This is not done in traditionally fueled scramjet engines due to the residence time of the chemically reacting species within the combustor. Due to the supersonic speeds within the scramjet flow path, residence in the order of the chemical reaction times are experienced. Hence relatively long combustor lengths are required to realize the potential chemical energy from the fuels. The lightcraft engine does not face this restriction, due to the nature of the propulsion system. Although some of the original inlet design compression is lost, the benefit of reduced inlet drag outweighs the resulting performance loss. Flow uniformity and total pressure loss are also maintained, and the inlets do not become any more sensitive to changes in flight conditions. One further benefit of the truncated inlet design is the increased radius of the parabolic receptive optic. By truncating the inlet, the laser energy capture area is significantly increased over the untruncated stream-traced inlet design, and is only slightly reduced compared to the LTD inlet geometry. Figure 4.15 shows a comparison of density contour plots between the original and truncated stream traced inlet design.

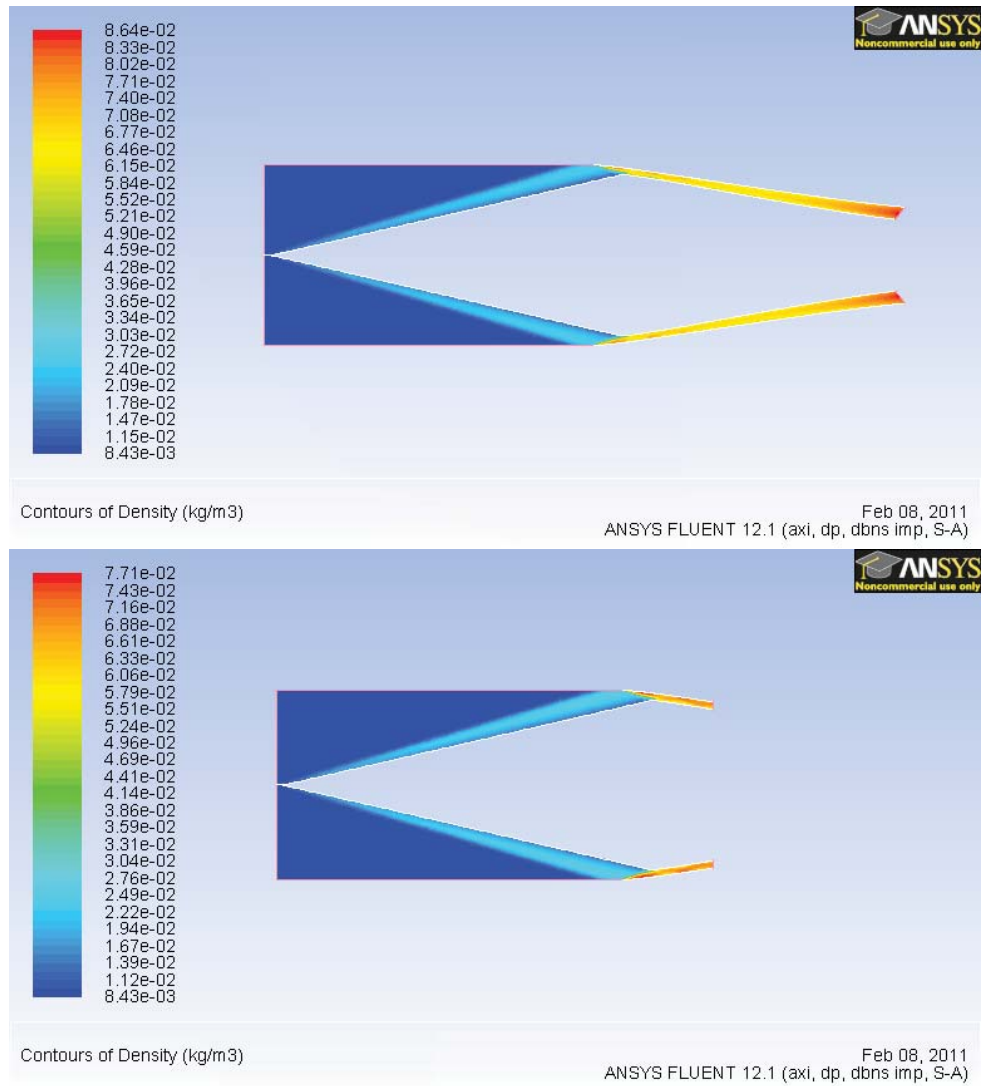


Figure 4.15: Original and truncated inlet simulations illustrating amount of total compression lost.

A total drag reduction over the initial inlet of approximately 47% is achieved in the truncated design, while the resulting loss in compression is only approximately 18%. There is therefore a significant benefit to truncate the initial stream traced inlet design. The amount that the inlet is truncated is the designers choice, and is a trade-off between total compression and inlet drag for a given flight configuration. It is also a requirement that the inlet length be sufficient that the expanding laser induced detonation wave is contained within the inlet isolator, and not allowed to protrude out the front of the lightcraft vehicle and unstart the inlet. The length that the detonation wave extends up the isolator walls can be established from the numerical simulations described in Section 7.1. The resulting geometry can be seen in Figure 4.16.

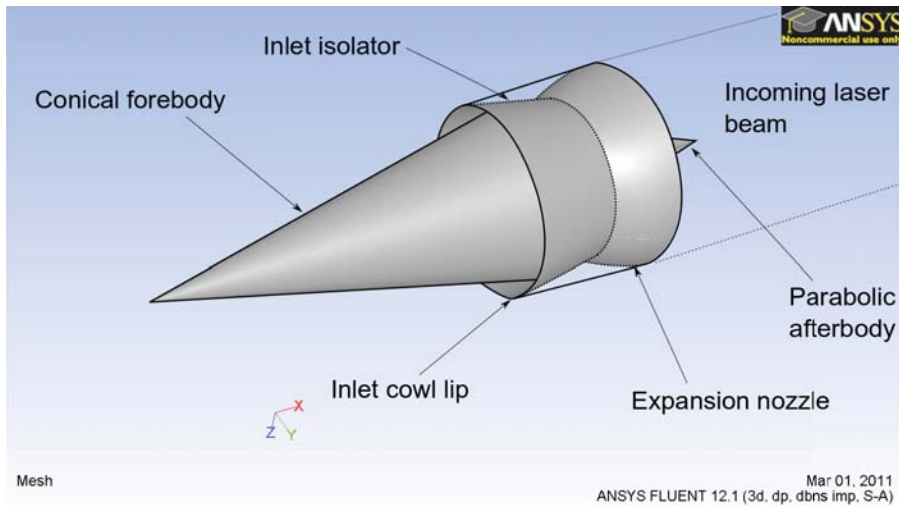


Figure 4.16: CAD representation of Stream traced axis-symmetric inlet geometry employed in this study.

A dimensioned CAD drawing displaying the major dimensions of the craft used in the simulations is shown in Figure 4.17.

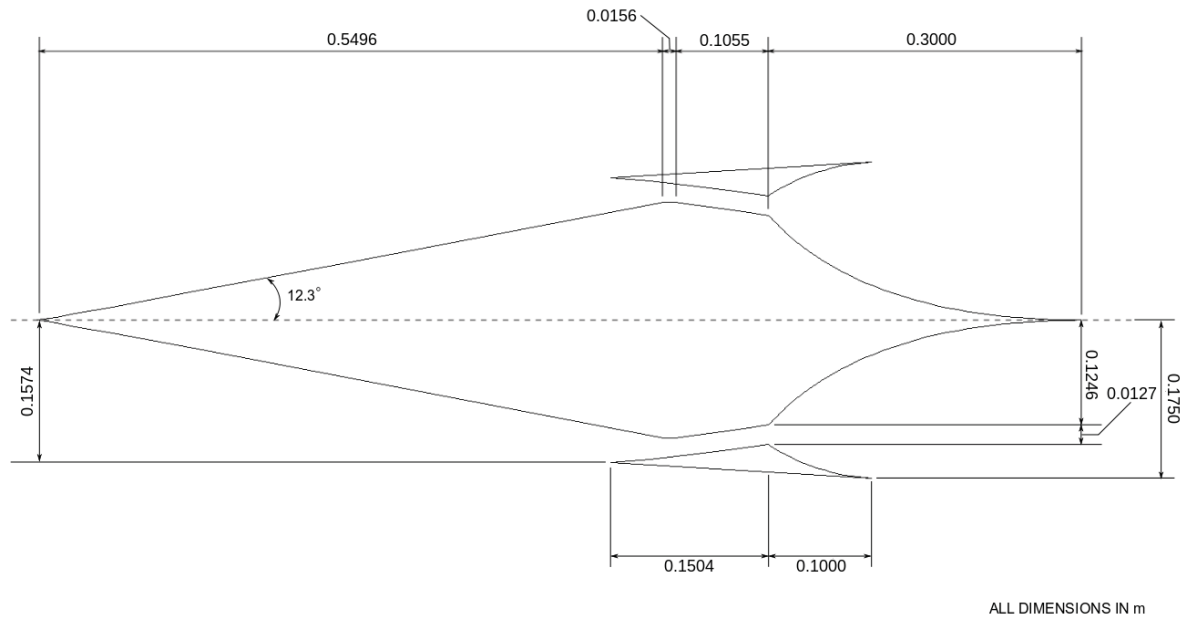


Figure 4.17: Dimensioned CAD drawing of the Stream traced axis-symmetric inlet geometry.

4.5 Stream traced modular axis-symmetric inlet

The third inlet design technique to be investigated in this study is that of stream traced modular axis-symmetric inlets. This inlet design technique again employs the stream traced inlet design methodology, however the inlet is comprised of a finite number of three

dimensional modular inlets arranged axially around the conical centre body. The modular inlets benefit from tangential sidewall compression as well as the radial compression of the external surface. Modular inlet design is more complicated than the previous two inlet design methodologies, however the additional benefit of three dimensional compression has been shown to improve their performance at off design conditions (Smart, 1999).

The shape of the isolator curve is fixed due to the stream tracing process, and is identical to that of the axi-symmetric stream traced design. The difference between the two designs is the number of modules being employed in the design - the straight axi-symmetric case has one module. The configuration investigated in this research consists of six evenly spaced modules arranged annually around the lightcraft centre-body. Six modules were chosen as this is a good compromise between flow performance at off design conditions and efficiency losses due to the addition of inlet struts between the modules. Each module spans a capture area of 58° , with the remaining area making up the strut member that holds the module in place. The major dimensions of the craft are shown in Figure 4.19.

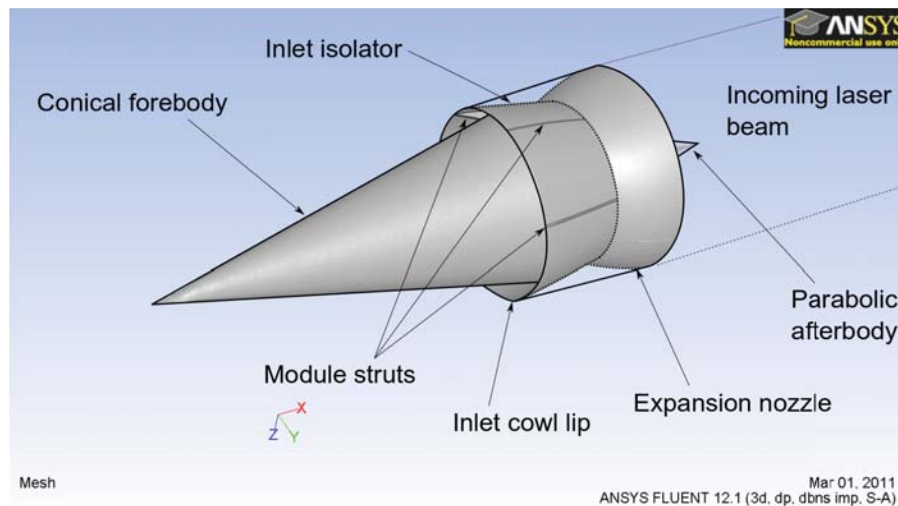


Figure 4.18: CAD representation of Stream traced axi-symmetric inlet geometry employed in this study.

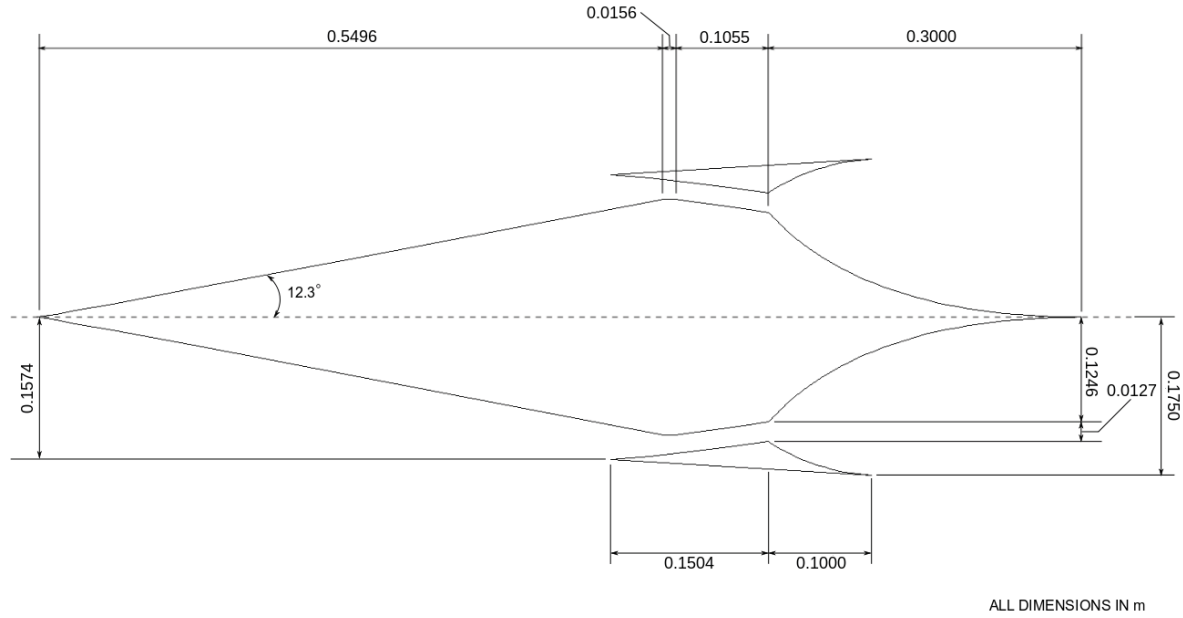


Figure 4.19: Technical CAD drawing of Stream traced modular axi-symmetric inlet geometry.

4.6 Stream traced modular scalloped inlet

The fourth and final inlet geometry produced again employs the stream traced inlet design methodology outlined in Section 4.4.1, however the stream line tracing is performed in three dimensions. The extension of the methodology to a three dimensional tracing technique creates a ‘scallop’ inlet arrangement, where the inlet forms the geometry of both the conical forebody and the isolator. In this design, there is no distinction from the initial forebody compression and the secondary cowl compression. The capture area geometry uses the axi-symmetric nature of the lightcraft to create a modular arrangement, as shown in Figure 4.20. The final lightcraft geometry is formed by arranging the individual modules around the lightcraft centre body.

A wedge configuration is employed in the capture area shape, as this results in a circular profile similar to a traditional missile configuration. The technique is the same as that employed by Billig (1995) and Matthews & Jones (2006). Six modules have been chosen in this design, resulting in a wedge angle of 58° . Due to the three dimensional tracing method employed in this configuration, the conical forebody is formed from the lower edge of the inlet module. The flow field is therefore required to be adjusted to maintain the same internal geometry of the lightcraft. This is important for the housing of ancillary equipment and payload. A generating flow field lip angle of 14.04° was employed to keep consistent with the other lightcraft inlet designs. The problems associated with

the over compression were not present in this flow field, due to the entrance Mach number being that of the free stream conditions - Mach 8. The modified flow field geometry is shown in Figure 4.21. The final inlet geometry can be seen in Figure 4.22. A dimensioned CAD drawing has also been produced to show the major dimensions of the craft, shown in Figure 4.23.

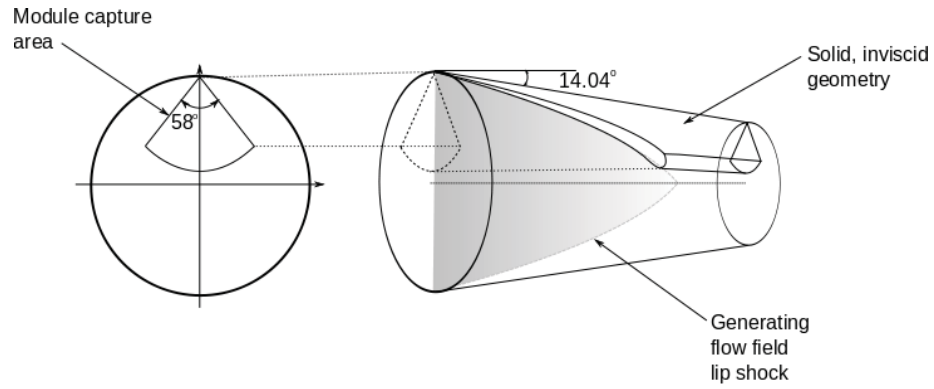


Figure 4.20: Three dimensional streamline tracing of scalloped inlet module

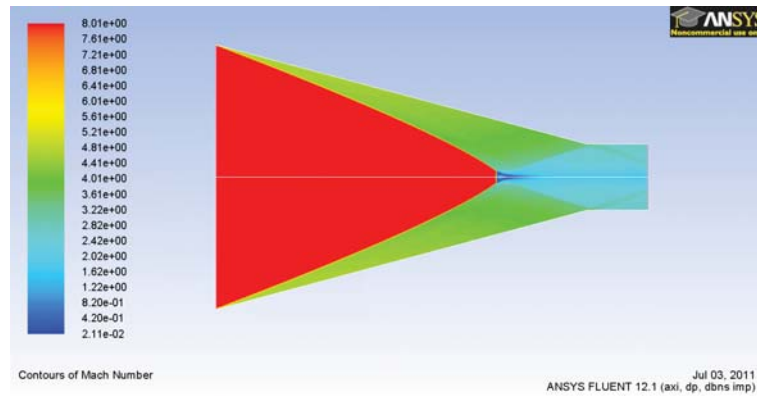


Figure 4.21: Modified generating flow field geometry used in stream traced modular scalloped inlet geometry.

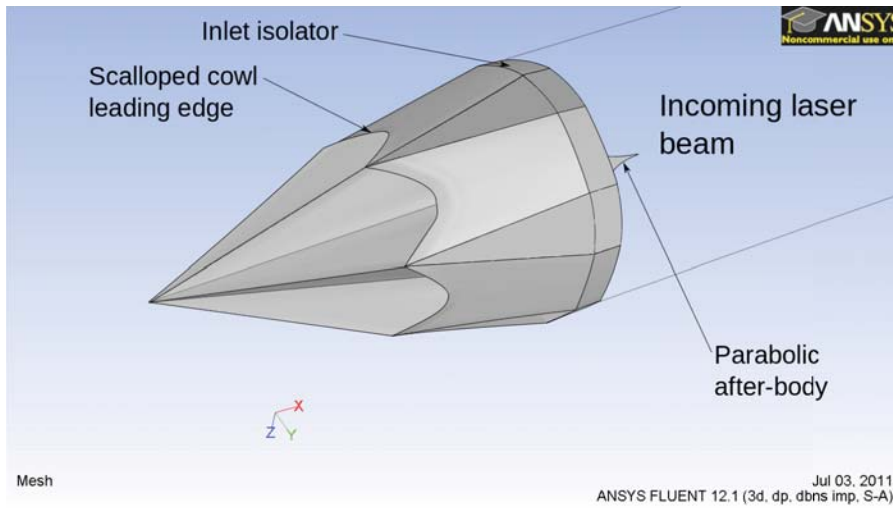


Figure 4.22: CAD representation of Stream traced modular scalloped inlet geometry employed in this study.

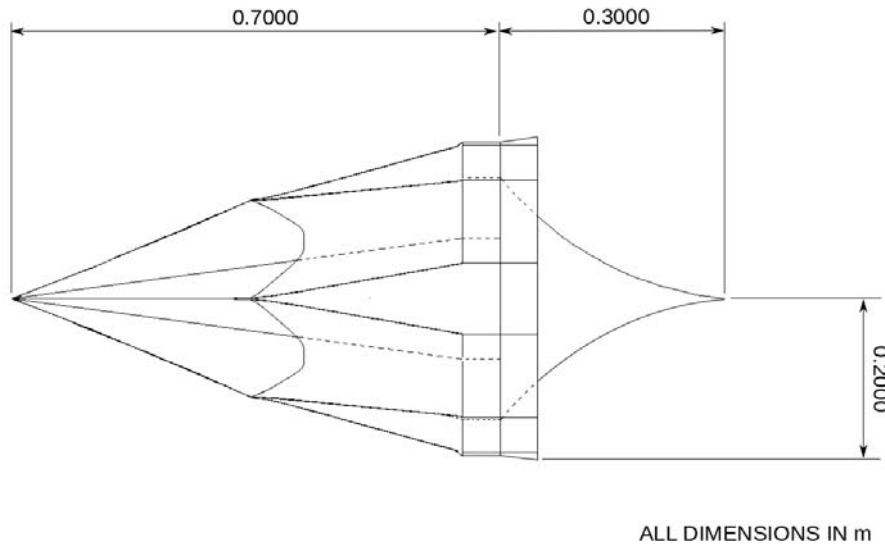


Figure 4.23: Dimensioned CAD drawing of Stream traced modular scalloped inlet geometry.

4.7 Inlet performance parameters

As discussed in Section 3, the purpose of the inlet is to compress and deliver air to the laser supported pulsed detonation process at suitable conditions over a range of flight conditions. To meaningfully compare a range of different inlet configurations, suitable performance analysis parameters need to be established. A good inlet design will maximise the compression and uniformity of the incoming airflow, while minimising the system losses. These parameters will all be evaluated at the exit of the isolator, as this is where the laser energy deposition occurs. The flow structure in this region is critical to the

performance of the pulsed laser detonation engine. While the nozzle configuration will have a significant effect on the performance of the vehicle as a whole, its design is outside the scope of this research, and as such will not be considered in the performance analysis.

The inlets are evaluated using five different performance parameters; total mass capture, average compression achieved, uniformity of isolator flow, total inlet viscous drag and total pressure loss of the inlet. The level of compression achieved by each inlet is evaluated on the average density across the isolator exit for each inlet at the three different angles of attack. This is obtained by taking the arithmetic average of the cell node values of density along a surface located at the isolator exit. A higher average density value, the greater level of compression the inlet achieves. To evaluate the flow uniformity, the standard deviation of the cell node values for density on the surface are computed. The lower the standard deviation, the higher the uniformity of the flow. Finally to evaluate the losses of the system, two approaches are taken. The first is based on the total drag of the inlet and isolator walls. Fluent is able to calculate a value for both viscous and pressure drag along a surface, and this is employed to give a quantity for the drag of the inlet. The second approach involves evaluating the total pressure loss in the system. This is done by dividing the average isolator exit total pressure by the free stream total pressure. The total pressure rise is an indicator of the shock losses in the system, and therefore a lower value implies a better performing inlet.

4.8 Summary and conclusions

Four different lightcraft inlet designs have been produced alongside performance evaluation criteria. This allows the fair comparison of their relative strengths and weaknesses within the hypersonic flight regime. The axi-symmetric, stream traced axi-symmetric, stream traced modular axi-symmetric and the stream traced modular ‘scaloped’ inlet design have been designed for maximum performance at design conditions. The three-dimensional geometries produced are now able to form the basis of computational meshes to be simulated in the CFD software. From the CFD software, a quantitative analysis of the inlets relative performance can be obtained.

5 Numerical Analysis

5.1 Introduction

Numerical simulations of the four different inlet designs presented in Chapter 4 have been performed at a range of flight conditions to provide the basis of the performance comparison. This chapter presents the numerical simulation results, and discusses the interesting flow processes occurring within the hypersonic inlets.

The evaluation of the axi-symmetric individual inlet designs was performed in two stages. The first step involved the two-dimensional, axi-symmetric simulation of the inlet at on design conditions. This first step was performed to allow the evaluation and ‘tweaking’ of inlet designs with minimal computational expense. Multiple two dimensional simulations could be performed in a matter of hours, as opposed to days for the three dimensional meshes, allowing the design to be altered as required.

Once the final axi-symmetric shape was produced, the two dimensional case could be extended to three dimensions. Three dimensional simulations were required for off design simulations at angles of attack. This is because a two-dimensional axisymmetric simulation would not be able to sufficiently resolve the tangential components of flow at angles of attack other than 0° . For both the axi-symmetric and the stream traced axi-symmetric cases, this was achieved by revolving the two-dimensional profile about the x -axis (as defined in Figure 5.1), creating a three-dimensional mesh. The nature of the symmetry of the problem allowed the meshes to be split in half about the $x - y$ plane. The mesh then used symmetry boundary conditions on the $x - z$ plane, halving the computational expense required to perform a three-dimensional simulation. The same mesh for each lightcraft geometry was used for all off design simulations by appropriately altering the boundary conditions. In all simulations at angles of attack, the windward side is the lower surface and the leeward side is the upper surface. A representation of the computational space employed in the simulations is shown in Figure 5.1, with the craft moving from right to left.

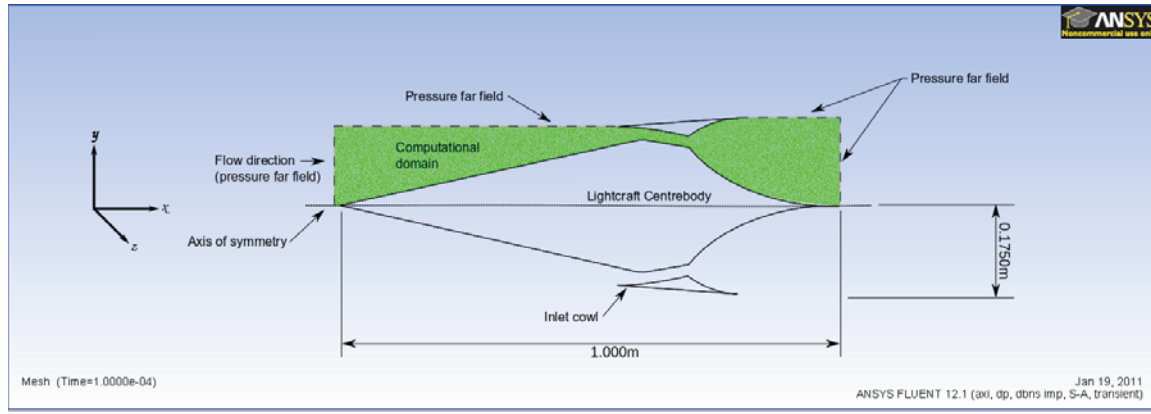


Figure 5.1: Computational domain for numerical simulations.

For the two modular inlet designs, the process is slightly more complicated due to the periodic location of ‘struts’ that form the sidewall compression component of the inlet module. The stream lines used in the generation of the stream traced axi-symmetric modular inlet are identical to the ones used in the stream traced axi-symmetric case, but modifications were required to the three dimensional mesh to produce a three dimensional modular mesh. For the stream traced modular ‘scaloped’ inlet design, a completely new three dimensional mesh was generated. This was done by creating an individual module in the stream tracer code, then revolving it around the axis of symmetry to form the final lightcraft shape.

In addition to the on design conditions outlined in Table 3.7, a set of off design conditions have also been investigated to form an understanding of each inlets behaviour throughout the accelerating flight envelope. An off design flight Mach number of 5 was chosen, corresponding to the design conditions listed in Table 5.1. As compression within the inlet is increased at lower Mach numbers, resulting in reduced Mach numbers through the inlet, the probability of unstart is increased (Van Wie, 2000). If an inlet is able to operate at both Mach 5 and 8 conditions, then it is will be suitable for the accelerating hypersonic portion of flight.

Parameter	Design value
Mach number	5
Altitude	21500m
Pressure	4500Pa
Temperature	220K
Air density	0.0711kg/m ³

Table 5.1: Inlet off design simulation values.

All simulations were performed in Fluent using a density based solver, where the conti-

nity equation is employed to obtain the density field. The pressure field is then obtained from an equation of state, in this case as an ideal gas with no dissociation or ionisation considered. Density based solvers have historically been employed in high speed compressible flows, and this research has continued in this vein (Ansys Inc., 2009). A Spalart-Allmaras one equation turbulence model was also employed. With the Spalart-Allmaras model, accuracy of the turbulent behaviour is reduced in favour of computational speed (Ansys Inc., 2009). This was considered acceptable as fine resolution of turbulent behaviour was not required in this study. The Fluent Spalart-Allmaras turbulence model also allows a coarsening of the mesh in the boundary layer region, and has been shown to model the behaviour of boundary layers subjected to adverse pressure gradients well. Fluent employs a standard upwind flux splitting technique, with the flux splitting handled by a Roe scheme (Ansys Inc., 2009). Fluent allows blending of the spatial discretization order, from a minimum of first order to a maximum of second order. Difficulty in achieving converged solutions was experienced at higher order spatial discretization, so first order was used for the three dimensional simulations. It was possible to achieve convergence at second order accuracy for the two-dimensional grids, so this was employed in two-dimensional simulations. A second order implicit time marching scheme has been employed in the steady state simulations. Far field boundary conditions were modelled using a Pressure Far Field boundary condition. The Pressure Far Field boundary condition models free-stream supersonic flow at infinity, with the freestream Mach number, static pressure and temperature specified. In the case where there is supersonic flow across a Pressure Far Field boundary, the code automatically computes the static pressure at the flow exit by extrapolating the flow within the domain. For the walls of the lightcraft, a standard wall function boundary condition is employed (Ansys Inc., 2009).

5.2 Mesh refinement study

To be confident in the accuracy of the numerical simulations, it is essential to ensure the solutions obtained are independent from the computational grid size. If a computational grid is not refined sufficiently around important flow features, the fidelity of the solution is reduced and vital information about the flow field may be lost. To ensure grid independence, a mesh refinement study was performed. This involved monitoring the flow conditions within the simulation domain as the mesh size is decreased, until there is no significant difference between mesh results. Due to the similarities in geometry between

the 2D and 3D cases, the mesh refinement study was done on the two dimensional axis-symmetric stream traced inlet case. The static pressure along the conical forebody, inlet isolator lower wall and parabolic reflective optic were used to determine whether mesh convergence had been achieved. Average (non-dimensionalised) mesh spacings of 0.004, 0.0033, 0.002, 0.0005, 0.0001 and 0.000075 were employed for an unstructured mesh in the axis-symmetric stream traced geometry, and simulated in Fluent at on design conditions. The average mesh spacing represents the average distance between node points along a connector (in metres), with a larger number representing a coarser mesh. The resulting mesh sizes can be seen in Table 5.2. The plot of static pressure along the bottom surface of the lightcraft model, shown in Figure 5.2, demonstrates the solution dependency on mesh density.

Average node spacing (m)	Number of cells in mesh
0.004	25,978
0.002	55,815
0.0005	82,447
0.0001	204,534
0.000075	232,082

Table 5.2: Mesh sizes employed in mesh refinement study.

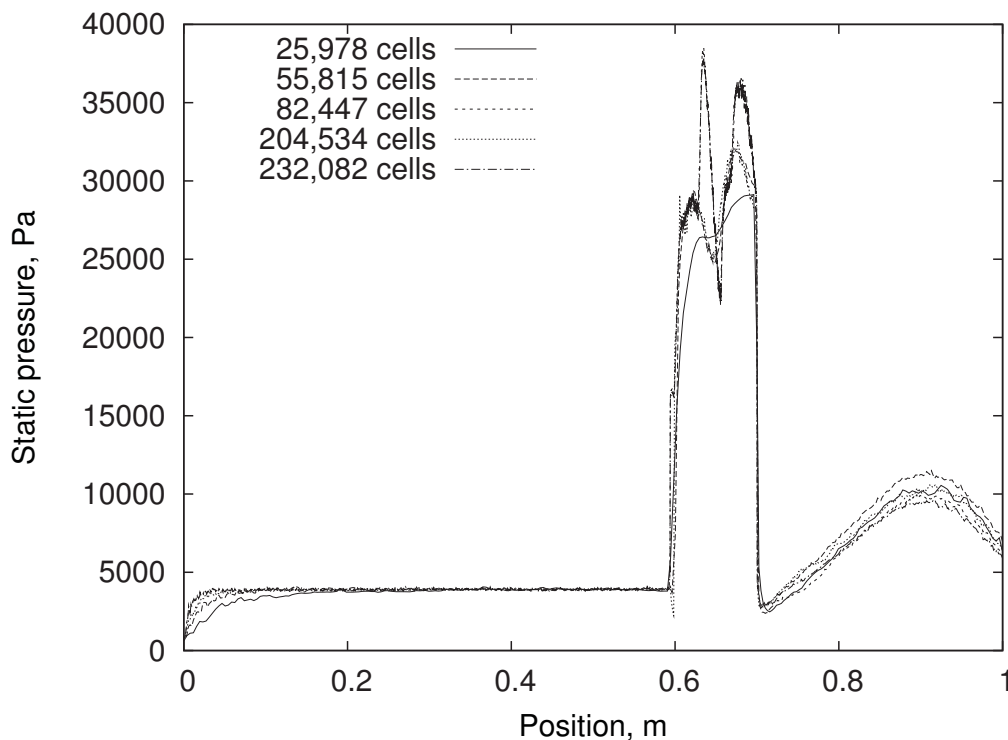


Figure 5.2: Density profile at mesh outlet for different mesh densities.

Figure 5.2 shows that the coarser meshes, while capturing the general flow properties, do not adequately resolve the peak pressures within the isolator resulting from the complex shock structure. Increasing the mesh density from 0.0005 to 0.000075 shows a clear trend of solution convergence, with minimal change between mesh densities of 0.0001 and 0.000075. The number of cells in the resulting meshes are 204,534 and 232,082 respectively. Since computational time is directly related to the number of cells in the computational space, the small increase in computational accuracy achieved with an average mesh spacing of 0.000075 over 0.0001 is not deemed necessary, and hence a mesh spacing of 0.0001 is employed in subsequent simulations.

It was found that when this mesh density was extended to the three dimensional models, the resulting mesh sizes were prohibitively large. Three dimensional meshes of over 40 million cells were required in order to accurately resolve the flow within the lightcraft isolator. The mesh was modified by coarsening in regions where the pressure gradient was low to reduce the mesh to manageable sizes. It was still found that the required level of resolution within the isolator still left the mesh sizes too large to solve on the available computing resources. The twelve core parallel machine used in this work was unable to produce results in a reasonable time frame for mesh sizes greater than approximately 8 million cells, and hence the resulting grid error introduced was required to be quantified.

By following the approach outlined by Stern *et al.* (2001), and estimation of the error introduced by the coarser grid solutions was obtained. Using the results of the mesh refinement study, a parameter convergence study was performed based on mesh node spacing assuming all other parameters are held constant. Grid convergence is established through the evaluation of the drag of the lightcraft body, which is calculated in the CFD code Fluent by summing the pressure forces on the body surfaces in the direction of flow. Four grid densities were employed, each with constant refinement factor. The grids employed in the study shown are outlined in Table 5.3 with the resulting value for drag force, and the percentage change from the previous value. It can be seen that there is little variation between the calculated drag value as the grid spacing is decreased, and the grids appear to yield the same result for the integrated variable within a suitable error bound. This indicates that even at the coarsest spacing, the grid error is still under 10%. For the three dimensional meshes, grid spacings of 0.0001 to 0.0005 were employed within the isolator where the flow physics were highly complicated. Free stream boundaries, and surfaces with reduced flow complexity were modeled with grid spacings up to 0.0015.

This approach allowed the creation of manageable grids, without significant introduction of error.

Grid number	r_k	x_k	Cells	F_d	ε
1	2	0.0020	55,815	313.40	-
2	2	0.0005	82,447	327.51	4.50%
3	2	0.0002	124,536	335.09	2.26%
4	2	0.0001	204,534	337.66	0.77%

Table 5.3: Grids employed in mesh refinement study.

It was determined in the mesh refinement study that the ‘bulk’ behaviour of the flow could be obtained at lower mesh densities, at the cost of some fidelity of the pressure peaks. It was then decided to simulate the three dimensional cases at the highest mesh resolution possible, and compare to the two dimensional axi-symmetric cases. This would allow the bulk behaviour of the flow to be captured with the three dimensional cases, while the complex flow structure within the isolator could be adequately resolved with the two dimensional axi-symmetric simulations. Unfortunately this approach was not possible for the two modular inlet designs, due to the inherent three dimensionality of the flow fields. The lower fidelity results produced from the three dimensional simulations are therefore the only numerical information available for these two inlet designs.

5.3 Axi-symmetric inlet design

5.3.1 Numerical results at Mach 8 conditions

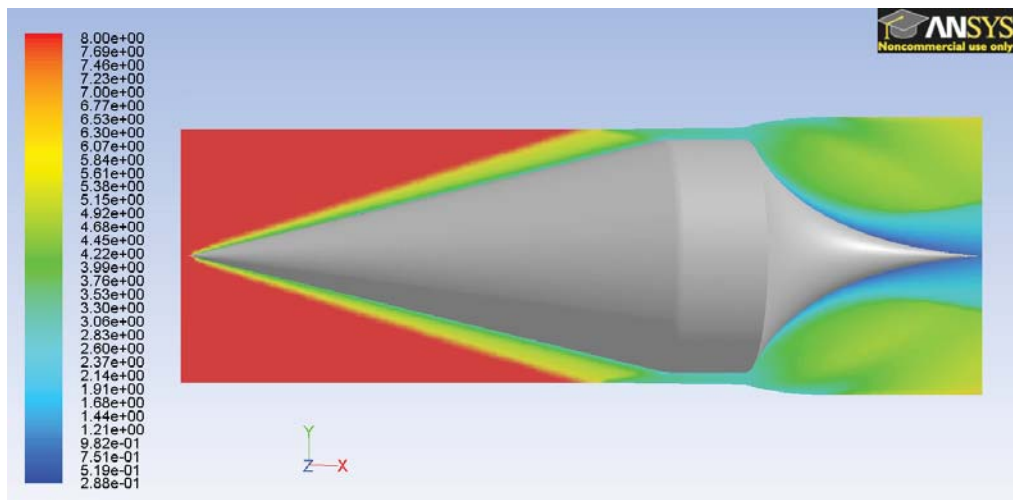
The first configuration simulated was that of the axi-symmetric inlet geometry. Contours of Mach number at angles of attack of 0° , 3° and 6° for the three dimensional mesh are shown in Figure 5.3 at a flight Mach number of 8. The initial compression off the conical forebody can be clearly seen, along with the growing boundary layer along the surface. This illustrates the necessity for the boundary layer correction, as the available core flow region is significantly reduced. The growing boundary layer along the conical forebody acts to push the forebody shock further away from the inlet cowl lip. Further compression due to the inlet can also be seen, in the form of a secondary shockwave off the cowl. This shockwave comes to rest on the expansion of the conical forebody, serving to correct the direction of the flow such that it is parallel to the isolator walls. This expansion is not ideal, as a small disruption to the flow in the form of an expansion wave can be seen to be present in the isolator. This can be clearly seen in Figure 5.4. This flow non-uniformity

is caused by the interaction of the secondary compression wave with the conical forebody boundary layer as they enter the inlet isolator.

Figure 5.4 shows a comparison between the refined two-dimensional axi-symmetric mesh, and the coarser three-dimensional mesh. Significant shock-smearing occurs within the isolator, resulting in a lower fidelity solution to the complex flow processes occurring. The static pressure within the isolator is approximately matched between the two grids, shown graphically in Figure 5.5, where the pressure profile across the isolator outlet are compared at 0° angle of attack. This confirms that the coarser three dimensional mesh, while not able to resolve the complex flow structure exactly, is able to provide an estimate of the conditions within the isolator.

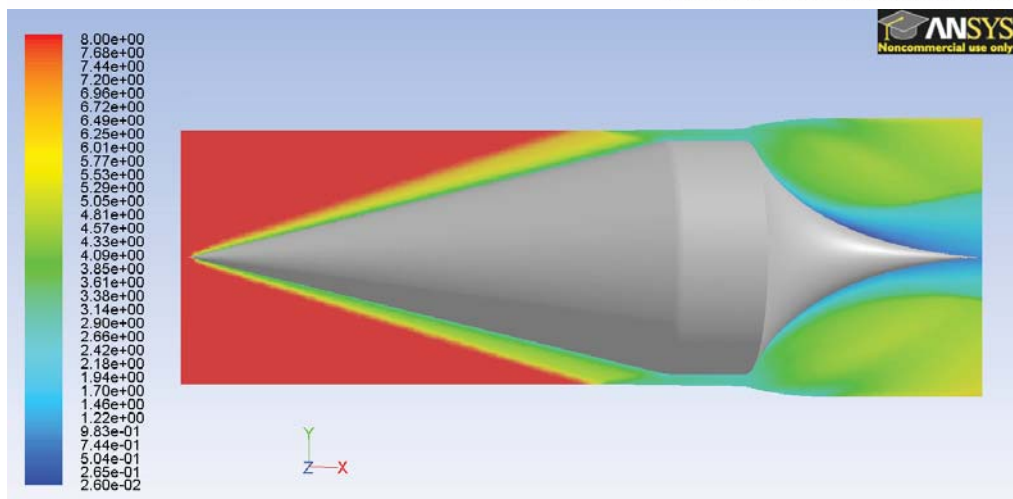
The flow uniformity within the isolator produced by the three dimensional grid is considered to be very good, as illustrated by the contour plots of density at the isolator exit in Figure 5.9. The flow exhibits a high level of uniformity, also appearing to behave well at angles of attack. The simulations indicate little loss in flow uniformity and no signs of inlet unstart. The contour plots at angle of attack demonstrate the strengthening of the windward shock, and conversely the weakening of the leeward shock off the conical forebody. This results in a change to the isolator flow structure with a strengthening of the expansion wave, decreasing the flow uniformity. This also shown in the two-dimensional axi-symmetric simulations, with significantly less shock smearing within the flow field.

The significance of this is illustrated in Figure 5.10, where contours of static pressure are shown on the outer isolator wall. An oblique shock can be seen to be forming as the angle of attack increases. The ‘rings’ that can be seen on the isolator walls are the regions where the expansion and shock waves are incident on the isolator walls. The two-dimensional simulations do appear to confirm that the coarser three-dimensional simulations are a valid means for determining inlet operation.



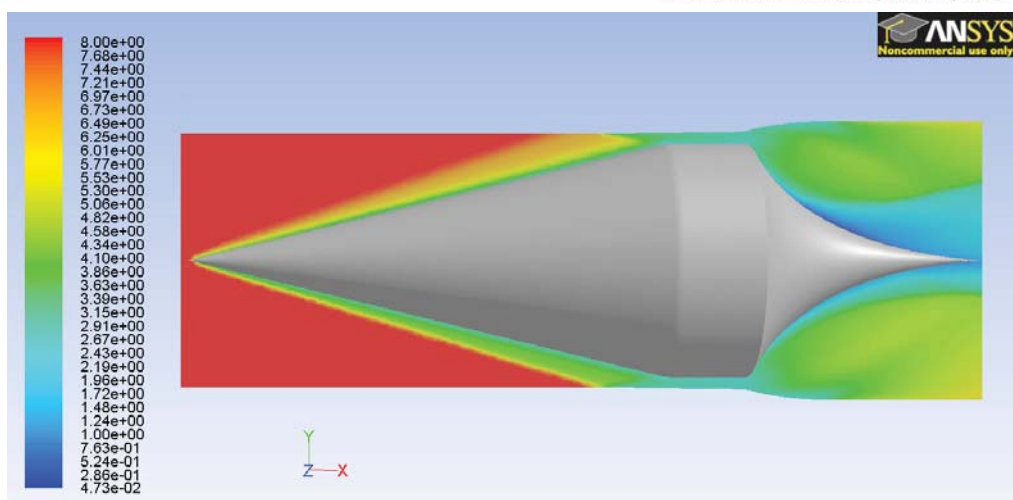
Contours of Mach Number

Feb 10, 2011
ANSYS FLUENT 12.1 (3d, dp, dbns imp, S-A)



Contours of Mach Number

Feb 10, 2011
ANSYS FLUENT 12.1 (3d, dp, dbns imp, S-A)



Contours of Mach Number

Feb 11, 2011
ANSYS FLUENT 12.1 (3d, dp, dbns imp, S-A)

Figure 5.3: Contours of Mach number for angles of attack of 0° , 3° and 6° for three dimensional mesh at Mach 8.

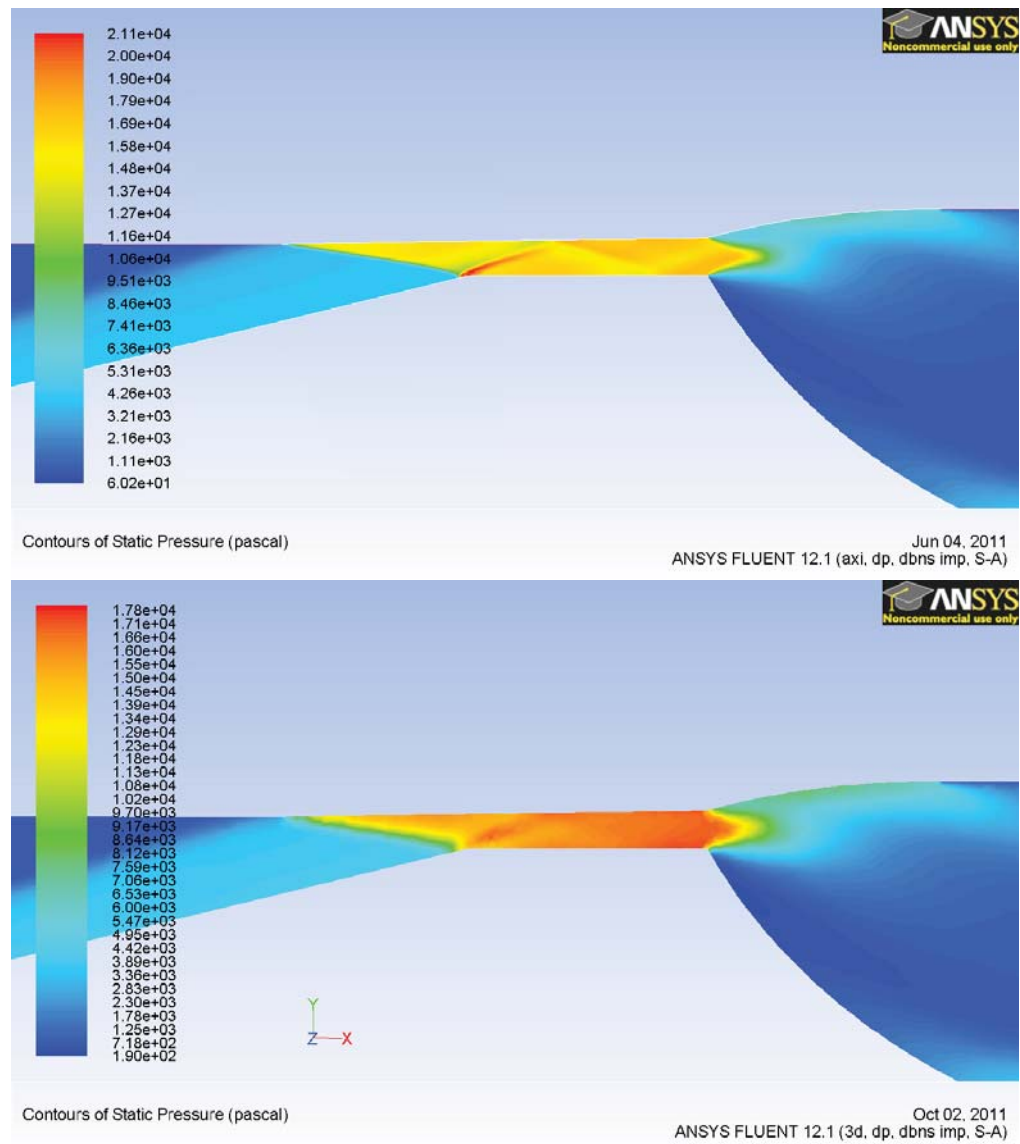


Figure 5.4: Close up of inlet contours of static pressure for an angle of attack of 0° at Mach 8 - 2D high resolution grid (top) and 3D grid (bottom).

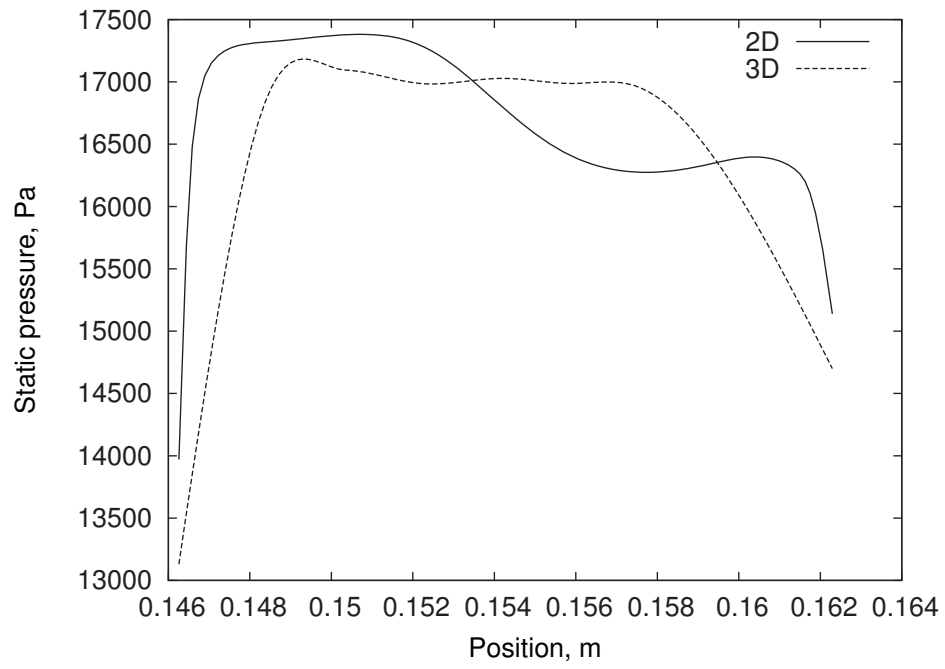


Figure 5.5: Static pressure profiles at isolator exit for 0° angle of attack and Mach 8.

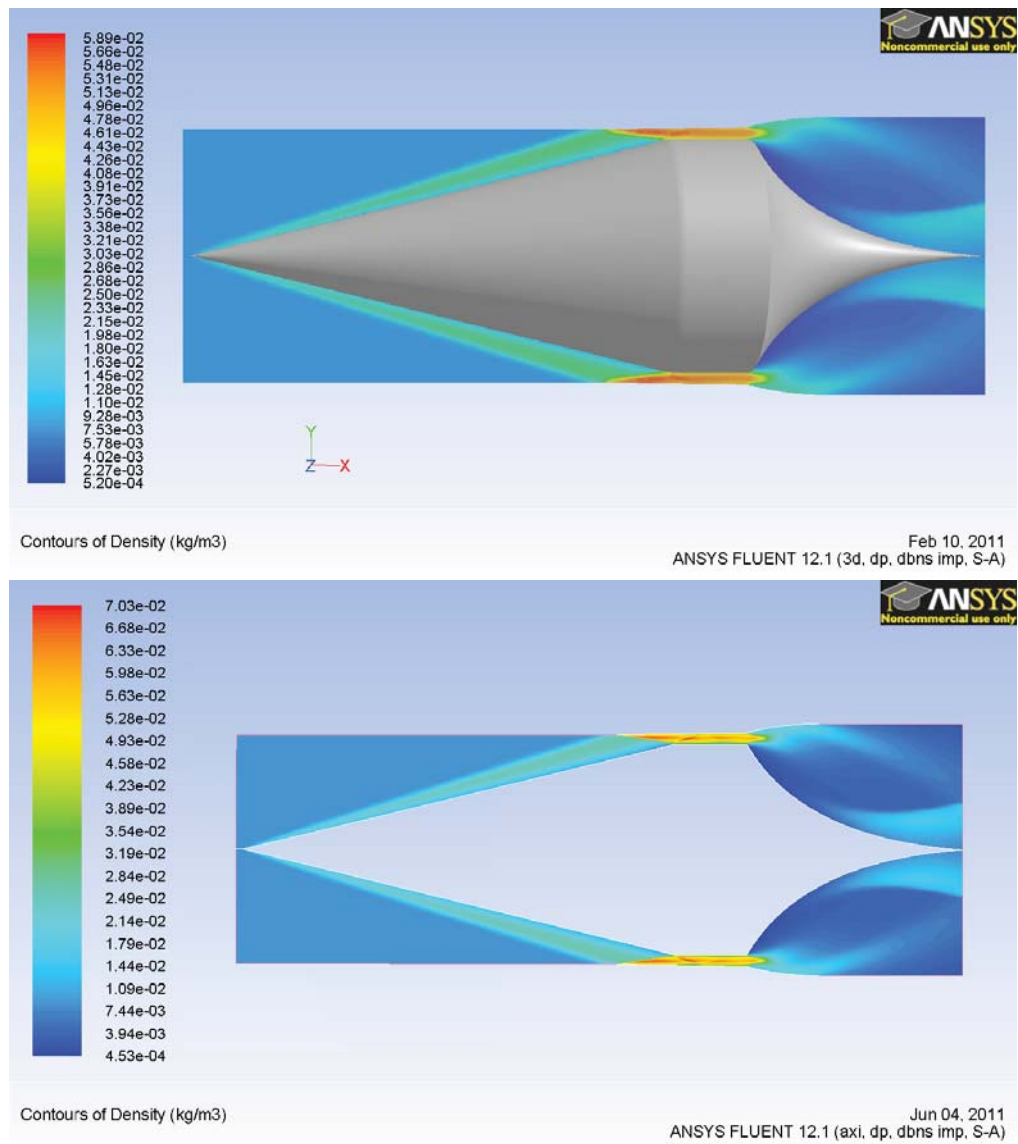


Figure 5.6: Contours of density for an angle of attack of 0° , 3D mesh (top) and 2D mesh (bottom).

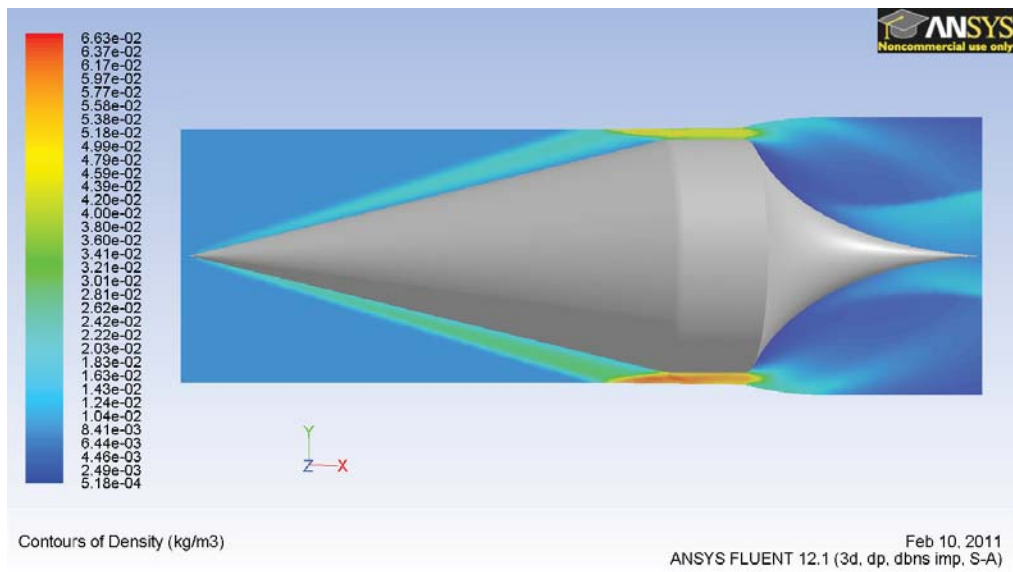


Figure 5.7: Contours of density for an angle of attack of 3° , 3D mesh.

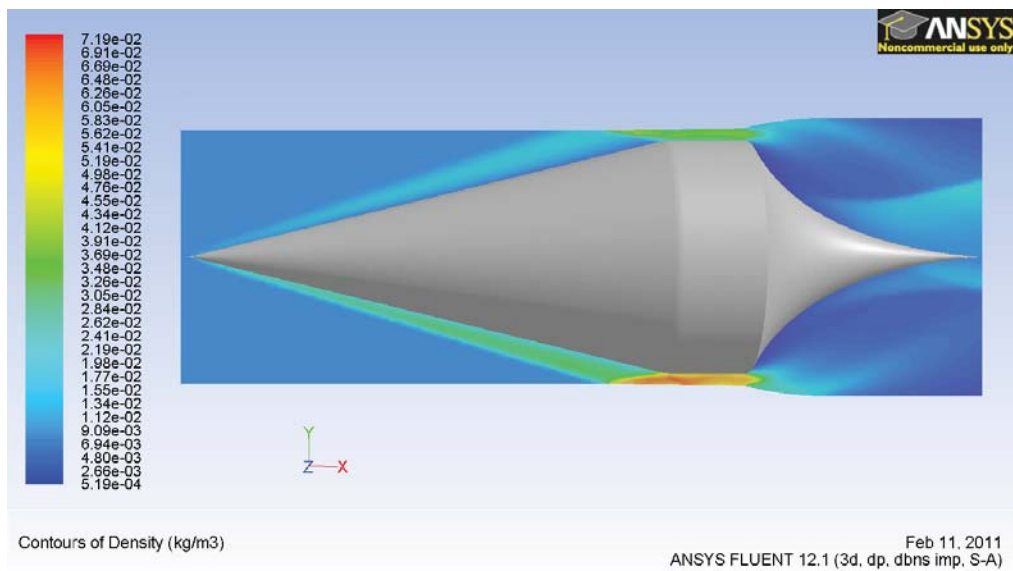


Figure 5.8: Contours of density for an angle of attack of 6° , 3D mesh.

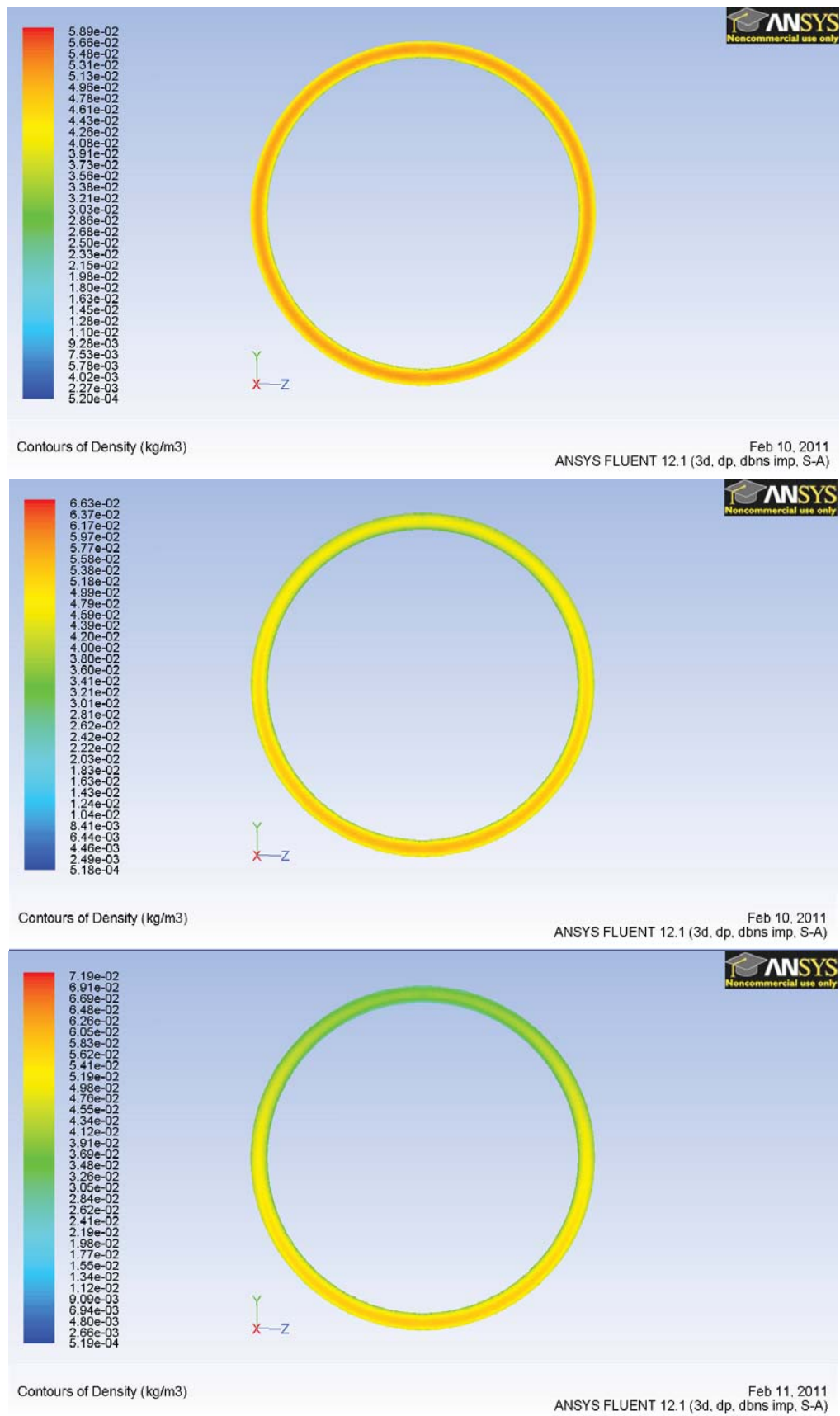
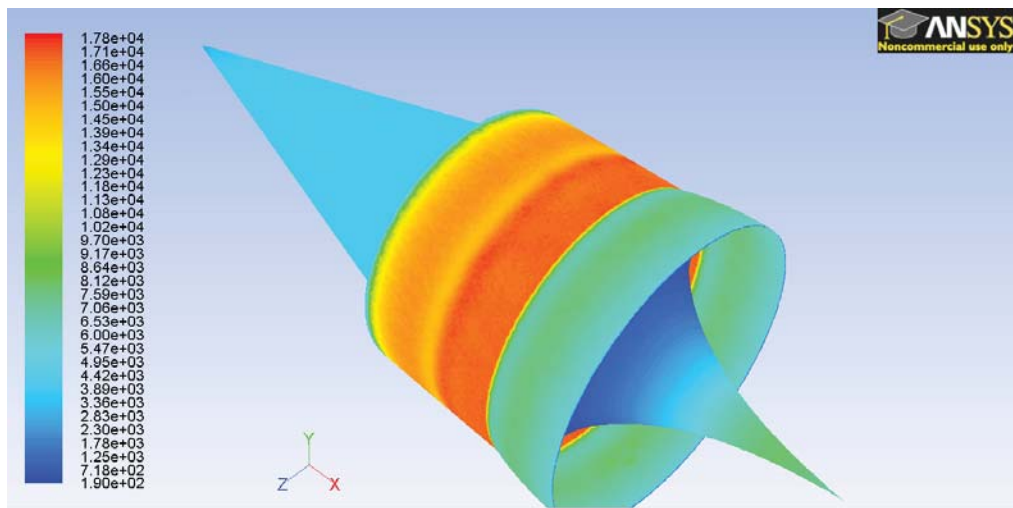
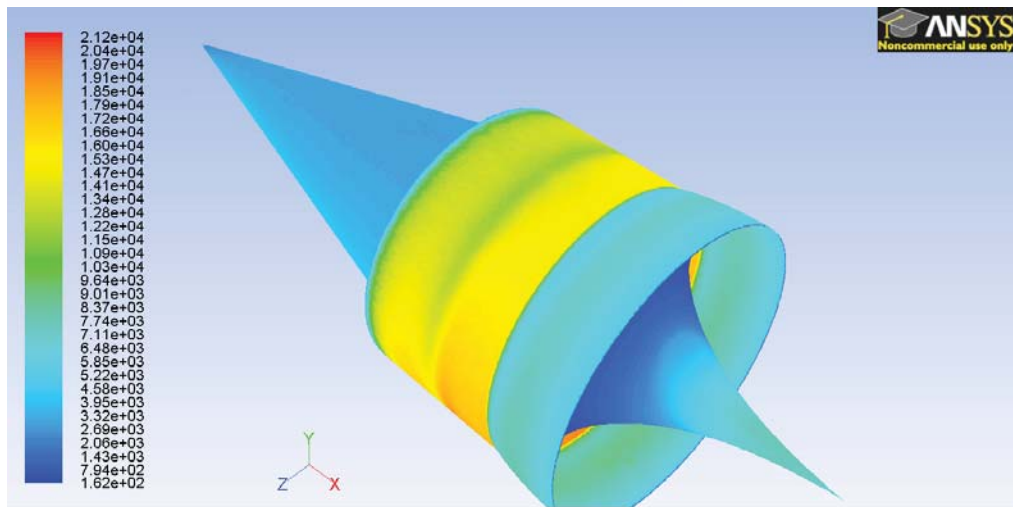


Figure 5.9: Contours of density at isolator outlet for angles of attack of 0° , 3° and 6° at Mach 8.



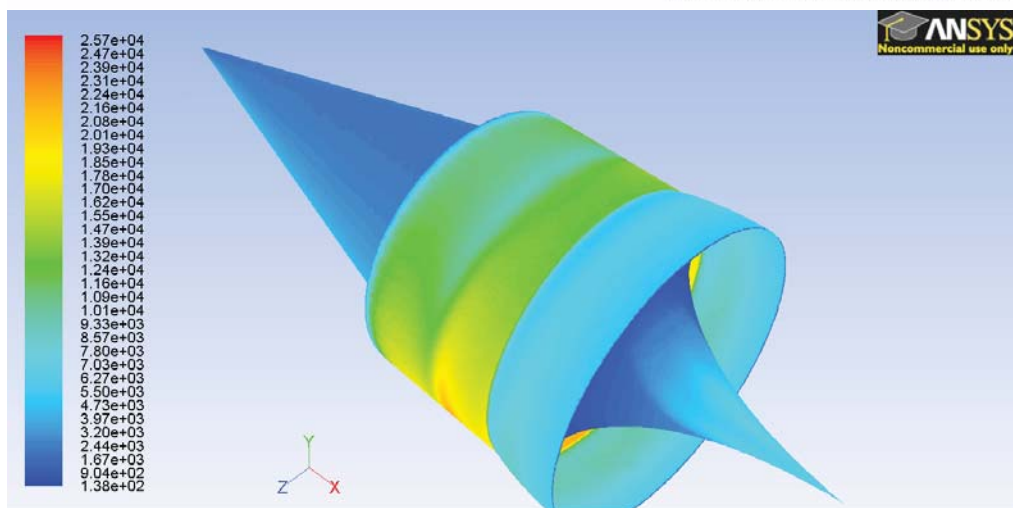
Contours of Static Pressure (pascal)

Feb 10, 2011
ANSYS FLUENT 12.1 (3d, dp, dbns imp, S-A)



Contours of Static Pressure (pascal)

Feb 10, 2011
ANSYS FLUENT 12.1 (3d, dp, dbns imp, S-A)



Contours of Static Pressure (pascal)

Feb 11, 2011
ANSYS FLUENT 12.1 (3d, dp, dbns imp, S-A)

Figure 5.10: Contours of surface pressure along lightcraft walls for angles of attack of 0° , 3° and 6° at Mach 8.

5.3.2 Numerical results at Mach 5 conditions

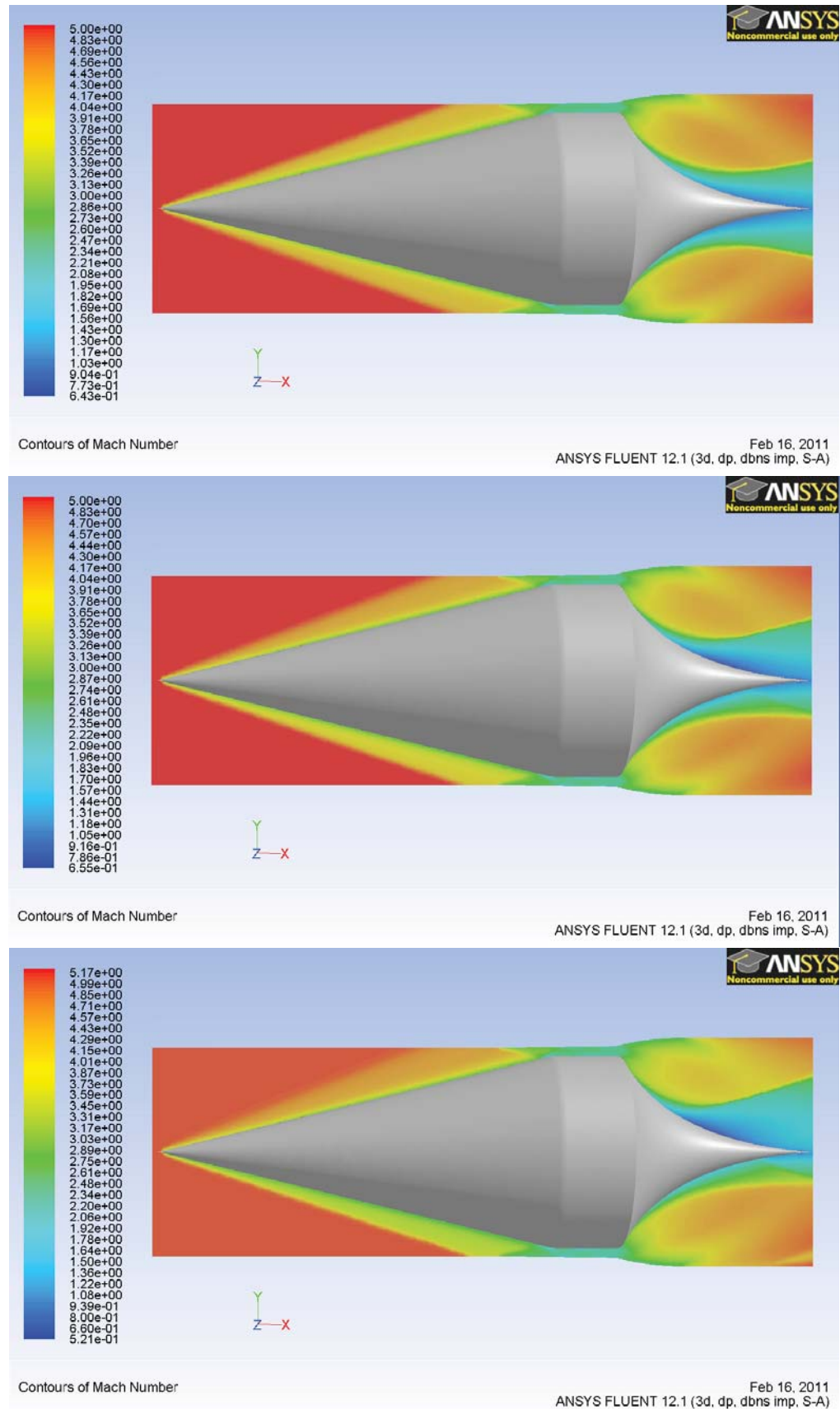


Figure 5.11: Contours of Mach number for 3D mesh at angles of attack of 0°, 3° and 6° and Mach 5.

Mach 5 simulations were performed to determine the inlets operating state at lower flight speeds, conditions of which are shown in Table 5.1. Contours of Mach number are shown in Figure 5.11, where the effect of the reduced flight speeds on the flow structure can be seen. The conical forebody shock angle increases, moving it further from the inlet cowl. The angle of the inlet cowl shock also increases, reducing the flow uniformity throughout the isolator. This can be seen with greater clarity in Figure 5.12, which shows contours of density along the axis of symmetry at all angles of attack. The strength of the expansion wave increases, propagating down through the isolator. The inlets all remain started at the lower Mach number, indicating that the inlet will remain in the started operating state within the flight speed range.

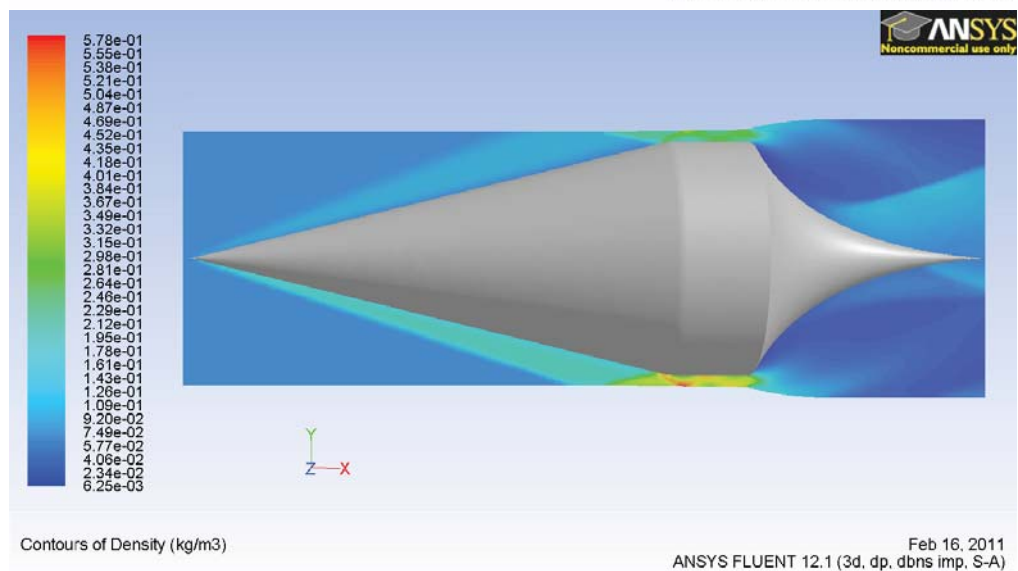
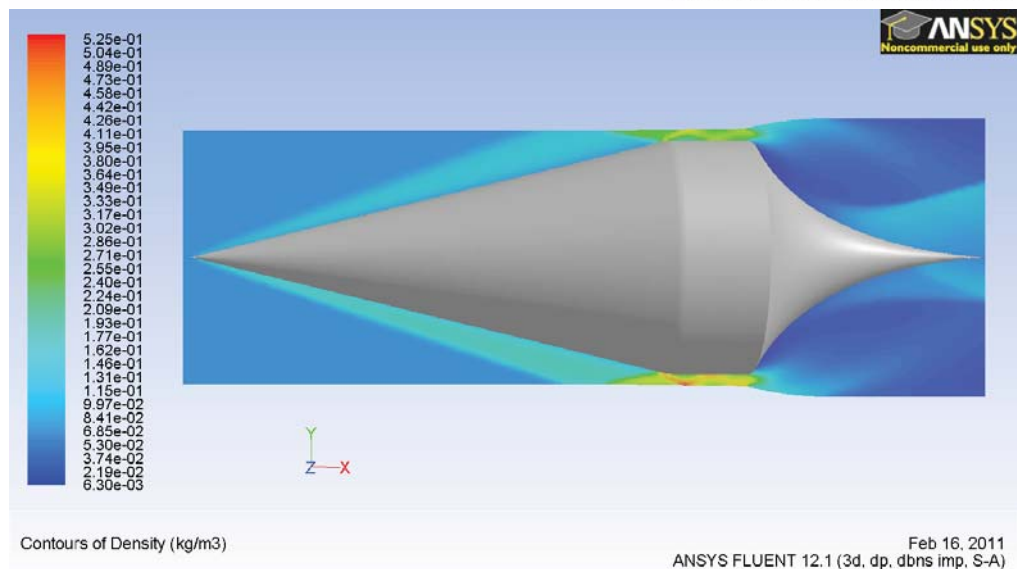
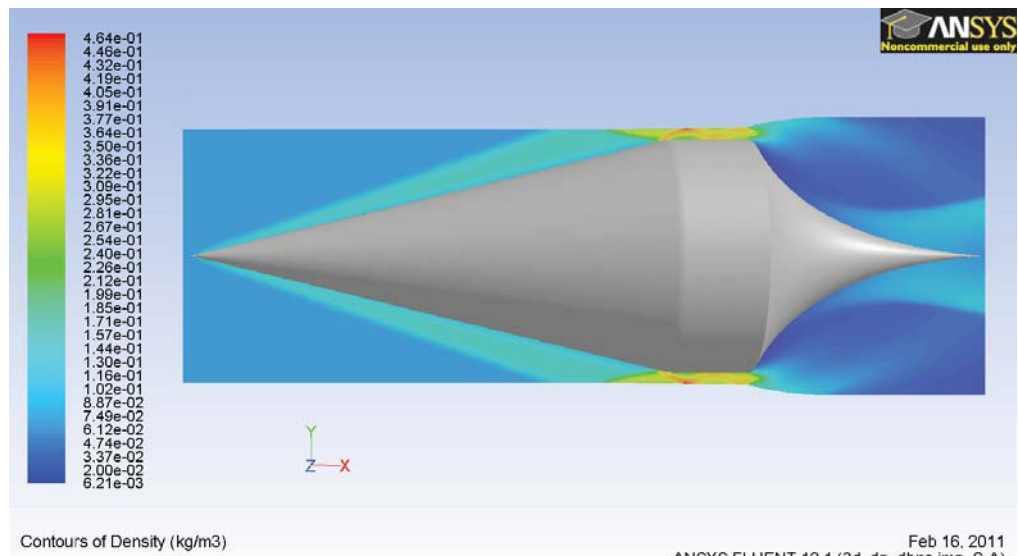


Figure 5.12: Contours of density for 3D mesh at angles of attack of 0° , 3° and 6° and Mach 5.

5.4 Axi-symmetric stream traced inlet design

5.4.1 Numerical results at Mach 8 conditions

Identical simulations were performed for the axi-symmetric stream traced inlet design. Both Mach 5 and 8 simulations at angles of attack of 0° , 3° and 6° were produced on a three-dimensional grid, with two-dimensional axi-symmetric simulations also performed on a refined mesh at 0° to resolve the inlet flow features more accurately. The axi-symmetric stream traced inlet design achieves a higher level of compression over the axi-symmetric inlet, due to the inward turning cowl. This increases the intensity of the interaction between the inlet cowl shock and the forebody boundary layer, reducing the uniformity of the flow throughout the isolator. A stronger shock train is present, which reduces the inlets efficiency through irreversible increases in entropy. A comparison between the three dimensional simulations and the refined two-dimensional axi-symmetric results is shown in Figures 5.14, 5.15 and 5.16. This reiterates what was found for the axi-symmetric inlet geometry - the general flow structure is resolved in the 3D case, however some degree of shock smearing occurs, with the pressure peaks underestimated in the three dimensional simulations. Again the inlet remains started in the finer simulations. Contours of density at the isolator outlet shown in Figure 5.14 again show good levels of flow uniformity.

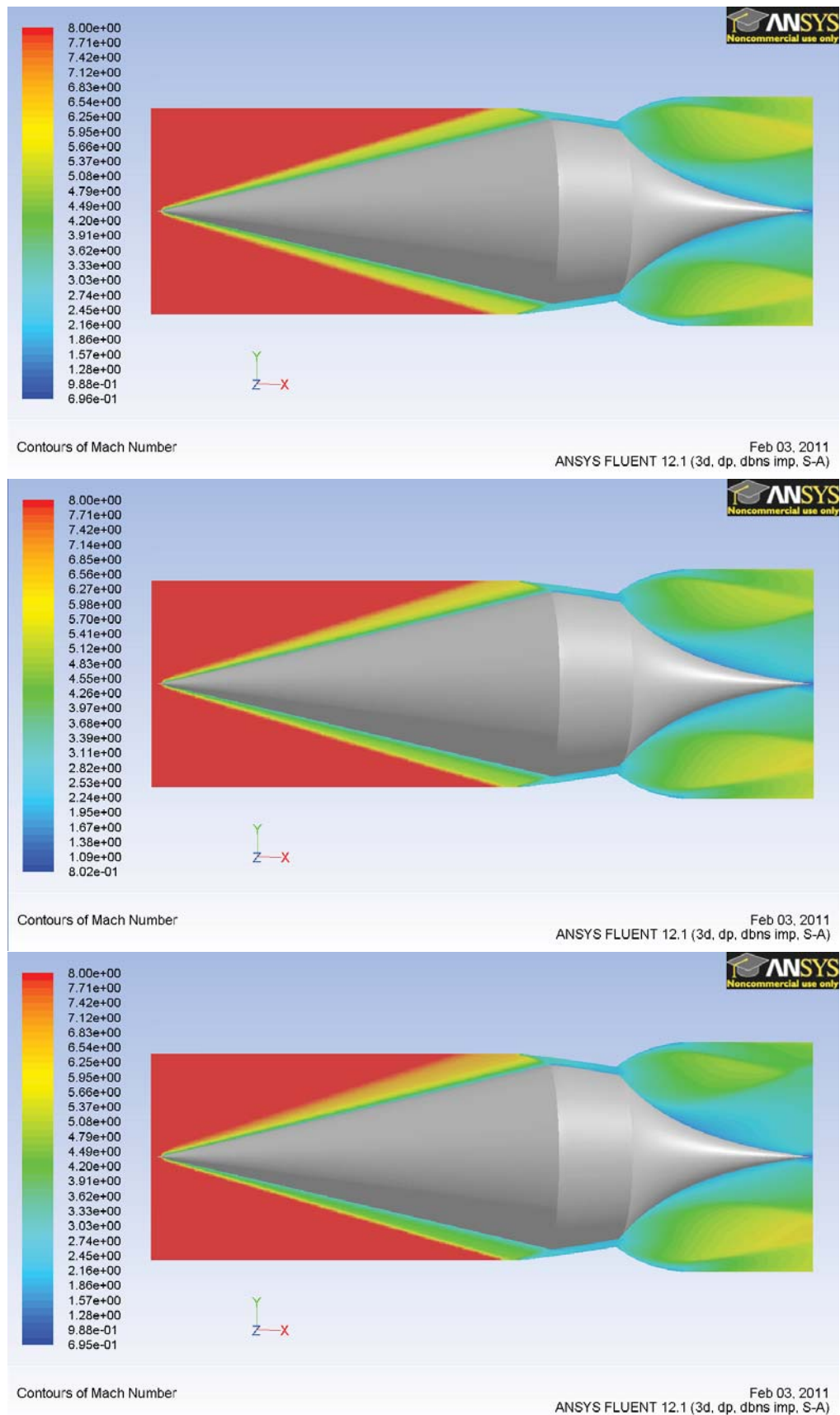
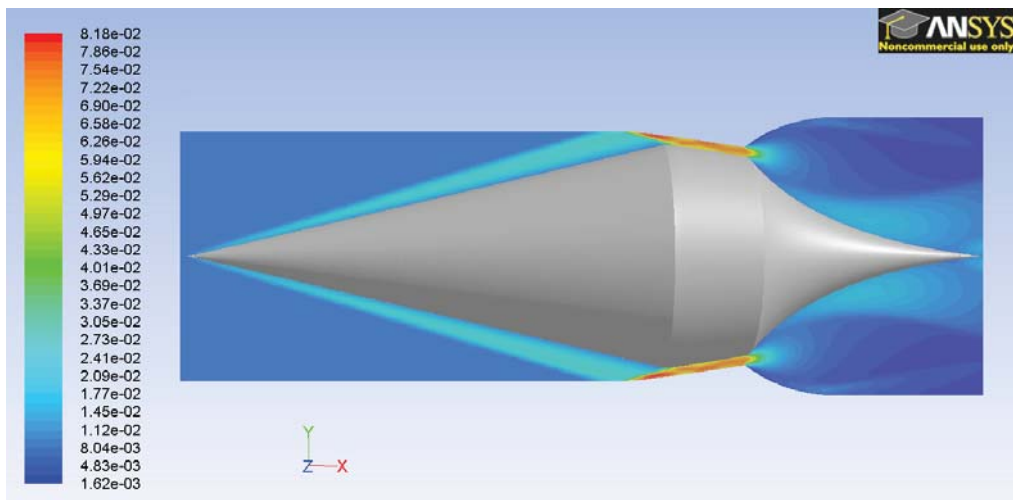
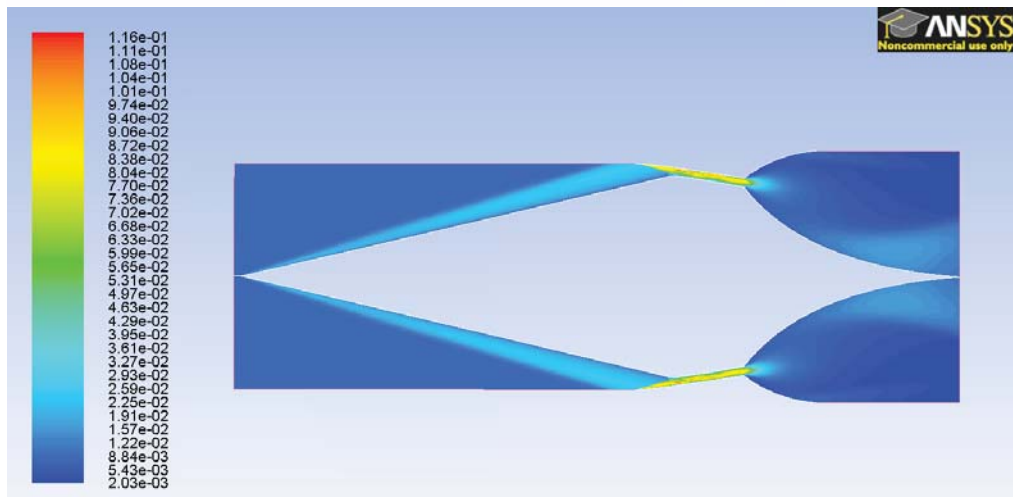


Figure 5.13: Contours of Mach number for the 3D mesh at angles of attack of 0°, 3° and 6° and Mach 8.



Contours of Density (kg/m3)

Feb 03, 2011
ANSYS FLUENT 12.1 (3d, dp, dbns imp, S-A)



Contours of Density (kg/m3)

Sep 20, 2011
ANSYS FLUENT 12.1 (axi, dp, dbns imp, S-A)

Figure 5.14: Contours of density for an angle of attack of 0° at Mach 8 - 3D mesh (top) and 2D mesh (bottom).

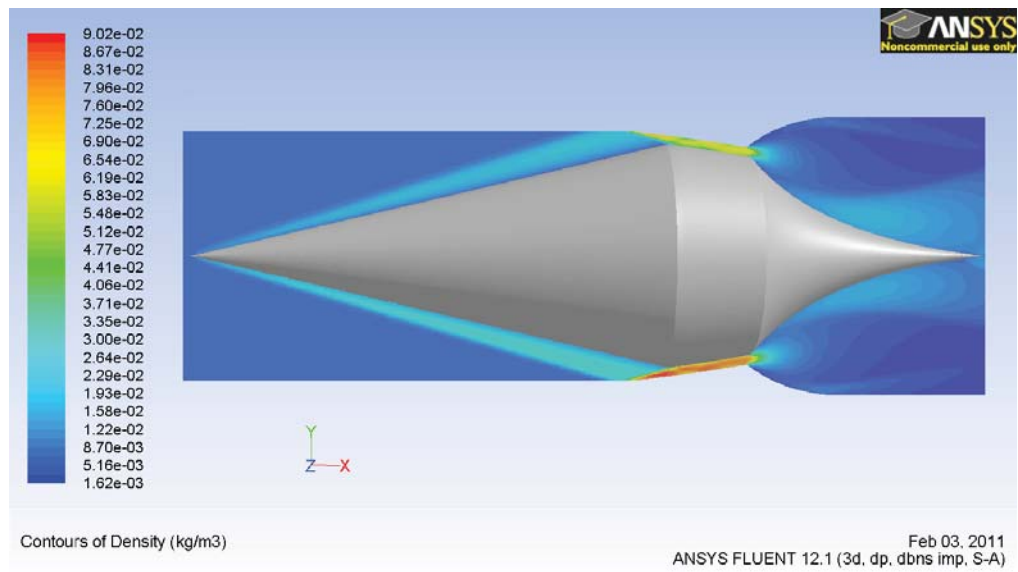


Figure 5.15: Contours of density for an angle of attack of 3° at Mach 8 - 3D mesh.

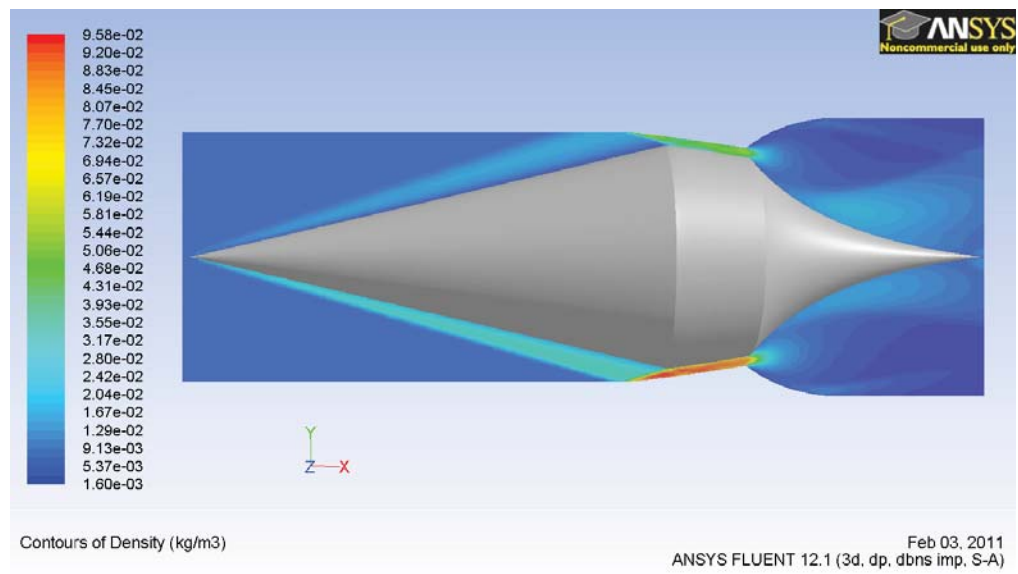
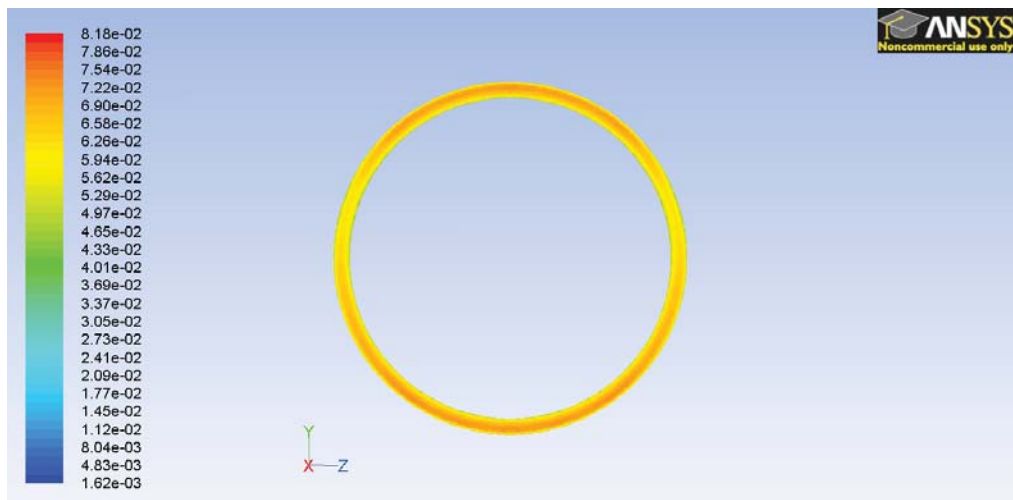
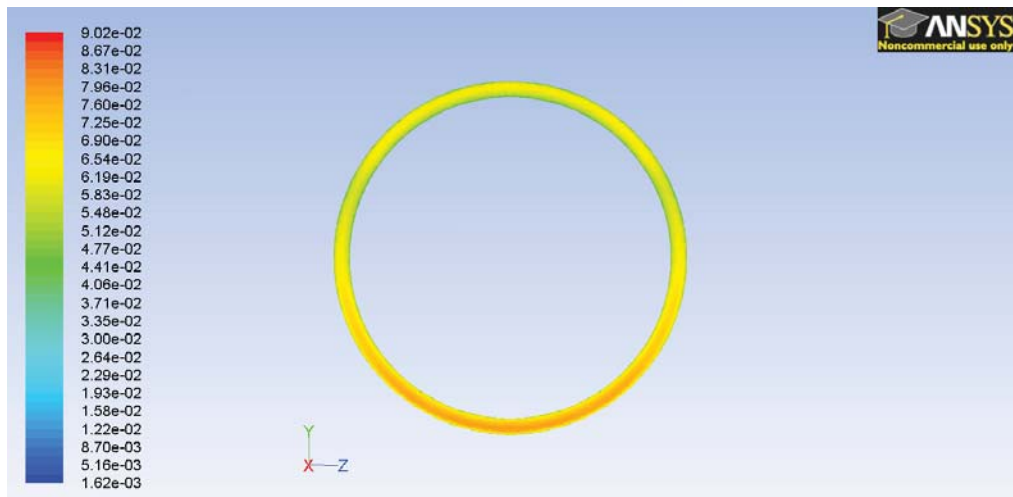


Figure 5.16: Contours of density for an angle of attack of 6° at Mach 8 - 3D mesh.



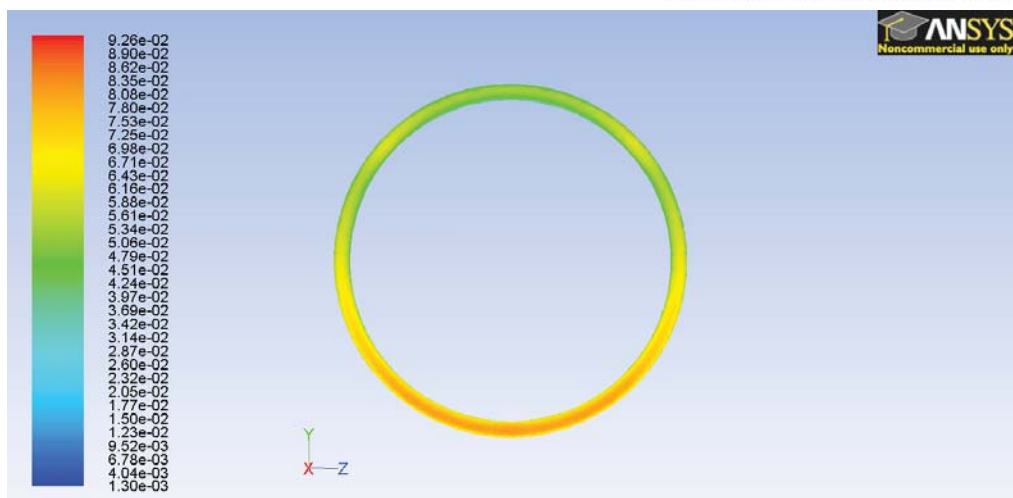
Contours of Density (kg/m3)

Feb 03, 2011
ANSYS FLUENT 12.1 (3d, dp, dbns imp, S-A)



Contours of Density (kg/m3)

Feb 03, 2011
ANSYS FLUENT 12.1 (3d, dp, dbns imp, S-A)



Contours of Density (kg/m3)

Feb 11, 2011
ANSYS FLUENT 12.1 (3d, dp, dbns imp, S-A)

Figure 5.17: Contours of density at isolator outlet for angles of attack of 0° , 3° and 6° .

Figure 5.18 illustrates the complex flow processes within the inlet obtained from the two dimensional axi-symmetric simulations. At the throat of the inlet, there is a separation bubble where the cowl shock and the forebody expansion wave meet. The separation bubble is a subsonic recirculation region, that is typically unstable and exerts oscillatory growth and decay (Tan *et al.* , 2009). If the separation bubble is able to grow sufficiently, it may cause the inlet to unstart. This bubble can be seen to grow at angles of attack, shown in Figure 5.14. There is a region of high heating where the inlet cowl shock meets the separation bubble, at the origin of the expansion fan. The temperature in this region can reach over $3000K$. The high temperatures across the shock may cause the air to ionise and dissociate (Anderson, 2000), which may adversely affect the performance of the laser induced detonation process. The incident cowl shock can be seen to penetrate somewhat into the separation bubble. This shock is a source of decreased efficiency of the inlet, as the some of the total pressure loss across it is unable to be recovered by the expansion through the nozzle. The difference between the core inlet flow and the boundary layer has been illustrated in Figure 5.18. The isolator shock train does not cause boundary layer separation. An illustration of the flow processes, from Segal (2009), is included in Figure 5.19 to clarify the complex flow interactions occurring within the inlet.

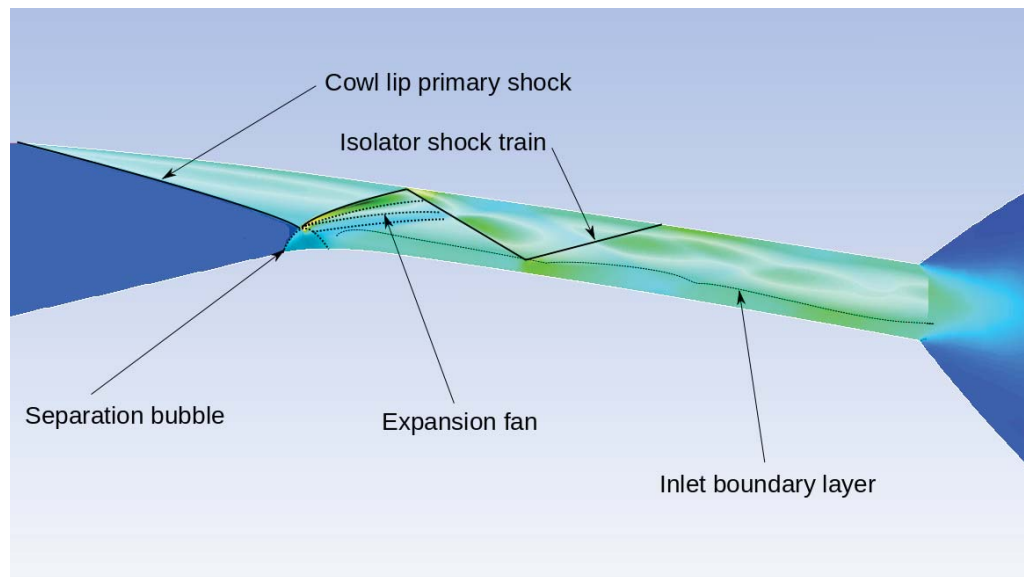


Figure 5.18: Close up of isolator flow field, Mach 8 at 0° angle of attack for the 2D mesh.

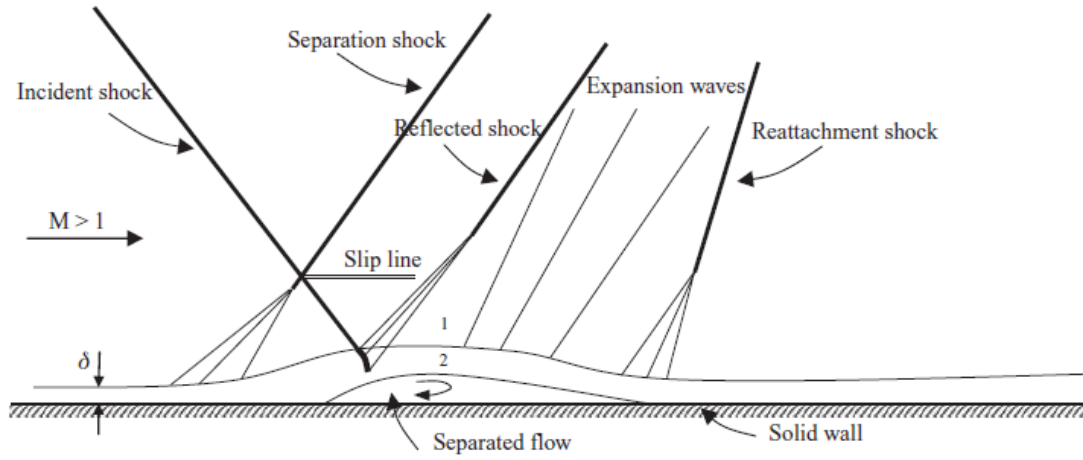


Figure 5.19: Illustration of flow processes about separation bubble. (Segal, 2009)

5.4.2 Numerical results at Mach 5 conditions

Figure 5.20 shows contours of Mach number for the reduced flight speed simulations. It is clear the stream traced axi-symmetric inlet geometry also remains in a started state for the investigated angle of attack range. Again a degradation in the isolator flow structure can be seen due to the change in cowl shock location.

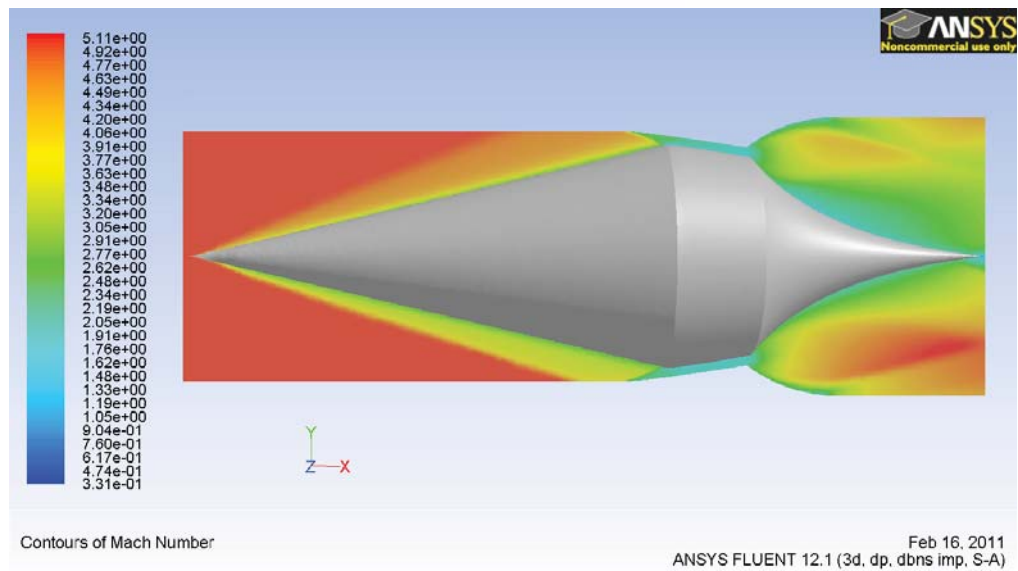
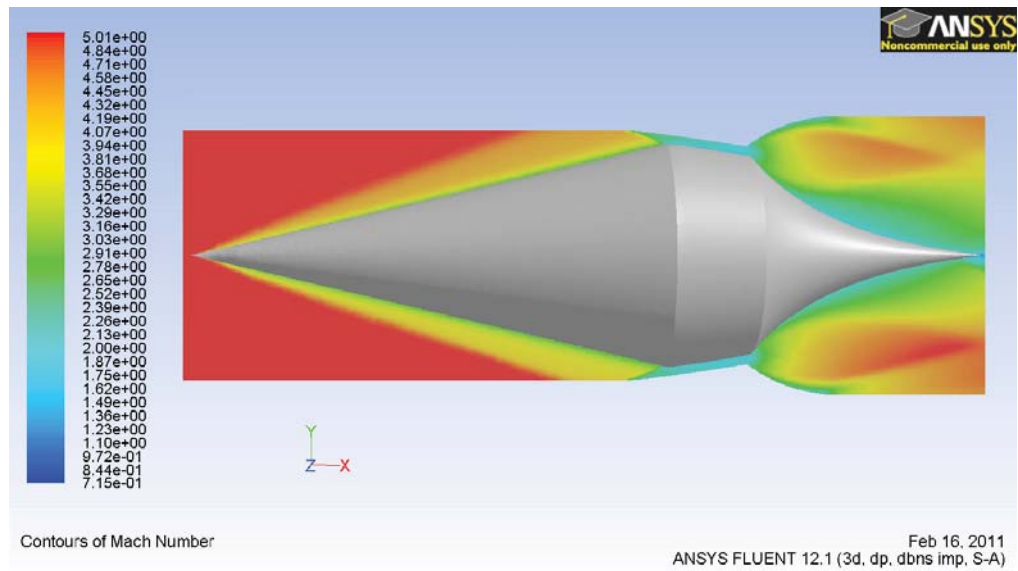
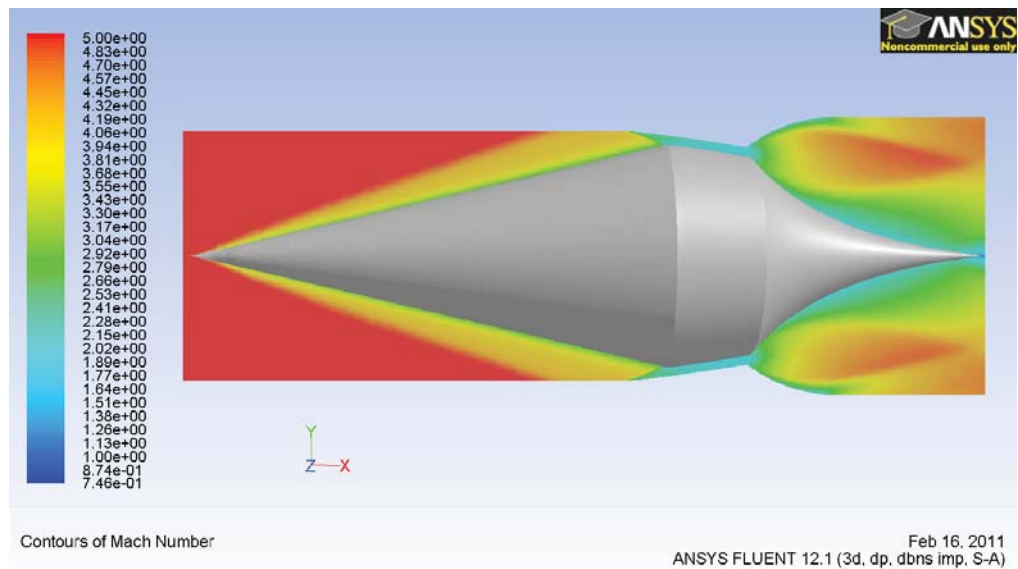


Figure 5.20: Contours of Mach number for angles of attack of 0° , 3° and 6°

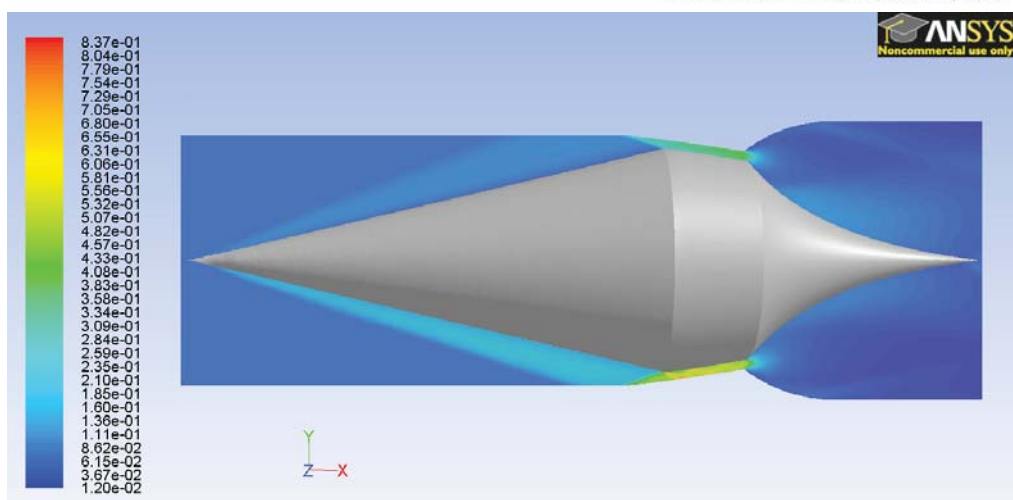
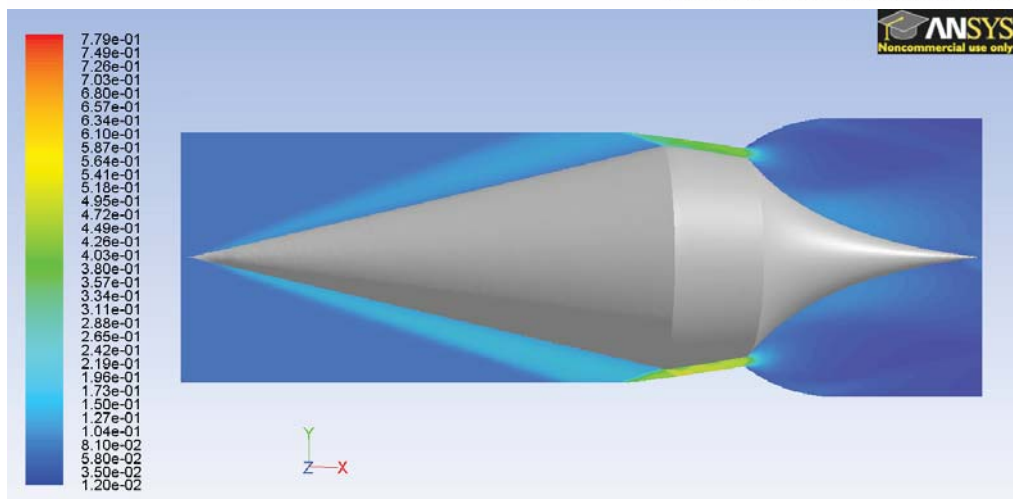
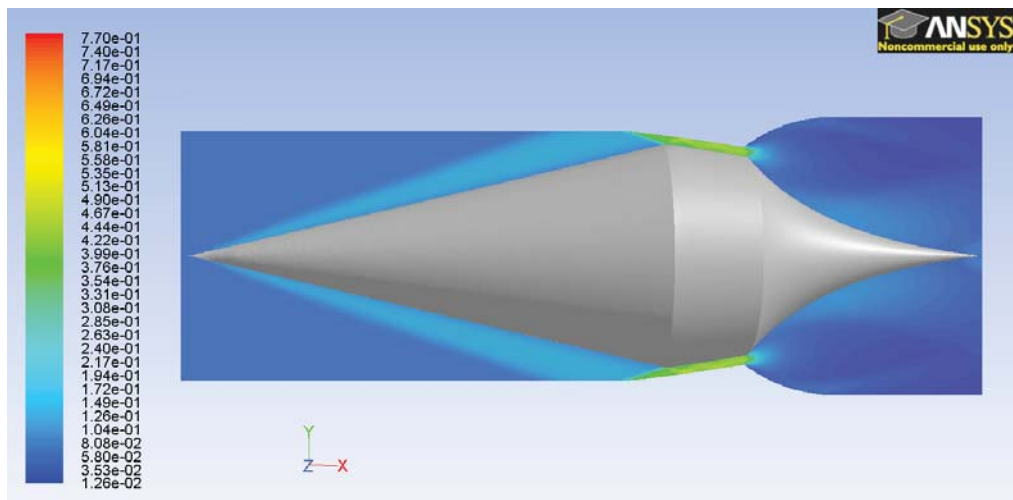
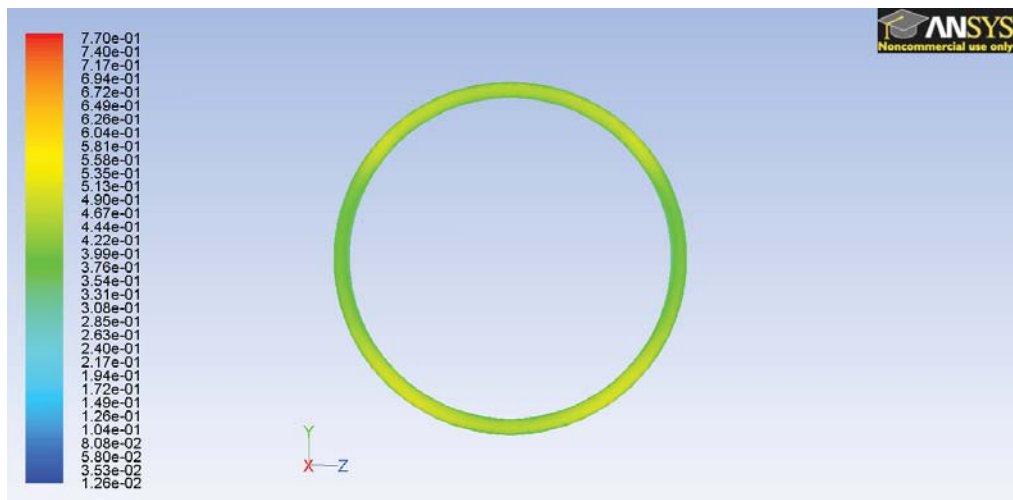


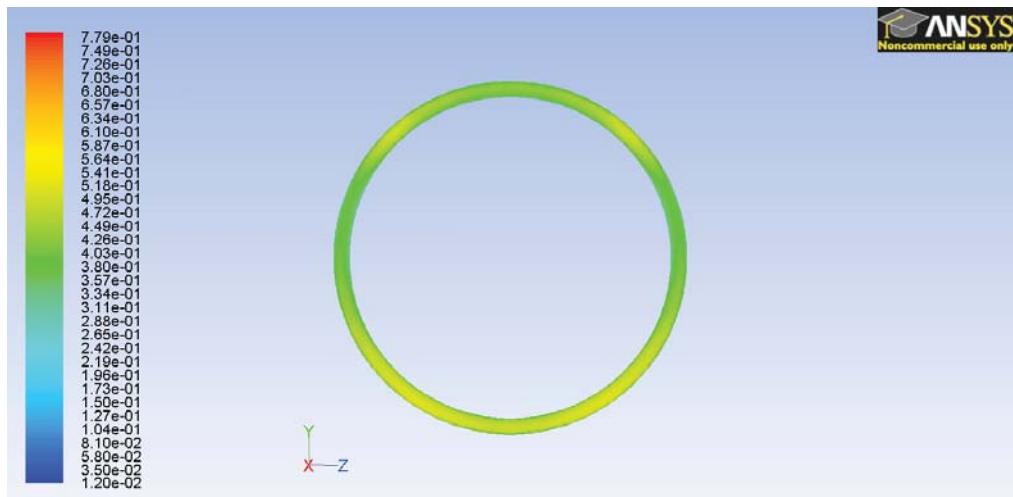
Figure 5.21: Contours of density for angles of attack of 0° , 3° and 6°

Contours of density at the isolator exit in Figure 5.22 again demonstrate high levels of uniformity achieved at all angles of attack, the standard deviation of density across the isolator outlet .



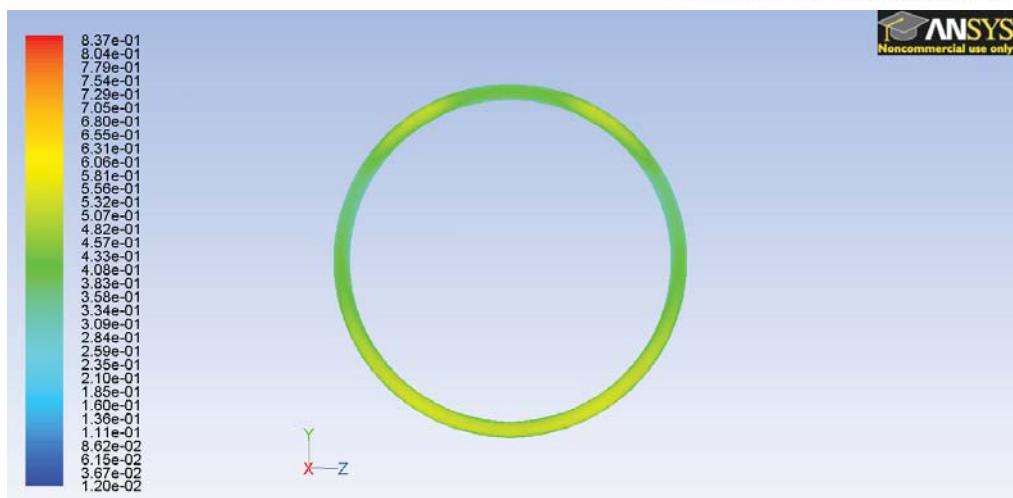
Contours of Density (kg/m3)

Feb 16, 2011
ANSYS FLUENT 12.1 (3d, dp, dbns imp, S-A)



Contours of Density (kg/m3)

Feb 16, 2011
ANSYS FLUENT 12.1 (3d, dp, dbns imp, S-A)



Contours of Density (kg/m3)

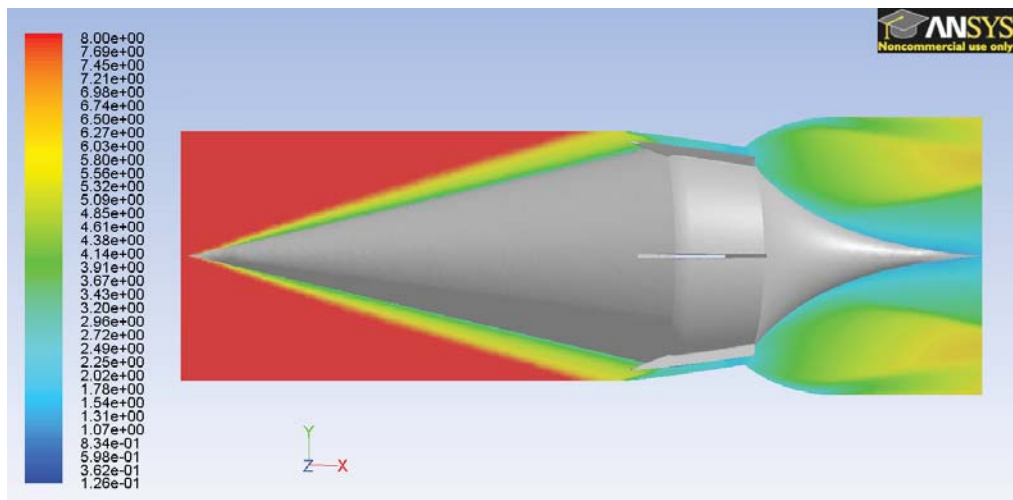
Feb 16, 2011
ANSYS FLUENT 12.1 (3d, dp, dbns imp, S-A)

Figure 5.22: Contours of density at isolator outlet for angles of attack of 0°, 3° and 6°

5.5 Stream traced axi-symmetric modular inlet design

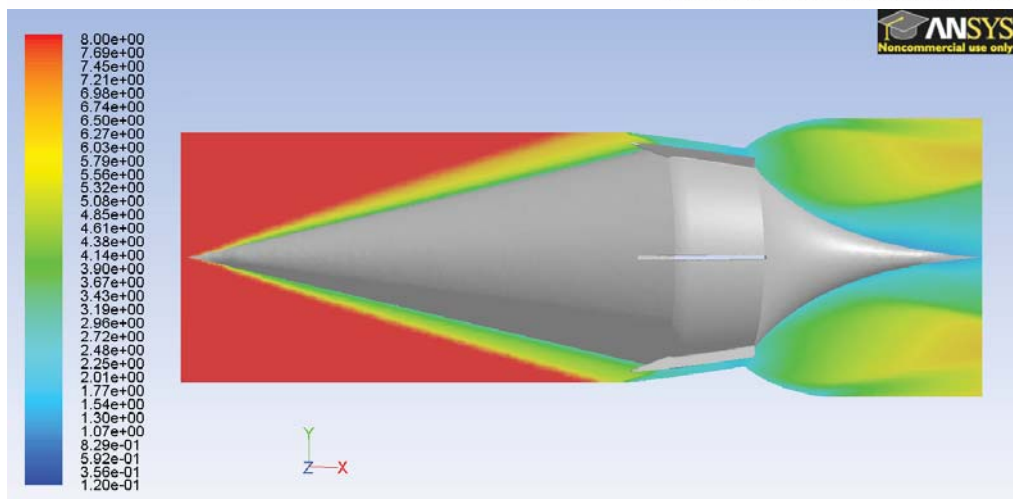
5.5.1 Numerical results at Mach 8 conditions

For the stream traced axi-symmetric modular inlet design, the inlet truncated geometry obtained from the streamTracer code (see Section 4.4.2) was mated to a viscous corrected conical forebody. The resulting shape is then mated to a parabolic receptive optic and an expansion nozzle, creating the final lightcraft geometry. The truncated inlet is then divided into six modules to form the modular arrangement. The geometry is again simulated at the conditions specified in Tables 3.7 and 5.1. The introduction of struts, while a realistic structural requirement, severely reduces the uniformity of the inlet flow field. Oblique shocks are formed, which are swallowed by the inlet. Contours of Mach number for the three angles of attack are shown in Figure 5.23, demonstrating all inlets remain in a started state.



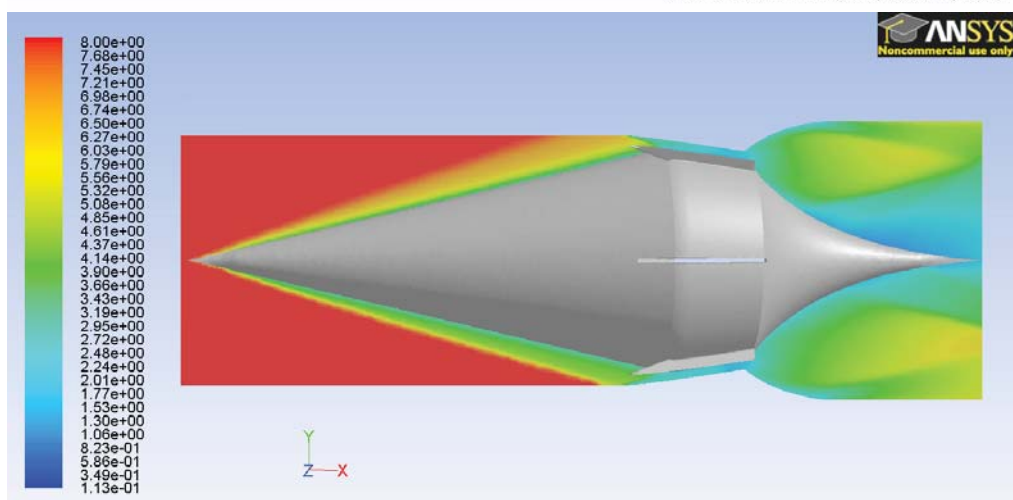
Contours of Mach Number

Feb 10, 2011
ANSYS FLUENT 12.1 (3d, dp, dbns imp, S-A)



Contours of Mach Number

Feb 10, 2011
ANSYS FLUENT 12.1 (3d, dp, dbns imp, S-A)



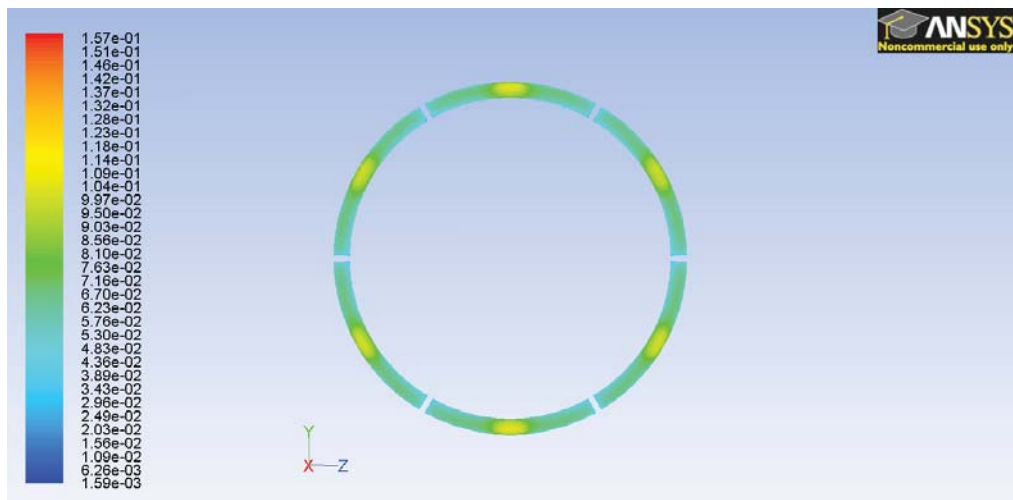
Contours of Mach Number

Feb 10, 2011
ANSYS FLUENT 12.1 (3d, dp, dbns imp, S-A)

Figure 5.23: Contours of Mach number for angles of attack of 0° , 3° and 6° at Mach 8.

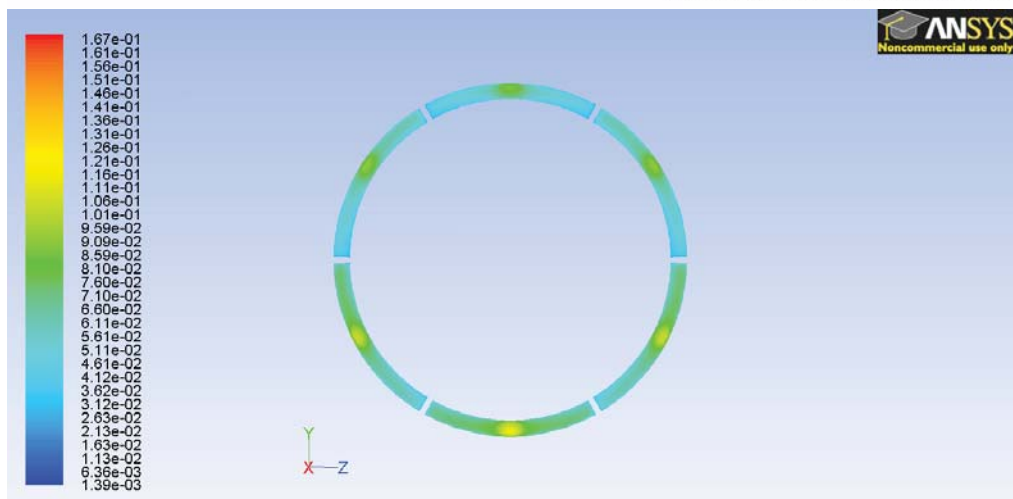
Contours of density at the exit of the isolator for the stream traced modular inlet arrangement are shown in Figure 5.24. It can be seen that the flow exhibits a high amount of non-uniformity due to the shock waves generated by the inlet module struts. This shock structure increases the flow non-uniformity and will add to the losses of the inlet. It will also decrease the performance and controllability of the laser induced detonation system. Regions of higher density will generate higher initial plasma pressures and temperatures, resulting in a non-uniform detonation wave structure. It is highly possible a detonation wave structure like this could cause catastrophic loads on the structure, and undesired or unexpected force moments on the body during flight.

Current research into the laser induced detonation process has not quantified the effect of total pressure losses on the performance of the system. Traditionally fueled hypersonic engine performance is highly dependant on the efficiency losses due to uncanceled shockwaves within the isolator (Heiser *et al.* , 1994). It is currently unknown what the effect of irreversible entropy changes due to shock waves will have on the performance of the laser lightcraft at supersonic speeds. While uncanceled shockwaves will present significant structural issues to the craft design, some level of flow efficiency losses may be acceptable in the laser induced detonation engine. The increases in density realised may actually be desirable in increasing the initial detonation wave front pressure, however the realizable energy of the flow may be somewhat reduced by real gas effects such as dissociation. It is most likely that efficiency losses from compression waves will not significantly reduce the amount of thrust able to be achieved by the propulsion system, with the additional compression benefiting the system substantially. The benefit of this additional compression achieved must be weighed against the drag penalty that will occur from the unnecessary shock structure.



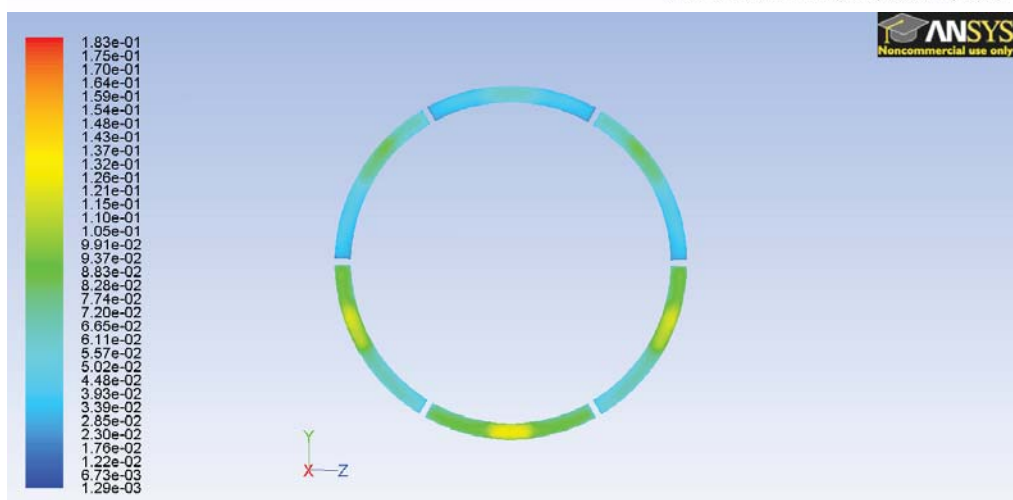
Contours of Density (kg/m3)

Feb 10, 2011
ANSYS FLUENT 12.1 (3d, dp, dbns imp, S-A)



Contours of Density (kg/m3)

Feb 10, 2011
ANSYS FLUENT 12.1 (3d, dp, dbns imp, S-A)



Contours of Density (kg/m3)

Feb 10, 2011
ANSYS FLUENT 12.1 (3d, dp, dbns imp, S-A)

Figure 5.24: Contours of density at isolator outlet for angles of attack of 0° , 3° and 6°

The shock structure resulting from the inlet module struts is illustrated with further detail in Figure 5.25. This image show contours of static pressure on the lightcraft external surfaces at the different flight angles of attack. The oblique shockwaves off the struts can be seen to travel backwards through the isolator, where they meet at the regions of high density visible in Figure 5.24. At angles of attack, this shock structure can be seen to weaken on the leeward side, and strengthen on the windward side. There is also significant heating along the struts, where the supersonic flow is brought to stagnation. The surface temperature here can reach as high as $3,330\text{ K}$.

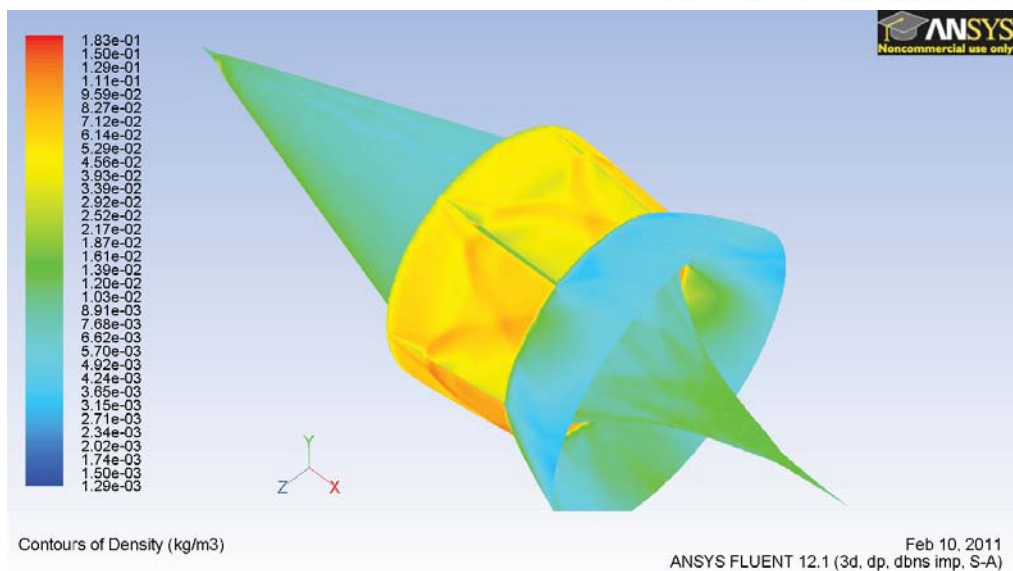
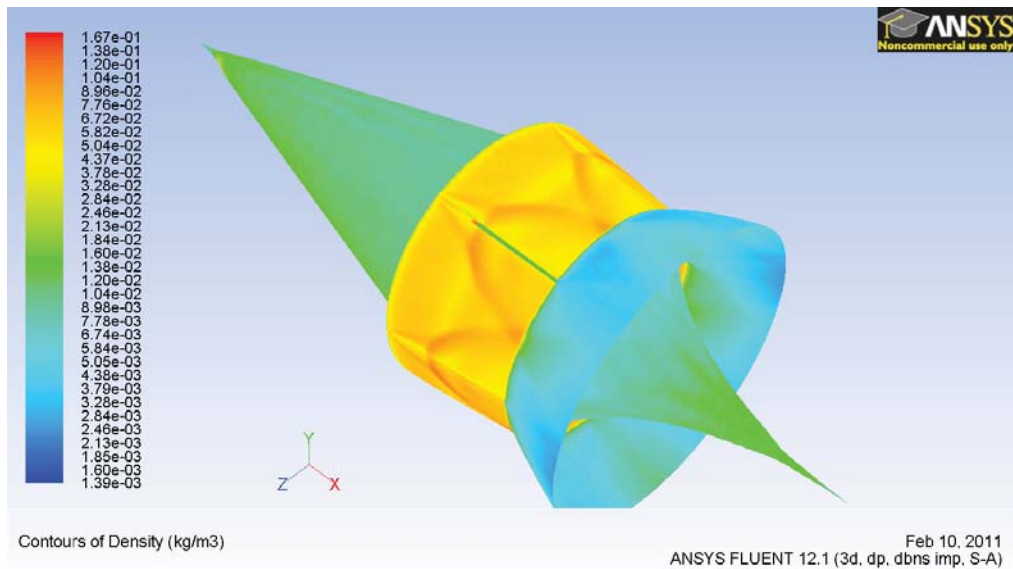
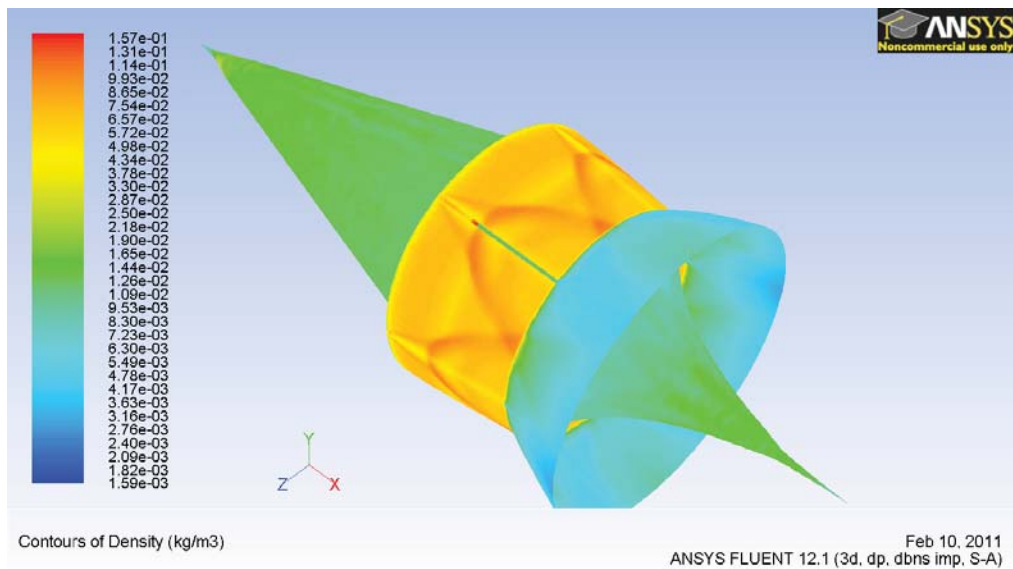


Figure 5.25: Surface contours of density for angles of attack of 0° , 3° and 6° at Mach 8 (logarithmic scale).

5.5.2 Numerical results at Mach 5 conditions

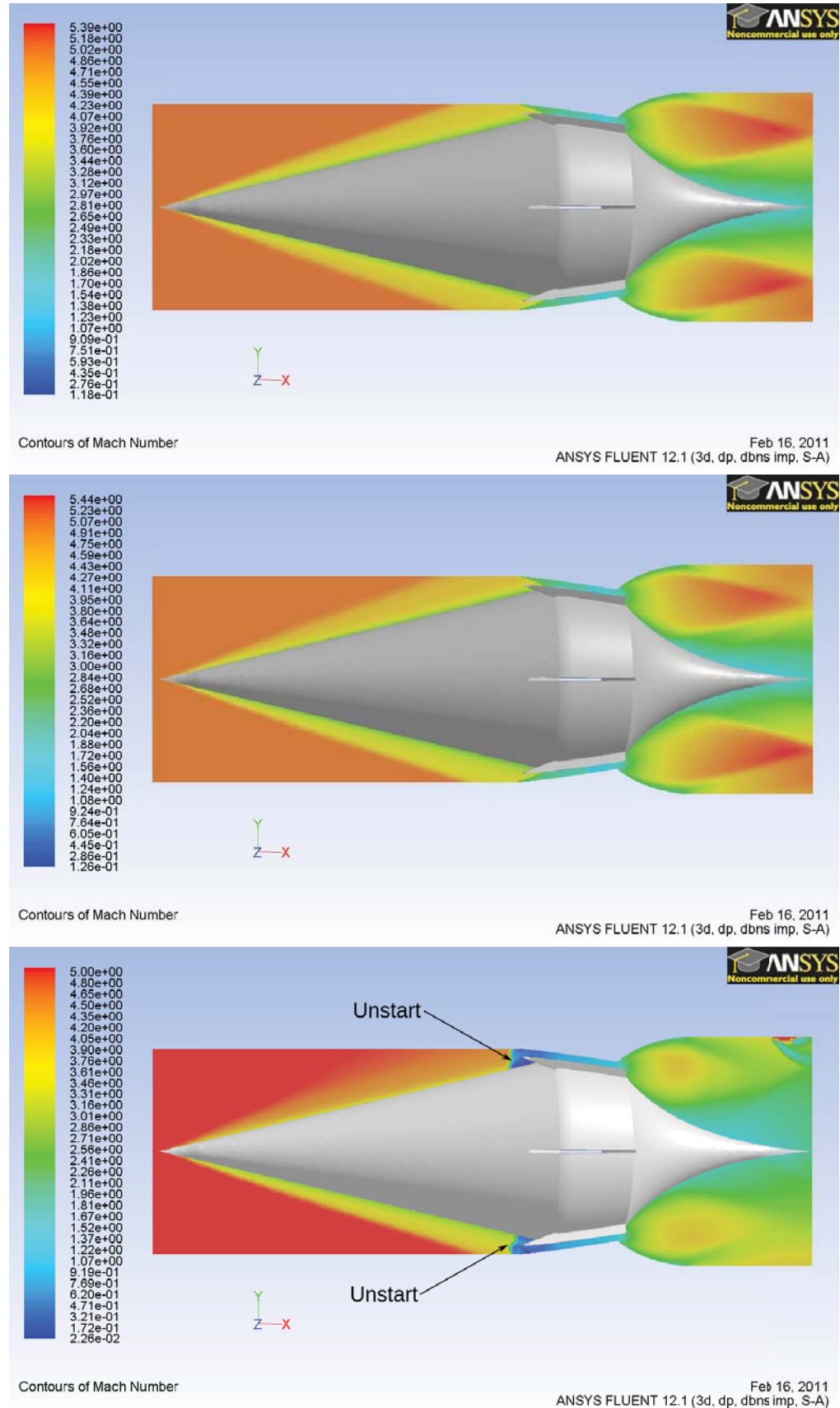


Figure 5.26: Contours of Mach number for angles of attack of 0°, 3° and 6° at Mach 5.

Mach 5 simulations show similar trends to the previous cases, however at angles of attack, it can be seen the flow uniformity is severely degraded. At the maximum angle of attack, the inlet can be seen to unstart - shown in Figure 5.26. A normal wave is disgorged from the inlet, severely reducing the mass flow rate through the engine. The effect of this can be clearly seen in Figure 5.27, where very low air densities are achieved at the isolator exit. It should be noted here that the numerical solutions obtained when an inlet is in unstarted mode are highly unstable, and cannot be used for quantitative results. The contours have been included for demonstration of the unstarted state. This does not necessarily exclude the inlet design from practical use, it just reduces the angle of attack envelope that the craft can fly within at certain flight conditions.

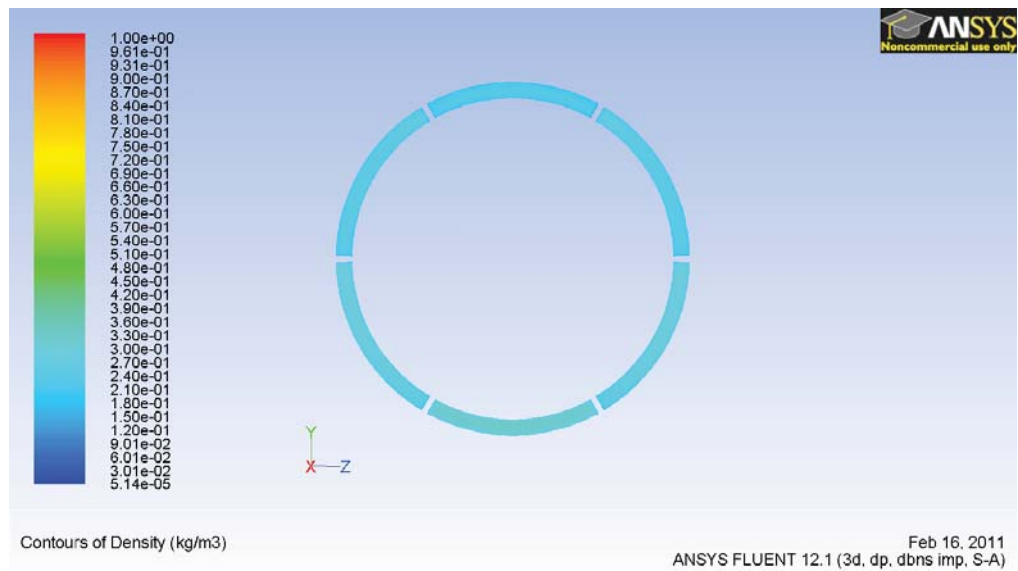
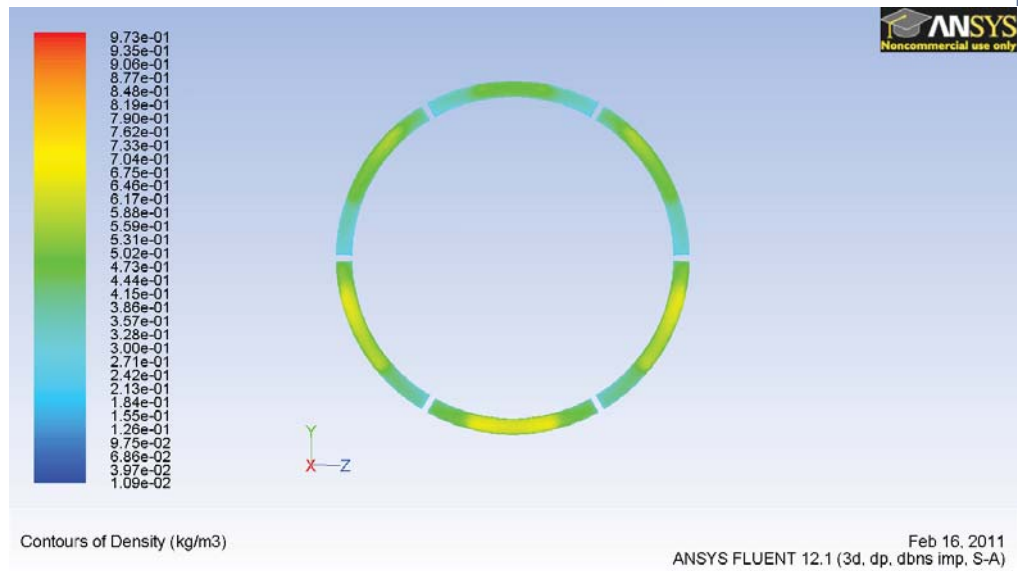
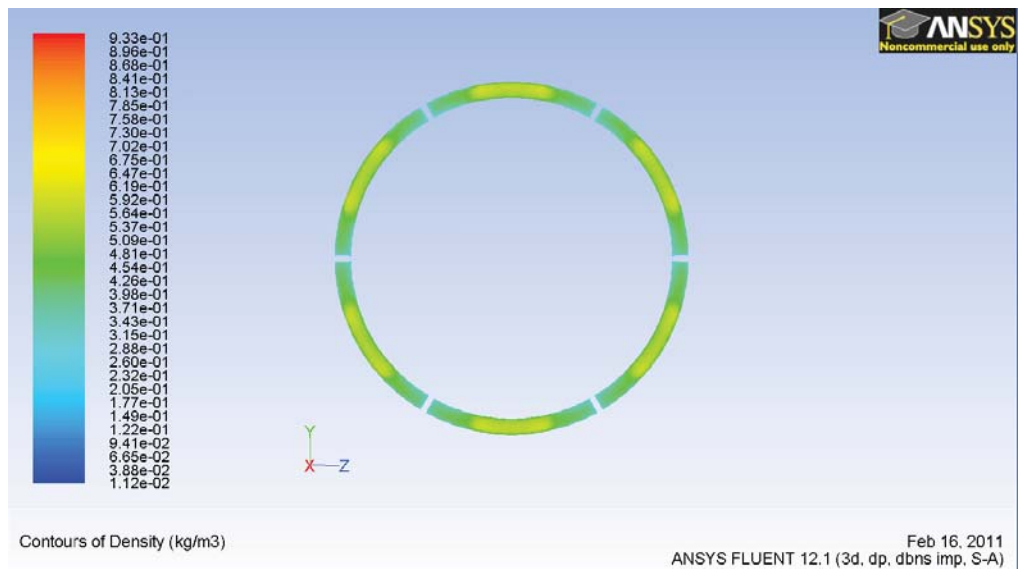
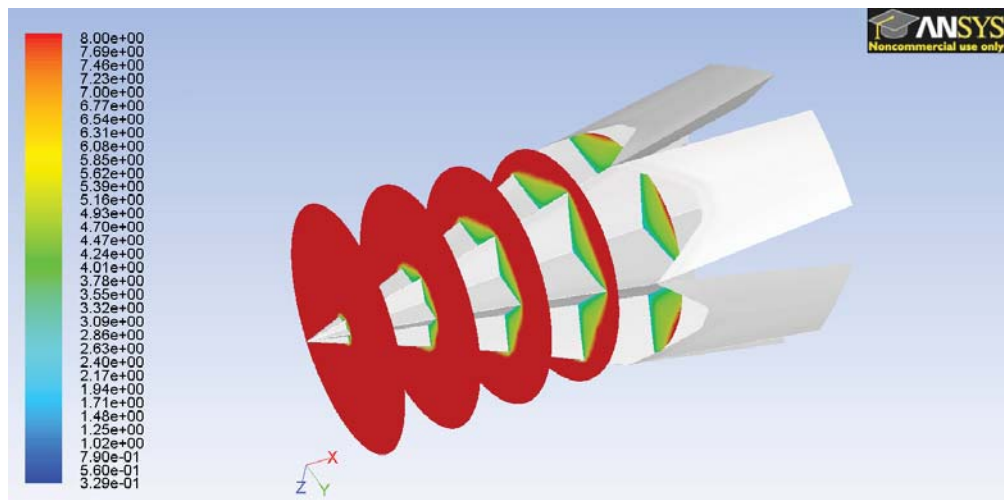


Figure 5.27: Contours of density at isolator outlet for angles of attack of 0° , 3° and 6° at Mach 5.

5.6 Stream traced modular ‘scalloped’ inlet design

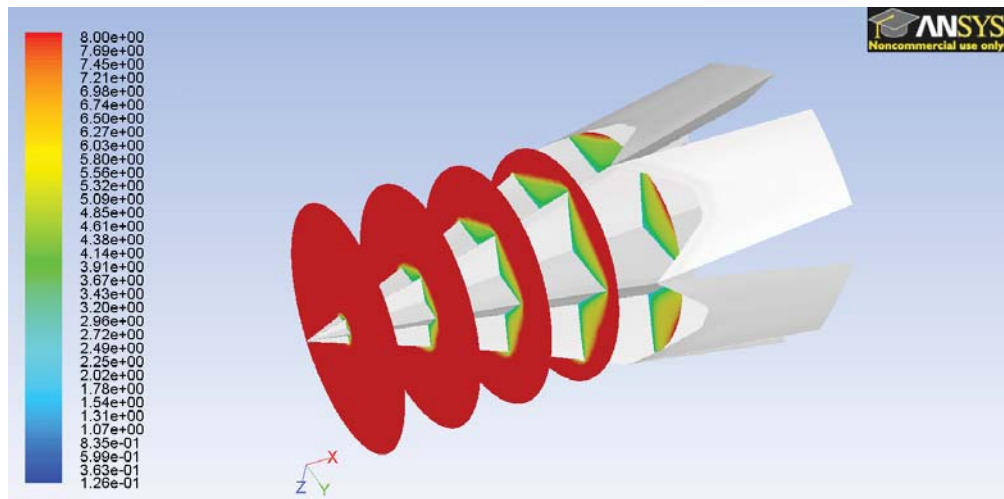
5.6.1 Numerical results at Mach 8 conditions

For the stream traced modular ‘scalloped’ inlet design, the three-dimensional inlet geometry obtained from the streamTracer code forms both the conical forebody and the inlet structure. An individual inlet geometry was created, which was then rotated annually around the centre-line to form the three-dimensional shape used in the numerical simulations. The resulting shape would typically be then be connected to a parabolic receptive optic and a expansion nozzle, creating the final lightcraft geometry. This was not done in this case due to mesh size restrictions. As the flow at the isolator exit is supersonic, with the exception of the boundary layer, there is no flow feedback across the majority of this boundary. This allows the nozzle to be neglected from the simulations without significant loss in solution accuracy. The geometry is then simulated at the conditions specified in Tables 3.7 and 5.1.



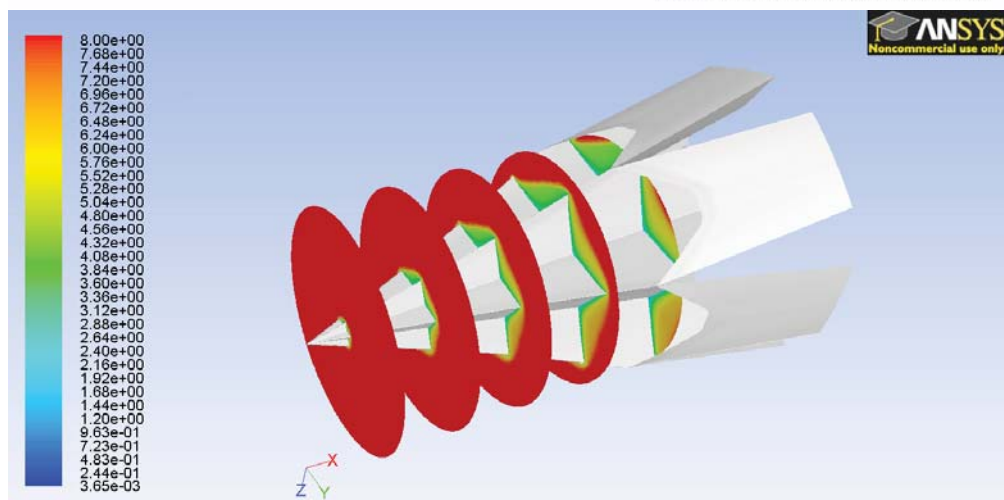
Contours of Mach Number

Aug 28, 2011
ANSYS FLUENT 12.1 (3d, dp, dbns imp, S-A)



Contours of Mach Number

Aug 28, 2011
ANSYS FLUENT 12.1 (3d, dp, dbns imp, S-A)



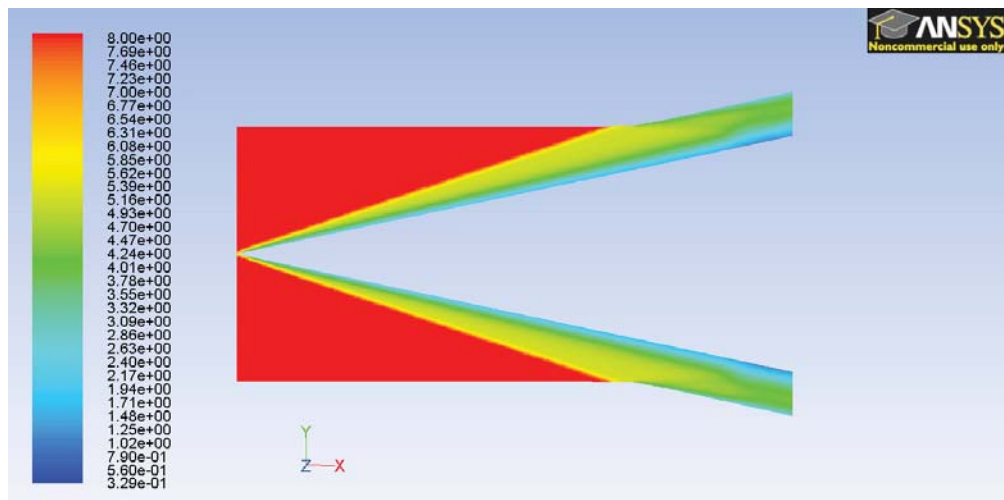
Contours of Mach Number

Aug 28, 2011
ANSYS FLUENT 12.1 (3d, dp, dbns imp, S-A)

Figure 5.28: Contours of Mach number, illustrating three-dimensional shock structure for angles of attack of 0° , 3° and 6° at Mach 8.

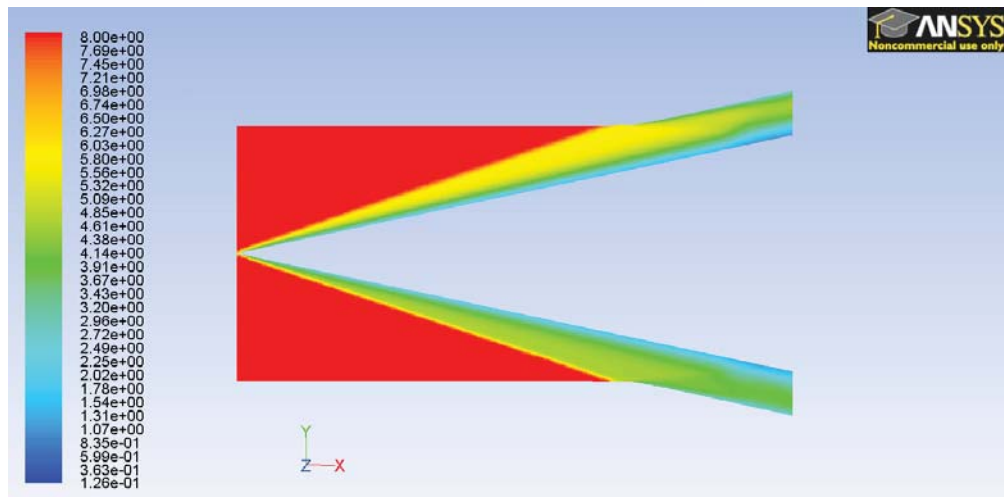
Figure 5.23 shows contours of Mach number for angles of attack of 0° , 3° and 6° in an isometric view perspective. This image illustrates the three-dimensional shock structure within the inlet. In the on-design case, the forebody shock can be seen to rest along the sharp edges of the lightcraft inlet, before entering the isolator. At angles of attack, the forebody shock appears to still remain attached to the inlet edge, however it becomes distorted due to change in the direction of the incoming air stream. At the 6° angle of attack case, significant distortion of the forebody shock can be seen.

Contours of Mach number along the axis of symmetry are shown in Figure 5.29. These images illustrate the growth of the boundary layer along the lower surface of the inlet. The secondary shock wave off the scalloped cowl of the inlet impinges on the boundary layer, causing its height to sharply increase. It does, however, still remain attached to the lower surface with the inlet remaining in a started state at all angles of attack.



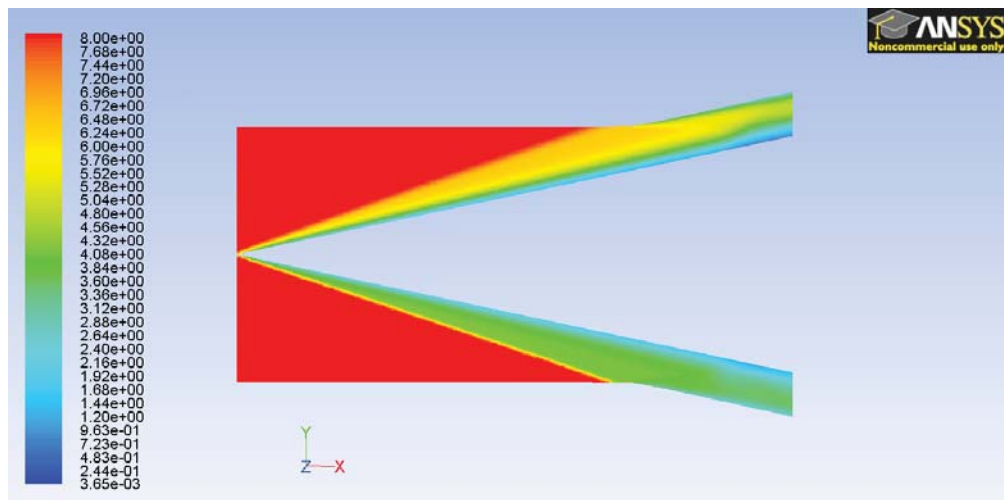
Contours of Mach Number

Aug 28, 2011
ANSYS FLUENT 12.1 (3d, dp, dbns imp, S-A)



Contours of Mach Number

Aug 28, 2011
ANSYS FLUENT 12.1 (3d, dp, dbns imp, S-A)



Contours of Mach Number

Aug 28, 2011
ANSYS FLUENT 12.1 (3d, dp, dbns imp, S-A)

Figure 5.29: Contours of Mach number for angles of attack of 0° , 3° and 6° at Mach 8.

Contours of density at the exit of the inlet isolator can be seen in Figure 5.30 for the modular scalloped inlet arrangement. The flow exhibits a high level of uniformity within the core flow region. The size of the boundary layer regions is relatively large compared to the other designs, with a significant decrease in the density. The separation of modules could possibly allow the control of the laser energy deposited in the individual modules, which would have performance benefits at angles of attack where turning moments would be produced due to different compression in the individual modules.

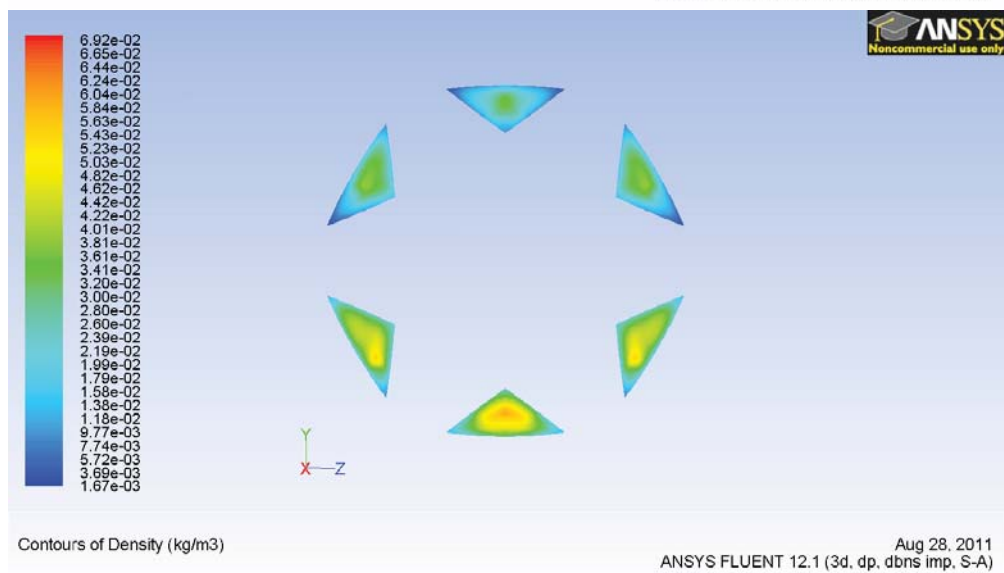
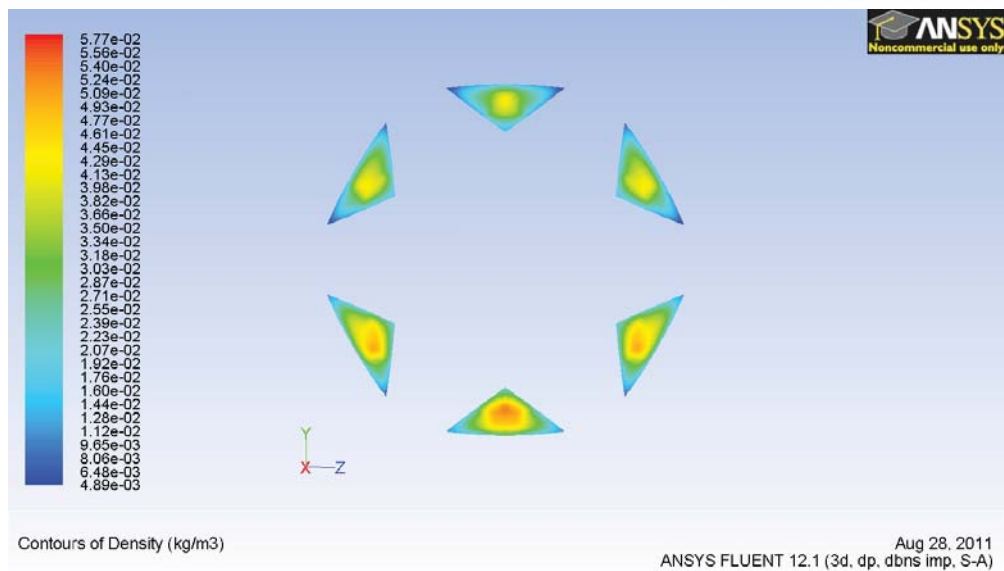
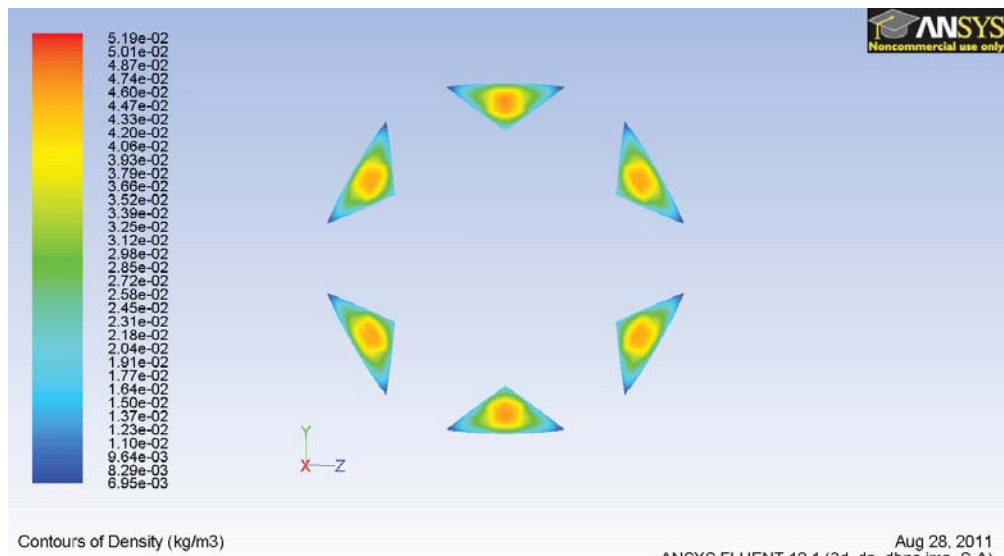
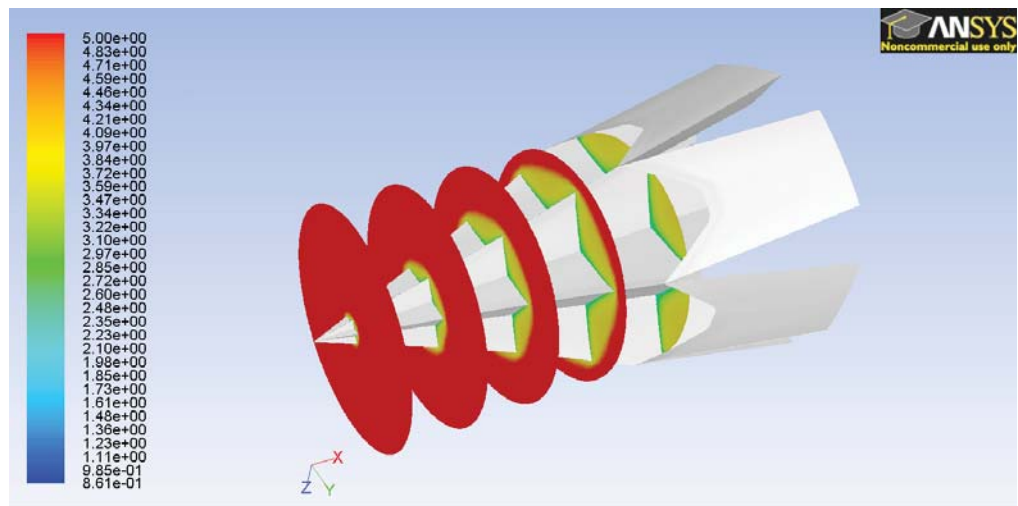


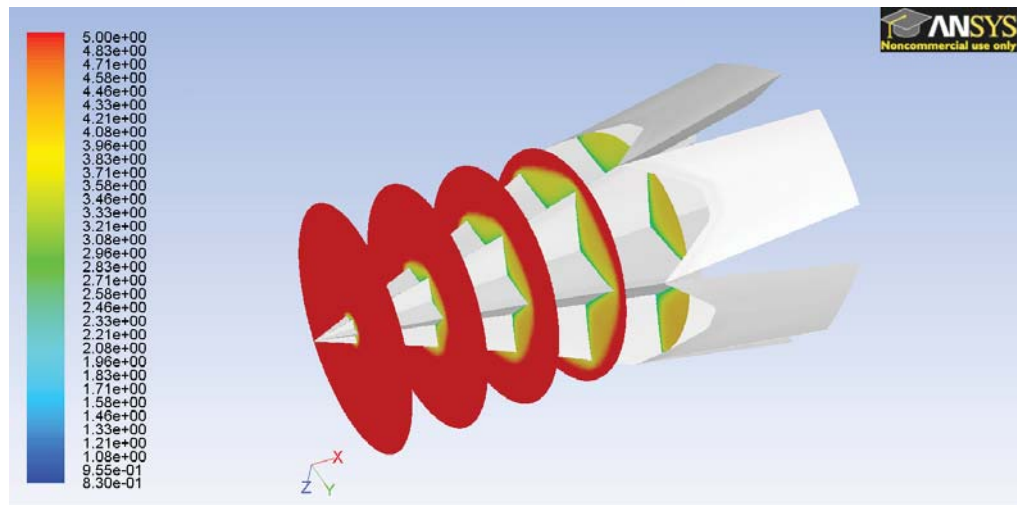
Figure 5.30: Contours of density at isolator outlet for angles of attack of 0°, 3° and 6°.

5.6.2 Numerical results at Mach 5 conditions

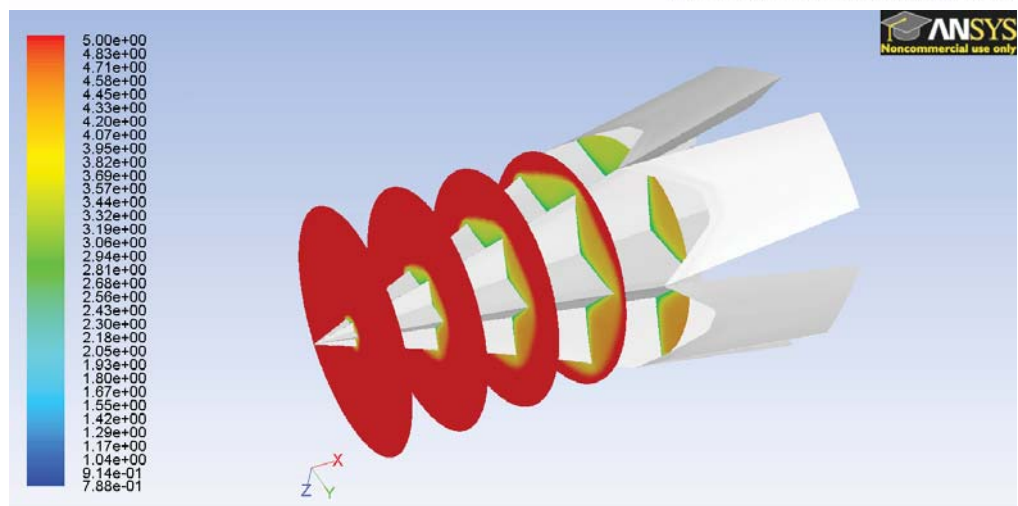
Contours of Mach number for the Mach 5 case are shown in Figures 5.31 and 5.32 for the isometric and axis of symmetry views. The forebody shock wave can be seen to stand off the inlet edges due to the lower flight speed. Again shock distortion can be seen in the angle of attack cases, with the inlet remaining started at all angles of attack.



Sep 10, 2011
ANSYS FLUENT 12.1 (3d, dp, dbns imp, S-A)

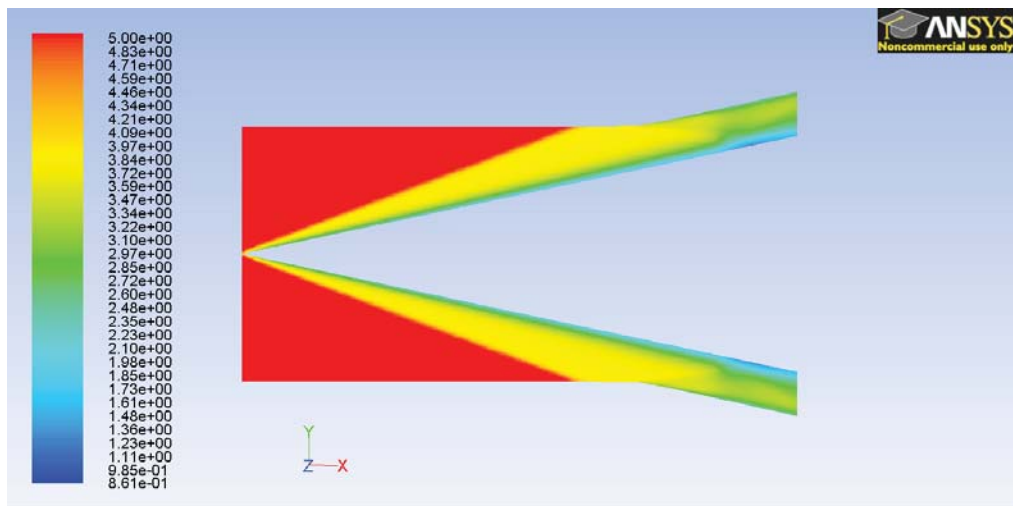


Sep 10, 2011
ANSYS FLUENT 12.1 (3d, dp, dbns imp, S-A)



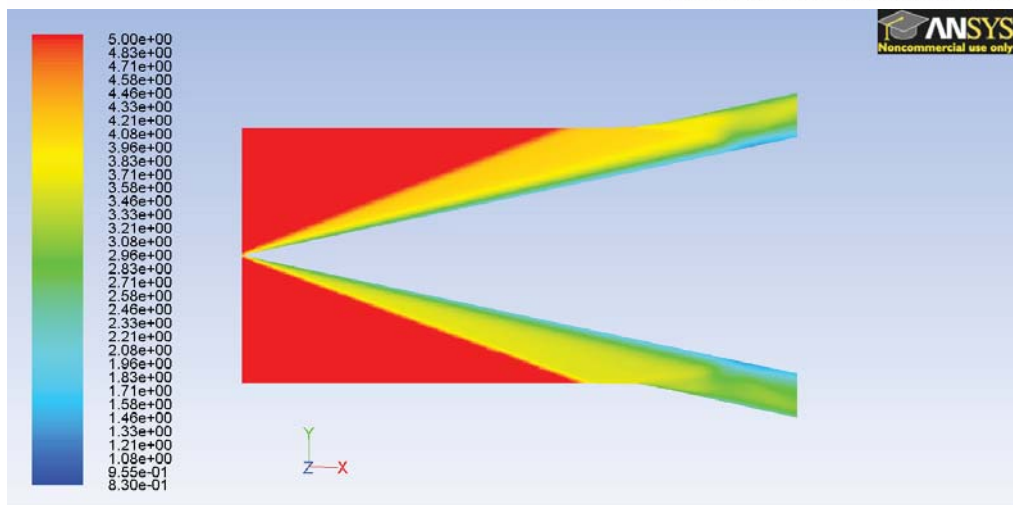
Sep 10, 2011
ANSYS FLUENT 12.1 (3d, dp, dbns imp, S-A)

Figure 5.31: Contours of Mach number, illustrating three-dimensional shock structure for angles of attack of 0° , 3° and 6° at Mach 5.



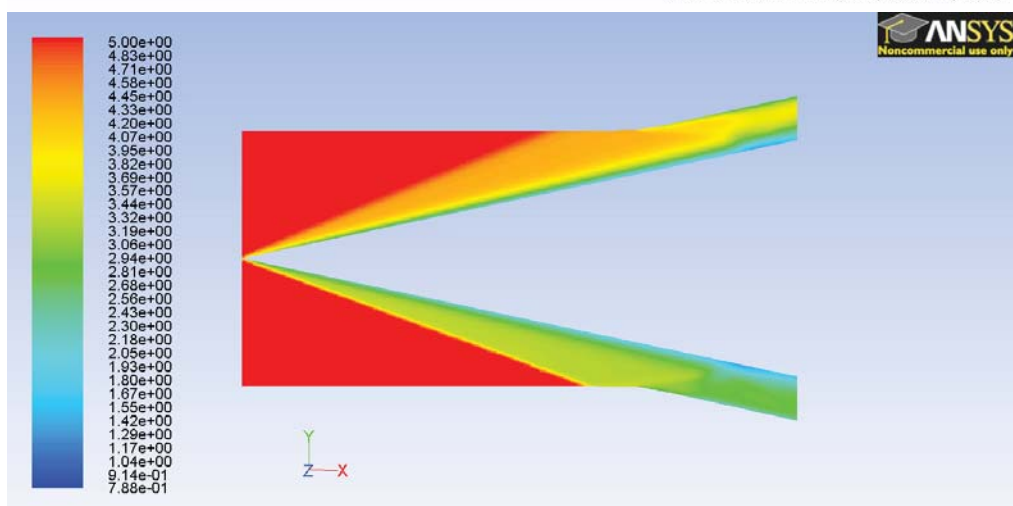
Contours of Mach Number

Sep 10, 2011
ANSYS FLUENT 12.1 (3d, dp, dbns imp, S-A)



Contours of Mach Number

Sep 10, 2011
ANSYS FLUENT 12.1 (3d, dp, dbns imp, S-A)



Contours of Mach Number

Sep 10, 2011
ANSYS FLUENT 12.1 (3d, dp, dbns imp, S-A)

Figure 5.32: Contours of Mach number for angles of attack of 0° , 3° and 6° at Mach 5.

At angles of attack, the flow uniformity is somewhat degraded over the Mach 8 case. The flow uniformity is still quite good, with the standard deviation of the density being approximately 0.06. This does represent an almost six fold increase over the vehicle operating at design conditions, however. Expansion waves can be seen in Figure 5.33 where the crotch shock generated by the inlet cowl meets the boundary layer. The uniformity at the isolator exit is good, with the core flow region slightly enlarged over the Mach 8 case.

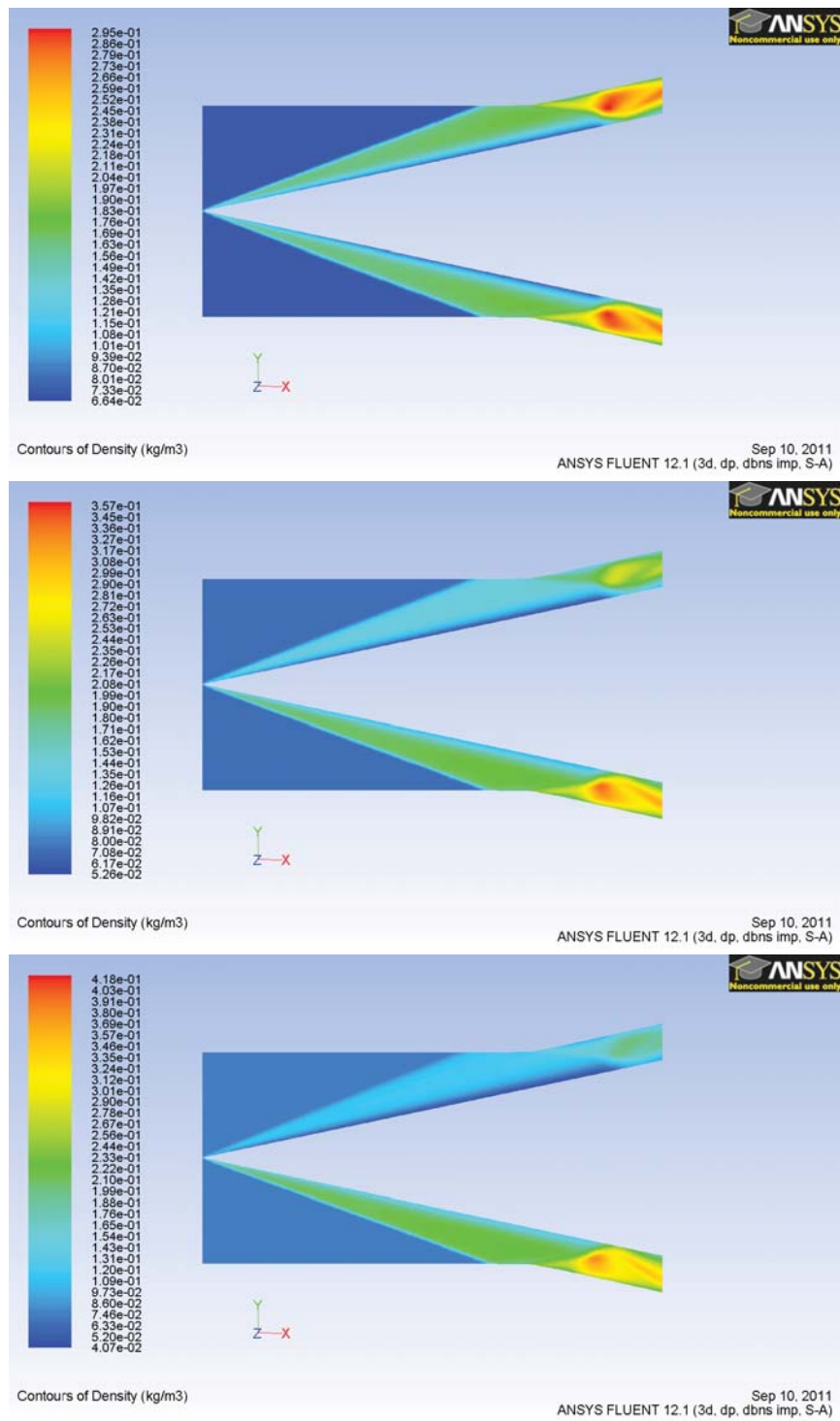


Figure 5.33: Contours of density for angles of attack of 0° , 3° and 6° at Mach 5.

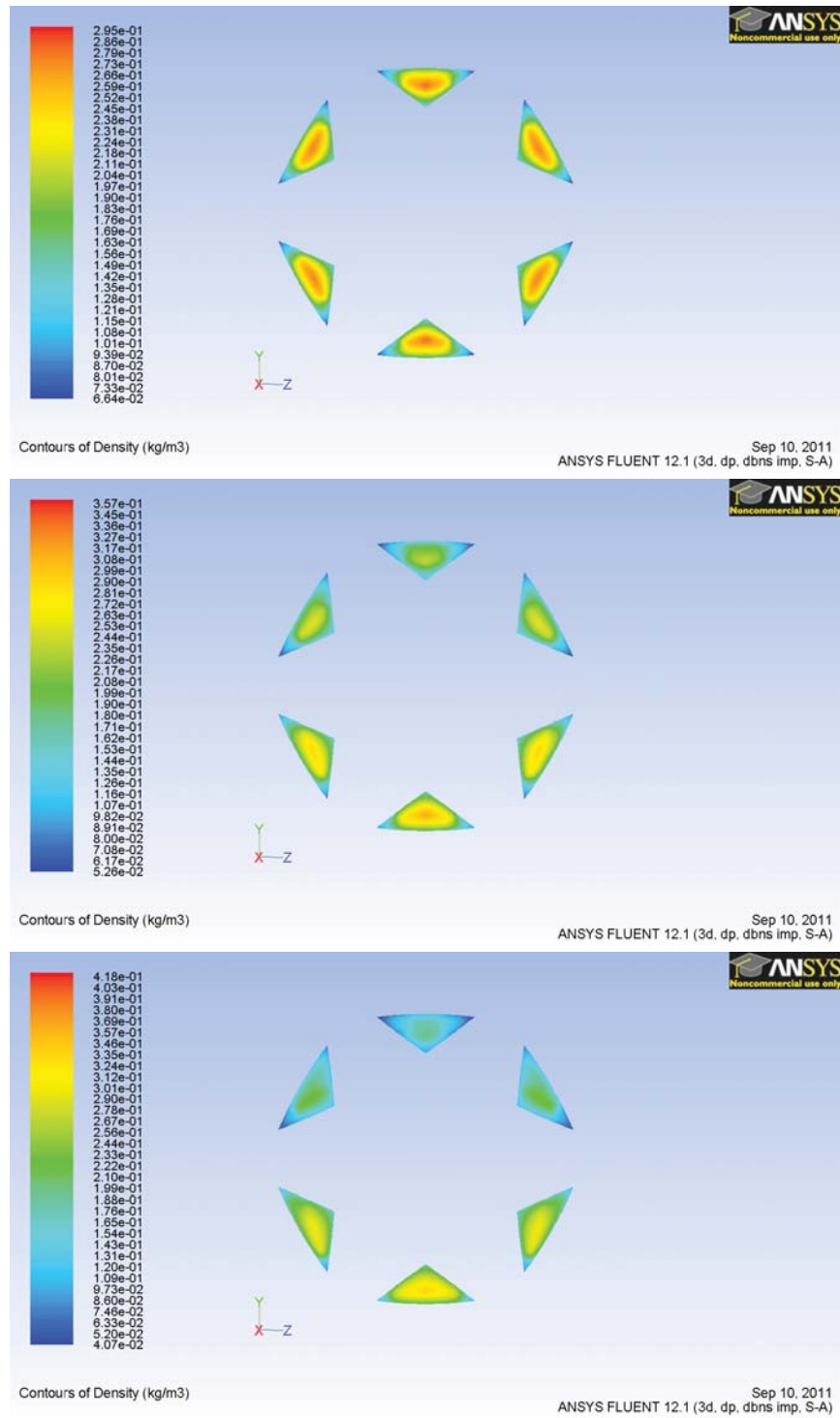


Figure 5.34: Contours of density at isolator outlet for angles of attack of 0°, 3° and 6° at Mach 5.

5.7 Summary and conclusions

Three-dimensional fully turbulent hypersonic numerical simulations were performed for the four lightcraft inlet designs outlined in Section 4. In addition to the three-dimensional

simulations, two-dimensional axi-symmetric simulations were also performed, where possible, to validate the three dimensional simulations. This was required as it was discovered that suitably refined meshes in three-dimensions contained too many cells, and the computer used could not produce results in a sufficient time frame. Comparison between the coarse three-dimensional and refined two-dimensional simulations showed that the coarser grids could capture the features of the isolator flow, however shock smearing reduced their use as a predictive tool. Some features of the flow, such as exact shock location and separation bubbles were not produced in the three-dimensional simulations however the general flow properties were reproduced to an adequate level. Based on the analysis outlined in Section 5.2, it is believed that the results obtained would only introduce an error of at most 10%, and as such can be used confidently in an inlet comparison.

6 Inlet performance evaluation

The numerical analysis of the inlet designs is performed to quantify and compare the performance at both on and off design conditions. A set of performance goals have been established to form the basis of the inlet comparison, outlined in Section 4.7. Inlet drag losses, inlet flow uniformity (density deviation), average compression (flow density), total pressure loss (compression efficiency), and total mass flow rate capture are explicitly measured for each inlet design through the numerical simulations. These results are then compared and discussed in order to establish the relative merits of each design.

Although all inlets possess the same ultimate goal, each design is significantly different. It is essential to ensure that assessment is performed in a fair and consistent manner. If this is not done, the results may not reflect the actual relative performance of the inlets. As discussed in Section 4, the inlets were designed in such a manner that fair comparison was achievable. Flight conditions simulated are identical for each inlet, with on-design performance at three different angles of attack - 0° , 3° and 6° , analysed. In addition, off-design conditions of Mach 5 were also simulated to evaluate each inlets sensitivity to lower flight speeds. Ideally the final inlet design will produce the highest density (and therefore greatest laser induced detonation wave pressure) with a uniform flow (to reduce the force moment associated with an uneven laser detonation process) at all angles of attack and flight Mach numbers, with minimal system losses. It is also essential that the final inlet design remains in a started state.

As discussed in Section 3.4, the initial pressure of the detonation wave created by the laser energy deposition is dependant on the density of the working fluid. A direct link can therefore be established between the density of the inlet flowfield and the thrust generated by the propulsion system. Higher levels of compression of the incoming flow will allow greater thrust to be generated, or less laser energy required for the same levels of thrust. To compare the inlets performance in this regard, the mass weighted average density at the isolator exit plane has been calculated. The mass weighted average density can be calculated automatically in the commercial numerical code employed. The mass-weighted average of the density is obtained by dividing the summation of the density value multiplied by the absolute value of the dot product of the facet area and momentum vectors by the summation of the absolute value of the dot product of the facet area and momentum vectors (Ansys Inc., 2009). This is expressed mathematically as

$$\frac{\int \phi \rho \left| \vec{v} \cdot d\vec{A} \right|}{\int \rho \left| \vec{v} \cdot d\vec{A} \right|} = \frac{\sum_{i=1}^n \phi_i \rho_i \left| \vec{v}_i \cdot \vec{A}_i \right|}{\sum_{i=1}^n \rho_i \left| \vec{v}_i \cdot \vec{A}_i \right|}$$

where i is the cell index, ρ the cell centred value of density, \vec{v} the momentum vector, \vec{A} the individual facet area of the cell on the surface being integrated over and ϕ the selected field variable, in this case density. The average density comparison shown in Figure 6.1 indicates that the stream traced modular inlet achieves the greatest average compression across the isolator exit. This can again be attributed to the additional compression associated with the module struts. The stream traced axi-symmetric design achieves the second highest level of compression, significantly greater than the axi-symmetric and scalloped designs. This is due to the inward turning cowl configuration, adding further compression to the flow. This is a good result, as the design achieves this high level of compression with minimal drag penalties. Another interesting result from the average density comparison is that the compression achieved does not vary significantly over the angle of attack range. This implies that (neglecting optical effects due to defocusing of the laser) the thrust will not be significantly altered during maneuvering of the craft.

The density standard deviation across the isolator exit gives an indication of the uniformity of the flow at the isolator exit for the inlet configuration. A higher deviation from the mean value signifies there is more variation across the surface, and is therefore less uniform. Flow uniformity will effect the performance of the propulsion system, with the possibility of uneven pressure distributions due to variations in density across the isolator exit. The density standard deviation is calculated by taking the root of the sum of difference between the facet value and the mean squared, divided by the total number of facets on the surface (Ansys Inc., 2009). This is expressed mathematically as

$$\sigma = \sqrt{\frac{\sum_{i=1}^n (\phi_i - \phi_{mean})^2}{n}}$$

The relative performance of the inlets is shown in Figure 6.1. The best performing design is that of the axi-symmetric geometry, which exhibits the least amount of variation from the average value. The stream traced axi-symmetric and the stream traced modular ‘scalloped’ inlet geometry also perform well, each with slightly less flow non-uniformity than the axi-symmetric design. It is also interesting to note that at increasing angle of attack, the stream traced modular ‘scalloped’ inlet geometry is the least affected indicating good off-design performance.

Although an increase in the compression achieved by the inlet design will result in greater levels a thrust generated by the propulsion system, there is a trade-off between against an increased level of drag. Any increases in thrust may be far outweighed by the increased drag due to the additional shock structure. To be able to compare the performance of the inlet designs in this regard, both the coefficient of drag and mass weighted average density normalised to coefficient of drag are shown in Figure 6.2. The coefficient of drag is calculated from the drag force of the inlet F_d , the speed of the vehicle V , the reference area A and the density of the fluid through which the craft travels. The coefficient of drag is therefore given as

$$C_d = \frac{2F_d}{\rho V^2 A}$$

The reference area in this case is taken as the plan-form area of the vehicle. The drag force is composed of a pressure component and a viscous component, and acts in the opposite direction of the velocity vector. The pressure component of drag is calculated by summing the individual force vectors on each wall cell face (Ansys Inc., 2009),

$$F_d = \sum_{i=1}^n (p - p_\infty) A \hat{n}$$

where A is the cell face area and \hat{n} is the unit direction vector normal to the cell face. The viscous component of drag is calculated by summing the viscous force over each cell face for all wall boundaries. The best performing inlet, based purely on a propulsion system efficiency, would be the inlet that has the highest density to coefficient of drag ratio. Both the axi-symmetric stream traced and axi-symmetric stream traced modular geometries perform best in this aspect, indicating they have the most efficient compression in terms of drag. It is interesting that the additional drag from the module struts does not penalise the performance of the lightcraft at the conditions simulated. The axi-symmetric inlet performs poorly due to a higher coefficient of drag. The axi-symmetric inlet has a significantly higher drag force than the other three designs, without increased compression to compensate. Another interesting aspect of the inlets performance is the relatively low variation in density to coefficient of drag ratio. Only the drag along the propulsion flowpath (excluding the nozzle) is considered, so the external drag of the vehicle body is not considered. The external drag would be more significantly affected by angles of attack, and as such more variation would be seen if external aerodynamics were included. This does indicate however (variations in thrust due to flow non-uniformity notwithstanding)

that the propulsion system flowpath will be insensitive to changes in angle of attack of the vehicle.

The next performance parameter analysed is mass flow rate normalised to vehicle drag, shown in Figure 6.3. Similar to mass weighted average density normalised to coefficient of drag, this performance parameter quantifies the efficiency of the inlet in terms of the amount of atmospheric air it can capture and effectively deliver to the propulsion system. The continuity equation can be used to calculate the mass flow rate within the system. Using the freestream density ρ_∞ and speed of the vehicle V_∞ with the effective capture area A , the mass flow rate is defined as

$$\dot{m} = \rho_\infty V_\infty A$$

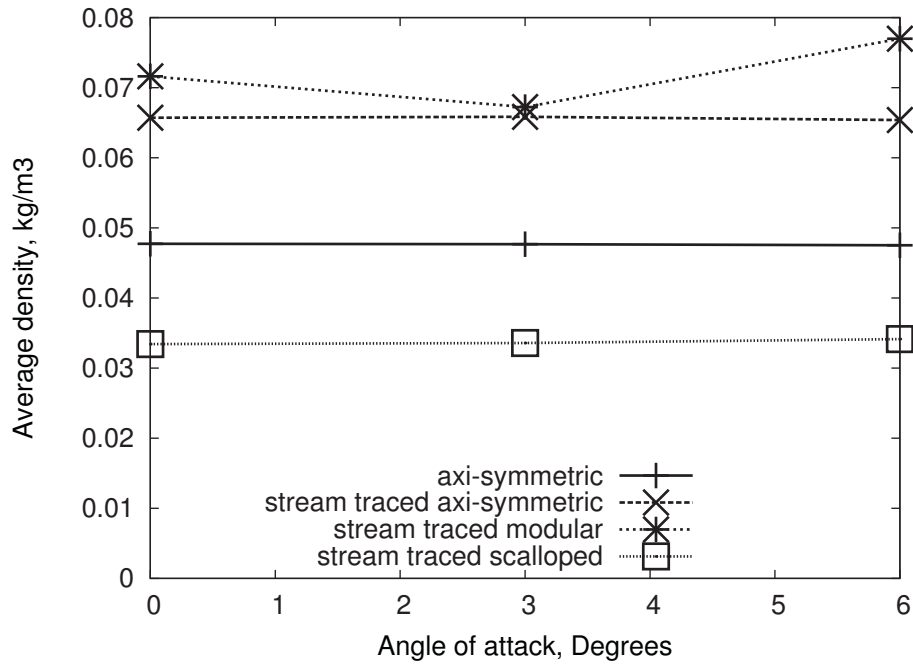
Comparison for the four inlet designs shows that at on design conditions the axisymmetric stream traced inlet performs the best, closely followed by the modular scalloped inlet design. As the angle of attack is increased, the performance of all inlets decrease due to increased flow spillage and vehicle drag. There is a crossover point in the angle of attack range that results in the scalloped inlet design performing better than the axisymmetric stream traced design, however no reason as to why this occurs is offered. The stream-traced modular inlet design is the worst performing at all angle of attack values, possible due to the increased pressure drag associated with the module strut shock waves.

The total pressure efficiency of the lightcraft inlet designs also present interesting insights into the performance of the vehicles. Total pressure efficiency is an often used performance measure for traditionally fueled high speed inlets (Heiser *et al.* , 1994), and gives an indication of the flow properties that can be recovered - i.e. not lost to irreversible processes. The total pressure efficiency of the vehicle is calculated by dividing the mass weighted average total pressure at the isolator exit by the free stream total pressure. This is expressed as

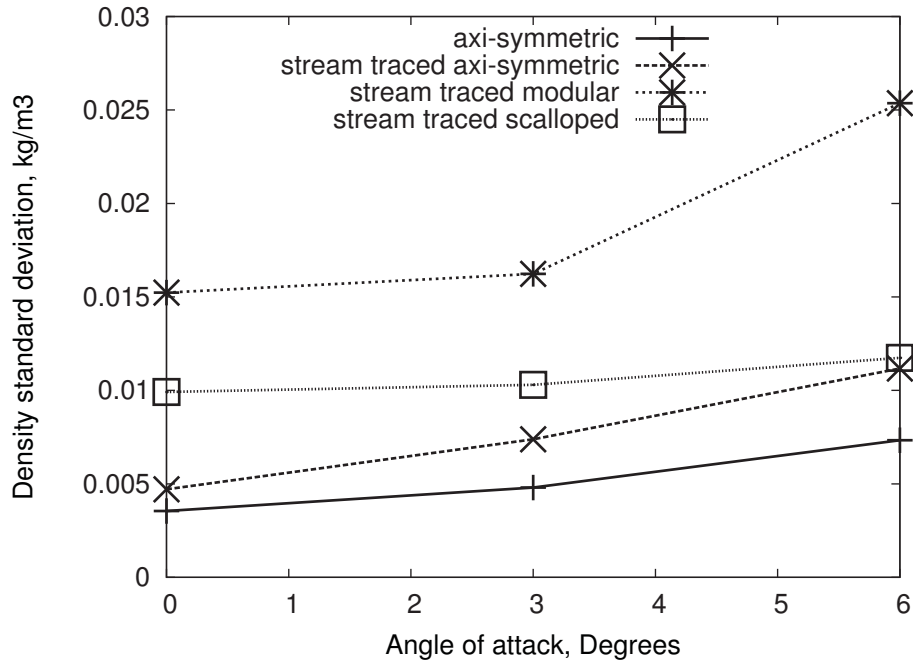
$$P_{T_{eff}} = \frac{P_{T_{isolator}}}{P_{T_\infty}}$$

Although it is not believed to be of great importance to the lightcraft performance due to the nature of the propulsion system, total pressure efficiency is included in this analysis as it is an important parameter for conventionally fueled scramjet inlets and can be seen in Figure 6.3. These design techniques are applicable to scramjet inlets, and will therefore be of interest not just to lightcraft designers. The three-dimensional stream traced modular

‘scalloped’ inlet design clearly possesses the greatest total pressure efficiency of the inlet designs. This is in agreement with previous literature, where the inlet design is noted for its pressure recovery performance (Molder & Szpiro, 1966), but is helped in-part by the fact that the inlet is operating at a lower compression ratio. Both the stream traced axisymmetric and stream traced modular inlet designs have similar total pressure efficiencies. This indicates that the total pressure efficiency of the inlet design is not highly sensitive to the secondary shock structure caused by the module struts.

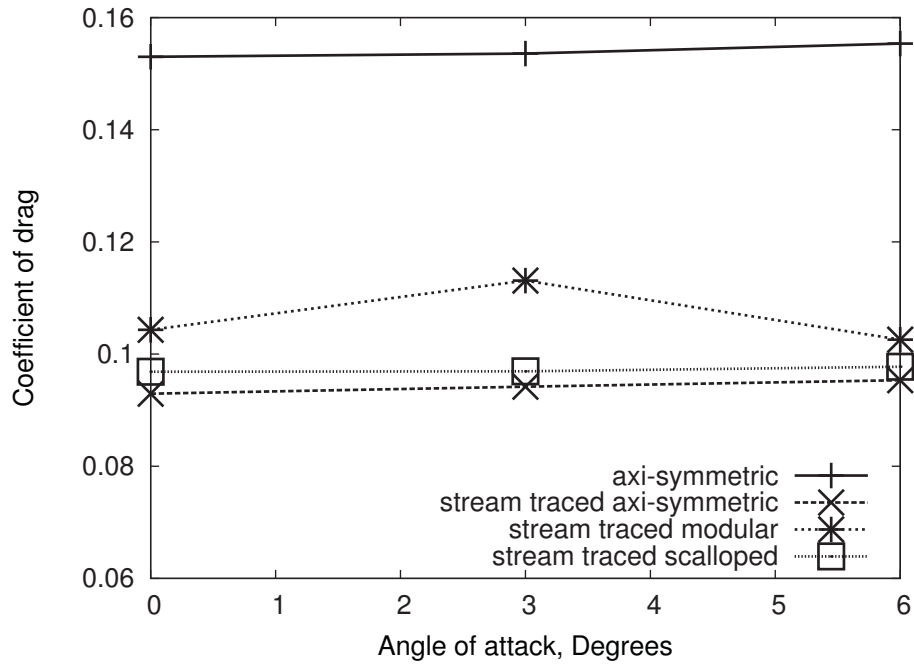


(a) Average density at isolator exit

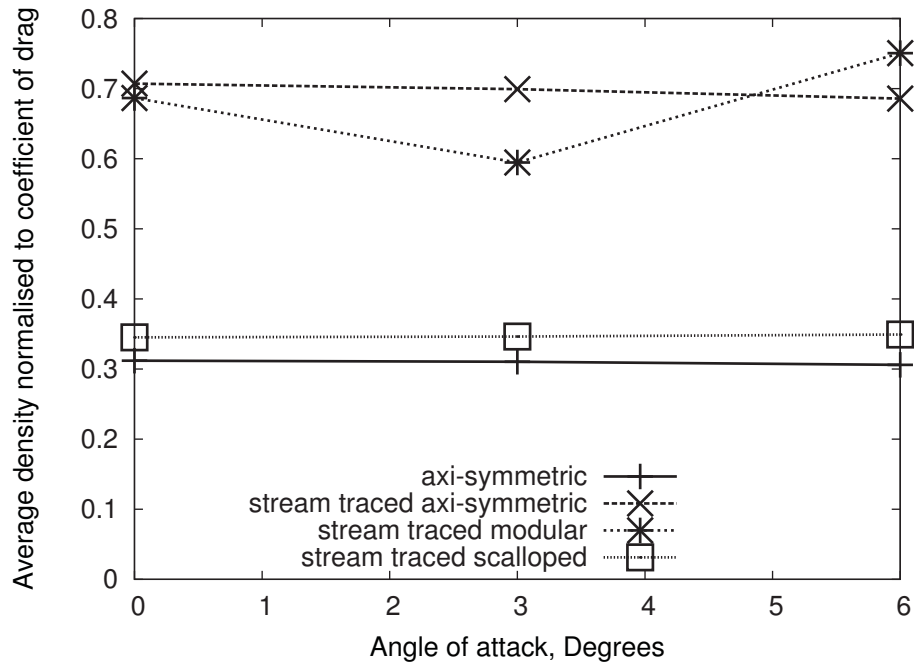


(b) Density standard deviation at isolator exit

Figure 6.1: Inlet performance comparison, Mach 8 flight conditions.

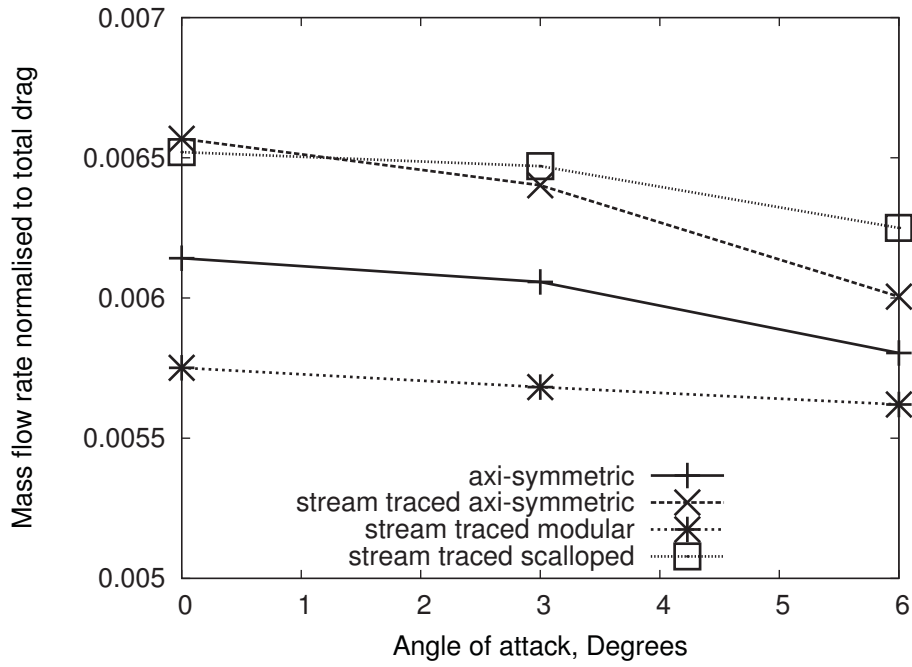


(a) Coefficient of drag

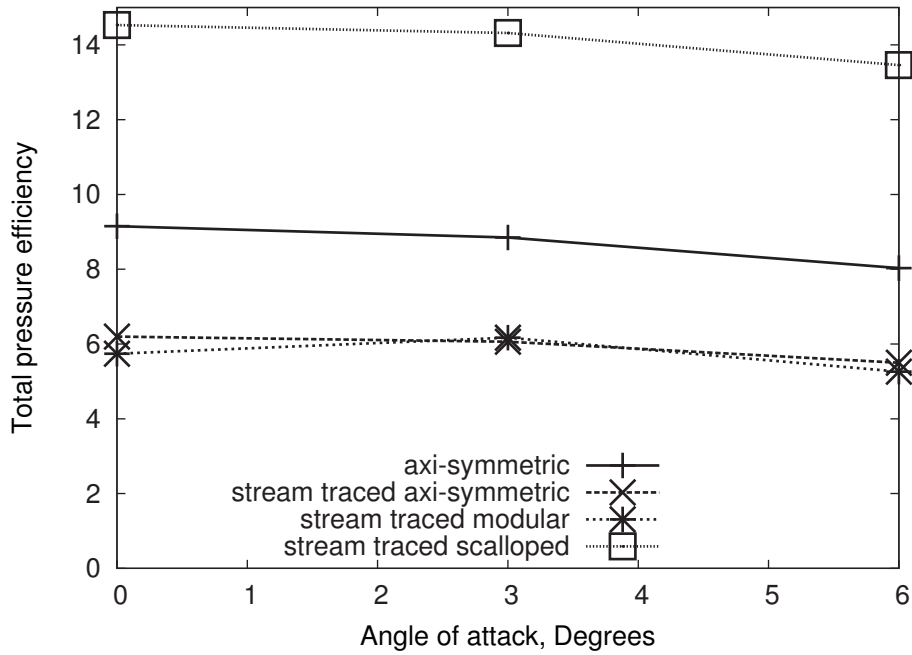


(b) Mass weighted average density normalised to coefficient of drag

Figure 6.2: Inlet performance comparison, Mach 8 flight conditions.



(a) Inlet mass flow rate capture, normalised to total inlet drag

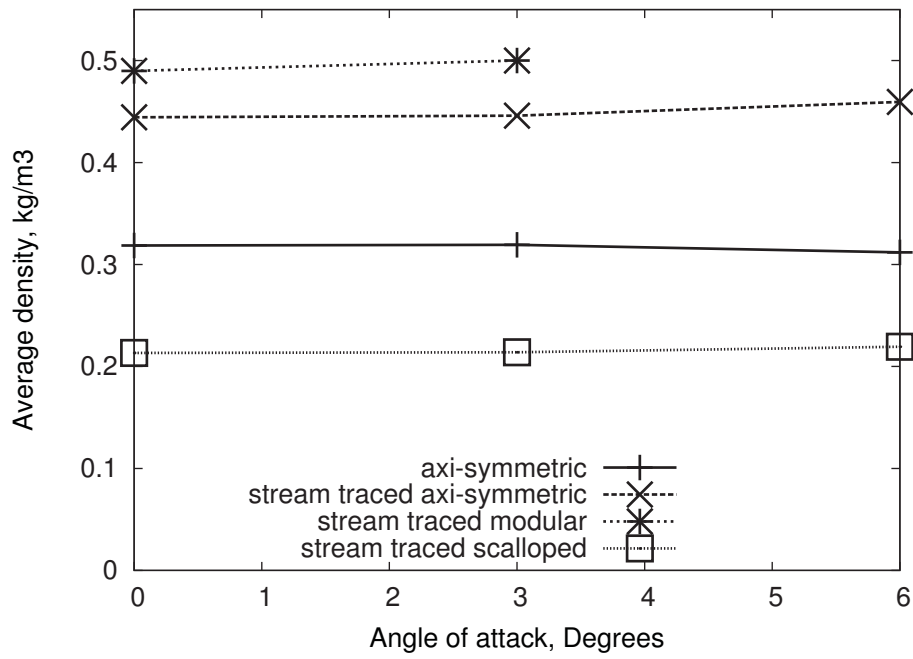


(b) Inlet total pressure efficiency

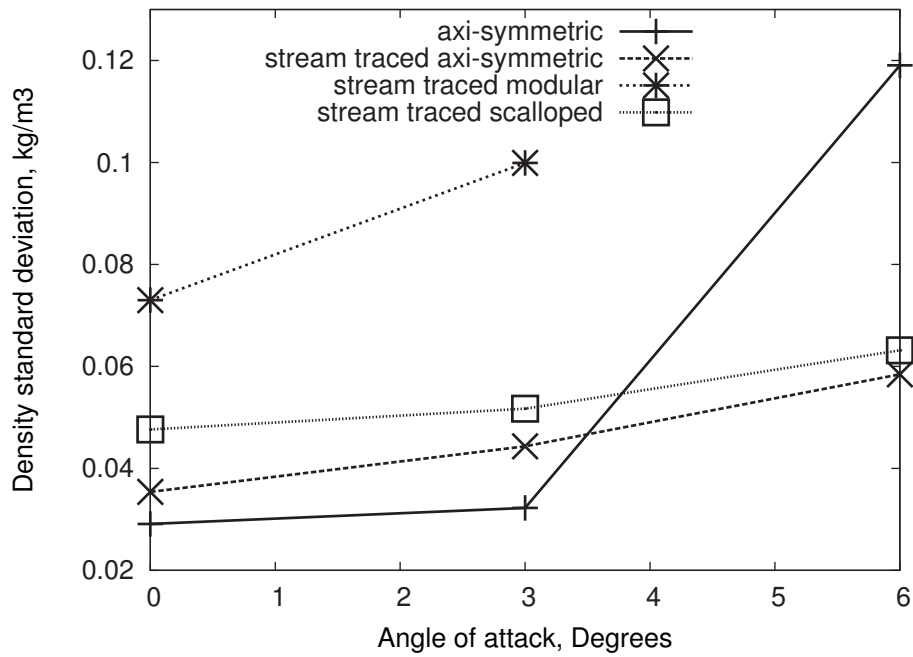
Figure 6.3: Inlet performance comparison, Mach 8 flight conditions.

The Mach 5 performance analysis is shown in Figures 6.4, 6.5 and 6.6. Values for the axi-symmetric stream traced modular design at a 6° angle of attack have not been included due to inlet unstart. The results show similar trends to the Mach 8 results, with a few anomalies worth mentioning. The first is the performance of the stream traced axi-symmetric design at Mach 5, it appears to perform much better in terms of mass

flow rate normalised to vehicle drag at the Mach 5 conditions relative to the other inlet designs. The second anomaly is the performance of the axi-symmetric inlet design at 6° angle of attack. The flow field uniformity appears to be severely reduced at the higher angle of attack. The cause for this is the strengthening of the oblique shock within the isolator (see Figure 5.10), which significantly increases the difference in compression between the leeward and windward sides of the vehicle. The discontinuity acts to form a distinct demarcation of density regions on the isolator exit. It is interesting that the other inlet designs (in particular the axi-symmetric stream traced inlet, which is not of module configuration) do not exhibit this behaviour.

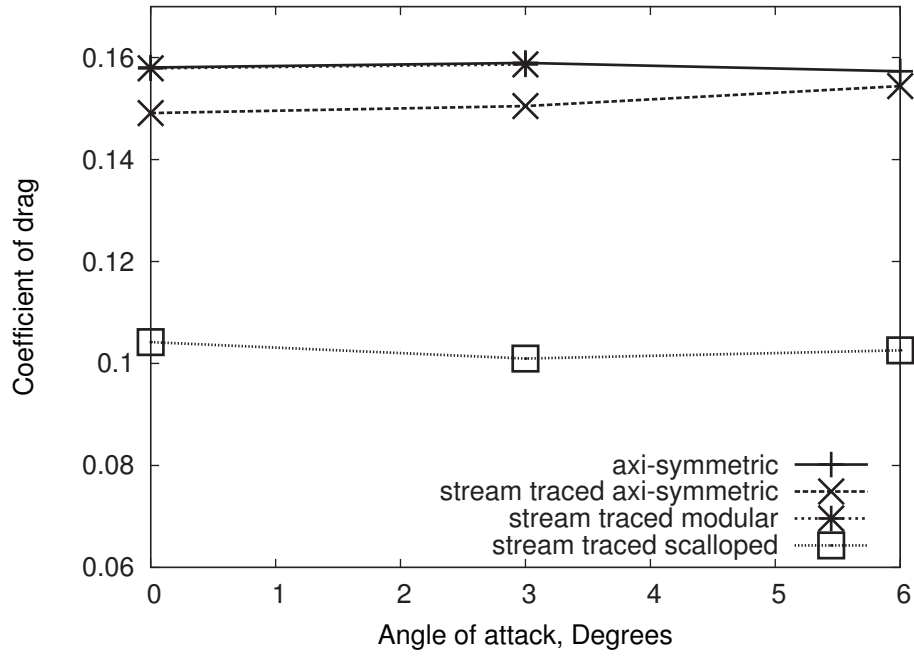


(a) Average density at isolator exit

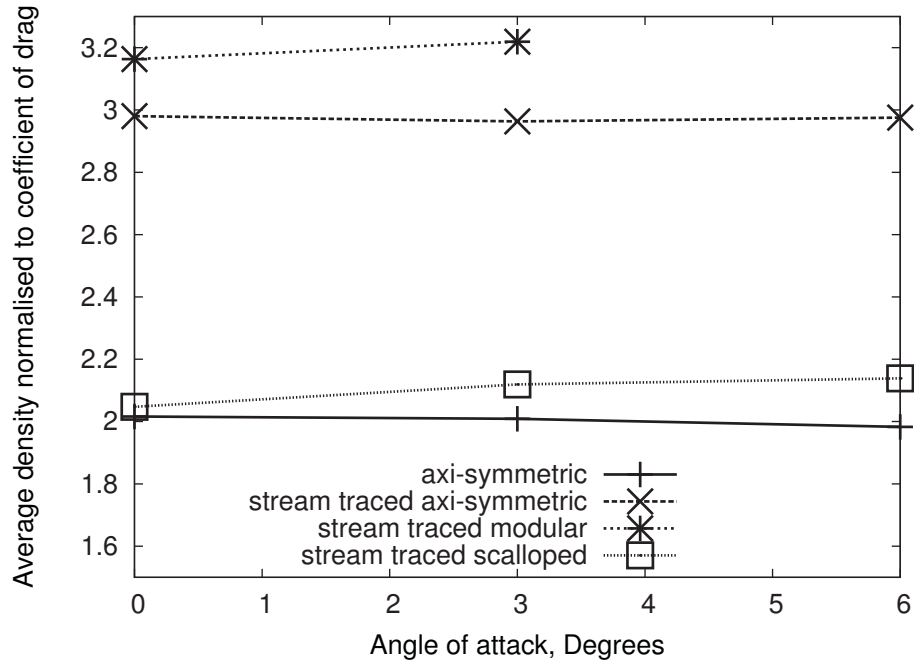


(b) Density standard deviation at isolator exit

Figure 6.4: Inlet performance comparison, Mach 5 flight conditions.

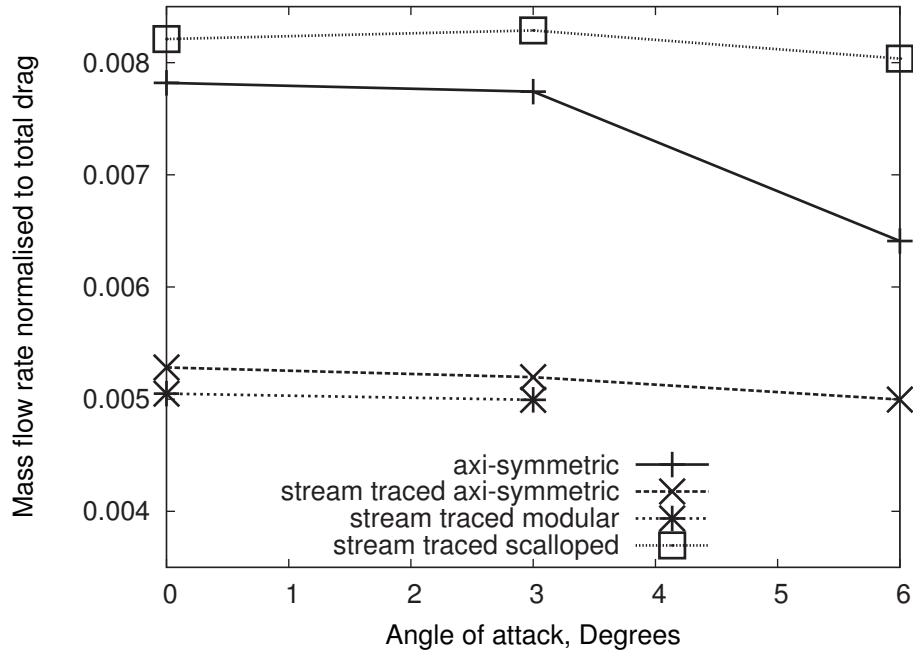


(a) Coefficient of drag

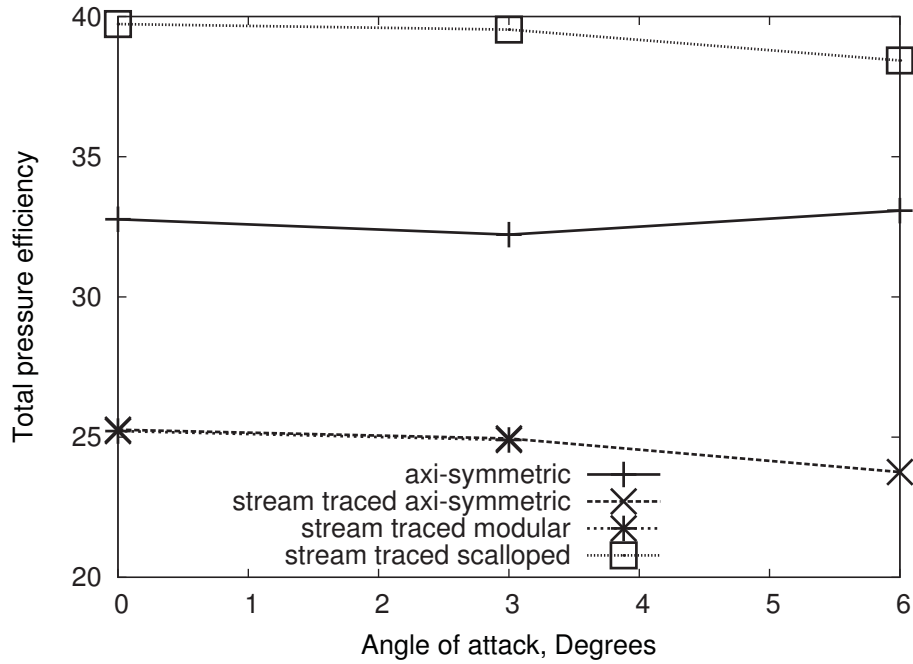


(b) Mass weighted average density normalised to coefficient of drag

Figure 6.5: Inlet performance comparison, Mach 5 flight conditions.



(a) Inlet mass flow rate capture, normalised to total inlet drag



(b) Inlet total pressure efficiency

Figure 6.6: Inlet performance comparison, Mach 5 flight conditions.

6.1 Summary and conclusions

For the performance analysis, it appears that there is not one inlet design that is superior, each design performs well in different areas. This necessitates the need for a holistic approach to the lightcraft design. In consideration of the laser powered propulsion sys-

tem, the axi-symmetric stream traced and the axi-symmetric stream traced modular inlet designs are the best options. They both perform well in regards to achieving high levels of compression at both flight conditions, without adversely high levels of drag. The inlet designs also exhibit comparable flow uniformity, with the modular design suffering somewhat from the strut induced shocks. The modular design does unstart at Mach 5 and an angle of attack of 6° , however this does not necessarily preclude it from selection. The trajectory could be modelled such that this extreme flight condition is avoided, or the strut configuration could be altered to reduce the influence on the inlet flow field.

It is a positive finding that a range of different inlet configurations are possible, giving flexibility and a wider scope to the vehicle designer. Not only do different aerodynamic considerations create considerable differences in performance, each inlet design has drawbacks and benefits, not only limited to the performance of the laser propulsion system. Size, weight, maneuverability, structural performance, payload capacity, cost and external aerodynamic performance are just small selection of the additional considerations required in the inlet selection process. Flexibility is an invaluable attribute in such a constricted design space.

7 Additional inlet numerical investigations

In addition to the numerical investigations performed in Section 5, a number of subsequent simulations were performed to check the validity of the design for the lightcraft application. This section outlines these ancillary investigations, and describes the methodology employed.

7.1 Laser induced detonation wave simulation

Although the primary focus of this research is concerned with the design of the hypersonic inlet, the lightcraft concept is highly complex - an integrated approach to all facets is required. One cannot simply design a single component of the vehicle independently of all the others and expect success. The purpose of the hypersonic inlet is to deliver air to the laser detonation process at optimal conditions; the performance of this process is determined by the quality of the inlet design. However the performance of hypersonic inlet is highly dependent on the laser detonation process - the two facets of the lightcraft vehicle are intrinsically linked and must be considered as a whole.

The major concern with the laser detonation process is the effect that the resulting detonation wave structure and propagation will have on the incoming compressed air flow. There is a risk of the detonation wave propagating back through the isolator and disrupting the sensitive hypersonic inlet flow field. This will in turn restrict the refreshment of the air being provided to the laser detonation process. It is essential to ensure that the design of the inlet is robust enough to adequately refresh the isolator after each laser pulse cycle. Figure 7.1 from Salvador (2010) illustrates the effect that the laser induced detonation wave has on the inlet flowfield, with the inlet becoming unstated due to the expanding detonation wave. In these experiments the laser deposition energy was significantly lower than those required for hypersonic flight, and it can be reasonably expected at proper flight laser powers the effects of the detonation wave on the inlet flow field will be much more significant.

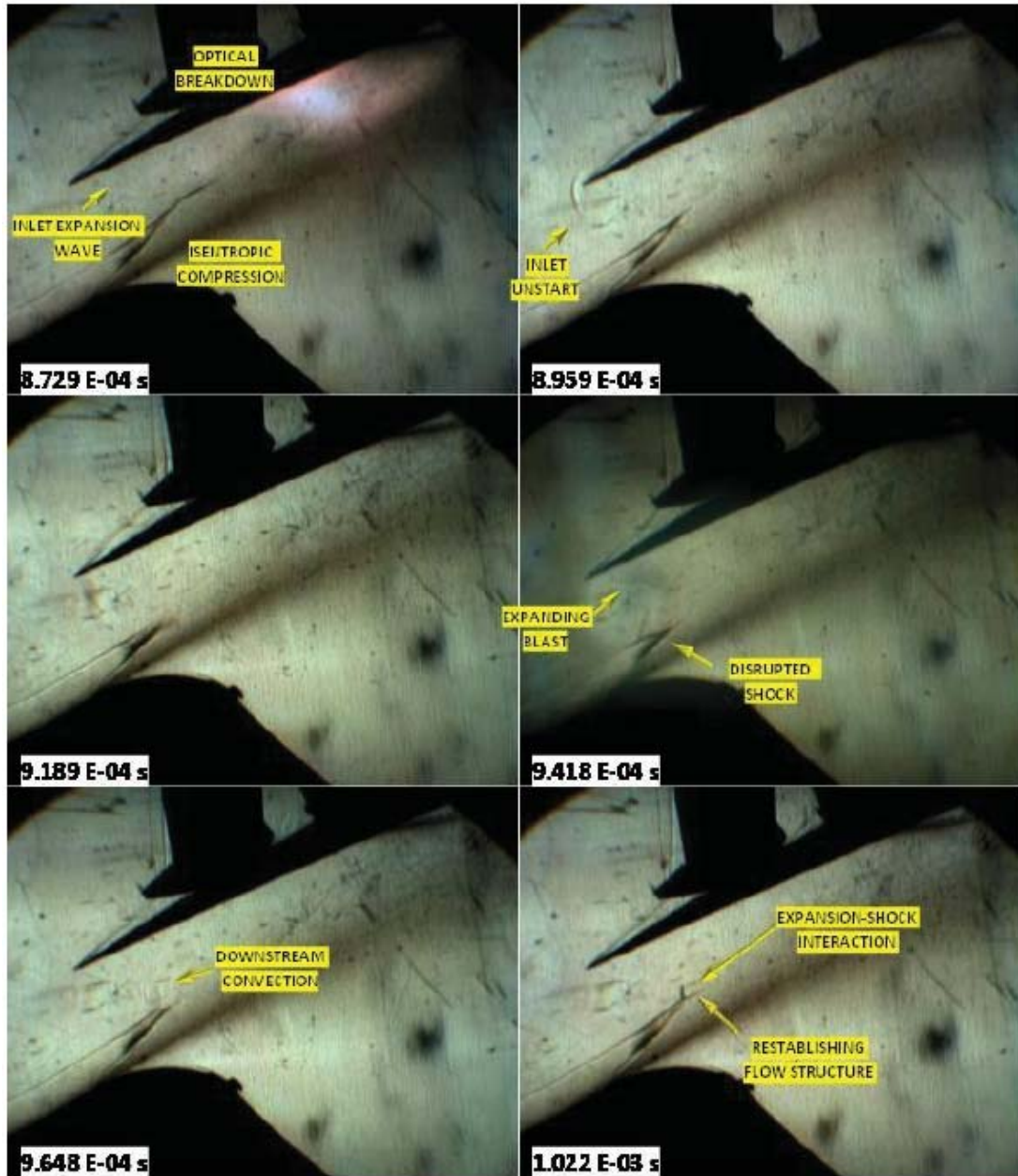


Figure 7.1: LTD inlet geometry at $M=9.43$ with laser induced breakdown (Salvador, 2010)

To investigate the inlet sensitivity to the laser detonation process, an idealised numerical model of the laser induced detonation wave present in the lightcraft has been produced. This model does not take into account real gas effects such as the dissociation, ionisation and recombination of the resulting plasma generation - rather a simple two dimensional model of the high pressure laser induced detonation wave is applied to the specific lightcraft geometry. Experimental evidence has shown that the time scale of plasma formation is of an order of magnitude less than that of the detonation wave formation (Ghosh & Mahesh, 2008), for this reason it is deemed acceptable to assume the

plasma is formed instantaneously and therefore has little to no effect on the surrounding fluid. Based on the work outlined by Feikema (2000) in Section 2.2, the initial properties of the blast wave created by each laser pulse cycle can be determined. These values are then patched into a region of cells in a CFD simulation representing the initial state of the laser induced detonation wave. A two-dimensional axi-symmetric turbulent transient simulation was performed to record the time dependent flow history of the detonation wave.

Parameter	Value
Initial diameter of laser induced plasma	5mm
Pressure	1,364,000Pa
Velocity	10,320m/s
Temperature	18,000K

Table 7.1: Laser induced detonation wave initial conditions

A two-dimensional axi-symmetric turbulent transient simulation was performed in the computational fluid dynamics code Fluent to record the time dependent flow history. The initial flow field shown in Figure 7.2 was employed to represent the initial conditions present during cruise flight conditions at zero degrees angle of attack, Mach number of 8 and no laser induced detonation. The values listed in Table 7.1 were then patched into a cell zone of diameter 5mm representing the completely cylindrically evolved laser induced detonation wave.

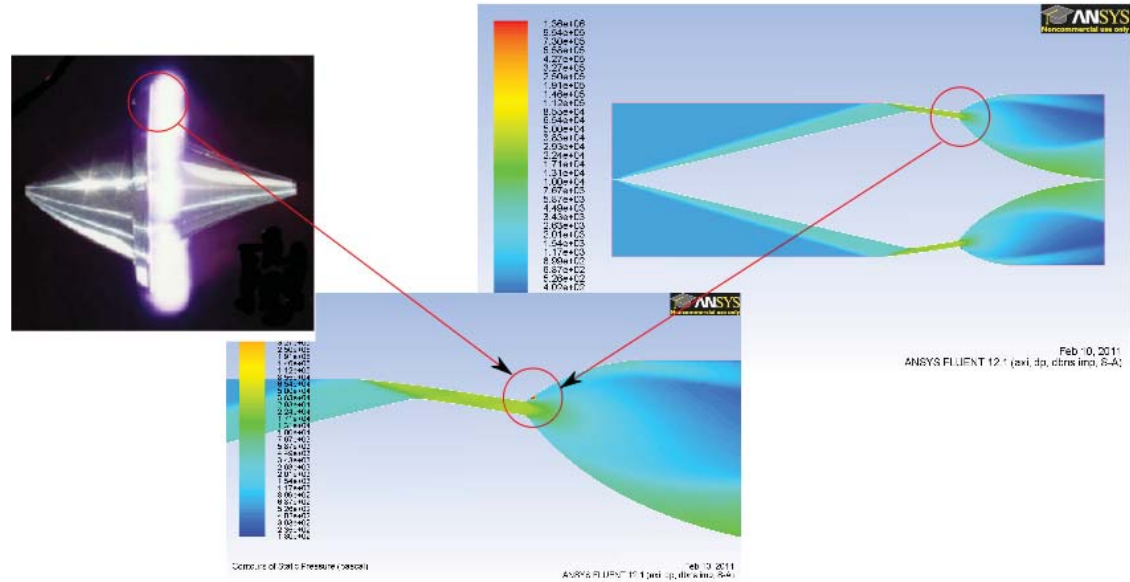


Figure 7.2: Laser induced detonation wave simulation initial setup.

Figure 7.3 shows the transient progression of the detonation wave as it expands and

relaxes over the lightcraft afterbody. The detonation wave front can be seen to expand over the lightcraft afterbody as the solution progresses. The high pressure region due to the laser induced detonation wave can also be seen to move up into the inlet isolator, where it remains for a period of time until it is exhausted by the inlet flow. The detonation wave must remain in the isolator for a period less than the laser pulse cycle, as it presents a blockage to the incoming air flow. The working gas is required to be refreshed for successive pulses in order for the maximum thrust to be achieved. This is a significant issue for the laser induced detonation process design, as the efficiency and performance will be decreased.

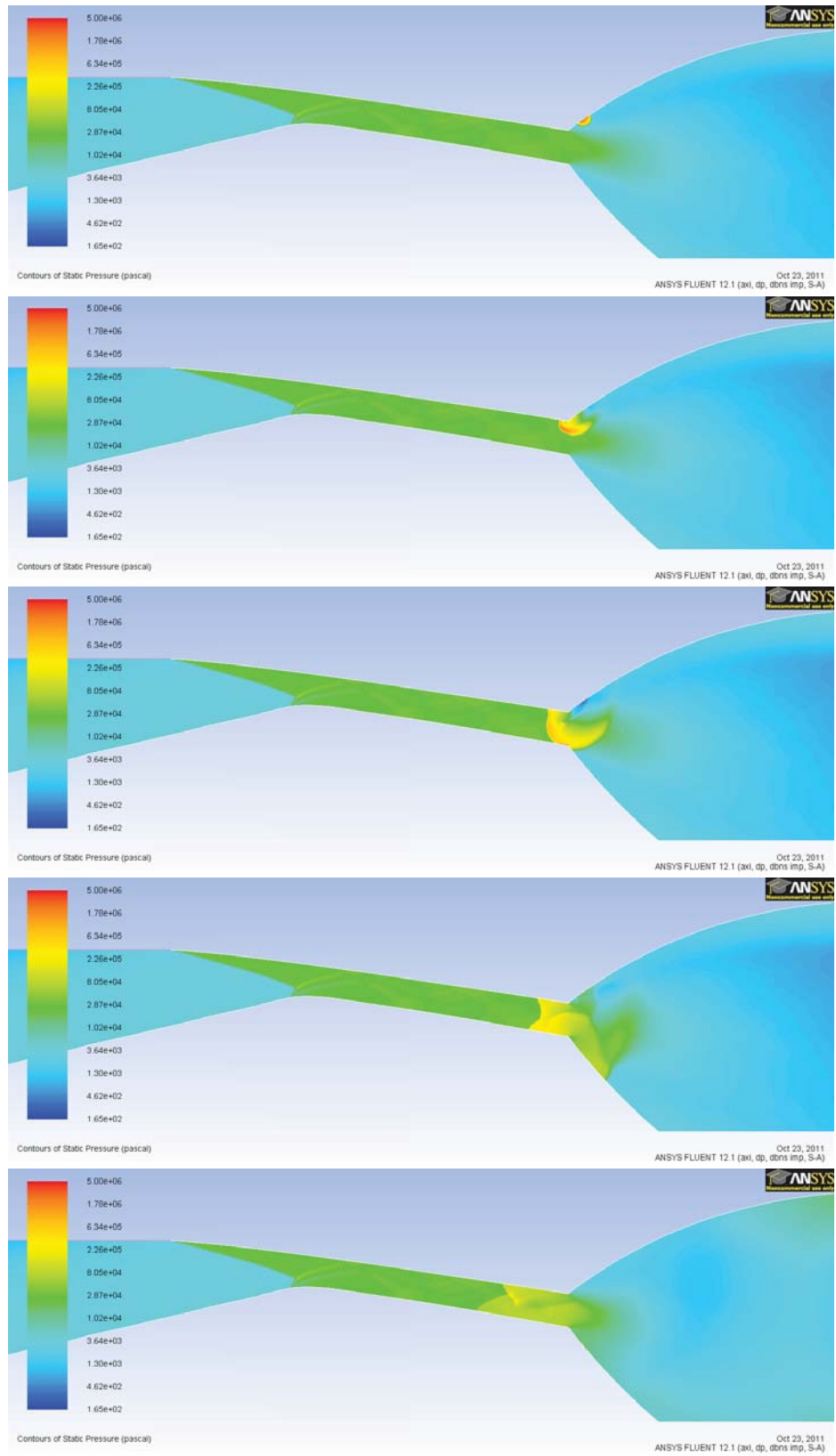


Figure 7.3: Contours of pressure for detonation wave evolution.

The blockage the laser induced detonation wave creates is further illustrated in Figure 7.4. The contours show the normal wave where the flow is decelerated to subsonic speeds,

before being expanded at the nozzle.

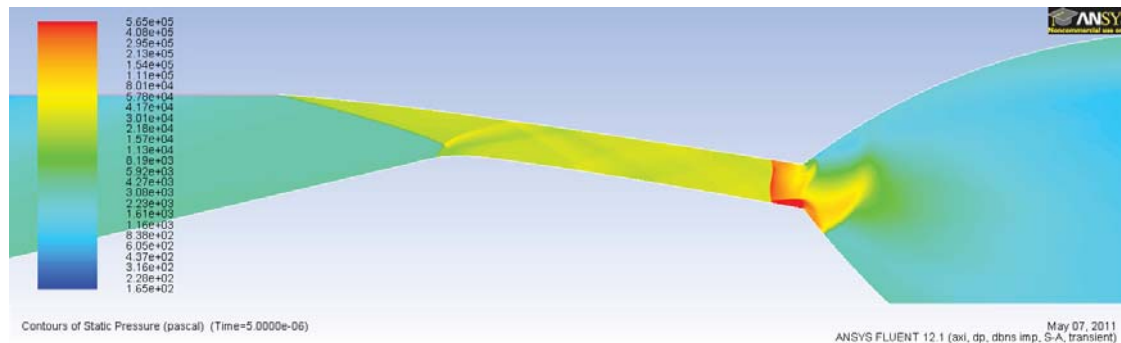


Figure 7.4: Inlet isolator normal wave.

From these numerical simulations it can be seen that the hypersonic inlets successfully restart between laser pulses. It is imperative this occurs, otherwise the inlet flow field will not be re-established between pulses. The laser induced detonation simulations also provide a upper limit on the laser pulse frequency, given by the time taken for the flow field to re-establish after a laser induced detonation. The laser induced detonation simulations indicate that the stream traced inlet design is able to refresh in the order of 1.5×10^{-4} seconds.

7.2 Gun tunnel model

To experimentally verify the numerical results obtained in this thesis, a scale model is to be produced and tested within the University of Southern Queensland hypersonic gun tunnel (Jacobs, n.d.). A simplistic explanation of gun tunnel operation is the model is separated from a region of high gas pressure in the test area by a diaphragm. When the high pressure region reaches a certain pre-specified pressure, the diaphragm ruptures. The expansion of the gas into the gun tunnel chamber creates a normal shock wave, with the experimental test conditions that the specimen is subjected to behind this shock. The normal shock passes over the model, with the test flow closely behind. This experimental work is external to this thesis, however supporting simulations have been performed to allow direct comparison between the experimental model and the numerical simulations. A simulation mirroring the normal shock wave the model is subjected to within the gun tunnel has been produced to ensure the inlet will start in the gun tunnel conditions. In order for the inlet to start and the test to be successful, it must swallow the initial normal shock. In addition to ensuring inlet start does occur, simulations at 0° , 3° and 6° angle of attack have been performed to provide pressure plots along the axis of symmetry.

7.2.1 Test specimen geometry

The geometry of the test specimen is based on the stream traced axi-symmetric modular inlet design, as shown in Figure 7.5. This design was chosen due to its relatively novel design and ease of manufacture. There are also many interesting flow phenomena present within the isolator due to the module struts. As it is the inlet with the most complicated flow structure, it is believed to provide the most robust verification of the numerical results.

Six modular stream traced inlets are spaced annually around the centre body of the lightcraft, which deposit the compressed gas at the source of the laser induced detonation wave. This detonation wave is then expanded across the axi-symmetric parabolic after body. Figure 7.6 is an image of the lightcraft with the cowl outer surface removed illustrating the modular arrangement of the inlets. Each module is separated by a strut that holds the upper surface of the engine cowl in place. Each individual module spans 58° , with the remaining 2° being the module strut.

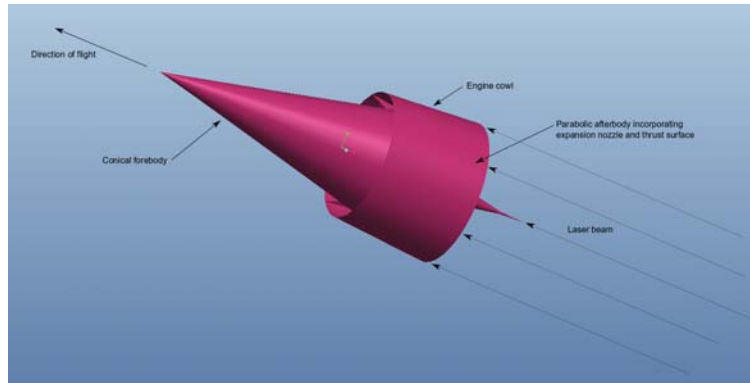


Figure 7.5: CAD representation of lightcraft configuration

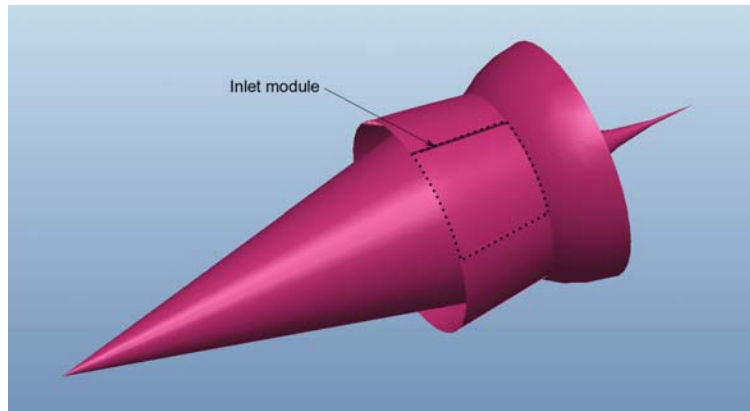


Figure 7.6: CAD representation of inlet geometry with outer surface of cowl removed

The geometry used for the test specimen is required to be altered slightly from the final design developed in this research. This is done in order to accommodate different gas conditions present in the gun tunnel experiment and the available test specimen space. It was found that by simply scaling down the final design to fit in the tunnel dimensions (a scale of 1:0.4762), problems arose with the inlet being unable to self-start. The conical forebody was therefore further modified to allow for the increased boundary layer height expected to be present in these gun tunnel experiments. This additional viscous correction results in the original inviscid 14.03° half angle of the conical forebody altered to 12.3° . Figure 7.7 illustrate the test specimen geometry in a technical drawing format.

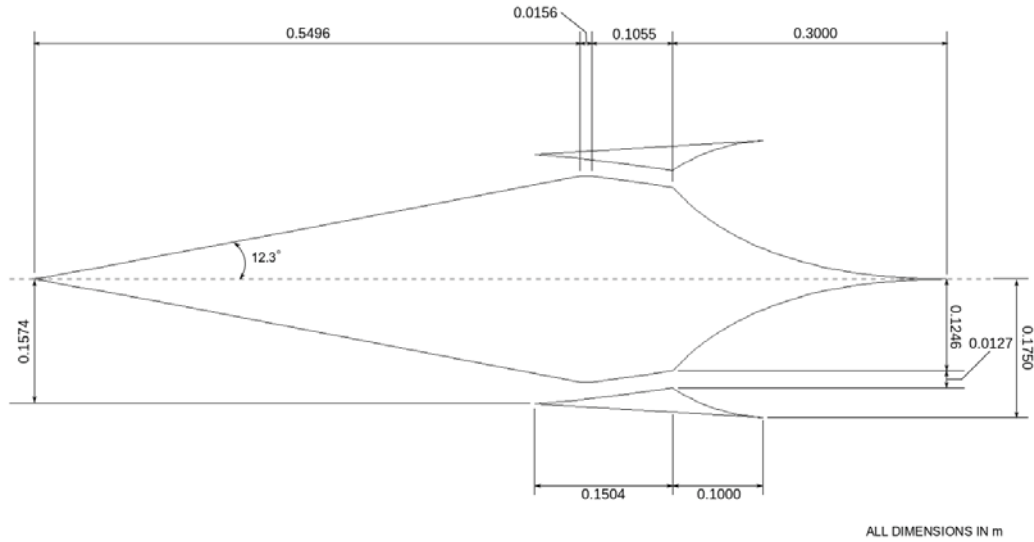


Figure 7.7: Lightcraft geometry section through inlet

It is desired to locate pressure transducers along the lightcraft body to verify the numerical simulations. The pressure transducers shall be located along the centre line of each individual module on the left hand side of the lightcraft (facing towards). It is not required to locate pressure sensors on the two modules on the right hand side due to the symmetry of the problem. The vehicle can be rotated if pressure readings are desired from the off-axis modules. The spacing in the longitudinal direction will be determined by the transducers and spatial availability.

7.2.2 Inlet gun tunnel start verification

A two-dimensional, axi-symmetric transient simulation with full viscous effects was performed to simulate the model in the gun tunnel. This was done to ensure inlet self-start was possible, and the expected steady state flow field was established within the limits of

the gun tunnel test times.

The simulation was performed using a two-dimensional mesh with appropriate boundary conditions, shown in Figure 5.1. The conditions for the free stream boundaries are listed in Table 7.2. The lightcraft body was modelled using an adiabatic wall boundary condition, with no slip shear properties.

Property	Value
Gauge pressure (Pa)	661
Mach number	5.8
Axial-component of flow	1
Radial-component of flow	0
Modified turbulent viscosity (m2/s)	1e-07
Temperature (K)	61

Table 7.2: Pressure far field boundary conditions

Due to the limitations of the CFD code fluent, it was not possible to initialise the solution at the specific initial gun tunnel conditions. Using a far field boundary condition would allow the leakage of high pressure gas into the flow field perpendicular to the incoming flow. This could be avoided by simulating the whole vehicle inside the experimental test area, however this was not done to reduce the computational grid size. The initial conditions shown in Table 7.3 were employed.

Property	Value
Gauge pressure (Pa)	661
Axial velocity (m/s)	0
Radial velocity (m/s)	0
Modified turbulent viscosity (m2/s)	1e-07
Temperature (K)	61

Table 7.3: Transient gun tunnel simulation initial conditions

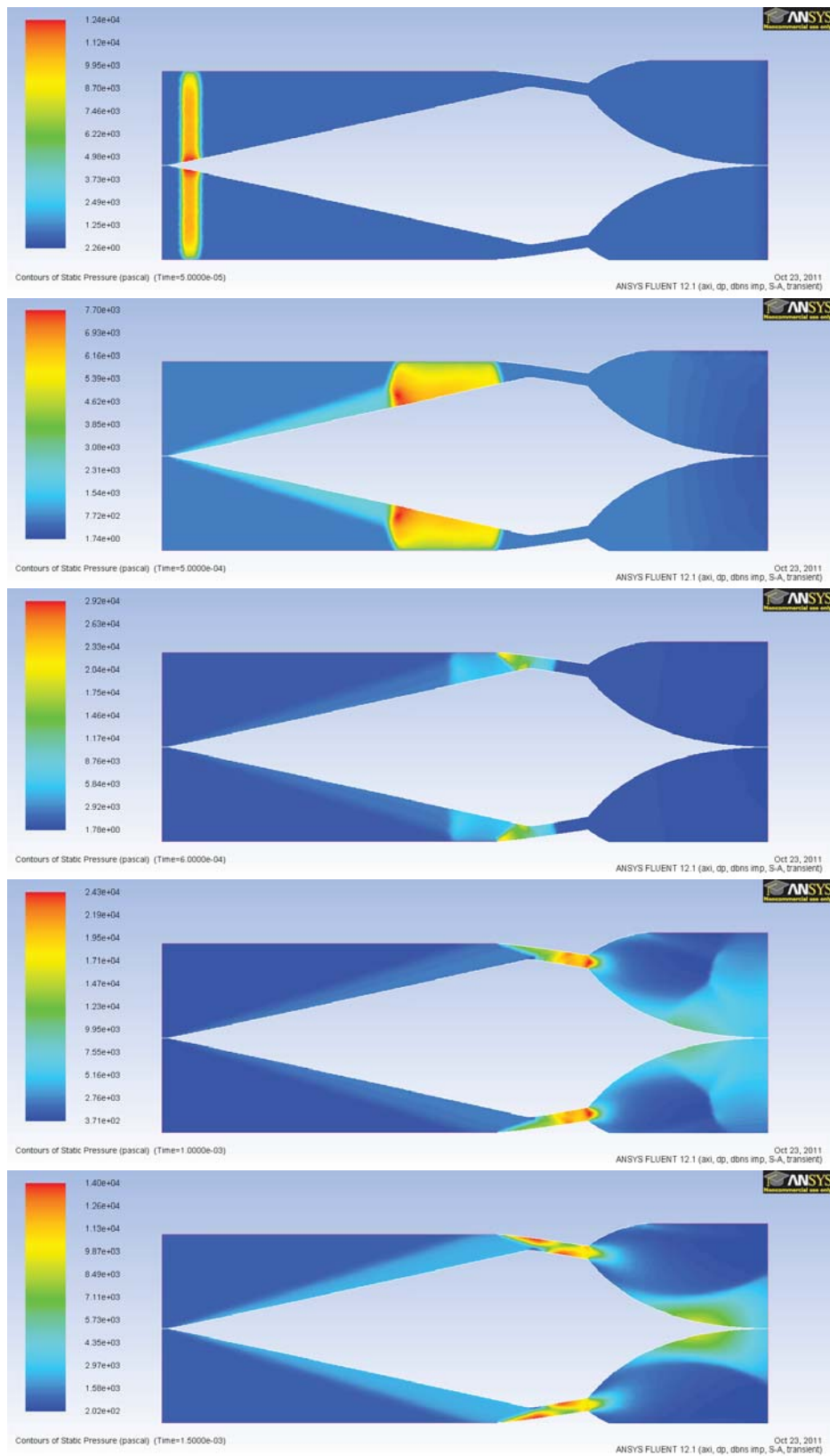


Figure 7.8: Transient gun tunnel simulation, contours of density

The evolution of the simulation solution is shown in Figure 7.8. The images progress from left to right, top to bottom. The initial images show the normal shock wave approach-

ing the cowl, then being swallowed into the isolator and expelled out of the expansion nozzle. The final image shows the established flow field in the inlet. A reasonable degree of flow non-uniformity is present in the lightcraft flow field, which can be attributed to the necessary geometry modifications employed to ensure inlet is self-starting. It should be noted that the inlet is designed for the lightcraft flight conditions, and is therefore operating significantly off-design. This is a promising finding for the final inlet design.

Property	Flight design condition	Gun tunnel condition
Gauge pressure (Pa)	575	661
Mach number	8	5.8
Temperature (K)	237	61
Density (kg/m ³)	8.45e-03	7.31e-03
Viscosity (kg/m-s)	1.53e-05	3.9875e-06

Table 7.4: Comparison on inlet design conditions in flight and gun tunnel

7.2.3 Inlet angle of attack simulations

Both two-dimensional axi-symmetric and three-dimensional steady state simulations with full viscous effects have been performed for the test specimen geometry at angles of attack of 0°, 3° and 6°. These show the expected inlet flow field at the range of flight angles of attack expected to be experienced in a typical launch. Figures 7.9, 7.10 and 7.11 show an x-y plot of surface pressure plot along the line of pressure transducer location for comparison to experimental results.

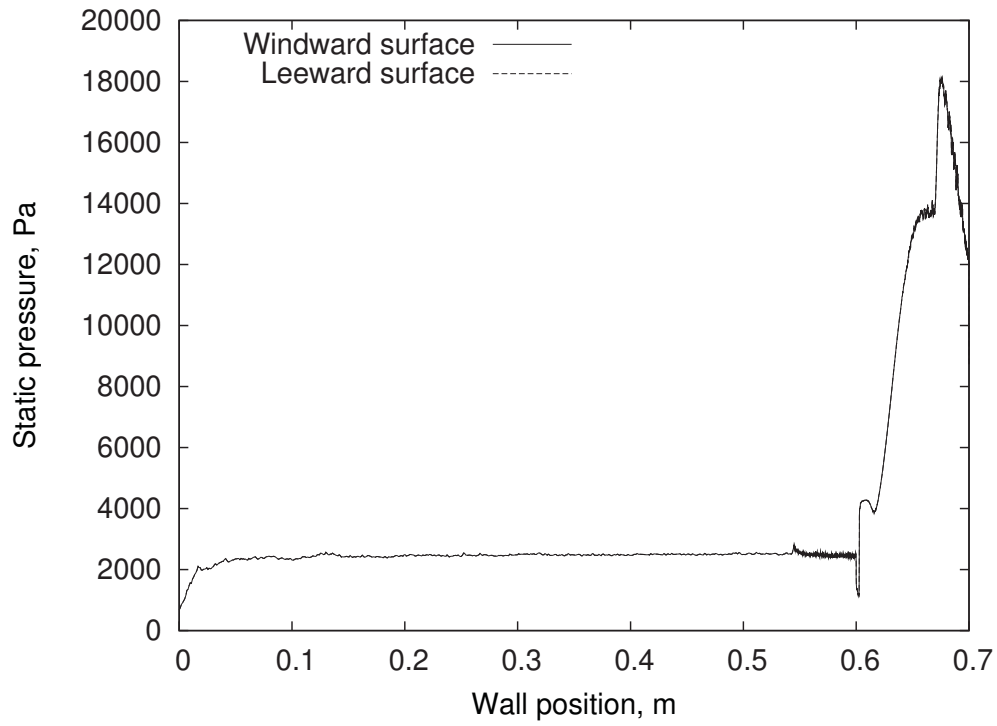


Figure 7.9: Static pressure values along pressure transducer locations of 0° and 180° for a lightcraft angle of attack of 0°

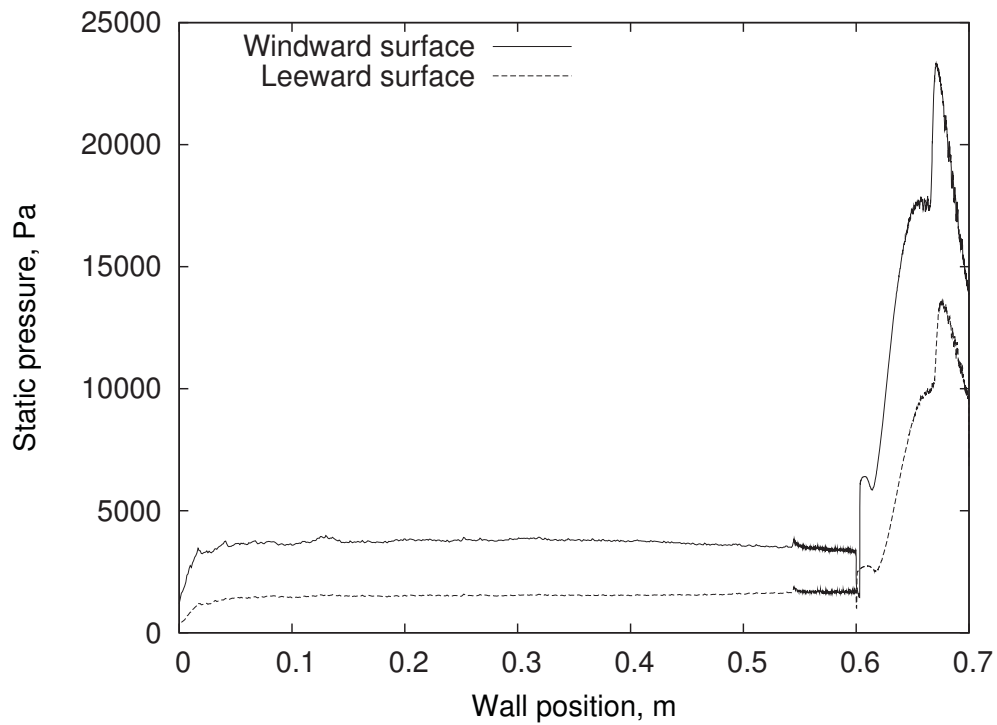


Figure 7.10: Static pressure values along pressure transducer locations of 0° and 180° for a lightcraft angle of attack of 3°

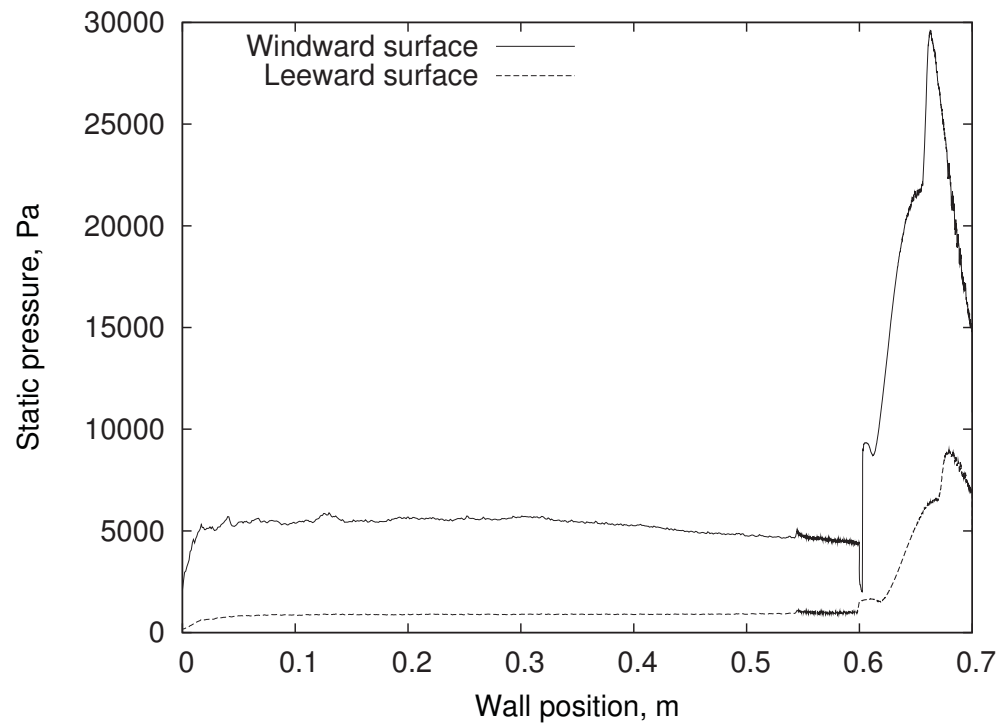


Figure 7.11: Static pressure values along pressure transducer locations of 0° and 180° for a lightcraft angle of attack of 6°

8 Conclusions and future work

8.1 Conclusions

In the quest to achieve the launch of an airbreathing laser powered propulsion system into lower earth orbit, a vehicle inlet is required that will provide sufficient air flow at hypersonic speeds. Current lightcraft concepts have not considered the performance of the vehicle at such high speeds - only recently have hypersonic laser induced detonation experiments been conducted on the configuration at speeds in excess of Mach 1 (Salvador, 2010). The sensitivity of the flow dynamics in the supersonic and hypersonic flow regimes render traditional inlet designs incapable of providing adequate flow conditions to the propulsion system. Poor performance relating from complex shock structure and high drag, even significantly reduced inlet flow due to unstart, can severely compromise the performance of the propulsion system.

Four hypersonic inlet designs were produced at design conditions established from a equations of motion trajectory analysis. Realistic flight conditions that the vehicle experiences during its air breathing ascent were determined. These were then used to form the baseline conditions to which the inlets were designed. A realistic aerodynamic model was employed that could approximate the lift and drag of the craft to a suitable level of accuracy. The aerodynamic model had a two-fold use for the analysis; the drag gave an indication of the levels of thrust required to be generated, while the lift helped to determine the range of angle of attack required for by the craft. A propulsion system model was also produced that allowed the inlet compression to be determined from the required thrust. This model was also used as a check to validate the vehicle was able to produce sufficient thrust with sensible laser powers. Sensible values of thrust and angle of attack were determined from the trajectory analysis, which were in good agreement with other studies conducted.

Four different inlet design techniques were then presented; the axi-symmetric, stream traced axi-symmetric, modular stream traced axi-symmetric and the modular stream traced ‘scalloped’ inlet. The axi-symmetric inlet design was similar to traditional lightcraft inlet designs, however modifications to the conical forebody and isolator length were performed to increase its suitability to hypersonic flight. A new method for producing axi-symmetric inlet designs using the stream tracing methodology was employed to generate the truncated stream traced axi-symmetric and modular stream traced axi-symmetric

inlets. In these inlets, an axi-symmetric generating flow field was used to form a two-dimensional inlet geometry that was then rotated about the axis of symmetry to form the inlet shape. The fourth inlet employed the stream traced inlet design technique to generate three-dimensional inlet modules with forebody shock resting on the inlet edges. Numerical simulations were performed on all inlet designs at the Mach 8 design conditions, as well as Mach 5 conditions to represent the vehicle flying at off-design speeds. Angle of attack simulations were also performed at values of 0° , 3° and 6° to establish the inlets sensitivities to vehicle maneuverability. All inlets behaved well, with the exception of the modular stream traced axi-symmetric inlet unstating at Mach 5, 6° angle of attack. The inlets were able to withstand a large range of flight speeds and angles of attack, demonstrating the robustness of the hypersonic inlet designs.

The four inlet designs were compared quantitatively against a range of performance parameters. Inlet compression achieved, inlet compression standard deviation, coefficient of drag, inlet density normalised to coefficient of drag, total pressure efficiency and inlet mass flow capture normalised to vehicle drag were all selected to provide a comprehensive review of each inlets performance. It was interesting to find that there was no inlet that clearly outperformed all the others - each inlet had its advantages and disadvantages. It is most important to the lightcraft propulsion system that high levels of density are achieved at minimal drag. The axi-symmetric stream traced and axi-symmetric stream traced modular inlets were chosen as the most suitable for this reason. Both these inlets exhibited a high density to coefficient of drag ratio, indicating they would be the most efficient laser powered propulsion system platforms.

Finally, the ancillary investigations verified the operation of the inlet in regards to both the laser powered propulsion system, and the experimental gun tunnel test conditions. The laser induced detonation simulations showed the inlet was capable of containing the expanding pressure wave within the isolator, without it exiting out the front of the vehicle. The inlet did not unstart at hypersonic speeds due to the influence of the laser induced detonation wave. From the simulations, it was also possible to establish a limit on the frequency of the repetitively pulsed laser beam. The stream traced inlet design also demonstrated its ability to be self starting at hypersonic speeds. This is an important attribute for the inlet to have, as it greatly improves the operability of the inlet.

8.2 Future Work

As with any research project with a finite time frame, many items originally intended for investigation were unable to be performed within the limited time frame of a Master's degree. Understandably for a complicated system like the lightcraft, only a tiny fraction of the available research space can be undertaken by an individual in a research project such as this. While every attempt was made to approach the task in a thorough manner, simplifications, assumptions and omissions were made to allow the research to progress in a timely manner. This section outlines some possible avenues for future work to continue in the same vein as the work presented herein. The following work will act to supplement and further the lightcraft project, with hopefully one day the concept becoming a reality.

8.2.1 Numerical simulations

The three dimensional simulations in this investigation, while adequate at providing an insight into the behaviour of the inlets at angles of attack, were not able to resolve the complex shock structures within the inlet isolators. At angles of attack intricate shock structures were observed to form in the radial direction of the flow. To analyse these phenomena in further detailed, higher resolution numerical simulations would need to be performed when adequate computing resources become available. A refined mesh will also allow more detailed studies of the shock/boundary layer interactions within the isolator.

In regards to laser induced detonation numerical simulations, a code that would model the breakdown of the air, and subsequent formation of plasma and wave front, would be an invaluable tool for evaluating a specific inlets performance at a range of flight conditions. Numerical codes have been developed that model this phenomena (Ghosh & Mahesh, 2008), however the application of a model of this detail to moving (both sub-, super- and hypersonic) flow in complex geometry has not been performed. Further, extending this capability to three-dimensions would allow the detailed investigation of the interaction between the laser powered propulsion system and the highly non-uniform isolator flows.

8.2.2 Experimental work

In addition to the work contained in this thesis, the University of Adelaide is currently performing hypersonic gun tunnel experiments on the modular stream traced axi-symmetric inlet geometry, with the aims of validating the numerical simulations performed in this work. In addition to the modular stream traced axi-symmetric inlet geometry, it is be-

lieved that the other three geometries should also be investigated in hypersonic ground experiments. It would also be of particular benefit to test the inlet configurations in a hypersonic test facility with laser propulsion capacity, such as the work performed by Salvador (2010). These test would not only provide estimates of the values of thrust able to be achieved in these craft, the results could also be used to evaluate numerical codes developed to model this phenomena.

9 References

References

- Anderson, J.D. 2000. *Hypersonic and High Temperature Gas Dynamics*. American Institute of Aeronautics and Astronautics.
- Anderson, J.D. Jr., Lewis, M.J., & Kothari, A.P. 1991. Hypersonic Waveriders for Planetary Atmospheres. *Journal of Spacecraft*, **28**, 401–410.
- Billig, F.S. 1995. Supersonic Combustion Ramjet Missile. *Journal of Propulsion and Power*, **11**, 1139 – 1146.
- Billig, F.S., & Jacobsen, L.S. 2003 (July). Comparison of Planar and Axisymmetric Flowpaths for Hydrogen Fueled Space Access Vehicles. *In: 39th AIAA/ASME/SAE/ASEE Joint Propulsion Conference and Exhibit*.
- Billig, F.S., & Kothari, A.P. 2000. Streamline Tracing: Technique for Designing Hypersonic Vehicles. *Journal of Propulsion and Power*, **16**, 465 – 471.
- Birkan, M. 2007. Beamed Energy Propulsion: Research Status and Needs - Part 1. *In: Fifth International Symposium on Beamed Energy Propulsion*.
- Bohn, W.L., & Schall, W.O. 2003. Laser Propulsion Activities in Germany. *In: First International Symposium on Beamed Energy Propulsion*.
- Boyce, R.R., Paull, A., Stalker, R.J., Wendt, M., Chinzei, N., & Miyajima, H. 2000. Comparison of Supersonic Combustion Between Impulse and Vibration-Heated Facilities. *Journal of Propulsion and Power*, **16**, 709–717.
- Brode, H.L. 1955. Numerical Simulation of Blast Waves. *Journal of Applied Physics*, **26**, 766–775.
- Buseman, A. 1942. Die achsensymmetrische kegelige Ueberschallströmung. *Luftfahrtforschung*, **19**, 137–144.
- Cook, J.R. 2008. Laser Propulsion - Is it Another Myth or a Real Potential? *In: Fifth International Symposium on Beamed Energy Propulsion*.
- Crocker, B.A. 2007. On the Design of Hypersonic Inward-Turning Inlets.

- Davis, E.W., & Mead Jr, F.B. 2007 (November). Review of Laser Lightcraft Propulsion System. *In: 5th International Symposium on Beamed Energy Propulsion*.
- Delery, J.M. 1985. Shock-Wave/Turbulent Boundary Layer Interaction and its Control. *Progress in Aerospace Sciences*, **22**.
- Doolan, C.J. 2007. Hypersonic Missile Performance and Sensitivity Analysis. *Journal of Spacecraft and Rockets*, **44**(1), 81–87.
- Feikema, D. 2000. Analysis of the Laser Propelled Lightcraft Vehicle. *In: 31st Plasma-dynamics and Lasers Conference*. American Institute of Aeronautics and Astronautics.
- Ghosh, S., & Mahesh, K. 2008. Numerical Simulation of the Fluid Dynamic Effects of Laser Energy Deposition in Air. *Journal of Fluid Mechanics*, **605**, 329–354.
- Gollan, R.J., & Smart, M.K. 2010. Design of Modular, Shape-transitioning Inlets for a Conical Hypersonic Vehicle. *American Institute of Astronautics and Aeronautics*.
- Heiser, W.H., Pratt, D.T., Daley, D.H., & Mehta, U.B. 1994. *Hypersonic Airbreathing Propulsion*. American Institute of Aeronautics and Astronautics.
- Hoerner, S.F. 1965. *Fluid Dynamic Drag*. Self published.
- Huwaldt, J.A. 2008. *Supersonic Cone*. Java Application.
- Jacobs, C. *No title*.
- Kantrowitz, A. 1972. Propulsion to Orbit by Ground Based Lasers. *Astronautics and Aeronautics*, **10**(May), 74–76.
- Katsurayama, H., Komurasaki, K., Momozawa, A., & Arakawa, Y. 2003. Numerical and Engine Cycle Analysis of a Pulse Laser Ramjet Vehicle. *Transactions of the Japan Society for Aeronautical and Space Sciences*, **1**, 9–16.
- Komurasaki, K., Yabe, T., Uchida, S., & Sasoh, A. (eds). 2006. *Fourth International Symposium on Beamed Energy Propulsion*. AIP Conference Proceedings.
- Langener, T., Myrabo, L.N., & Rusak, Z. 2009. Inlet Aerodynamics and Ram Drag of Laser-propelled Lightcraft Vehicles. *In: Sixth International Symposium on Beamed Energy Propulsion*.

- Lewis, M.J. 1993. Designing Hypersonic Inlets for Bow Shock Location Control. *Journal of Propulsion and Power*, **9**, 313–321.
- Matthews, A.J., & Jones, T.V. 2006. Design and Test of a Modular Waverider Hypersonic Intake. *Journal of Propulsion and Power*, **22**, 913–920.
- Matthews, A.J., Jones, T.V., & Cain, T.M. 2005. Design and Test of a Hypersonic Insentropic-Spike Intake with Aligned Cowl. *Journal of Propulsion and Power*, **21**, 838–843.
- Mead Jr., F.B., Larson, W.C., & Knecht, S.D. 2005. An Overview of the Experimental 50cm Laser Ramjet (X-50LR) Program. *In: Fourth International Symposium on Beamed Energy Propulsion*.
- Miele, A. 1962. *Flight Mechanics*. Vol. 1: Theory of Flight Paths. Addison-Wesley Publishing Company, Inc.
- Minovitch, M.A. 1972. Reactorless Nuclear Propulsion - The Laser Rocket. *In: 8th Joint Propulsion Conference*.
- Minucci, M.A.S. 2008. An Overview of Brazilian Developments in Beamed Energy Aerospace Propulsion and Vehicle Performance Control. *Pages 70–83 of: Fifth International Symposium on Beamed Energy Propulsion*, vol. 997.
- Molder, S., & Szpiro, E.J. 1966. Busemann Inlet for Hypersonic Speeds. *Journal of Spacecraft*, **3**, 1303 – 1304.
- Morgan, C.G. 1975. Laser-induced Breakdown of Gases. *Reports on Progress in Physics*, **38**, No. 5, 621–666.
- Myrabo, L.N., Messitt, D.G., & Mead Jr, F.B. 1998. Ground and Flight Tests of a Laser Propelled Vehicle. *American Institute of Astronautics and Aeronautics*.
- Nonweiler, T. 1963. Delta Wing of Shape Amenable to Exact Shockwave Theory. *Royal Aeronautical Society*, **67**.
- Pakhomov, A.V. (ed). 2007. *Fifth International Symposium on Beamed Energy Propulsion*. AIP Conference Proceedings.
- Phipps, C., Komurasaki, K., & Sinko, J. (eds). 2009. *Sixth International Symposium on Beamed Energy Propulsion*. AIP Conference Proceedings.

- Phipps, C., Birkan, M., Bohn, W., Eckel, H.A., Horisawa, H., Lippert, T., Michaelis, M., Rezunkov, Y., Sasoh, A., Schall, W., Scharring, S., & Sinko, J. 2010. Review: Laser-Ablation Propulsion. *Journal of Propulsion and Power*, **26**, 609–636.
- Pirri, A.N., & Weiss, R.F. 1972. Laser Propulsion. *In: AIAA 5th Fluid and Plasma Dynamics Conference*.
- Prime, Z. 2011. *Newtonian Flow Aerodynamics*. February 9, 2011.
- Raizer, Y.P. 1965. Heating of a Gas by a Powerful Light Pulse. *Soviet Physics JETP*, **21**, 55.
- Rather, J.D.G. 2003. Ground to Space Laser Power Beaming: Missions, Technologies, and Economic Advantage. *In: First International Symposium on Beamed Energy Propulsion*.
- Reilly, J.P., Ballantyne, A., & Woodroffe, J.A. 1979. Modelling of Momentum Transfer to a Surface by Laser-Supported Absorption Waves. *American Institute of Astronautics and Aeronautics*, **17**(10), 1098–1105.
- Richard, J.C., & Myrabo, L.N. 2005. Analysis of a Laser-Generated Impulse in an Air-breathing Pulsed Detonation Engine: Part 1. *In: Third International Symposium on Beamed Energy Propulsion*.
- Richard, J.C., Morales, C., Smith, W.L., & Myrabo, L.N. 2006. Earth-to-Orbit Laser Launch Simulation for a Lightcraft Technology Demonstrator. *In: Fourth International Symposium on Beamed Energy Propulsion*.
- Salvador, I.I. 2010. *Static and Hypersonic Experimental Analysis of Impulse Generation in Air-Breathing Laser-Thermal Propulsion*. M.Phil. thesis, Rensselaer Polytechnic Institute.
- Scharring, S., Eckel, H., & Roser, H. 2008. Flight Analysis of a Parabolic Lightcraft - Ground-based Launch. *In: Fifth International Symposium on Beamed Energy Propulsion*.
- Sedov, L.L. 1959. *Similarity and Dimensional Methods in Mechanics*. Academic Press.
- Segal, C. 2009. *The Scramjet Engine - Processes and Characteristics*. Cambridge University Press.

- Simons, G.A., & Pirri, A.N. 1977. The Fluid Mechanics of Pulsed Laser Propulsion. *American Institute of Astronautics and Aeronautics*, **15**(6), 835–842.
- Smart, M. 2007. Scramjets. *Aeronautical Journal*, **111**, 605–619.
- Smart, M.K. 1999. Design of Three-Dimensional Hypersonic Inlets with Rectangular-to-Elliptical Shape Transition. *Journal of Propulsion and Power*, **15**, 408–416.
- Smart, M.K., & Trexler, C.A. 2003. Mach 4 performance of a fixed-geometry hypersonic inlet with rectangular-to-elliptical shape transition. *41st AIAA Aerospace Sciences Meeting*, **2pp**, 288–293.
- Song, W., & Zhao, Z. 2009. Effect of Truncation on the Performance of Busemann Inlet. *Modern Applied Science*, **3**, 168–171.
- Stengel, R. 2004. *Flight Dynamics*. Princeton, USA: Princeton University Press.
- Stern, F., Wilson, R.V., Coleman, H.W., & Paterson, E.G. 2001. Comprehensive approach to verification and validation of CFD simulations - Part 1: Methodology and procedures. *Journal of Fluids Engineering*, **123**, 793–802.
- Stollery, J.L. 1990. *Some Aspects of Shock-Wave/Boundary Layer Interaction Relevant to Intake Flow*. Tech. rept. AGARD-CP-479.
- Sun, B., Zhang, K.Y., Wang, C.P., & Wu, X.S. 2010. Investigation on a Streamtraced Hypersonic Busemann Inlet. *Proceedings of the Institution of Mechanical Engineers, Part G: Journal of Aerospace Engineering*, **224**, 57–63.
- Tan, H., & Guo, R. 2007. Experimental Study of the Unstable-Unstarted Condition of a Hypersonic Inlet at Mach 6. *Journal of Propulsion and Power*, **23.**, **No. 4**, 783–788.
- Tan, H., Sun, S., & Yin, Z. 2009. Oscillatory Flows of Rectangular Hypersonic Inlet Unstart Caused by Downstream Mass Choking. *Journal of Propulsion and Power*, **25**, 138–147.
- Tan, H., Li, L., Wen, Y., & Zhang, Q. 2011. Experimental Investigation of the Unstart Process of a Generic Hypersonic Inlet. *American Institute of Astronautics and Aeronautics*, **49**, 279–288.

- Ushio, M., Katsurayama, H., K., Komurasaki, & Arakawa, Y. 2004. Analytical Study on Flight Performance of an Air Breathing RP Laser Launcher. *In: 40th AIAA/ASME/SAE/ASEE Joint Propulsion Conference and Exhibit.*
- Van Wie, D.M. 2000. *Scramjet Propulsion.* American Institute of Aeronautics and Astronautics. Chap. Scramjet Inlets, pages 447–511.
- Woodroffe, J.A., Stankevics, J.O.A., Ballantyne, A., & Reilly, J.P. 1979. Pulsed Laser-Generated Impulse on a Surface in Supersonic Flow. *American Institute of Astronautics and Aeronautics*, **18**, No.1, 94 – 95.
- You, Y., & Liang, D. 2009. Design and concept of three-dimensional section controllable internal waverider hypersonic inlet. *Science in China Series E: Technological Sciences*, **52**, 2017–2028.
- Yu, D., Chang, J., Bao, W., & Xie, Z. 2007. Optimal Classification Criteria of Hypersonic Inlet Start/Unstart. *Journal of Propulsion and Power*, **23**, No. 2, 310 – 316.

A Trajectory analysis code

```

function pointmass
%      Based on an example in Robert Stengel's Book "Flight
%      Dynamics", Princeton University Press, Princeton, USA, 2004

close all;

global A m g0

A          =      0.017;          % Reference Area - vehicle frontal area, m^2
g0         =      9.8;           % Gravitational acceleration at sea level, m/s^2
m          =      8;             % Mass, kg

%      Initial conditions
h          =      0;             % Initial Height, m
R          =      0;             % Initial Range, m
to         =      0;             % Initial Time, sec
tf         =      90;            % Final Time, sec
GAM        =      90*pi/180;     % Flight angle, Rad
V_E        =      0+1e-8;        % Launch speed, m/s

V          =      V_E;
tspan      =      [to tf];
xo         =      [V;GAM;h;R];

%Solve system of equations based on initial conditions and simulation time
[ta,xa]    =      ode15s(@lightcraft,tspan,xo);

%Calculate flow properties for launch
[airDens, airPres, temp, soundSpeed, Ma]          =      atmosphere(xa(:,3),xa(:,1));
[rhoRatio, rhoStag, rhoSonic]                    =      stagnation(Ma, airDens);

%Save results to file for plotting
save flight2.mat xa ta airDens airPres temp soundSpeed Ma rhoStag rhoSonic;

%Plot results
figure
plot(xa(:,4),xa(:,3),'*r')
xlabel('Range, m'), ylabel('Height, m'), grid

figure
subplot(1,2,1)
plot(Ma,xa(:,3))
xlabel('Mach Number'), ylabel('Altitude, m'), grid
subplot(1,2,2)
plot(ta,Ma)
xlabel('Time, s'), ylabel('Mach Number'), grid

figure
subplot(3,3,1)
plot(ta,xa(:,1))
xlabel('Time, s'), ylabel('Velocity, m/s'), grid
subplot(3,3,2)
plot(ta,xa(:,2))
xlabel('Time, s'), ylabel('Flight Path Angle, rad'), grid
subplot(3,3,3)
plot(ta,xa(:,3))
xlabel('Time, s'), ylabel('Altitude, m'), grid
subplot(3,3,4)
plot(ta,xa(:,4))
xlabel('Time, s'), ylabel('Range, m'), grid
subplot(3,3,5)
plot(ta,airDens)
xlabel('Time, s'), ylabel('Air density, kg/m^3'), grid
subplot(3,3,6)
plot(ta,airPres)
xlabel('Time, s'), ylabel('Pressure, Pa'), grid
subplot(3,3,7)
plot(ta,temp)
xlabel('Time, s'), ylabel('Temperature, K'), grid
subplot(3,3,8)
plot(ta,soundSpeed)
xlabel('Time, s'), ylabel('Speed of Sound, m/s'), grid
subplot(3,3,9)

```

```

plot(ta, Ma)
xlabel('Time, s'), ylabel('Mach Number'), grid

return;

function [xdot] = lightcraft(t,x)
%Main function to set up the equations of motion, solved by ode15s
%point-mass equations of motion constrained to a plane.

global m g0 Re

xdot = zeros(4,1);    % a column vector, initialised to zero

V      = x(1);
Gam     = x(2);
h      = x(3);
R      = x(4);

%Calculate atmospheric properties at current altitude, and velocity.
[airDens, airPres, temp, soundSpeed] = atmosphere(h,V);

M      = V / soundSpeed;           % Mach number
q      = 0.5 * airDens * V^2;       % Dynamic Pressure, N/m^2
gh     = g0*((Re / (Re+h))^2);      % Acceleration due to gravity at
height h

%If lightcraft has exited sensible atmosphere, exit loop.
if h >= 70000
    return;
end

%Read in thrust and angle of attack from schedule.
[T, AOA] = flight1(h);

thetaC = 14.03 * pi / 180;          %Cone half angle, rad
alpha  = AOA * pi / 180;            %Angle of attack, rad
r      = 0.015;                     %Radius of lightcraft
base, m = sqrt(0.6^2 + 0.015^2);    %Length of cone
hypotonuse, m
surfA = pi * s * r;                 %Surface area of cone, m2

%Drag schedule
%Subsonic
if M < 0.9
    L = 0;
    D = 0.5 * airDens * V^2 * surfA * 0.45;
%Transonic
elseif (M>=0.9 && M < 1.5)
    L = 0;
    D = 0.5 * airDens * V^2 * surfA * (0.5833*M - 0.07495);
%Supersonic, using Newtonian theory.
else
    L = 0.5 * pi * airDens * V^2 * 0.015^2 * (sin(2*alpha)*(cos(thetaC)^2)*cos
(alpha) - ((sin(alpha))^2 + 2 * (sin(thetaC)^2) - 3 * (sin(alpha)^2) * (sin(thetaC)^2)) * sin(alpha));
    D = 0.5 * pi * airDens * V^2 * 0.015^2 * (sin(2*alpha)*(cos(thetaC)^2)*sin
(alpha) + ((sin(alpha))^2 + 2 * (sin(thetaC)^2) - 3 * (sin(alpha)^2) * (sin(thetaC)^2)) * cos(alpha));
end

%System of ordinary differential equations
%-----
%V_dot
xdot(1) = (T - D - m * gh * sin(Gam)) / m;
%Gamma_dot
xdot(2) = (L - m*gh*cos(Gam)) / (m*V);
%h_dot
xdot(3) = V*sin(Gam);
%R_dot
xdot(4) = V*cos(Gam);

return;

```

```

%-----

```

% Flight parameters, No. 1

%-----

function [T, AOA, reqDens] = flight1(h)

```
    if h < 50
        T = 300;                                %Minimum thrust to overcome drag at transonic speeds
        AOA = 0;
        reqDens = 0.055;
    elseif (h >=50 && h < 10000)
        T = 400;
        AOA = 0;
        reqDens = 0.13;
    elseif (h >=10000 && h < 15000)
        T = 623;
        AOA = 0;
        reqDens = 0.5;
    elseif (h >=15000 && h < 32000)
        T = 700;
        AOA = 0;
        reqDens = 0.7;
    elseif (h >=32000 && h < 40000)
        T = 623;
        AOA = 0;
        reqDens = 0.5;
    else
        T = 400;
        AOA = 0;
        reqDens = 0.13;
    end
```

return;

B streamTracer code


```

%-----
%Main routine
%-----
function streamTracer

%Clear any existing files
delete('geometry.dat');
delete('data.txt');
delete('data1.txt');

%Cartesian co-ordinates of the perimeter of the inlet geometry is entered in the
%format [y z]. An example is given for 2D and 3D geometries.

%2D inlet geometry example. Upper surface and lower surface are entered seperately
%in order to apply the viscous correction in the correct direction.
%-----
%Lower surface
profile      = [0.155 0];
%Upper surface
%profile      = [0.1735 0];

%Modular inlet geometry example. Again the surfaces are entered seperately to allow
%the correct application of the viscous correction.
%Lower surface
%profile      = [0.4554 0.0208;0.4594 0.0413;0.4661 0.061;0.4754 0.07975];
%Upper surface
%profile      = [0.5445 0.0399];

%Read in CFD flowfield data from input file and remove headers. Adjust the location/file name
%as required.
unix('cp ~/Documents/Uni/Fluent/Flowfields/VelocityFields/axi0758degMa8DATA data.txt');
unix('sed /^#/d <data.txt> data1.txt');

%Sets the number of stream lines to be traced.
[a b]        = size(profile);

%This code segment 'transforms' the cartesian co-ordinates supplied above
%into a cylindrical co-ordinate system to match that of the axi-symmetric
%solution. 'inlet' is the radial distance of the point from the centre
%line- it is the value that dictates the path of the streamline.
for i=1:a
    if profile(i,2) == 0
        angle(i)    = pi / 2;
    else
        angle(i)      = atan(profile(i,1) ./ profile(i,2));
    end
    inlet(i)          = sqrt(profile(i,1).^2 + profile(i,2).^2);
end

[a b]          = size(inlet);

%Open file for writing solution to.
fid    = fopen('geometry.dat','w');

%Write to file a line defining the centre line for reference.
%For Pointwise, the format is:
%-----
%n                - No. of points on line
%x1 y1 z1        - Cartesian co-ordinates of point one
%...
%xn yn zn        - Cartesian co-ordinates of point n
%-----
fprintf(fid,'2\n');
fprintf(fid,'0 0 0\n');
fprintf(fid,'1 0 0\n\n');

for i=1:b

    %Calculate streamlines for the ith defined sector point.
    [A]    = streamLines(inlet(i));
    theta  = angle(i);

    %Detect the flowfield lip shock. Flow is uniform, so shock is detected when the flow deviates.
    count  = 0;

```

```

[k, j]      = size(A);

for m=1:(k-1)
test        = -1 * ((A(m+1,2) - A(m,2)) / (A(m+1,1) - A(m,1)));
if test > 1.2e-01
    count = count+1;
    x(count) = m;
end
end

%Calculate the actual inlet start, i.e. at the flowfield lip shock.
start = x(1);

%Create truncated inlet geometry from shock detection. This starts the inlet geometry
%at the forebody shock, and ends it at the reflected shock.
for m=1:count
    l      = m + start;
    Atrunc(m,1) = A(l,1);
    Atrunc(m,2) = A(l,2);
end

%Perform viscous correction on the truncated geometry.
[Avis] = viscousCorrection(Atrunc);

%Convert the cylindrical co-ordinates outputted from the function stream2
%back to cartesian co-ordinates for the importation into meshing software.
for m=1:count
    pathx(m) = Avis(m,1);
    pathy(m) = Avis(m,2) * sin(theta);
    pathz(m) = sqrt(Avis(m,2).^2 - pathy(m)^2) ;
end

%Writing to the segment file for importation into Pointwise.
[k, j] = size(pathx);
fprintf(fid, '%d\n', j);
for k=1:j
    fprintf(fid, '%6.4d %6.4d %6.4d\n', pathx(k), pathy(k), pathz(k));
end
fprintf(fid, '\n');

end

fclose(fid);

return;

%-----
%This function calculates the two-dimensional path that the streamlines follow,
%based on the CFD data imported.
%-----
function [A] = streamlines2D2(inlet)

%Load CFD flowfield data into memory
load data1.txt -ascii

%Function to plot the data in data1 - also makes postscript files
%x and y co-ordinates
xd = data1(:,2);
yd = data1(:,3);
%x and y velocity components
Uxd = data1(:,4);
Vxd = data1(:,5);

%Generate a mesh for the streamlines
ti1 = 0:0.01:5;           %streamwise
ti2 = 0:0.01:0.6135;     %normal
[XI,YI] = meshgrid(ti1,ti2);

U = griddata(xd,yd,Uxd,XI,YI);
V = griddata(xd,yd,Vxd,XI,YI);

%Starting line (from which stream particles are released)
[Sx Sy] = meshgrid(0.01,0:0.01:0.6135);

```

```

%Stream plot
h = streamline(XI,YI,U,V,Sx,Sy);

%This finds the inlet g
p1 = stream2(XI,YI,U,V,0.01,inlet,[0.1 3000]);
A = p1{1};

return;

%-----
%This function applies the viscous correction to the inviscid streamline
%obtained from the streamLines function.
%-----
function [Avis] = viscousCorrection(Atrunc)

%Conditions at which the correlation is calculated. Taken as
%representative values for the inlet flow.
rho = 0.1;
M = 2.6;
mu = 1.53e-05;
a = 585;
x = 0;
L = 0;

%Calculate the number of points to correct.
[j, k] = size(Atrunc(:,1));

%Calculate the total length of the streamline
for i=2:j
    L = L + sqrt((Atrunc(i,1) - Atrunc(i-1,1))^2 + (Atrunc(i,2) - Atrunc(i-1,2))^2);
end

%Initial conditions
Avis(1,2) = Atrunc(1,2);
Avis(1,1) = Atrunc(1,1);

%End point condition
Avis(j,1) = Avis(1,1) + L;

%Correct the inviscid geometry along the streamline
for i=2:(j-1)
    %Position along surface
    x = x + sqrt((Atrunc(i,1) - Atrunc(i-1,1))^2 + (Atrunc(i,2) - Atrunc(i-1,2))^2);
    %Reynolds number
    Re = rho * M * a * x / (L * mu) ;
    %Displacement thickness
    deltaStar = 0.2145 * (M ^ 0.375) * (0.08801 * M + 0.06385) * x / (L * Re .^ 0.166);
    %Angle of line segment
    theta = atan (( Atrunc(i,1) - Atrunc(i-1,1)) / (Atrunc(i,2) - Atrunc(i-1,2)));
    %x component of correction
    deltax = -1 * deltaStar * cos (theta);
    %y component of correction
    deltay = -1 * deltaStar / sin (theta);
    %x co-ordinates of corrected geometry
    Avis(i,1) = Atrunc(i,1);
    %y co-ordinates of corrected geometry. Note correction is only applied in the y direction.
    Avis(i,2) = Atrunc(i,2) + deltay;
end

%Repeat for the final point
x = x + sqrt((Atrunc(j,1) - Atrunc(j-1,1))^2 + (Atrunc(j,2) - Atrunc(j-1,2))^2);
Re = rho * M * a * x / (L * mu);
deltaStar = 0.2145 * (M ^ 0.375) * (0.08801 * M + 0.06385) * x / (L * Re .^ 0.166);
theta = atan (( Atrunc(j,1) - Atrunc(j-1,1)) / (Atrunc(j,2) - Atrunc(j-1,2)));
deltax = -1 * deltaStar * cos (theta);
deltay = -1 * deltaStar / sin (theta);
Avis(i,1) = Atrunc(j,1);
Avis(j,2) = Atrunc(j,2) + deltay;

return;

```

Part 2

Experimental ground testing

Testing of a Lightcraft Model in the TUSQ Facility – August 2011

David Buttsworth, Con Doolan, Vince Wheatley

May 10, 2012

Abstract

A model lightcraft inlet with a conical forebody was tested in a hypersonic wind tunnel facility at Mach 5.8. Pressure measurements and schlieren flow visualisation were obtained for angles of attack between -6° and $+6^\circ$. Results demonstrate separation of the forebody boundary layer at all angles of attack.

1 Introduction

Lightcraft will need to have inlets which efficiently compress the flow. Various approaches to hypersonic inlet design are possible and computational fluid dynamics (CFD) solutions certainly play an important role. However, physical simulation of the prototype inlet arrangement is also necessary because of the large uncertainties in the CFD modelling of turbulent boundary layers in adverse pressure gradients with strong compressibility and 3 dimensional effects.

A number of lightcraft inlets designs have been describe by Harrland [1]. One of these designs has been tested in the hypersonic wind tunnel facility at the University of Southern Queensland, TUSQ [2]. This report describes these experiments.

2 Apparatus

2.1 Model and Instrumentation

The model lightcraft tested in the present work was derived from the work of Harrland [1]. The arrangement involves a conical forebody with a half angle of 12.28° followed by a stream-traced cowl and centrebody for further compression of the incoming stream as illustrated in Fig. 1. The afterbody is required for focussing of laser light but does not form part of the current investigation, and so did not need to be included in the wind tunnel model. Engineering drawings of the model used for manufacture can be found in Appendix A.

The model as manufactured is pictured in Fig. 2, and an illustration of the model at the nozzle exit of the hypersonic facility is presented in Fig. 3. Five piezoresistive pressure transducers (SensorTechnics BSDX2000A2R) were connected via short pneumatic tubes to the tap locations shown in Fig. 3. For the work in this report, the nose-down orientation in the tunnel is treated as a positive angle of attack (AoA) as illustrated in Fig. 3.

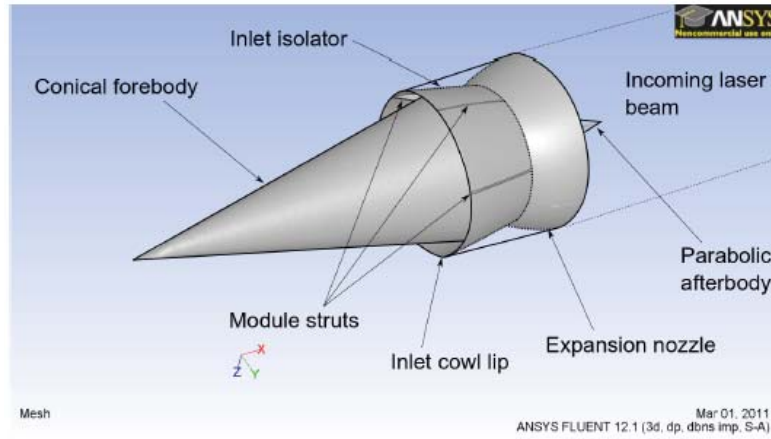


Figure 1: Lightcraft model concept: inner surface of the cowl is shown.

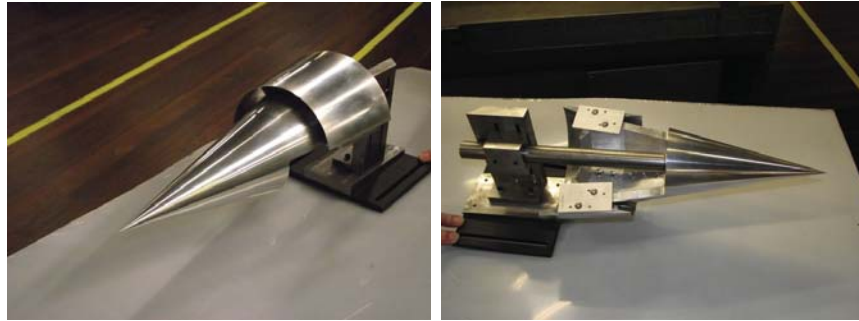


Figure 2: Photographs of the lightcraft model as manufactured. Left: orientation of the model used in the wind tunnel. Right: inverted model position showing the pressure tap locations.

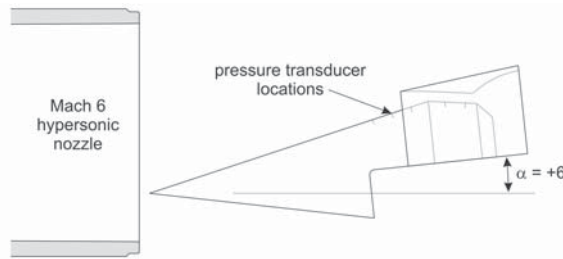


Figure 3: Illustration of the lightcraft model in TUSQ facility. Five pressure transducers locations are shown and the axial distances from the tip of the cone are: 229, 248, 268, 303, and 322 mm.

2.2 Facility and Flow Visualisation

Figure 4 illustrates the wind tunnel used in the present work. The facility, known as TUSQ, is a light, free piston compression tunnel, similar to the isentropic light piston tunnels first developed in the UK during the 1970's [3, 4]. The barrel of the TUSQ facility is 16 m long with an internal diameter of 130 mm and for the current work, the Mach 6 contoured nozzle was used. This nozzle has a physical exit diameter of 217.5 mm. Further details of the facility hardware are provided elsewhere [2].

The facility is charged with high pressure air in the reservoir, and the barrel is charged with the test gas to a moderate pressure. A run is initiated by opening the primary valve which results in the nylon piston (about 350 grams) being driven down the barrel, compressing the test gas in an approximately isentropic manner. A representative pressure history measured within in the barrel (at 130 mm upstream of the nozzle entrance) is presented in Fig. 5. The plateau region on the pressure history which begins at 0 s on the timescale in Fig. 5 corresponds to the period of flow discharge from the barrel into the test section which is initiated by the rupture of a diaphragm at the entrance to the nozzle. The facility operating condition is designed so that the volumetric rate of discharge of gas from the barrel is matched by the air entering the barrel from the high pressure air reservoir and this enables the mean pressure of the nozzle reservoir to remain approximately constant during the run time which lasts about 200 ms.

Schlieren images were obtained during the experimental program. The arrangement of the system is illustrated in Fig. 6. The system consisted of a red LED light source, collimated by a 120 mm diameter lens with a focal length of 1000 mm. A similar lens is used to focus the image of the light source onto a horizontal knife edge. An Olympus I-speed3 operating at 1000 fps was used for image capture. The maximum field of view on the schlieren images is restricted to approximately 100 mm because of the aperture of the windows on the test section.

2.3 Operating Conditions

Table 1 gives essential operating conditions for each run of the hypersonic facility performed for this program. Mean and 2σ variations have been reported in this table. Initial pressure p_i and temperature T_i of the air in the barrel correspond to the local atmospheric pressure and ambient temperature respectively. The pressure of the air reservoir used in the program was 3 MPa (gauge). Data from repeated runs for the different angles of attack α are generally available.

The values of the nozzle stagnation pressure p_0 reported in Table 1 were determined from the pressures measured in the barrel (e.g., Fig. 5) when averaged over the first 150 ms of the flow duration. The values of the nozzle stagnation temperature T_0 reported in Table 1 have been deduced on the assumption of isentropic compression of the air test gas from the initial conditions to the reported values of p_0 . Energy loss through heat transfer from the test gas during the compression and discharge process is known to occur [5] but recent measurements have shown that the isentropic compression is a good approximation for the test flow which is first discharged from the barrel.

A survey of nozzle exit pitot pressure was performed for the current operating

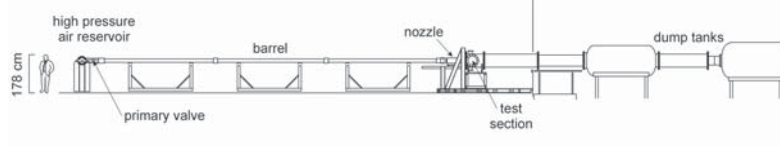


Figure 4: Schematic diagram showing the TUSQ facility arrangement.

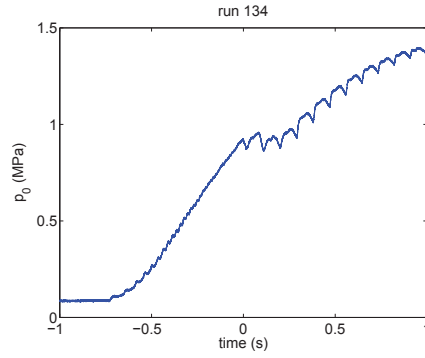


Figure 5: Sample barrel pressure history, result for run 134 shown.

condition. Results indicate that the central 160 mm diameter core of the nozzle is uniform in pitot pressure to within $\pm 2\%$. At 50 ms from the start of the flow, the Mach number deduced for the central core was 5.84 with a spatial variation of about $\pm 0.4\%$ and at 150 ms after the start of the flow, the corresponding values were $5.79 \pm 0.5\%$. Flow conditions at the nozzle exit based on stagnation conditions reported in Table 1 and the pitot survey results are reported in Table 2.

3 Results

3.1 Visualization

Schlieren images presented in Figs. 7, 8, 9, 10, and 11 were extracted from the video records at 100 ms from the start of the flow. The scale of the images

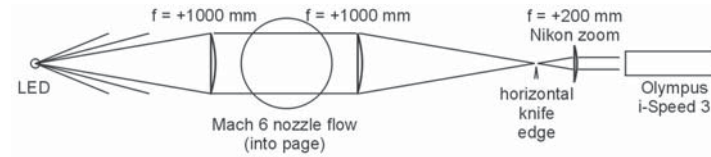


Figure 6: Arrangement of the schlieren system.

Table 1: Facility operating conditions

run number	p_i (kPa)	T_i (K)	α ($^\circ$)	p_0 (kPa)	T_0 (K)	comment
132	94.86	294.5	0	926	565	
133	94.85	293.6	0	925	563	
134	94.86	295.5	0	914	565	
135	94.75	295.5	0	913	565	
136	94.75	295.5	+3	—	—	p_0 not acquired no data acquired
137	94.74	—	+3	—	—	
138	94.82	287.0	+3	938	552	
139	94.87	287.0	-3	937	552	
140	94.84	289.7	-3	945	559	
141	94.86	289.7	+6	921	555	
142	94.88	289.7	+6	939	558	
143	94.63	292.6	-6	934	563	
144	94.63	292.6	-6	922	561	
94.80 ± 0.18		292 ± 6		928 ± 21	560 ± 10	

Table 2: Nozzle exit flow conditions

M_∞	p (Pa)	T (K)	u (m/s)	Re_u (m^{-1})
5.84	690	72	990	7.0×10^6

can be derived from the cowl height which is 18.0 mm relative to the adjacent position on the conical forebody.

In the case of the images for the zero degrees angle of attack ($\alpha = 0$, Fig. 7), two positions of the model were tested. For run 132 and 133, the test section window was positioned on the centreline of the nozzle flow with the tip of the conical forebody positioned in the lower half of the nozzle exit flow. For run 134 and 135, the tip of the model was moved closer to the nozzle centre line and the flange holding the test section window was rotated through 30° to enable visualisation of a larger fraction of the flow. In the images from run 134 and 135, a weak wave from the Mach 6 nozzle lip is observed to enter the field of view and impinges on the model down stream of the leading edge of the cowl – see annotations in the image from run 135 (in Fig. 7).

Oblique compression waves running upwards from the forebody of the model are visible, Fig. 7. The shock wave from the tip of the model appears as a relatively weak feature embedded within a series of compression waves which originate from the forebody surface of the model. The appearance of compression waves at locations beyond, and at steeper angles than the shock cone from the tip of the model, suggests unresolved unsteadiness in the schlieren images. In the video record, the shock from the tip of the model appears steady whereas the additional compression features exhibit unsteady characteristics. The likely origin of these additional compression waves is boundary layer separation on the forebody. The exposure time of each video frame is almost 1 ms and with a free stream flow velocity of around 990 m/s (Table 2), the free stream convection distance during the exposure time is almost 1 m so unsteady structures associated with boundary layer features will not be resolved in the current images.

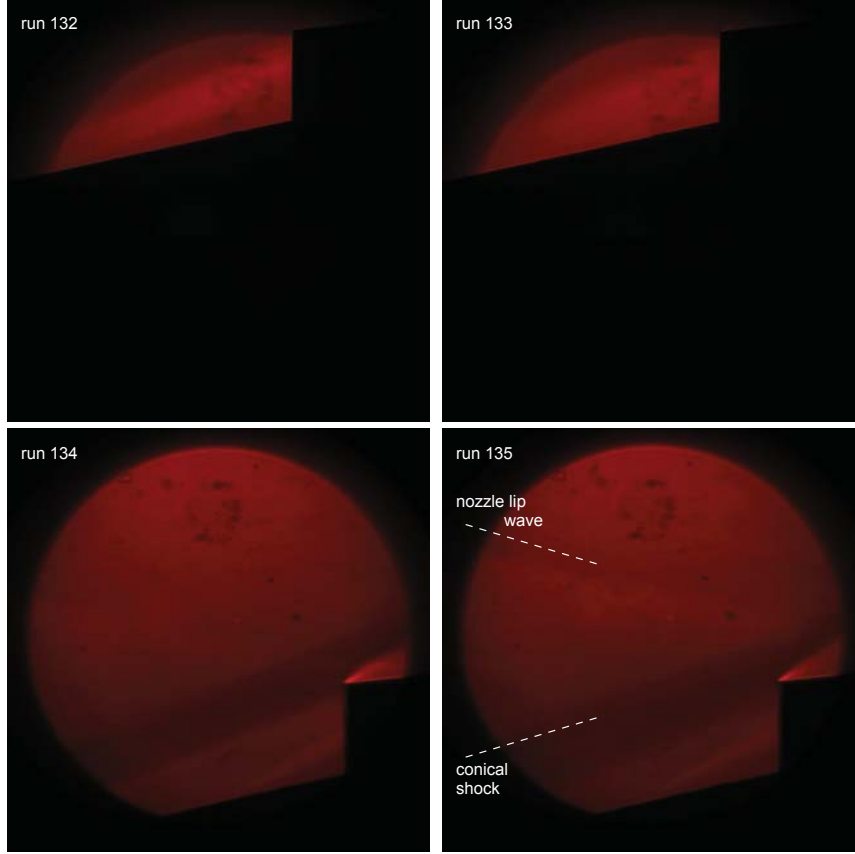


Figure 7: Schlieren images from runs performed at $\alpha = 0^\circ$.

Visualisation at $\alpha = +3^\circ$, Fig. 8, demonstrates similar features to those observed in the case of $\alpha = 0$. However, at $\alpha = -3^\circ$, Fig. 9, the point of origin of the disturbances from the separated boundary layer is within the field of view – much closer to the cowl tip than in the $\alpha = 0$ or $+3^\circ$ cases. Another significant feature which differentiates the visualisation at $\alpha = -3^\circ$ from other cases is the downwards traveling shock from the nozzle lip which enters the inlet in the case of run 139 and appears to impinge close to the cowl tip in the case of run 140. Compression waves from the nozzle lip increase in strength with time due to the accumulation of test gas in the test section which increases the pressure in the test section during the run. Results at $\alpha = +6^\circ$ and -6° (Figs. 10 and 11) exhibit similar features to those observed in other cases.

4 Time-resolved pressure measurements

Pressure measurements from the 5 pressure transducers within the model are presented as a function of time for the 5 angle of attacks are presented in Figs. 12,

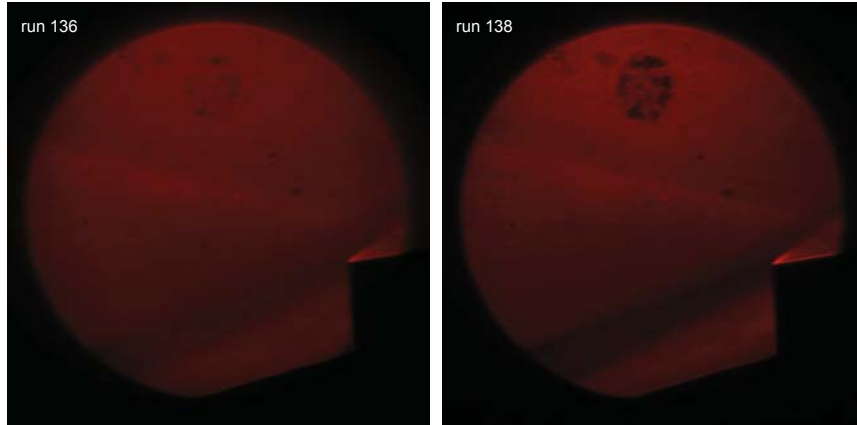


Figure 8: Schlieren images from runs performed at $\alpha = +3^\circ$.

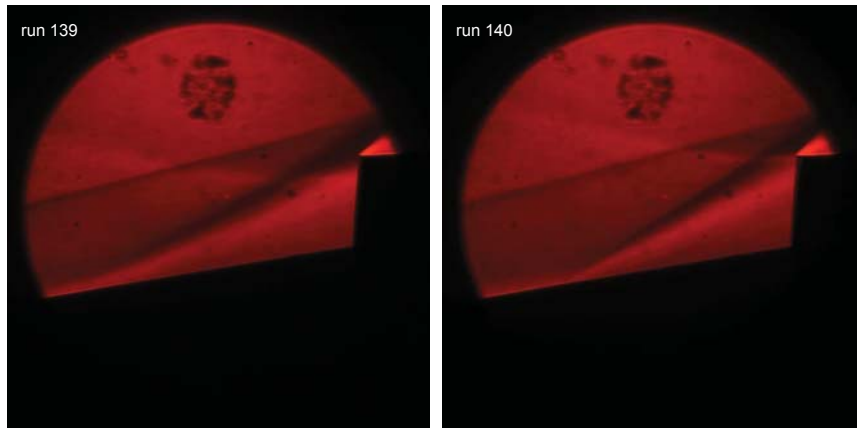


Figure 9: Schlieren images from run performed at $\alpha = -3^\circ$.

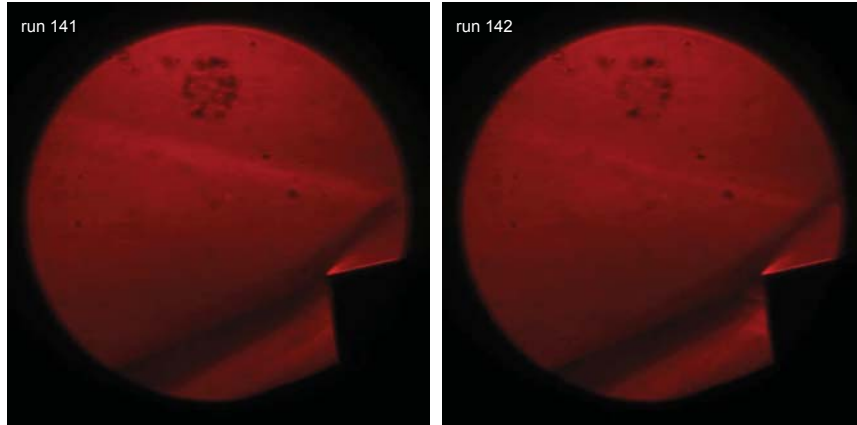


Figure 10: Schlieren images from runs performed at $\alpha = +6^\circ$.

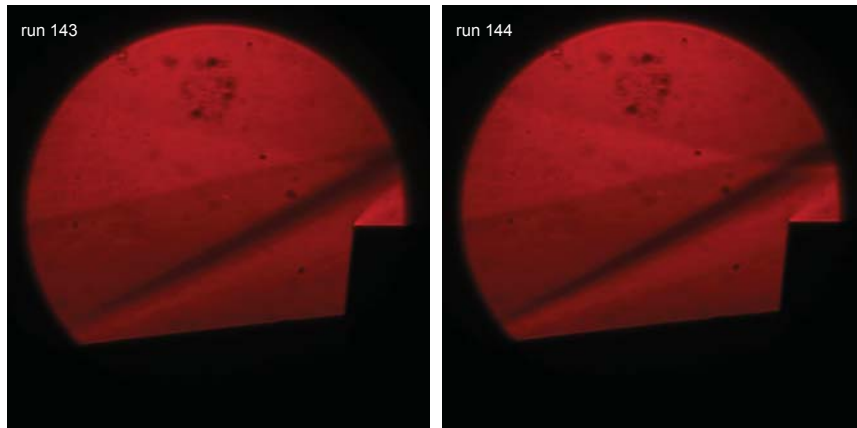


Figure 11: Schlieren images from runs performed at $\alpha = -6^\circ$.

13, 14, 15, and 16. The time-resolved pressure measurements suggest that the flows in general are moderately steady over relatively long time scales – the response time of the static pressure measurement arrangement is around 10 ms.

With the results for $\alpha = -3^\circ$, the schlieren images (Fig. 9) indicate that the shock from the nozzle lip passes into the cowl relatively early during the nominal test period. The pressure data of Fig. 14, demonstrates that the static pressures are increasing over the first 100 ms of the run time, and that downstream transducers detect a rising pressure sooner than those on the forebody. The nozzle lip shock strengthens with time due to increases in the background pressure in the test section and this shock is captured within the cowl relatively soon after flow start. The capture of the shock from the nozzle lip increases the pressure registered by the transducers in the vicinity of the cowl lip, and the flow disturbance is sensed on the conical forebody with the boundary layer separation being driven further forward by the increase in the adverse pressure gradient. Therefore, static pressures towards the start of the test time are more representative of the model performance in the absence of facility interaction disturbances.

The repeated results at $\alpha = +6^\circ$ are strikingly different, Fig. 15. In the case of run 141, the pressures dip prior to climbing and reaching similar values to run 142 towards the end of the run time. Likewise in the case of $\alpha = -6^\circ$ (Fig. 16), the pressure registered on the two most downstream transducers appears unsteady in the case of run 143 and yet the wave from the nozzle lip is not observed to be captured within the cowl during the first 100 ms of the flow duration (Fig. 16).

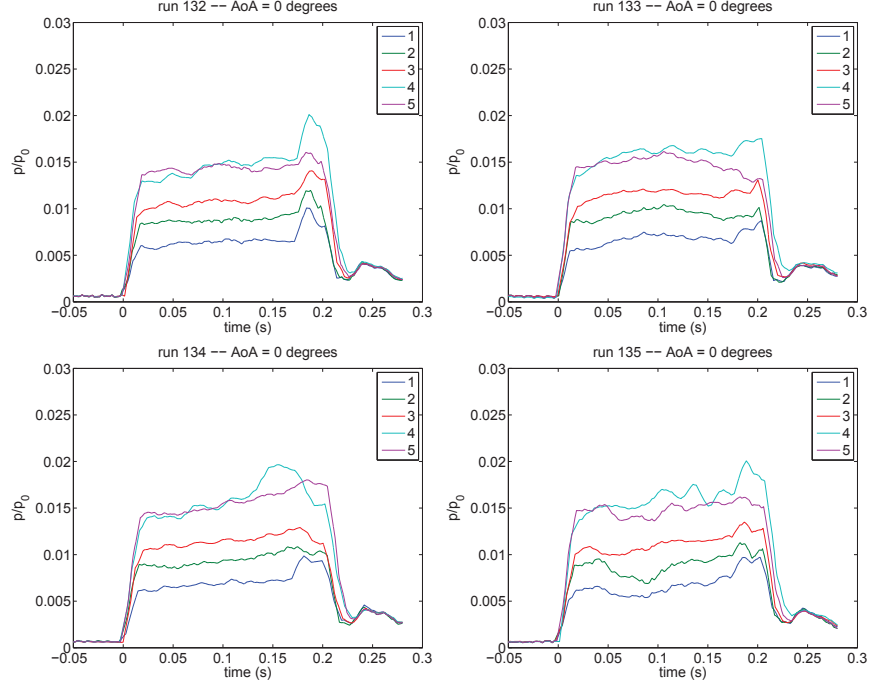


Figure 12: Normalized static pressure histories for $\alpha = 0^\circ$, runs 132 to 135.

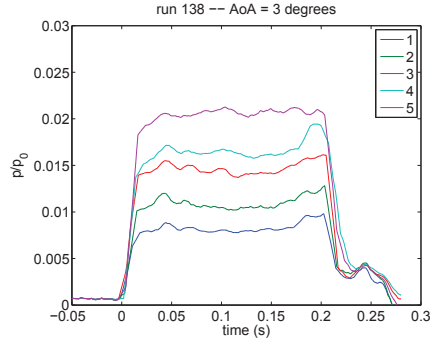


Figure 13: Normalized static pressure histories for $\alpha = +3^\circ$, run 138.

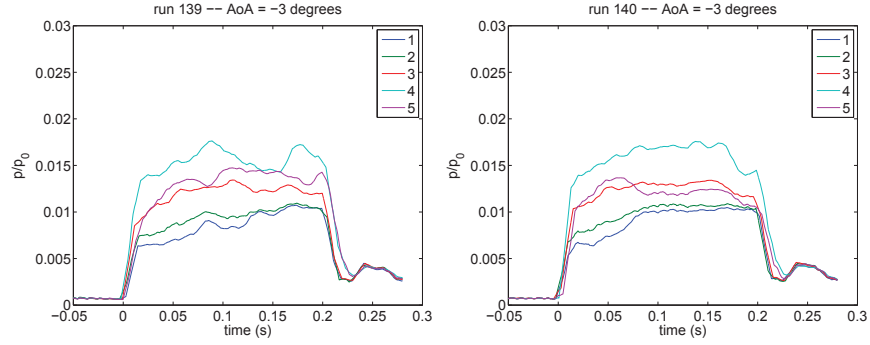


Figure 14: Normalized static pressure histories for $\alpha = -3^\circ$, runs 139 & 140.

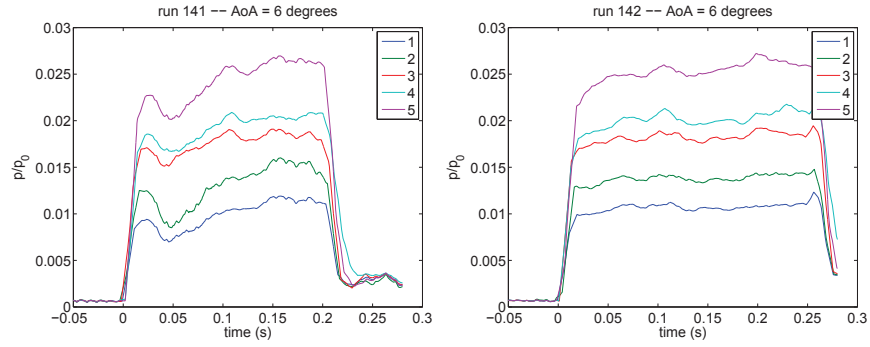


Figure 15: Normalized static pressure histories for $\alpha = +6^\circ$, runs 141 & 142.

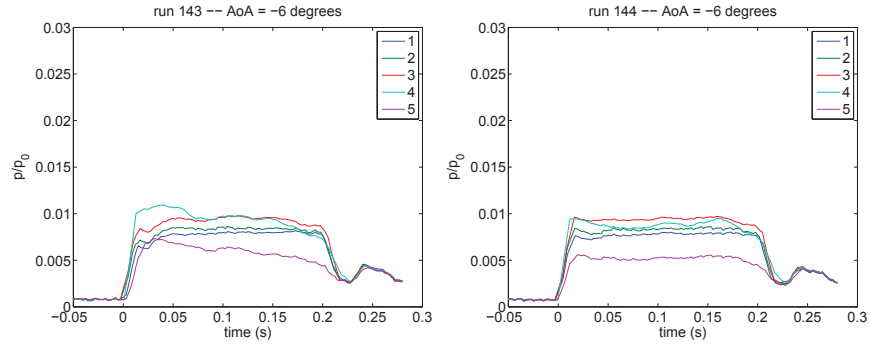


Figure 16: Normalized static pressure histories for $\alpha = -6^\circ$, runs 143 & 144.

5 Spatial variation of pressure

Static pressure results in Figs. 12 to 16 have been presented in terms of spatial distributions in Fig. 17, based on pressure values averaged from 10 ms at 30 ms from the start of the hypersonic test flow. A relatively short test flow window (20 ms) near the start of the flow has been specified in an effort to eliminate the influence of Mach 6 nozzle lip disturbances being captured by the cowl which was observed to occur later in the test flow in the case of $\alpha = -3^\circ$. A compilation of results is presented in Fig. 18.

6 Conclusions

A model lightcraft inlet has been designed at the University of Adelaide and tested in the TUSQ hypersonic wind tunnel facility at the University of Southern Queensland. Schlieren imaging has been performed and static pressures have been measured at Mach 5.8 and a unit Reynolds number of $7.0 \times 10^6 \text{ m}^{-1}$. The model lightcraft was tested at angles of attack between -6° and $+6^\circ$. Results demonstrate that the boundary layer on the forebody is disturbed by the presence of the cowl – some separation of the forebody boundary layer occurs at all of the angles of attack tested.

Acknowledgements This work was funded by the United States Air Force Research Laboratory’s Asian Office of Aerospace R&D under grant AOARD-FA2386-09-1-4088. Mr Alan Harrland designed the inlet, Ms Carolyn Jacobs designed the physical model and contributed to the model testing, Mr Sudantha Balage contributed to the instrumentation and schlieren system set up as well as the tunnel operation.

References

- [1] Harrland, A., Hypersonic Inlet for a Laser Powered Propulsion System, MPhil Dissertation, School of Engineering, Computer and Mathematical Sciences, University of Adelaide, 2012.
- [2] Buttsworth, D.R., Ludwig Tunnel Facility with Free Piston Compression Heating for Supersonic and Hypersonic Testing, Proceedings: Australian Space Science Conference, Sydney, September, 2009.
- [3] Jones, T. V., Schultz, D. L. and Hendley, A. D., On the Flow in an Isentropic Light Piston Tunnel, Aeronautical Research Council, Reports and Memoranda, R&M No. 3731, 1973.
- [4] R.A. East and A.M.S. Qasrawi, A long Stroke Free Isentropic Free Piston Hypersonic Wind Tunnel, Aeronautics Research Council, Report and Memorandum, R&M No.3844, 1978.
- [5] Widodo, A.S. and Buttsworth, D.R., Stagnation Temperature Measurements in the USQ Hypersonic Wind Tunnel, 17th Australasian Fluid Mechanics Conference, Auckland, New Zealand, 5-9 December 2010.

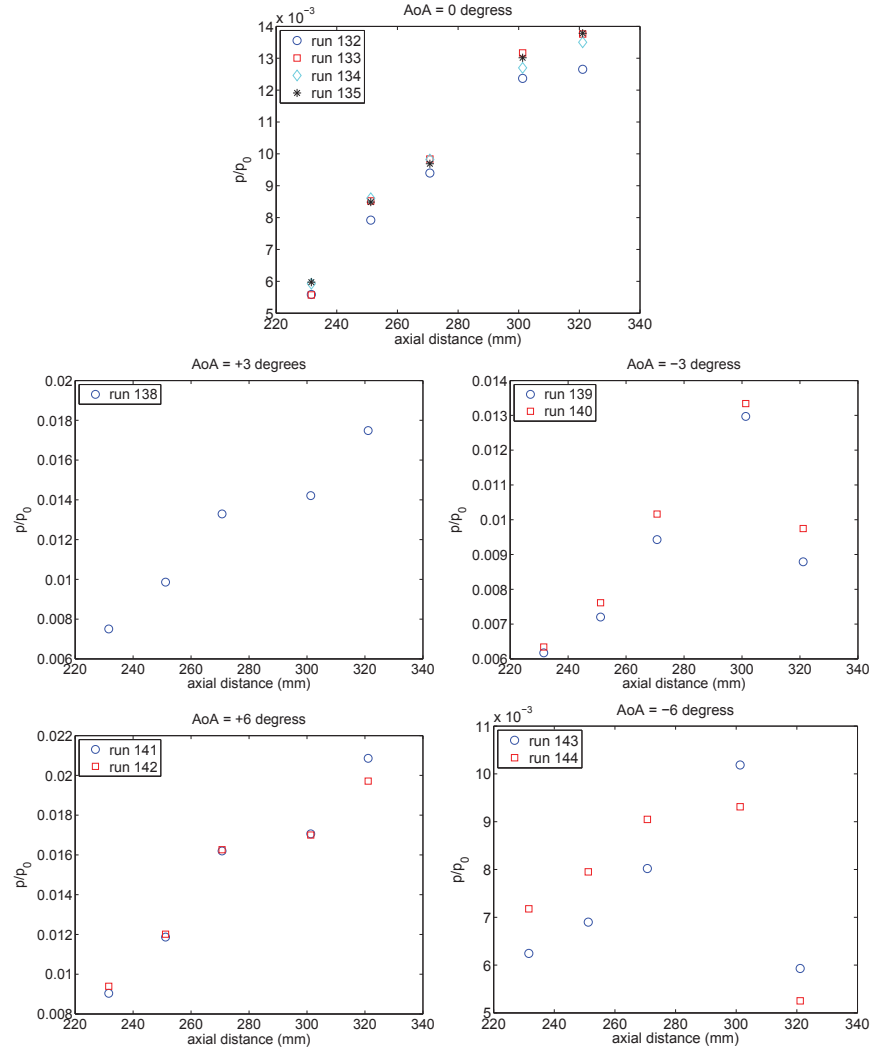


Figure 17: Normalized static pressure results for the different angles of attack as a function of axial position along the model. For this figure, results in Fig. 12 to Fig. 16 were averaged over a period from 10 ms to 30 ms relative to the start of the run time.

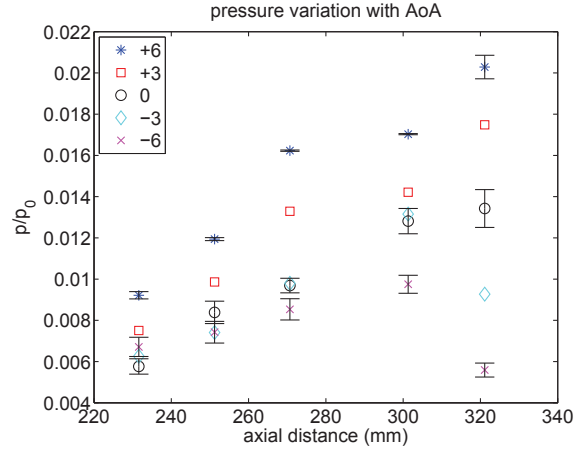


Figure 18: Normalized static pressure results at 20 ms from the start of the flow and compiled for all tested angles of attack. In the case of $+6^\circ$ and -6° , error bar denote maximum and minimum values for the two runs at those angles and in the case of the 0° results, the error bars denote the $\pm 2\sigma$ values for the four runs at that angle. Error bars for the -3° case are not shown for clarity and only one run was performed at -3° .

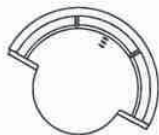
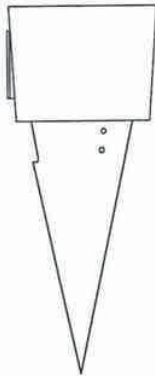
Appendix A. Ground Test Model Drawings

Drawing List: All Components			
PART	DRG NO	NO REQ	MATERIAL
Lightcraft assembly	ASSY-1	0	
Lightcraft assembly (exploded)	ASSY-2	0	
Lightcraft assembly (exploded)	ASSY-3	0	
Cowl	COWL-4	1	Aluminium alloy 6061
Cowl detail	COWL-5	0	
Strut	STRUT-6	2	Aluminium alloy 6061
Intake	INTAKE-7	1	Aluminium alloy 6061
Intake detail	INTAKE-8	0	
Mounting assembly (3 degree)	ASSY-M3-1	0	
Mounting assembly (3 degree, exploded)	ASSY-M3-2	0	
Mounting base	BASE-M3-3	1	Mild steel
3 degree wedge	WEDGE-M3-4	1	Mild steel
Mounting frame	FRAME-M3-5	1	Mild steel
Mounting sting block	BLOCK-M3-6	1	Mild steel
Mounting sting	STING-M3-7	1	Mild steel
Mounting assembly (6 degree)	ASSY-M6-1	0	
6 degree wedge	WEDGE-M6-2	1	Mild steel
Mounting assembly (0 degree)	ASSY-FM-1	0	

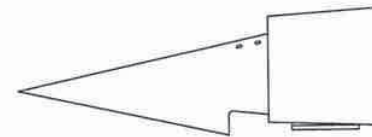
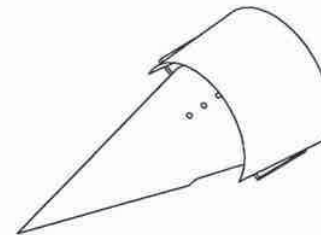
Connectors Required	
Ø 2.50 x 15 dowel	8
M5 grub screws	2
M5 screws	14
M8 screws	4

ALL DIMENSIONS ARE IN MILLIMETERS		FINISH:	$\sqrt{6.3}$	DEBUR AND BREAK SHARP EDGES	DO NOT SCALE DRAWING	VERSION	8
NAME	SIGNATURE	DATE	25/03/2011	 Third angle		TITLE: Drawing List	
DRAWN	NAME	Cathryn Jacobs		DWG NO:		DRG-0	
CHKD				MATERIAL:		A3	
APPRD				WEIGHT:		SHEET 1 OF 1	
MFG				SCALE:1:1			
QA							

17



REVISIONS				
ZONE	REV.	DESCRIPTION	DATE	APPROVED



ITEM NO.	PART NUMBER	DESCRIPTION	QTY.
1	intake3		1
2	rib-end3		2
3	cowl3		1

UNLESS OTHERWISE SPECIFIED:
DIMENSIONS ARE IN MILLIMETERS
SURFACE FINISH: $\sqrt{\text{ }}$
TOLERANCES:
LINEAR: ± 0.2
ANGULAR: $\pm 1^\circ$

FINISH:

$\sqrt{\text{ }}$ = 6.3

DEBUR AND
BREAK SHARP
EDGES

DO NOT SCALE DRAWING

VERSION

B

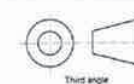
DRAWN: Carolyn Jacobs
CHKD:
APPVD:
MFG:
QA:

NAME

SIGNATURE

DATE

25/03/2011



Third angle

MATERIAL:

Aluminium Alloy 6061

WEIGHT:

TITLE:

Lightcraft

DWG NO.:

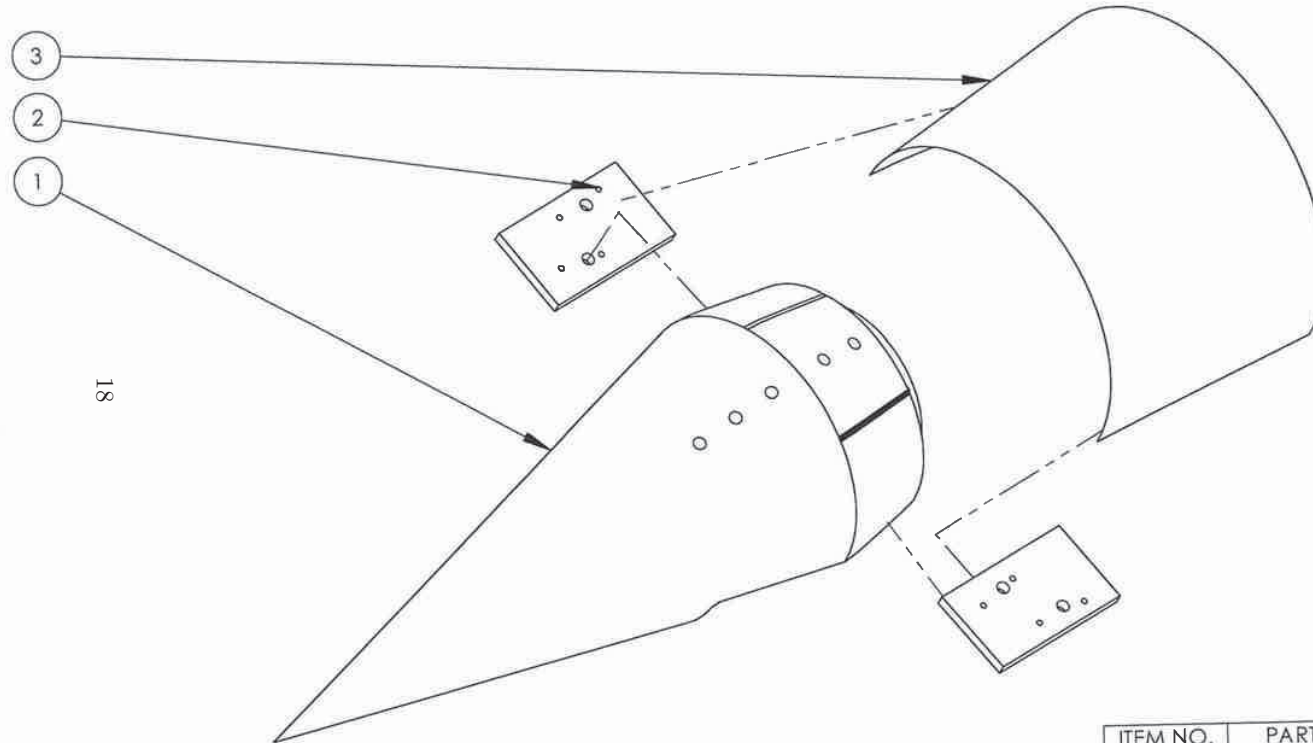
ASSY-1

SCALE:1:5

SHEET 1 OF 8

A3

REVISIONS				
ZONE	REV.	DESCRIPTION	DATE	APPROVED
-	-	See Sheet1	-	-



ITEM NO.	PART NUMBER	DESCRIPTION	QTY.
1	intake3		1
2	rib-end3		2
3	cowl3		1

UNLESS OTHERWISE SPECIFIED:
DIMENSIONS ARE IN MILLIMETERS
SURFACE FINISH: $\sqrt{6.3}$
TOLERANCES:
LINEAR: ± 0.2
ANGULAR: $\pm 1^\circ$

FINISH:

$\sqrt{6.3}$

DEBUR AND
BREAK SHARP
EDGES

DO NOT SCALE DRAWING.

VERSION

B

NAME:
DRAWN: Carolyn Jooos
CHKD:
APPVD:
MFG:
QA:

SIGNATURE

DATE
25/03/2011



MATERIAL:
Aluminium Alloy 6061

WEIGHT:

TITLE:

Lightcraft - Exp1

DWG NO.

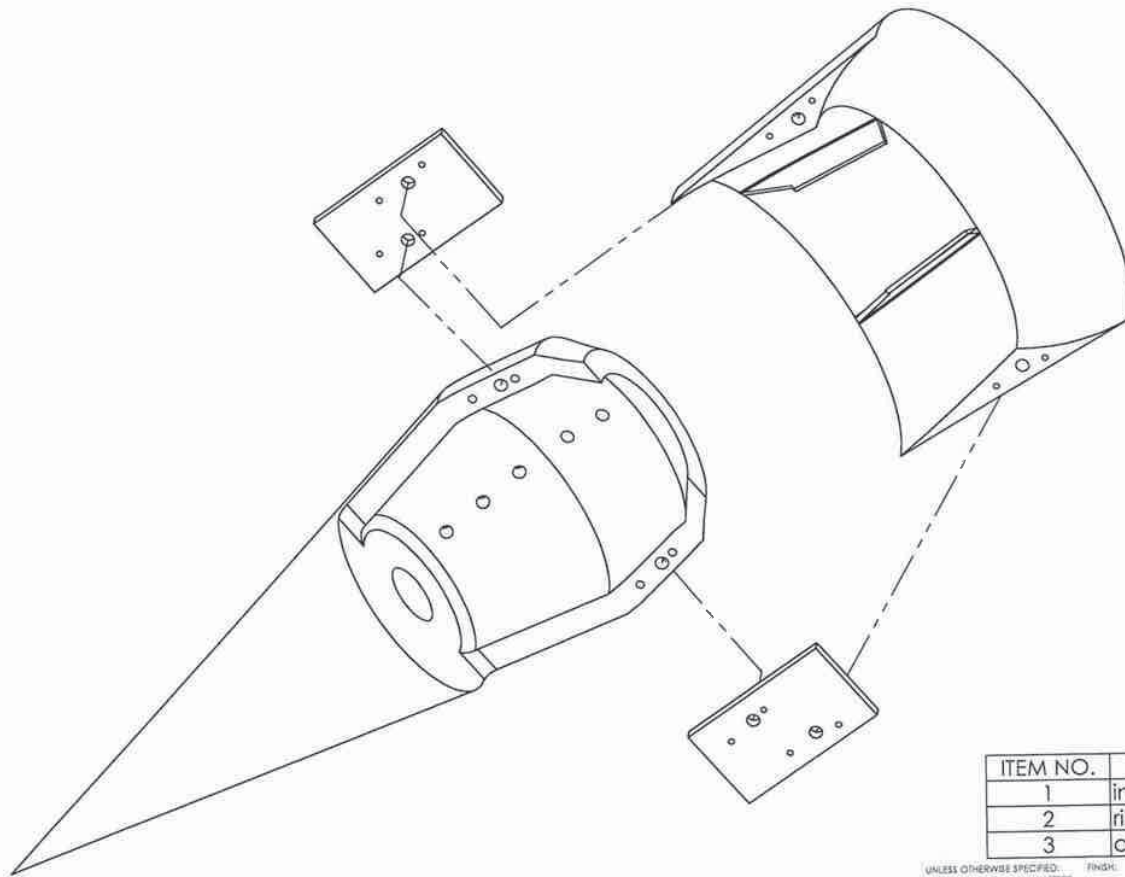
ASSY-2

SCALE:1:2

SHEET 2 OF 8

A3

61



REVISIONS				
ZONE	REV.	DESCRIPTION	DATE	APPROVED
-	-	See Assembly	-	-

ITEM NO.	PART NUMBER	DESCRIPTION	QTY.
1	intake3		1
2	rib-end3		2
3	cowl3		1

UNLESS OTHERWISE SPECIFIED:
DIMENSIONS ARE IN MILLIMETERS
SURFACE FINISH: $\sqrt{6.3}$
TOLERANCES:
LINEAR: ± 0.2
ANGULAR: $\pm 1^\circ$

FINISH:

$\sqrt{6.3}$

DEBUR AND
BREAK SHARP
EDGES

DO NOT SCALE DRAWING.

VERSION

B

NAME
DRAWN: Carolyn Jobobi
CHKD
APPVD
MFG
Q.A

SIGNATURE

DATE
25/03/2011



Third angle

MATERIAL:
Aluminium Alloy 6061

WEIGHT:

TITLE

Lightcraft - Exp2

DWG NO.

ASSY-3

SCALE:1:2

SHEET 3 OF 8

A3

A

B

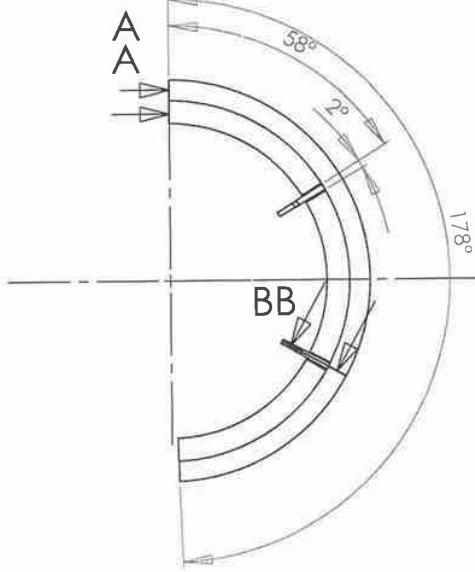
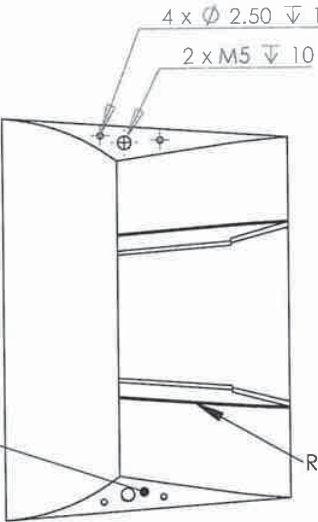
C

D

E

F

20

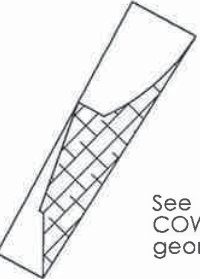
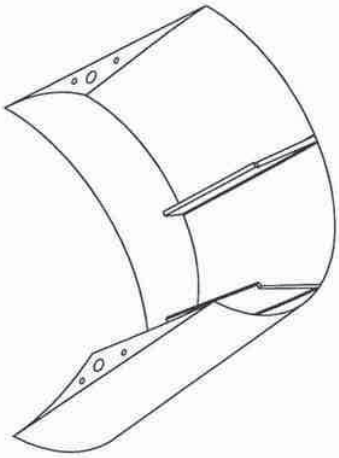


SECTION A-A

ORIGIN POINT
for geometry information

Corner angle 133.67°

See Drawing
COWL-5 for
geometry details



See Drawing
COWL-5 for
geometry details

SECTION B-B

Surface Finish:
1.6/ ∇ on all interior
cowl surfaces
including the inner
struts

General Tolerances	
Dimensions	Tolerances
0.5 < 3	±0.05
3 < 6	±0.05
6 < 30	±0.1
30 < 120	±0.15
120 < 400	±0.2

ALL DIMENSIONS ARE IN
MILLIMETERS

FINISH:

∇ 6.3

DEBUR AND
BREAK SHARP
EDGES

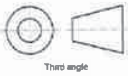
DO NOT SCALE DRAWING

VERSION

NAME
DRAWN Carolyn Jacobs
CHKD
APPV D
MFG
Q.A.

SIGNATURE

DATE
25/03/2011



Third angle

MATERIAL:
Aluminium Alloy 6061

WEIGHT:

TITLE:

Lightcraft - Cowl

DWG NO:

COWL-4

SCALE:1:2

SHEET 4 OF 8

A3

4

The outer surface is a straight surface from the first point to the last point.

This geometry is valid for the two end locations (0° and 178°)

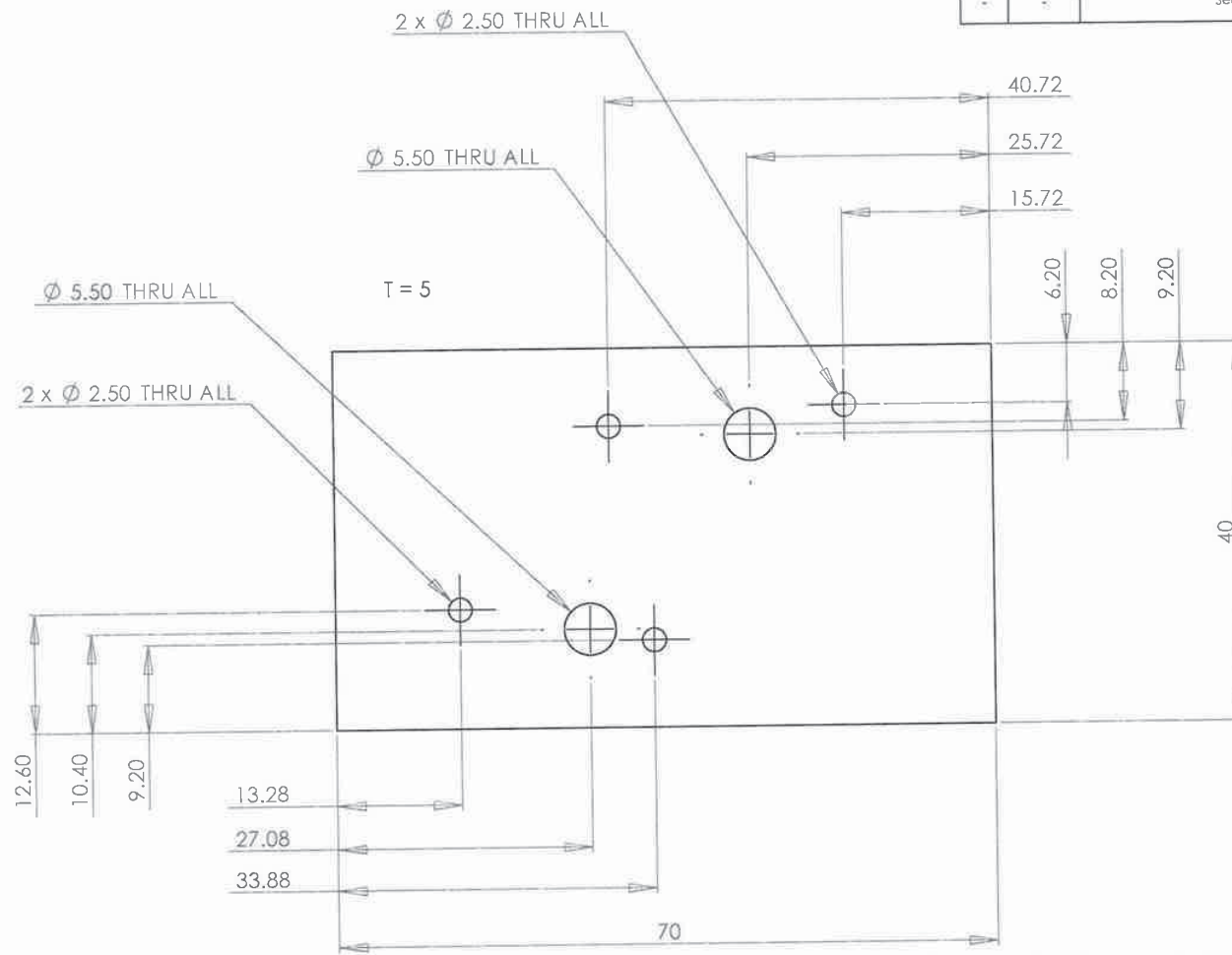
8

The outer surface is a straight surface from the first point to the last point.

VERSION

SHEET 5 OF 8

22

ALL DIMENSIONS ARE IN
MILLIMETERS

FINISH:

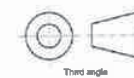
 $\sqrt{6.3}$ DEBUR AND
BREAK SHARP
EDGES

DO NOT SCALE DRAWING

VERSION 8

NAME
DRAWN Carolyn Jacobs
CHECKED
APPROVED
MFG
Q.A.

SIGNATURE
DATE 25/03/2011



Third angle

MATERIAL:
Aluminium Alloy 6061

WEIGHT:

TITLE:

Lightcraft - Strut

DWG NO.

STRUT-6

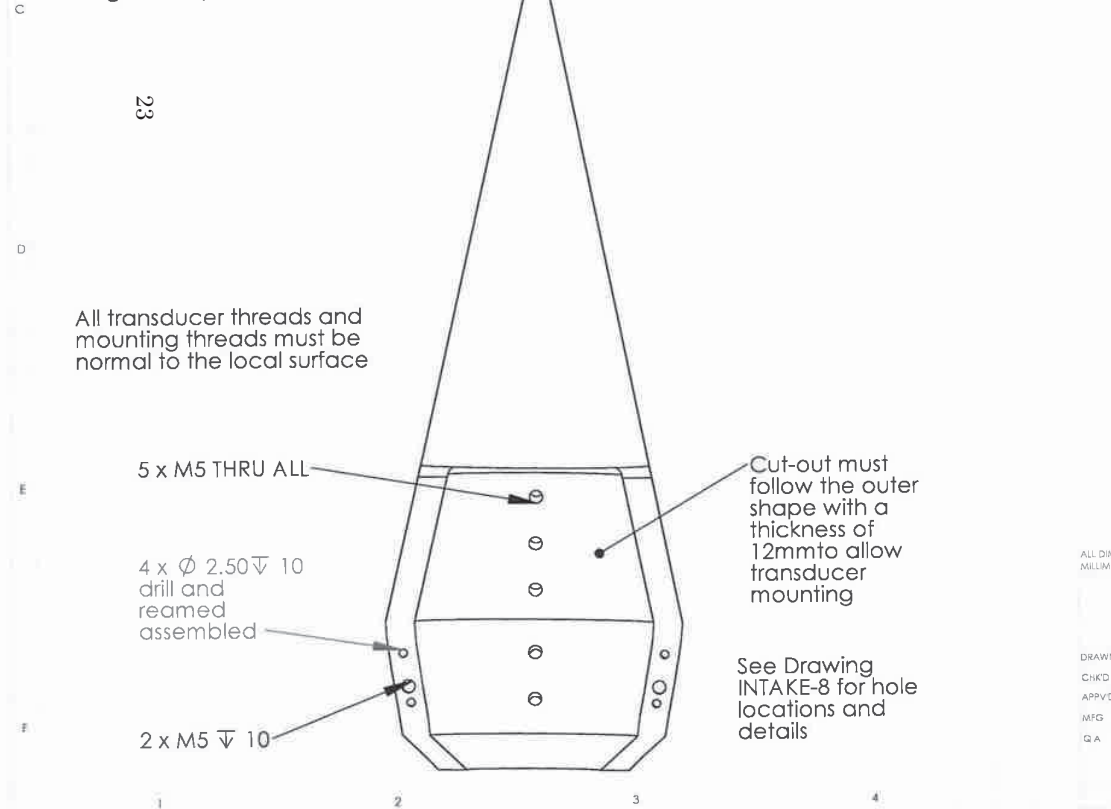
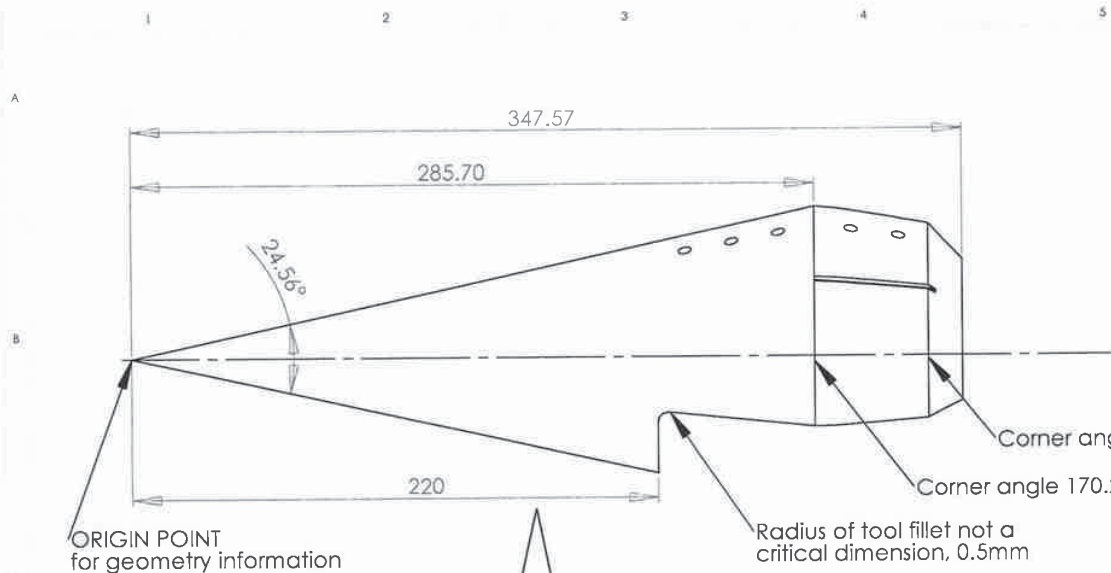
SCALE:2:1

SHEET 6 OF 8

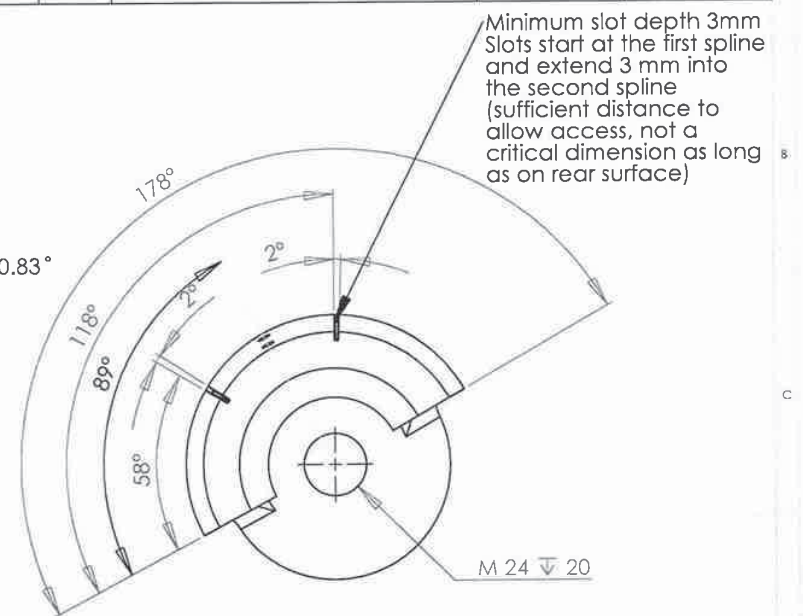
REVISIONS				
ZONE	REV.	DESCRIPTION	DATE	APPROVED
-	-	See Assembly	-	-

General Tolerances	
Dimensions	Tolerances
0.5 < 3	±0.05
3 < 6	±0.05
6 < 30	±0.1
30 < 120	±0.15
120 < 400	±0.2

A3



REVISIONS				
ZONE	REV.	DESCRIPTION	DATE	APPROVED
-	-	See Assembly	-	-



Surface Finish:
 $\sqrt{1.6}$ on all exterior surfaces

General Tolerances	
Dimensions	Tolerances
0.5 < 3	±0.05
3 < 6	±0.05
6 < 30	±0.1
30 < 120	±0.15
120 < 400	±0.2

ALL DIMENSIONS ARE IN MILLIMETERS

FINISH:

$\sqrt{6.3}$

DEBUR AND BREAK SHARP EDGES

DO NOT SCALE DRAWING

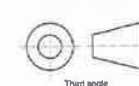
VERSION

B

NAME
 DRAWN Carolyn Jacobs
 CHK'D
 APP'D
 JMG
 Q A

SIGNATURE

DATE
 25/03/2011



MATERIAL:
 Aluminium Alloy 6061

WEIGHT:

TITLE:

Lightcraft - Intake

DWG NO.

INTAKE-7

A3

SCALE: 1:2

SHEET 7 OF 8

Outer Surface Geometry for Intake		
Axial Dimension	Radial Dimension	Note
0.0	0.0	Straight
285.7	62.2	
292.1	61.8	
299.0	60.8	
305.9	59.7	
312.8	58.6	First spline
319.6	57.4	
326.5	56.2	
333.3	55.0	
347.57	40.0	
350.0	37.8	Second spline
370.0	23.79	
390.0	14.2	
410.0	7.73	
430.0	3.51	
450.0	1.07	
476.2	0.0	

Point (347.57,40.0) marks the end of the model. Additional spline geometry is given in the table for reference.

Hole Positioning Details		
Axial Dimension	Radial Dimension	Type
299.0	54.8	Dowel
312.8	52.6	M5 thread
319.6	51.4	Dowel

Axial Location of Transducer Threads	
1	231.62
2	251.16
3	270.70
4	301.33
5	321.06

The transducer locations are flexible. The critical requirements are:

- 3 transducers on the intake surface
- 2 transducers on the spline surface
- transducers should be 20 mm apart on each surface
- transducer holes have an M5 thread
- the plane of the transducers is at the midpoint between the two strut slots

General Tolerances	
Dimensions	Tolerances
0.5 < 3	±0.05
3 < 6	±0.05
6 < 30	±0.1
30 < 120	±0.15
120 < 400	±0.2

ALL DIMENSIONS ARE IN MILLIMETERS

FINISH:

$\sqrt{6.3}$

DEBUR AND BREAK SHARP EDGES

DO NOT SCALE DRAWING

VERSION

8

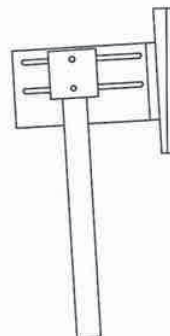
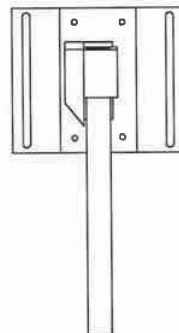
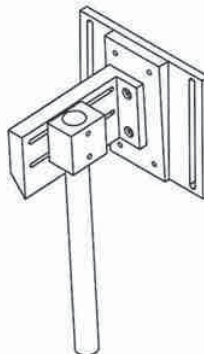
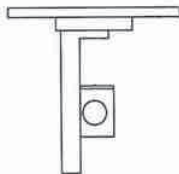
DRAWN: Carolyn Jacobs
 APPVD:
 MFG:
 Q.A:

DATE: 25/03/2011
 THIRD ANGLE
 MATERIAL: Aluminium Alloy 6061
 WEIGHT:

TITLE: Lightcraft - Intake(detl)
 DWG NO: INTAKE-8
 SCALE: 1:2
 SHEET 8 OF 8

A3

25



REVISIONS				
ZONE	REV.	DESCRIPTION	DATE	APPROVED

ITEM NO.	PART NUMBER	DESCRIPTION	QTY.
1	base		1
2	wedge-3deg		1
3	frame		1
4	sting-block		1
5	sting		1

ALL DIMENSIONS ARE IN
MILLIMETERS

FINISH

$\sqrt{\quad} = 6.3$

DEBUR AND
BREAK SHARP
EDGES

DO NOT SCALE DRAWING

VERSION

B

NAME
DRAWN Carolyn Jacobs
CHKD
APPVD
MFG
Q.A.

SIGNATURE

DATE
25/03/2011



Third angle

MATERIAL

Mild Steel

WEIGHT

TITLE

3deg Mount - ASSY

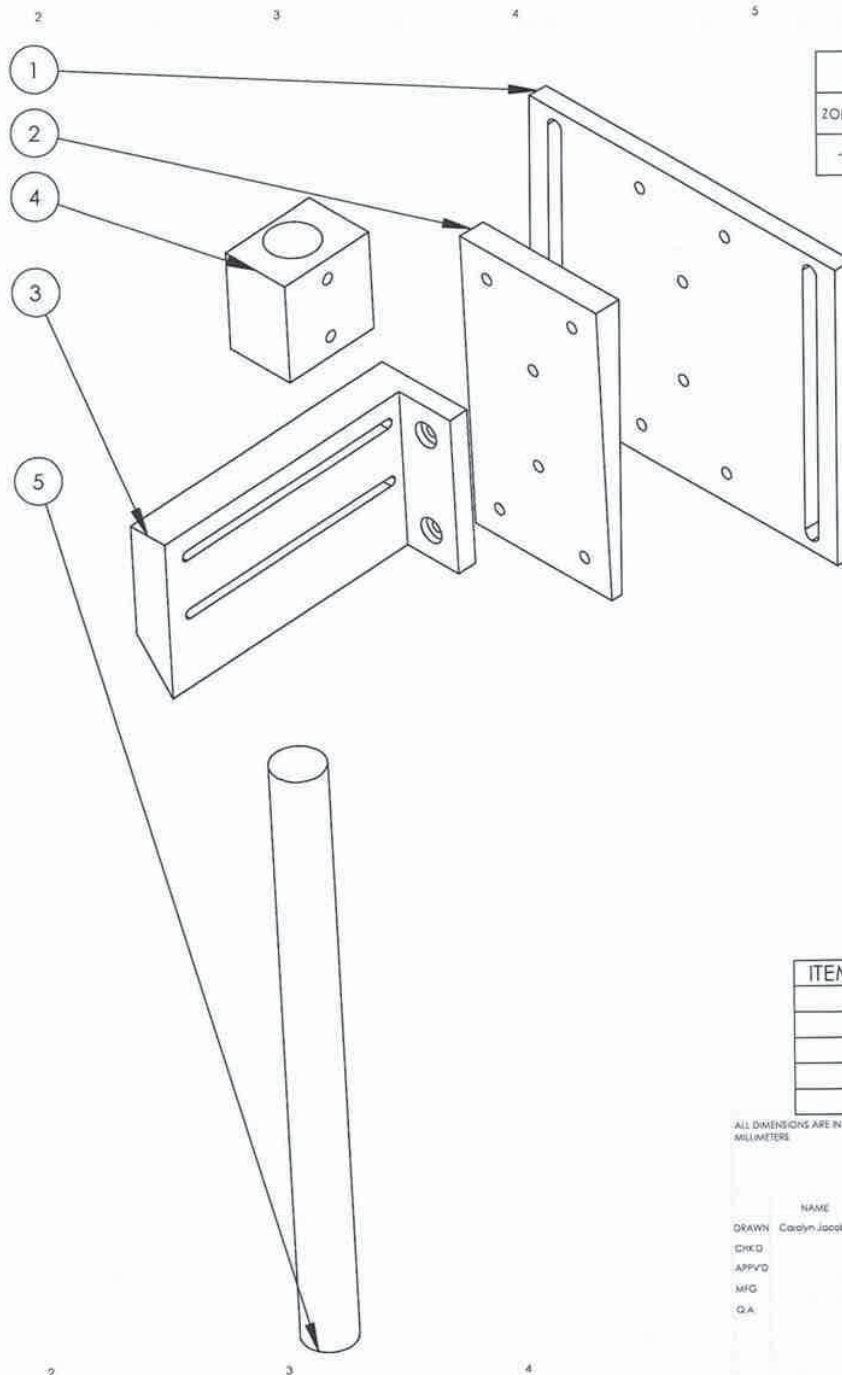
DWG NO.

ASSY-M3-1

SCALE:1:5

SHEET 1 OF 10

A3



REVISIONS				
ZONE	REV.	DESCRIPTION	DATE	APPROVED
-	-	See Assembly	-	-

ITEM NO.	PART NUMBER	DESCRIPTION	QTY.
1	base		1
2	wedge-3deg		1
3	frame		1
4	sting-block		1
5	sting		1

ALL DIMENSIONS ARE IN
MILLIMETERS

FINISH:

✓ = 6.3

DEBUR AND
BREAK SHARP
EDGES

DO NOT SCALE DRAWING

VERSION

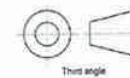
8

DRAWN
CHKD
APPVD
MFG
QA

NAME
Carolyn Jacobs

SIGNATURE

DATE
25/03/2011



Third angle

MATERIAL:

Mild Steel

WEIGHT:

TITLE:

3deg Mount - Exp

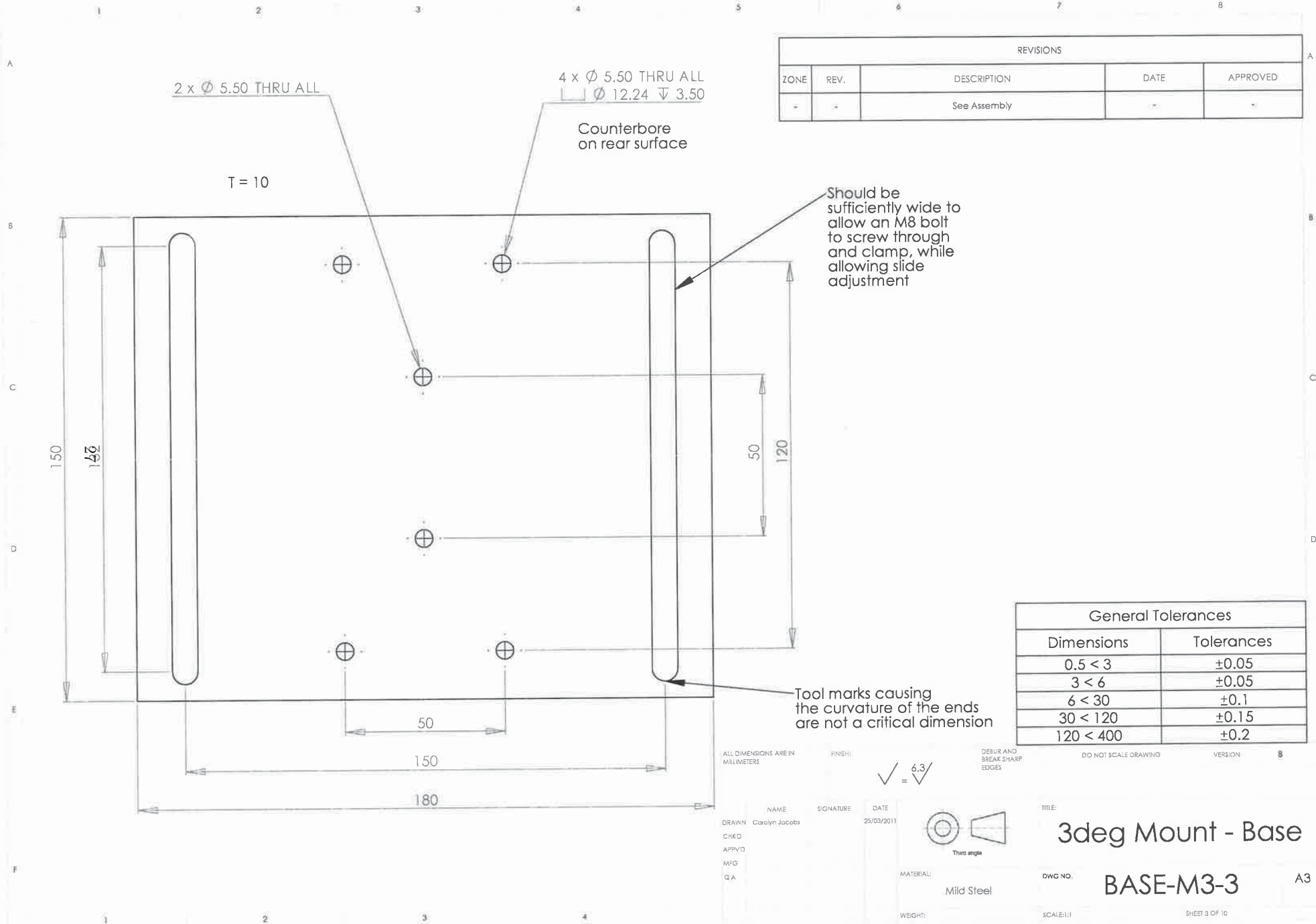
DWG NO:

ASSY-M3-2

SCALE:1:2

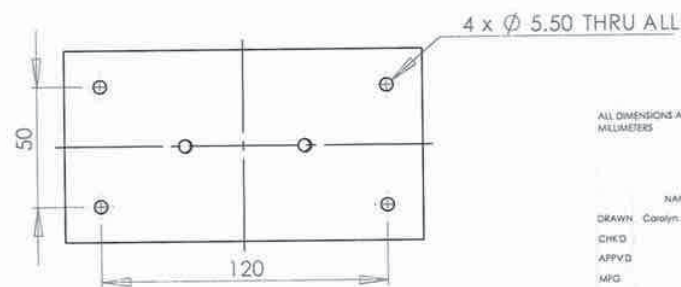
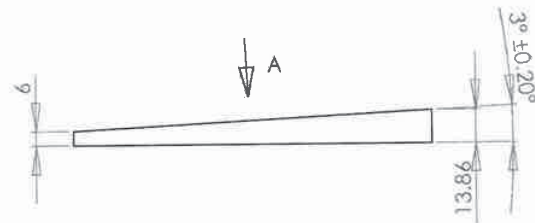
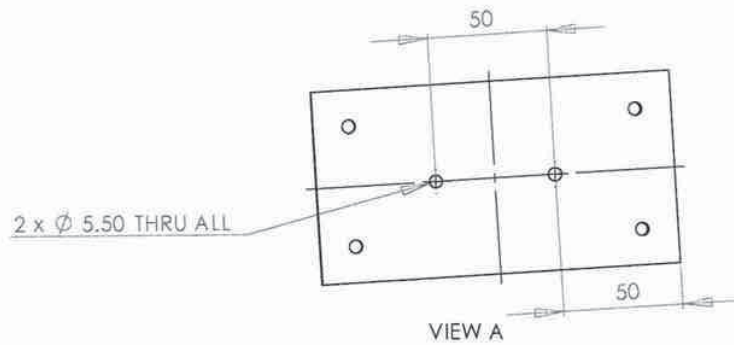
SHEET 2 OF 10

A3

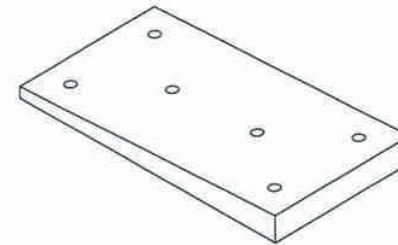


REVISIONS				
ZONE	REV.	DESCRIPTION	DATE	APPROVED
-	-	See Assembly	-	-

General Tolerances	
Dimensions	Tolerances
0.5 < 3	±0.05
3 < 6	±0.05
6 < 30	±0.1
30 < 120	±0.15
120 < 400	±0.2



REVISIONS:				
ZONE	REV.	DESCRIPTION	DATE	APPROVED
-	-	See Assembly	-	-



General Tolerances	
Dimensions	Tolerances
0.5 < 3	± 0.05
3 < 6	± 0.05
6 < 30	± 0.1
30 < 120	± 0.15
120 < 400	± 0.2

DO NOT SCALE DRAWING

VERSION B

ALL DIMENSIONS ARE IN MILLIMETERS

FINISH:

 $\sqrt{\quad} = 6.3$

DEBUR AND BREAK SHARP EDGES

NAME
DRAWN: Carolyn Jacobs
CHK'D
APP'D
MPG
G.A.

SIGNATURE

DATE
05/03/2011

Third angle

MATERIAL:

Mild Steel

WEIGHT:

TITLE:

3deg Mount - Wedge

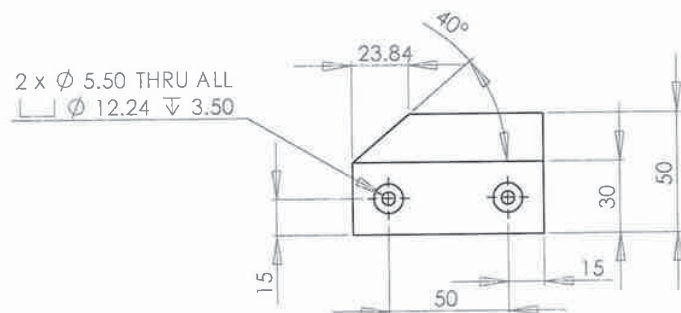
DWG NO.

WEDGE-M3-4

A3

SCALE: 1:2

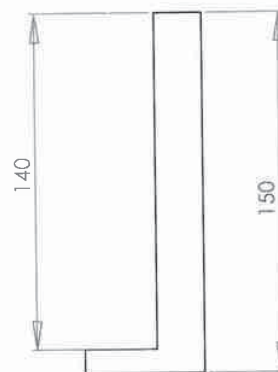
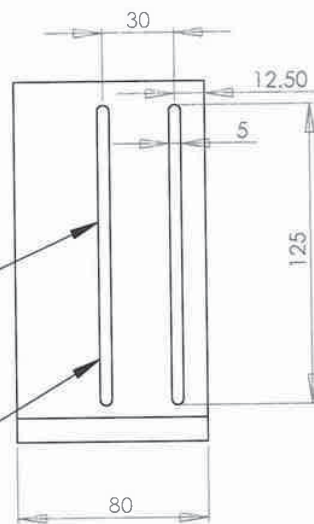
SHEET 4 OF 10



29

Needs to be sufficiently wide for an M5 bolt to screw through from the back into the mounting plate of the sting and slide while maintaining height when clamped

Tool marks causing the curvature of the ends are not a critical dimension



REVISIONS				
ZONE	REV.	DESCRIPTION	DATE	APPROVED
-	-	See Assembly	-	-

General Tolerances	
Dimensions	Tolerances
0.5 < 3	±0.05
3 < 6	±0.05
6 < 30	±0.1
30 < 120	±0.15
120 < 400	±0.2

ALL DIMENSIONS ARE IN MILLIMETERS

FINISH:

✓ = 6.3

DEBUR AND BREAK SHARP EDGES

DO NOT SCALE DRAWING

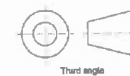
VERSION

B

NAME
DRAWN: Carolyn Jacobs
CHKD
APPVD
MFO
QA

SIGNATURE

DATE
25/03/2011



MATERIAL:
Mild Steel

WGHT:

TITLE:

3deg Model - Frame

DWG NO.

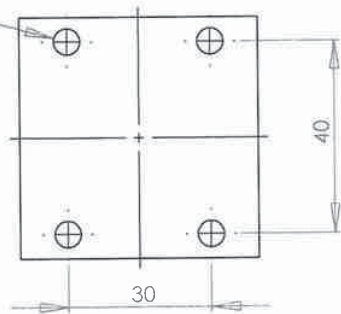
FRAME-M3-5

A3

SCALE:1:2

SHEET 3 OF 10

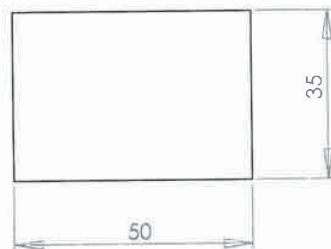
A

4 x \varnothing 5.50 ∇ 10

B

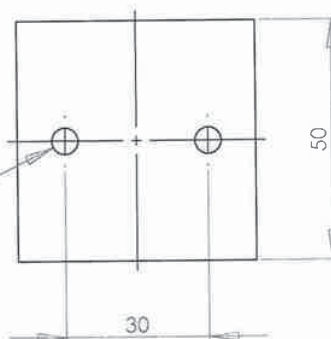
C

30



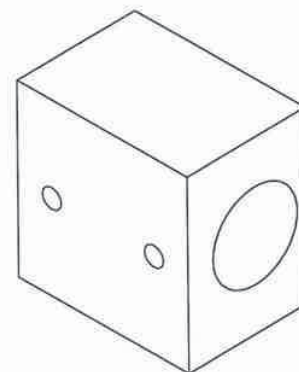
D

E

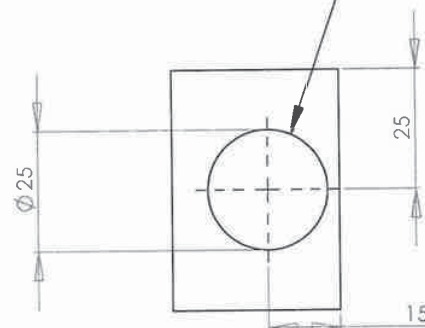
2 x \varnothing 5.50 THRU

F

REVISIONS				
ZONE	REV.	DESCRIPTION	DATE	APPROVED
-	-	See Assembly	-	-



Fit with sting should be close fit, but allow smooth sliding and rotating



ALL DIMENSIONS ARE IN MILLIMETERS

FINISH:

 $\sqrt{\text{6.3}}$

DEBUR AND
BREAK SHARP
EDGES

DO NOT SCALE DRAWING

VERSION

B

General Tolerances

Dimensions	Tolerances
0.5 < 3	±0.05
3 < 6	±0.05
6 < 30	±0.1
30 < 120	±0.15
120 < 400	±0.2

DRAWN: Carlyn Jacobs
CHKD:
APPVD:
MFG:
QA:

SIGNATURE

DATE

25/03/2011



Third angle

MATERIAL:

Mild Steel

WEIGHT:

TITLE:

3deg Mount - Block

DWG NO.

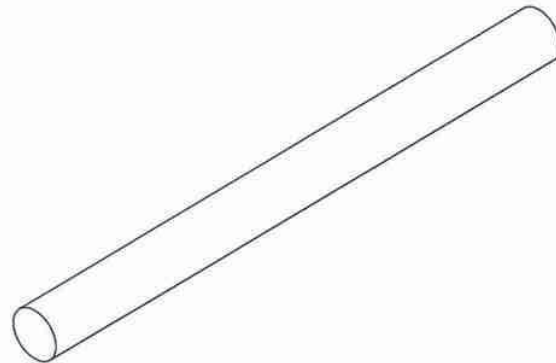
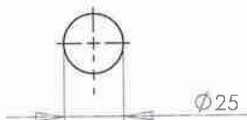
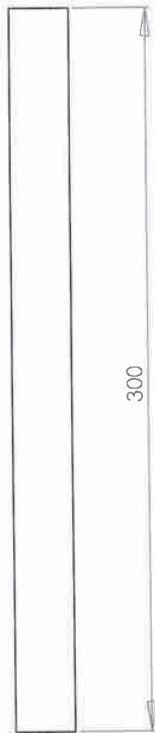
BLOCK-M3-6

A3

SCALE:1:1

SHEET 6 OF 10

31



This end requires an M24 thread to a length of 20mm from the end face

This end fits with the sting block as a sliding clearance fit



REVISIONS				
ZONE	REV.	DESCRIPTION	DATE	APPROVED
		See Assembly		

General Tolerances	
Dimensions	Tolerances
0.5 < 3	±0.05
3 < 6	±0.05
6 < 30	±0.1
30 < 120	±0.15
120 < 400	±0.2

ALL DIMENSIONS ARE IN MILLIMETERS

FINISH:



DEBUR AND BREAK SHARP EDGES

DO NOT SCALE DRAWING

VERSION: B

NAME
DRAWN: Carolyn Jacobs
CHKD
APPVD
MFG
QA

SIGNATURE

DATE
25/03/2011



Third angle

MATERIAL:

Mild Steel

WEIGHT:

TITLE:

3deg Mount - Sting

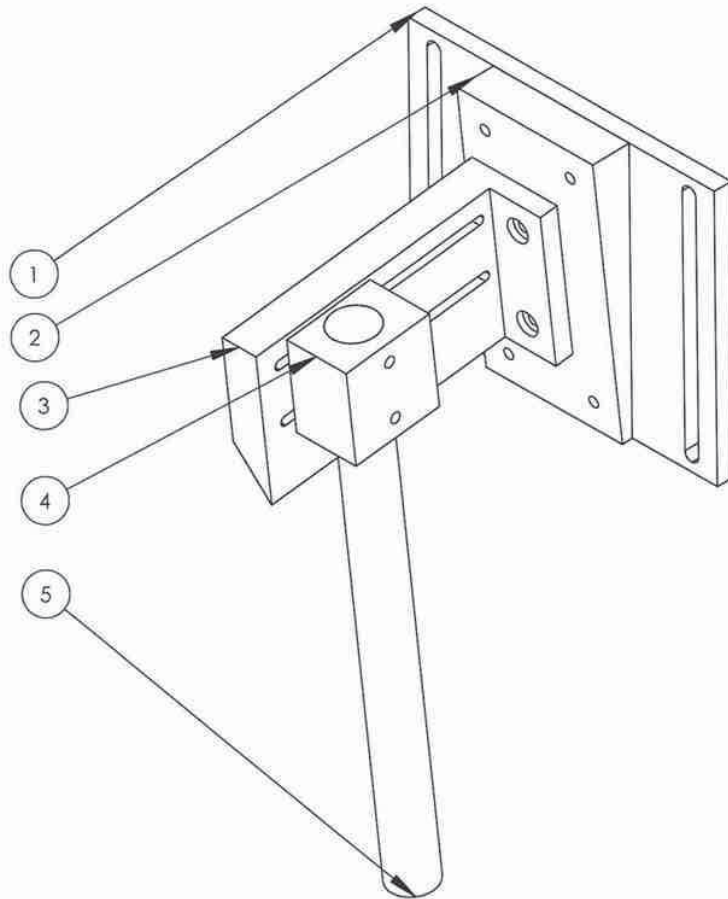
DWG NO.

STING-M3-7

A3

SCALE:1:1

SHEET 7 OF 10



REVISIONS				
ZONE	REV.	DESCRIPTION	DATE	APPROVED
-	-	See Assembly	-	-

ITEM NO.	PART NUMBER	DESCRIPTION	QTY.
1	base		1
2	wedge-6deg		1
3	frame		1
4	sting-block		1
5	sting		1

ALL DIMENSIONS ARE IN MILLIMETERS

FINISH:

$\sqrt{6.3}$

DEBUR AND BREAK SHARP EDGES

DO NOT SCALE DRAWING

VERSION

B

NAME
DRAWN Carolyn Jacobs
CHKD
APPRD
MFD
Q/A

SIGNATURE

DATE
25/03/2011



MATERIAL:

Mild Steel

WEIGHT:

TITLE:

6deg Mount - ASSY

DWG NO.

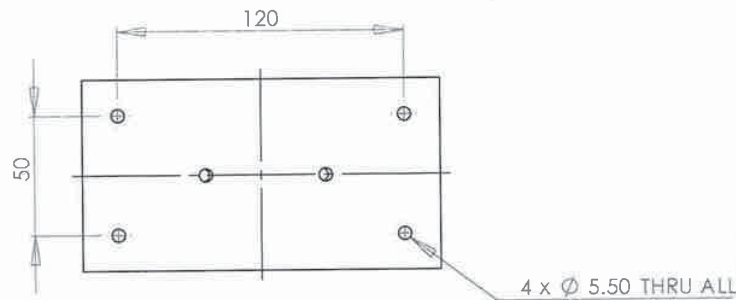
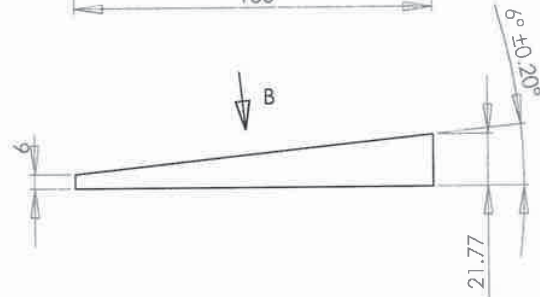
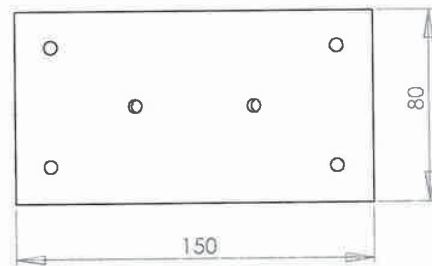
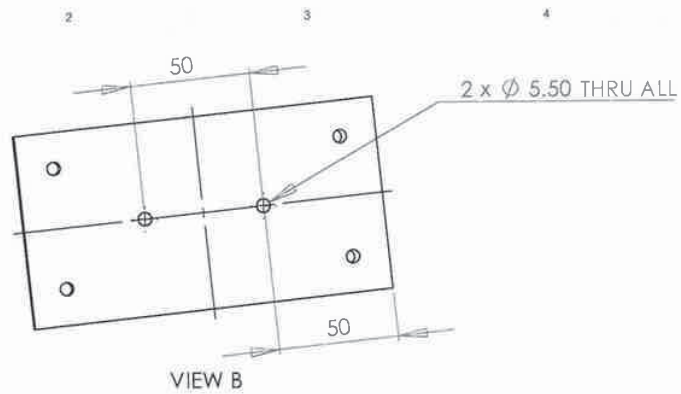
ASSY-M6-1

SCALE:1:2

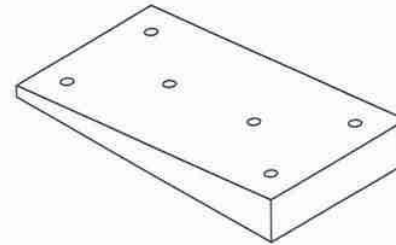
SHEET 8 OF 10

A3

33



REVISIONS				
ZONE	REV.	DESCRIPTION	DATE	APPROVED
-	-	See Assembly 1	-	-



General Tolerances	
Dimensions	Tolerances
0.5 < 3	±0.05
3 < 6	±0.05
6 < 30	±0.1
30 < 120	±0.15
120 < 400	±0.2

ALL DIMENSIONS ARE IN MILLIMETERS

FINISH:

✓ = 6.3

DEBUR AND BREAK SHARP EDGES

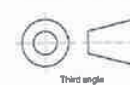
DO NOT SCALE DRAWING

VERSION B

NAME
DRAWN: Carolyn Jacobs
CHKD:
APPVD:
MFG:
QA:

SIGNATURE

DATE
25/03/2011



MATERIAL:

Mild Steel

WEIGHT:

TITLE:

6deg Mount - Wedge

DWG NO.

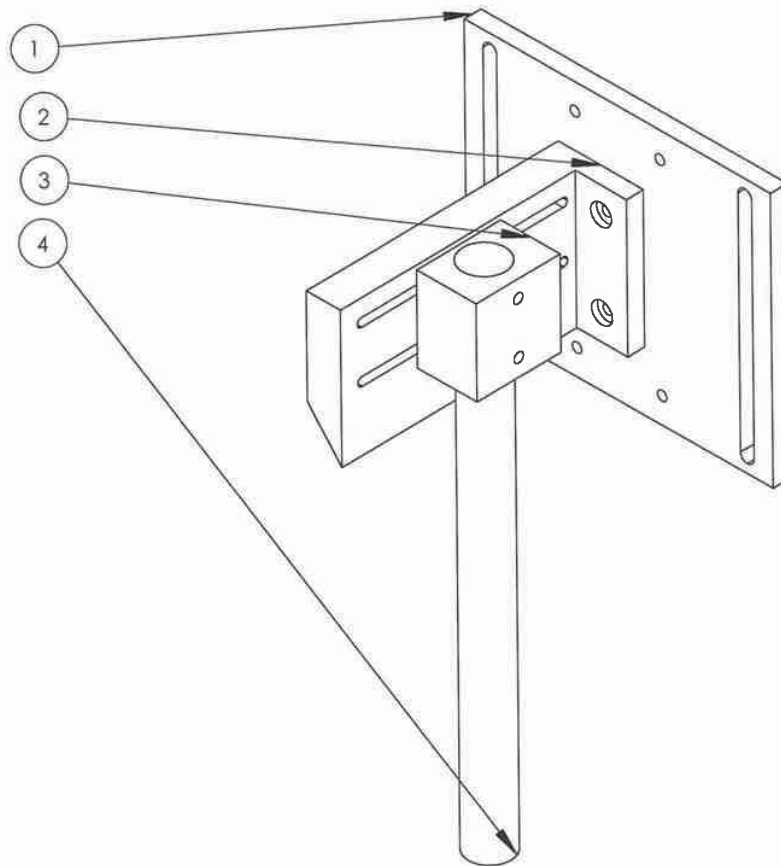
WEDGE-M6-2

A3

SCALE:1:2

SHEET 9 OF 10

34



REVISIONS				
ZONE	REV.	DESCRIPTION	DATE	APPROVED
-	-	See Assembly	-	-

ITEM NO.	PART NUMBER	DESCRIPTION	QTY.
1	base		1
2	frame		1
3	sting-block		1
4	sting		1

ALL DIMENSIONS ARE IN MILLIMETERS

FINISH:

✓ = 6.3

DEBUR AND BREAK SHARP EDGES

DO NOT SCALE DRAWING

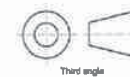
VERSION

B

NAME
DRAWN Carolyn Jacobs
CHKD
APPROV
MFG
Q.A

SIGNATURE

DATE
23/03/2011



Third angle

MATERIAL:

Mild Steel

WEIGHT:

TITLE:

Flat Mount - ASSY

DWG NO:

ASSY-FM-1

SCALE:1:2

SHEET 10 OF 10

A3

Part 3

Future flight test program

Logistics and Costs of a Future Lightcraft Test Program

AFOSR/AOARD Reference Number: AOARD-FA2386-09-1-4088

Author:

Dr Matthew Tetlow
School of Mechanical Engineering
University of Adelaide
South Australia 5005

Date: May 2012

Introduction

Lightcraft are an advanced technology at an embryonic stage of development. Considerable development and testing will be required before the technology can be used reliably. To that end a test program is proposed to investigate and develop hypersonic inlet design and laser combustor design and operation.

The idea is to move along the development path by incrementally increasing the complexity of the system, until a final free flying system is developed. Currently, analysis and modelling studies are under way on the development of the lightcraft itself as well as development of the laser to power it. One such study is the hypersonic inlet design study [1]. Once the technology has matured a flight test program would be conducted to test and further develop the technology.

It is proposed that a low risk approach would be to develop a stable test platform based on existing technologies to run repeated tests. This would enable many aspects and designs of lightcraft to be investigated without risking the loss of the vehicle. Also, the test article would be recovered in each case enabling easier post flight analysis.

Aim

The aim of this report is to present the results of an analysis of a test program for the development of lightcraft, including range, logistics and trajectory information. The lightcraft design would be based on the modular stream traced inlet design study by Harrland [1], shown in Figure 1, and weigh 8kg, with a 350mm diameter and a 960mm length. The test program would be broken down into three sections, each one progressing the technology a little further.

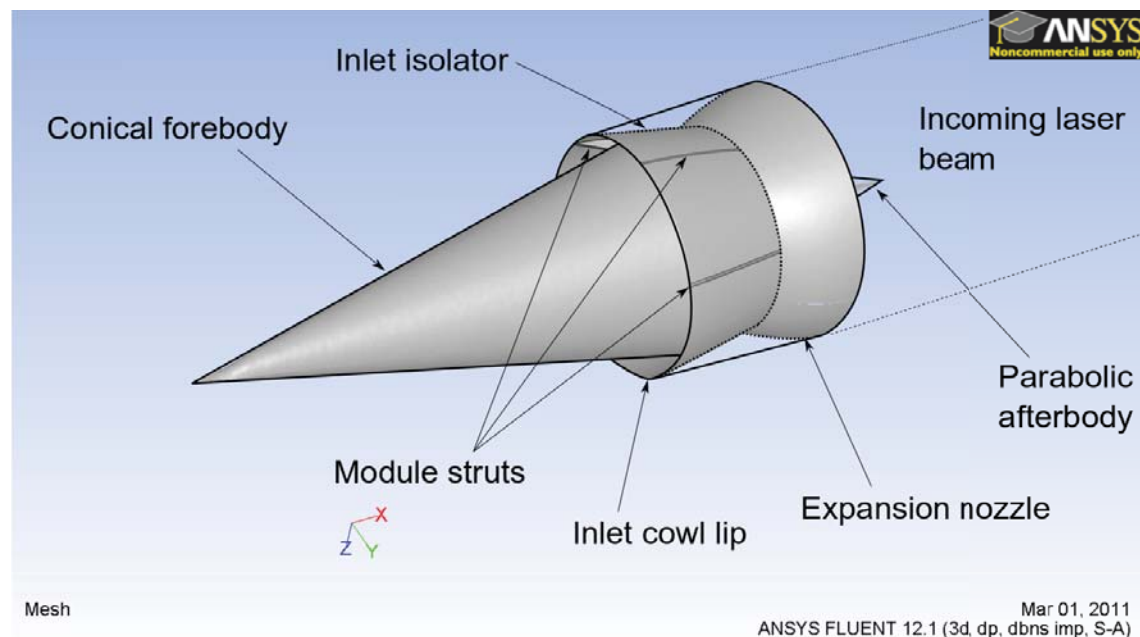


Figure 1. Stream traced modular axis symmetric lightcraft design [1]

The first test campaign will be an inlet investigation program. A recoverable/reusable X-plane booster will be developed to boost the lightcraft to the required operating conditions. The light craft will remain attached to the booster and operate in a captive-carry mode. The booster will provide a stable platform that can maintain the required operating condition for up to 20 seconds, enabling forebody and inlet development as well as materials investigations. The test vehicle will also be recoverable to aid in post flight analysis

Once most of the inlet and materials issues have been overcome, the same booster will be used to propel the lightcraft to a particular operating condition where it will be released. At this point the laser will propel the lightcraft for a short duration flight. The lightcraft will be passively stable, so no advanced control systems will be needed. Initially the program will focus on demonstrating a drag-matched thrust cruise flight condition. After this has been successfully demonstrated, the laser power will be increased gradually and the program will progress to establishing accelerating flight. These latter tests would mature the technology related to combustor design and thrust production in the Mach 6 - 10 operating regime.

The final phase of testing will be to investigate laser ground launch of the lightcraft and will include all aspects of lightcraft vehicle design.

Trajectory simulation model

A three-degree of freedom simulation environment was used to model the vehicle trajectory. The seven state model was integrated using a 4th order Runge Kutta integration technique. Full details of state model can be found in [2]. A Newton-Raphson two point boundary condition solver was used to achieve the correct conditions at the end of the boost phase [3].

A MSISE93 (Mass-Spectrometer-Incoherent-Scatter) atmospheric model [4] was used to calculate the atmospheric density, pressure and temperature during the mission. This is a position specific model that uses both satellite and terrestrially based measurements and averages to calculate the atmospheric composition and parameters based on a specific location and time, considering solar and geomagnetic activity. No wind model was used in this study. An oblate earth shape model [5] was used with a fourth order earth gravitation model [5].

Winged booster model

A conceptual booster model was developed in order to perform a trajectory analysis of the first two test phases discussed above, ie the captive-carry inlet design test phase and the Mach 8 release test phase. The maximum take-off weight of the conceptual booster is 7 tonnes. It has a pair forward canard wings in addition to two large aft wings. The booster uses a liquid oxygen (LOx)/Kerosene rocket propulsion system. Although solid propulsion would be well suited to a booster of this size, the requirement to be versatile and operate at different altitudes and Mach Numbers makes a throttleable liquid engine the best option. The aerodynamics model used in these simulations was based on data from a winged booster stage of a conceptual launch system called Ariane-X (see Figure 2). Figure 3 shows a schematic of what the booster would look like.

The maximum propellant capacity of the booster was 5510kg. A structural coefficient of 25% was chosen for the design; as the vehicle has relatively large aerodynamic surfaces and has a relatively small initial mass. The booster was designed to test different flight conditions for different lengths of time. This wide range of operating requirements means that the booster must be versatile, rather than optimal for any specific mission. In test cases where the whole fuel load was not required, the saved fuel mass could be used as extra payload. For a mission that requires a lightcraft to be boosted to Mach 8 and maintain this flight condition for 20 seconds, around 300kg of additional experimental equipment (instrumentation, data acquisition systems, etc.) may be flown on-board.

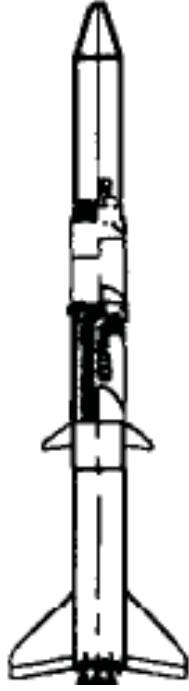


Figure 2 ArianeX conceptual launch system

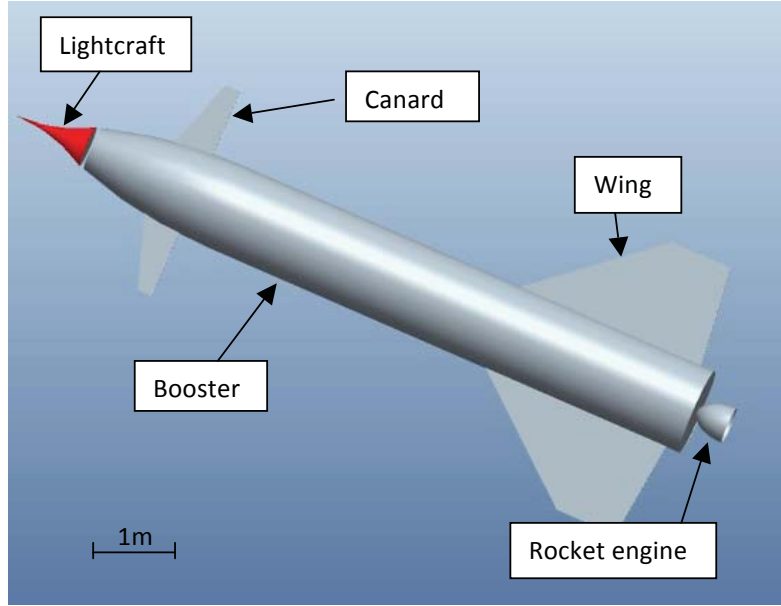


Figure 3 Booster concept vehicle

Trajectory parameterisation

The trajectory was broken into four flight segments for analysis purposes. Each segment had its own control methods and parameters, depending on the mission requirements. The first segment was a vertical climb, in which the angle of attack is set to zero. This is a very short segment, only a few seconds. The boost segment was the second segment and it was controlled by five angle of attack parameters linearly interpolated between time-based grid points. The third segment was the test phase, during which two decoupled controllers were used to regulate altitude and dynamic pressure. A proportional-derivative angle of attack controller was used to maintain the desired altitude and had the form:

$$\alpha = \alpha_{current} + k_{alf1} (h_{required} - h_{current}) - k_{alf2} (v \sin \gamma)$$

Where α is angle of attack, γ is flight path angle and v is velocity.

A simple linear proportional controller was used to regulate the engine throttle to control dynamic pressure, and had the following form:

$$th = th_{current} \left(\frac{q_{required}}{q_{current}} \right)$$

Where q is dynamic pressure and th is engine throttle setting.

Provided the altitude controller maintained the correct altitude, dynamic pressure control ensured the correct Mach number during the test phase.

Segment four was the turn and descent phase. No specific landing site was chosen, as this would require ground access to the Woomera range to look at various areas and assess their suitability for landing and this was not possible in the context of this study. Instead, a fixed bank angle of 30 degrees and a fixed angle of attack of 8 degrees was commanded to demonstrate down range and cross range capability. Figure 4. Booster flight segments Figure 4 shows these flight segments in more detail.

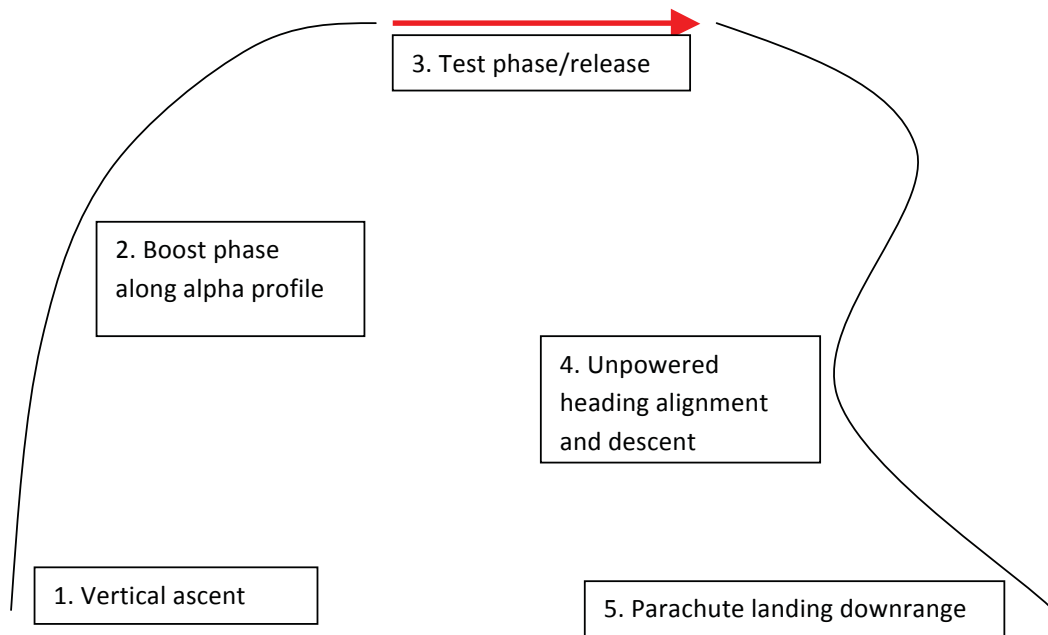


Figure 4. Booster flight segments

Following these flight segments, the vehicle would perform a heading alignment and controlled descent to a condition at which a parachute could be deployed. A set of skis would be deployed to land on, in order to protect the under-side of the vehicle.

Test phase 1 – Mach 8 captive-carry mission

The purpose of the first test phase will be for hypersonic inlet and materials development. The booster will launch vertically from the South Eastern corner of the Woomera test range, near the town of Woomera in South Australia and propel the vehicle to Mach 8. The test phase will be in a captive-carry configuration where the payload will remain attached to the booster while maintaining sustained Mach 8 flight for 20 seconds. After the test flight, the booster will perform cross range adjustments while performing an unpowered descent flight followed by a parachute landing, and helicopter recovery of the whole system. Figure 5 shows the mission profile.

Running a test campaign such as this will require significant equipment and personnel, which will need to be transported and set up in the relatively remote Australian outback. Approximately 25 people would be needed during the test campaign, with each test taking approximately 1 week. Ten technicians/engineers would prepare the booster for flight, including system checks, fuelling and integrating on the launch rail. There are processing hangars at the launch site, which could be rented

from the range operators. Three range safety officers will be required as well as ten range technicians to operate tracking equipment and for administrative tasks. Two defence observers will also be needed. The personnel required for the tests would be housed in Woomera and would commute to the launch site each day by road.

Each test will require half of an 8000 L iso-tanker¹ of LOx and one seventh of an 8000 L iso-tanker of kerosene. A temporary storage system for the LOx may be set up if a large number of tests were going to be conducted, slightly reducing the transportation costs. A CH-47 helicopter will need to be leased to recover the booster from down range and return it to the launch site. As the CH-47 does not have sufficient range to complete the mission, a fuel tanker will need to meet the helicopter along the road to Coober Pedy (A87) to refuel the helicopter

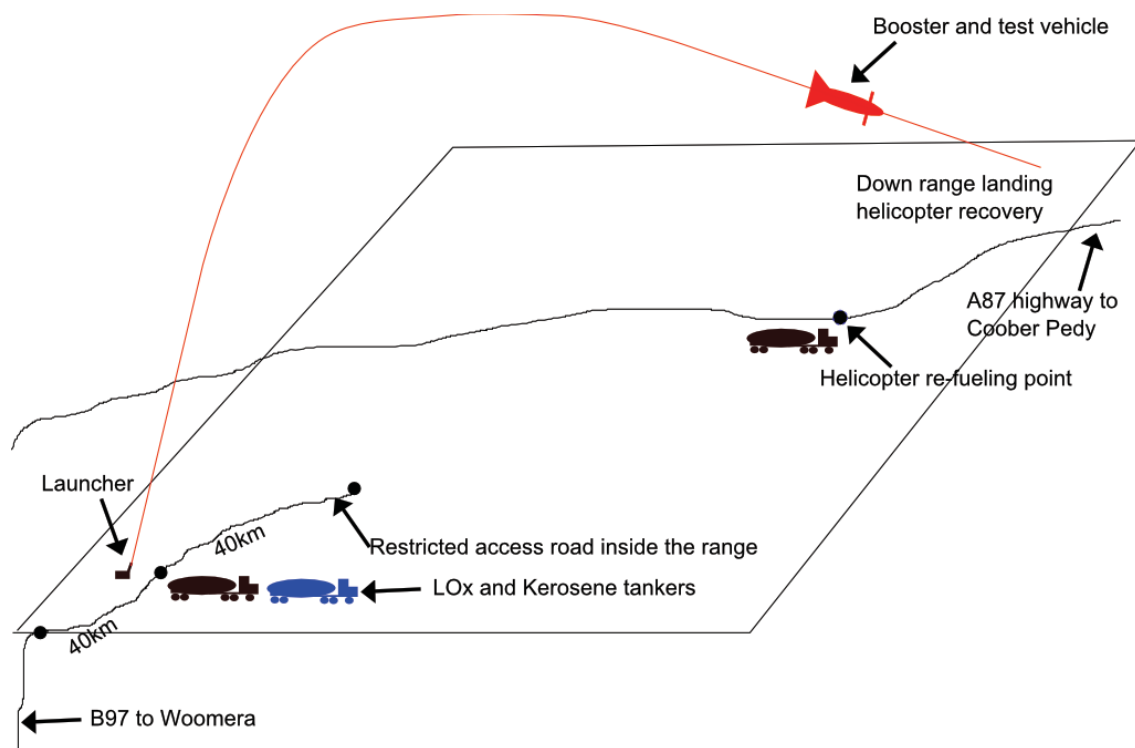


Figure 5 Mach 8 captive-carry mission profile

Trajectory

Figure 6 shows the ground track of the mission relative to the Woomera Prohibited Area (WPA) test range. The launch, test and recovery can all be undertaken within the range boundaries. The booster has considerable downrange and cross range capabilities so may land at a many different sites.

¹ An iso-tanker refers to a "pill shaped" steel tank within an International Standards Organisation frame, transported on a truck trailer. Iso-tankers vary in size from as low as 4000 L up to 25000 L.

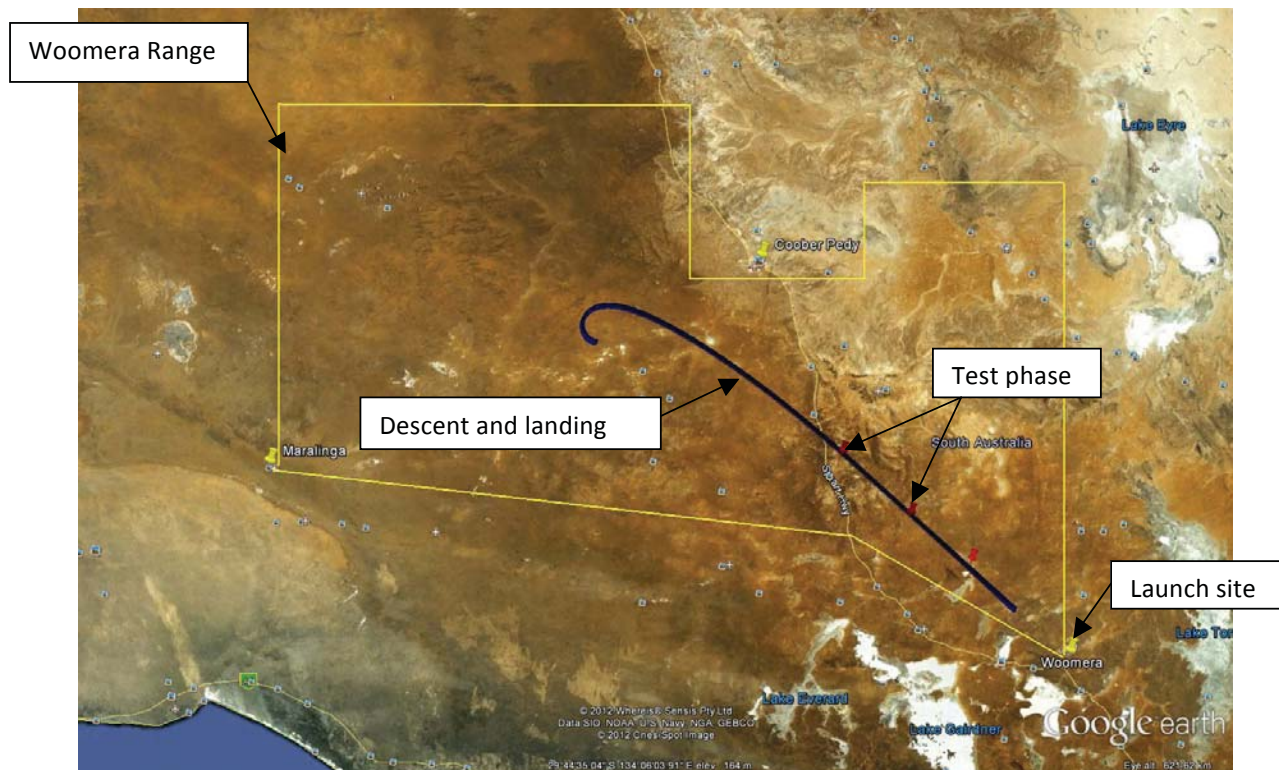


Figure 6 Ground track

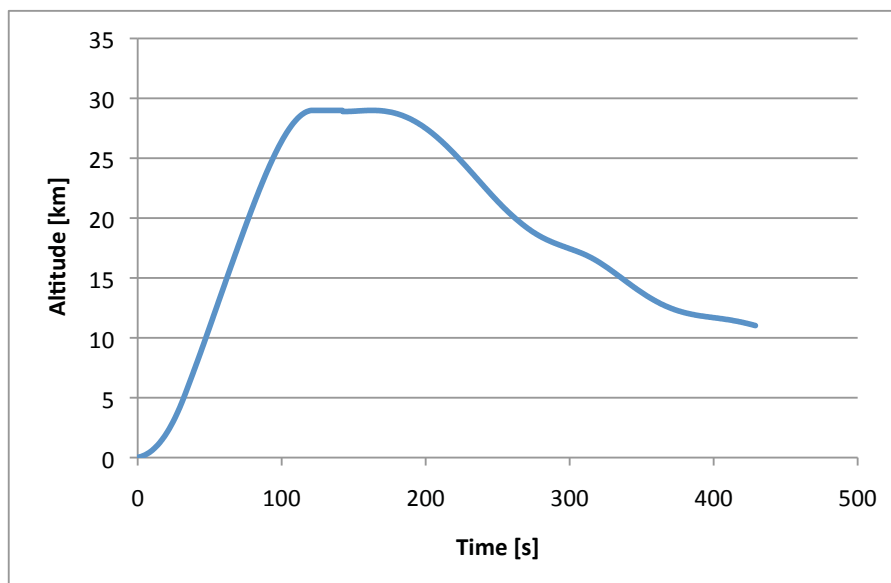


Figure 7 Altitude vs time

Figure 7 shows the altitude time history of the test flight. The long period oscillation seen in the graph is a result of constant control parameters being implemented. Again, the simulation of the descent and turn phase was purely to demonstrate cross range and down range capability.

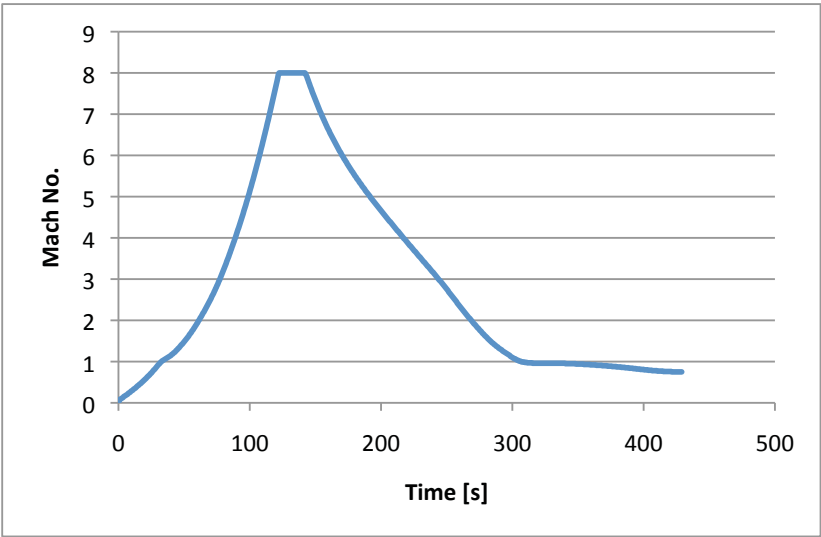


Figure 8 Mach Number vs time

Figure 8 shows the Mach number history of the flight showing a sustained Mach 8 test phase for 20 seconds, followed by a rapid reduction in Mach Number during descent.

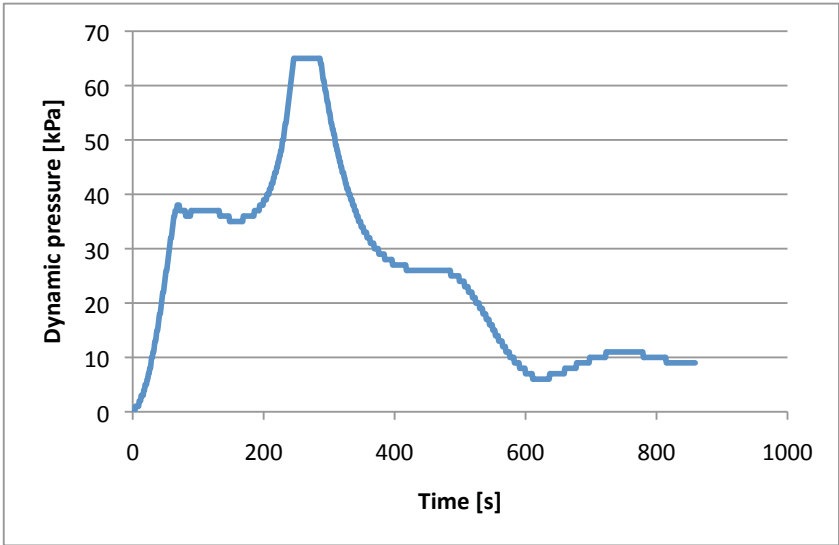


Figure 9 Dynamic pressure vs time

Figure 9 shows the dynamic pressure history for the flight. The dynamic pressure is relatively low for the flight, with a maximum of around 65kPa seen during the test phase. There is a slight decrease in dynamic pressure between 80s and 200s flight time. This is caused by the steep ascent profile.

Future challenges

This phase of the test campaign does not require any significant advances in technology and there are no large infrastructure costs. The only major cost would be the development of the winged booster. This would however involve using existing low risk rocket and aircraft type technology. The facilities to conduct these tests currently exist in Woomera.

Test phase 2 – Mach 8 release mission

The second test phase would be to demonstrate sustained thrust from a passively stable lightcraft. Again, the booster will launch vertically from the South Eastern corner of the Woomera test range, near the town of Woomera in South Australia and boost to Mach 8. At this point, the lightcraft will separate from the booster; the laser will beam energy to the lightcraft thereby producing thrust, after which the lightcraft would descend and land down range. After separation, the booster would again perform cross range adjustments while performing an unpowered descent flight followed by a parachute landing, and helicopter recovery.

Figure 10 shows the mission profile for the case where the lightcraft is released at Mach 8 and conducts a laser-powered test. A laser will be positioned 40km up range from the release point, providing a 35 degree incidence angle and slant range of 50km at initiation of the test.

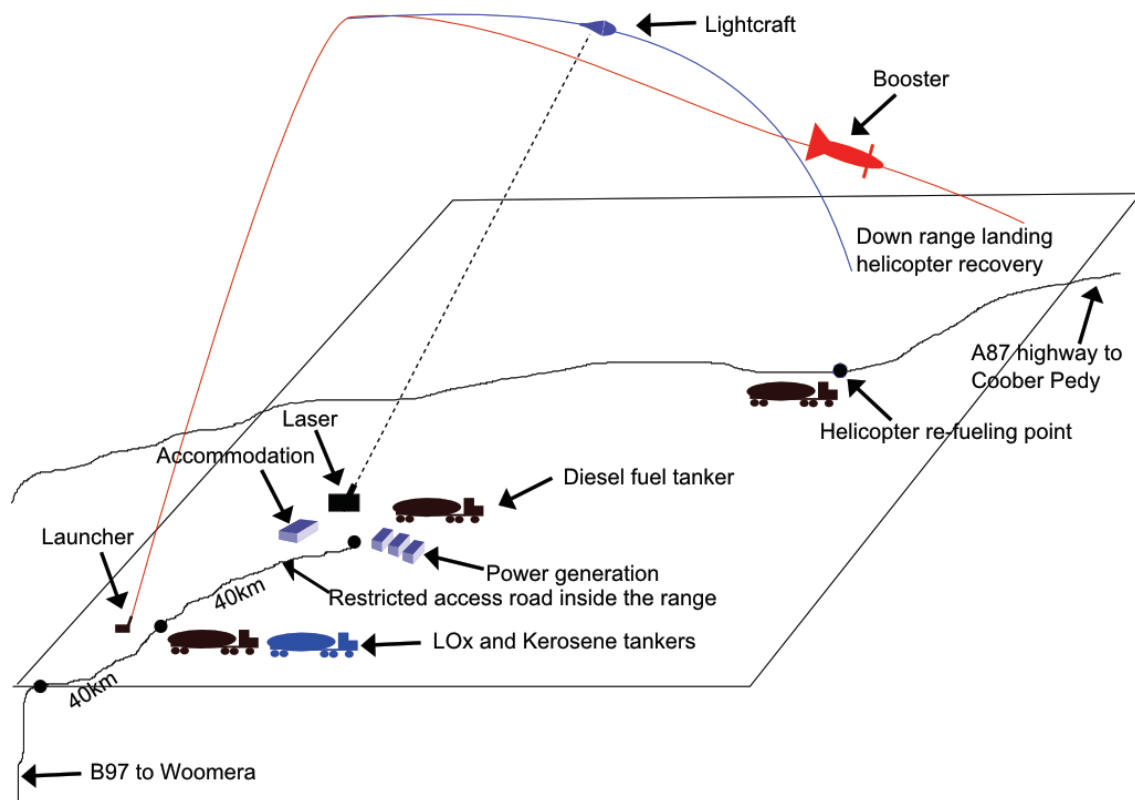


Figure 10 Mach 8 release mission profile

Approximately 40 people will be needed during the test campaign, with each test requiring approximately 1 week. Ten technicians/engineers would again be required to prepare the booster. Three range safety officers and ten range technicians would again be required as well as two defence observers. These personnel will again be housed in Woomera and would commute to the launch site each day by road.

In addition to these personnel, fifteen engineers and technicians would be required to operate the laser and power generation system. They would be housed in a camp set up within the range, about 40km downrange from the launch site. All consumables would need to be trucked into this camp, including food, water, fuel, etc.

Assuming the 10MW laser operates at 60% efficiency, approximately 18MW of power will be required to operate the laser. Although it would be possible to install a small gas turbine power station, there are a number of problems related to this, such as the availability of water. Combustion engines attached to generators or gensets are a practical alternative to a small power station. Gensets are available in both natural gas and diesel fuel variants, with similar logistics in relation to trucking and storage of the fuels. Diesel was assumed for this analysis. There are a number of options and configurations currently available on the second hand market to achieve the required power output, for example, 9 X 2MW gensets or 4 X 4.2MW gensets.

The laser and the gensets will be trucked in along a sealed road to the laser camp. The gensets will consume approximately 1800 L of diesel per test. A smaller genset will also be required to run the camp and would consume 360 L per day. One 15000 L tanker will be required for two test flights over 2 weeks.

Again, each test would require half an 8000 L iso-tanker of LOx and a seventh of a 8000 L iso-tanker of kerosene. A CH-47 helicopter will need to be leased to recover the booster from down range and return it to the launch site. As the CH-47 does not have sufficient range to complete the mission, a fuel tanker needs to meet the helicopter along the road to Coober Pedy (A87) to refuel.

Trajectory

Figure 11 shows the ground track for the Mach 8 release mission. After release, the booster is seen to bank away from the lightcraft and begin turning to the South. The lightcraft continues along a planar trajectory through the test phase for the descent and landing.

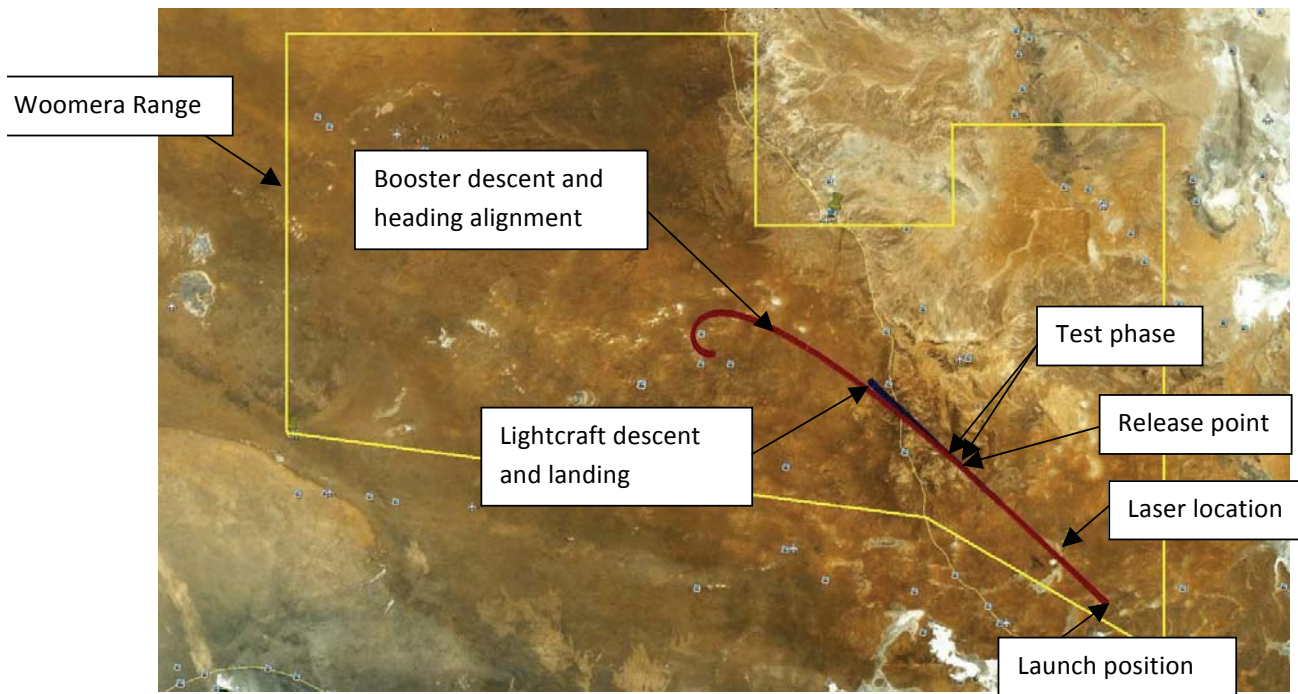


Figure 11 Ground track

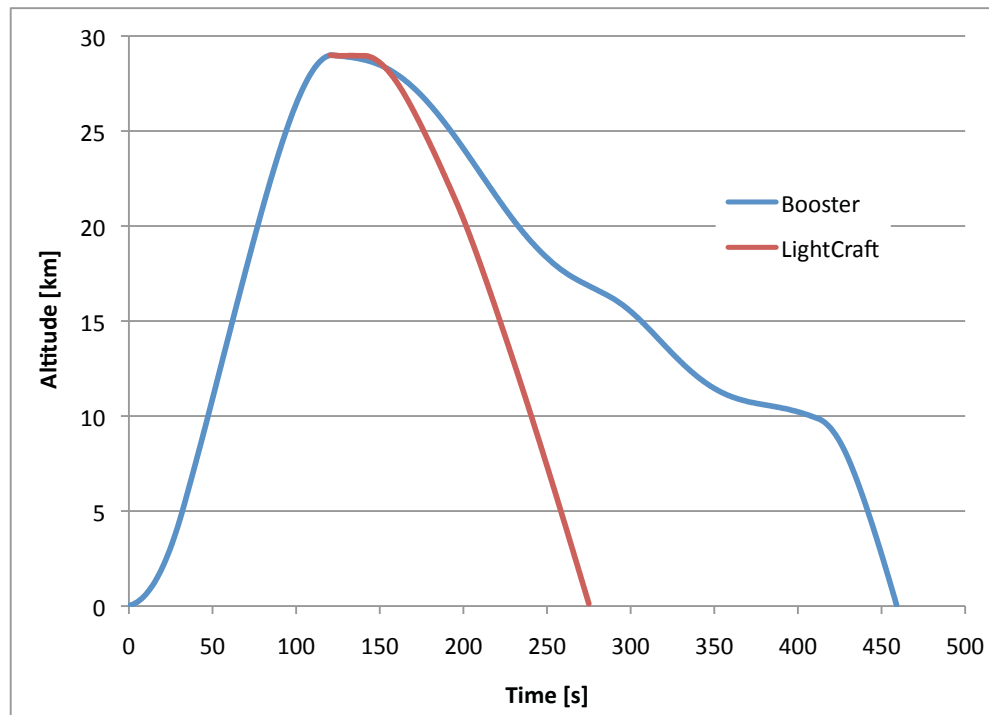


Figure 12 Altitude vs time

Figure 12 shows the altitude vs time profile for the Mach 8 release mission. As soon as the lightcraft is released, at an altitude of 29km, the booster is seen to descend to the landing site. The lightcraft has a sustained period of cruise at Mach 8 under its own power before descending and landing.

Future challenges

This test phase requires advancement in laser technology as well as a better understanding on inlet design and how it affects vehicle design and stability. To the author's knowledge no 10MW lasers exist. Lasers are becoming more powerful [6], but some advancement is required before a large enough laser is available. An advanced laser steering or control system will also be necessary to ensure the laser beam is aimed directly onto the moving lightcraft.

Another challenge will be the logistics of installing a large laser in the outback of Australia. It may need to be shipped to Woomera and built onsite as transportation of such a large laser in one piece is unlikely. The remaining infrastructure and required power generation systems can be met with existing technologies.

Some advancement in vehicle stability is needed to release the lightcraft and maintain controlled flight and this would be a major technical task as part of any future lightcraft flight test development.

Test phase 3 – ground launch

The third and final test phase will be to demonstrate ground launch of a lightcraft. The lightcraft will be launched from a launch stand above the laser. The laser will fire and provide the energy to produce thrust and propel the lightcraft. The first set of launches in the test phase will only launch the lightcraft a short distance to demonstrate launch and low speed flight control. This will be followed by flights of several hundred meters. Gradually, this range will be expanded over several tests, until it finally reaches orbit. The initial flights could be recovered in the Woomera range, however once they trajectories take the lightcraft outside the Woomera range, the craft may have to be dumped in the ocean.

Figure 13 shows the mission profile for the case for the ground-launched lightcraft.

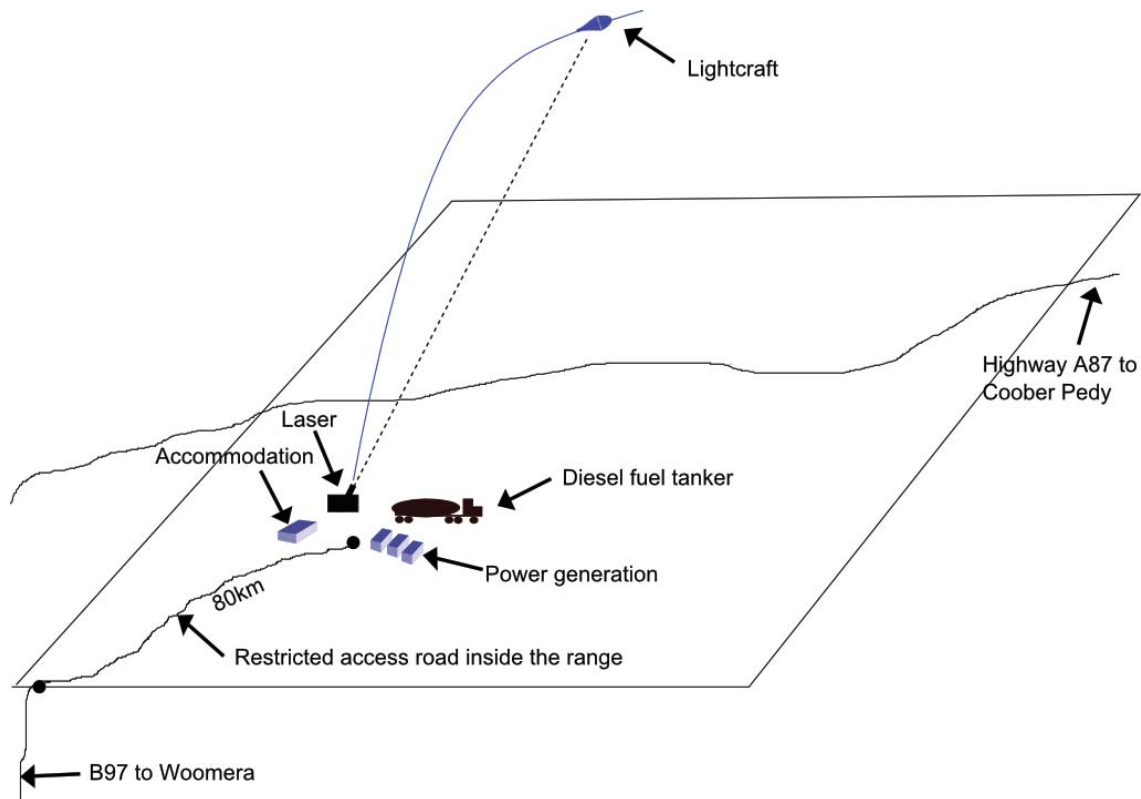


Figure 13 Ground launch mission profile

The logistics would be similar to that of phase two, except that the personnel working at the launch camp would move out to the laser camp. There would be some additional housing brought in to the laser camp to house the additional staff members. The only fuels needed for this test phase would be that for the power generation system, which would consume around 3200kg per hour. Again, supplies would be trucked into the site.

Trajectory

The trajectory modelling for this section was performed by Harrland [1] and is described in detail in Section 3 of his thesis. This model shows the lightcraft reaching an altitude of 70km, however the final target is to achieve orbit. Orbital insertion requires laser ignition/consumption of propellant; however, this part of the mission is not considered in this study.

Future challenges

In addition to the issues identified at phase 2, significant advancements in lightcraft stability and control systems would be required to launch the lightcraft from a stationary point.

Budget

The budget comprises development costs as well as costs associated with each test. The personnel costs were based on \$130,000 per year per person and 30% extra for meals and housing in existing facilities. The diesel and kerosene costs were based on \$2 per L while BOC Australia provided the LOx and propellant logistics cost estimates. The power generation system costing was based on currently available prices of second-hand systems. The helicopter operating costs were based on

estimates in Ref. [7]. The development cost for the winger booster would be around \$250mil. This estimate is based on the Space-X Falcon development cost of \$450mil [unconfirmed].

Budget – phase 1

Capital cost:

- Booster development \$250mil

Operational costs:

- Personnel \$100,000
 - Propellants \$18,000
 - Helicopter \$34,000
- Total \$162,000 per test

Budget – phase 2

Capital costs:

- Laser \$unknown
- Power generation \$1.5mil
- Housing/infrastructure \$1.0mil

Operational costs:

- Personnel \$160,000
 - Propellants \$18,000
 - Helicopter \$34,000
 - Power generation \$13,000
- Total \$225,000 per test

Budget per test – phase 3

Capital costs:

- Extra infrastructure \$200,000
- Launch structure \$500,000

Operational costs

- Personnel \$160,000
 - Propellants \$13,000
 - Helicopter \$34,000
 - Power generation \$13,000
- Total \$220,000 per test

Conclusions

A three-step approach to develop lightcraft technology was presented, looking at the mission profiles, equipment and logistics as well as personnel required. An approximate cost estimate was also provided along with the identification of major technical advancements required through the test phases.

References

1. Harrland A, Hypersonic Inlet for a Laser Powered Propulsion System, 2012, Masters Thesis, The University of Adelaide.
2. Burkhardt, J., REENT6D a Simulation and Optimization Tool for Re-entry Missions. 2000, IRS - Internal report IRS-01B7: Stuttgart.
3. Speyer, J.L., Kelly, H.J., Levine, N., and Denhams, W.F., Accelerated Gradient Projection Technique with Application to Rocket Trajectory Optimization, 1971, Automatica, Vol. 7, pp 37-43
4. Labitske, J.J., and Edwards, B., editors. Middle Atmosphere Program (MAP), Handbook Vol. 16, July 1985, SCOSTEP
5. Regan, F.J. and S.M. Anandakrishnan, Dynamics of Atmospheric Reentry. Education Edition. 1993: AIAA.
6. Birkan, M., Beamed Energy Propulsion: Research Status and Needs – Part 1, Beamed Energy Propulsion, Fifty International Symposium, American Institute of Physics, 2008.
7. Colucci. F, Upgraded Chinook: More Cargo at Higher Altitudes, National Defence Magazine, July 2002